Plume-Surface Interactions due to Spacecraft Landings and The Discovery of Water on Mars

by

Manish Mehta

A dissertation submitted in partial fulfillment
of the requirements for the degree of
Doctor of Philosophy
(Atmospheric and Space Sciences)
in The University of Michigan
2010

Doctoral Committee:

Professor Nilton O. Renno, Chair
Professor Alec D. Gallimore
Research Professor Stephen W. Bougher
Anita Sengupta, NASA Jet Propulsion Laboratory

SSI Image (SS000EFF896228288_10C96L1M1; SSI Image (SS020ESF897999668_12A30LCM1; SSI Image (SS024ESF898355027_12E50LBM1; [*Di Lorenzo* and *Kremer*, 2008]; *Courtesy of NASA/JPL-Caltech/U. of Arizona/Texas A&M/Max Planck Inst.*

"We choose to go to the moon. We choose to go to the moon in this decade and do the other things, not because they are easy, but because they are hard, because that goal will serve to organize and measure the best of our energies and skills, because that challenge is one that we are willing to accept, one we are unwilling to postpone, and one which we intend to win, and the others, too."

- *John F. Kennedy, 35th President of United States of America*

2010

DEDICATION

In memory of my beloved grandparents: Dadee (Parvati Mehta), Dadaa (Shree Nath Mehta) and Nana (Ram Krishna Joshi).

ACKNOWLEDGEMENTS

I would first like to acknowledge the unwavering support I received from my research advisor, Dr. Nilton O. Renno, Professor of Atmospheric and Space Sciences. He has provided outstanding mentorship and guidance in regards to this research investigation and the doctoral training that I received at The University of Michigan College of Engineering. He provided me with all the resources needed to start and finish this research investigation. His extensive knowledge in both engineering and planetary science opened up avenues and ideas for my research to flourish and succeed. His enthusiasm in the new discoveries that we made showed me the wonders of both planetary and aerospace sciences. Most importantly, I was excited in learning about our universe and its' various processes that we only partially understand. With detailed conversations with my advisor, I realized that we have limited knowledge of the vast final frontier which we call space.

Another mentor who allowed me to pursue my research was Rob M. Grover of the Jet Propulsion Laboratory (JPL). He put me under his wing and showed me the interesting engineering aspects of space exploration. He opened my eyes for the first time to the United States federal agency called National Aeronautics and Space Administration (NASA). He introduced me to various terminologies and reviews that NASA participates in while preparing for a spaceflight mission. Since he was the systems entry, descent and landing (EDL) lead for the 2007 NASA Phoenix Mars Scout Mission, we discussed many space system issues and risks related to this landing mission. This inspired me to conduct various engineering analyses and tests to minimize a few of the landing risks associated with the Phoenix spacecraft. Through his tenacity, I had obtained a NASA graduate fellowship that allowed me to pursue my doctorate and conduct the necessary work for the spaceflight mission. Rob has provided me with a good foundation

of systems engineering and I am quite grateful for his unwavering mentorship through my doctoral training.

Also, the entire Phoenix EDL and Science teams were very supportive of my research and encouraged me to continue my work despite momentary obstacles. Important feedback and review of our results were obtained from the Phoenix EDL Team: Erik S. Bailey, Wayne Lee, Dara Sabahi, Dr. David Adams, Robert Shotwell, Jim Chase and Dan Eldred of NASA JPL. The Phoenix Science Team who reviewed our research was: Dr. P.H. Smith, Dr. Leslie K. Tamppari, Dr. Deborah Bass, Dr. Ray E. Arvidson, Dr. Wojtek Markiewicz, Dr. Mike Mellon, and Dr. Benton C. Clark. My countless summers spent at JPL were very beneficial for I was able to work with teams on various engineering and science issues. Rob Grover facilitated these interactions which truly augmented my research experience. I would also like to thank the general support of George Chen's Section 313. Other NASA engineers/scientists contributed to my doctoral work such as Dr. Phil T. Metzger of NASA Kennedy Space Center (KSC), Clay Woosley, Ken Smith and J.T. Heineck of NASA Ames Research Center (ARC), Dr. Pieter Buning and John van Norman of NASA Langley Research Center (LaRC) and Dr. John Marshall of the Search for Extraterrestrial Intelligence (SETI) Institute.

I would also like to acknowledge my three mentors from Lockheed Martin (LM) Space Systems who first introduced me to the interesting fields of aerospace sciences and gas dynamics. Pete G. Huseman, senior manager of the Aerosciences group at LM, first presented a very interesting problem to me which eventually started my doctoral dissertation topic. Ever since that moment, he has supported all my research endeavors and provided valuable feedback. Through his guidance, I was able to interact with Doug S. Gulick, a senior engineer at LM, whose strong background in numerical modeling of transient supersonic flows strongly influenced my numerical and experimental approaches. The third mentor from LM, Tim A. Priser, space systems engineer lead, was most interested in our research for understanding the system risks associated with the last few seconds of spacecraft landing of the Phoenix spacecraft. There were many other LM engineers that provided critical support of our investigation such as Brad Haack, Greg McAllister, Joe Bomba and Jesse D. Chuhta. I would also like to thank Grady L. Romine,

one of the pioneers of our research topic, for the extensive insight he provided to our experimental approach.

As my research investigations took shape, Dr. Anita Sengupta of JPL, provided some very valuable and critical assessment of my current and future work. Her knowledge in both space systems and fluid dynamics showed me areas where more work was required. Together, we applied our research in support of the Phoenix Mars mission to the future 2011 NASA Mars Science Laboratory spaceflight mission. She also graciously volunteered her time to be on my Dissertation Committee.

There were important members of the University of Michigan College of Engineering that supported my doctoral work such as Dr. Alec D. Gallimore (Aerospace Engineering) and Dr. Steve W. Bougher (Atmospheric & Space Sciences) who both critically evaluated my dissertation and volunteered their time to being on my Dissertation Committee. Dr. Roman Hryciw (Geotechnical Engineering), Dr. Aline Cotel (Civil and Environmental Engineering) and Dr. Phil Roe (Aerospace Engineering) also provided valuable input to the research. The entire staff of AOSS such as Sandra Pytlinski, Margaret Reid, Sue Griffin, Mary Nehls-Frumkin and Bobbi Walunas has been very supportive and helpful in administrative issues during my doctoral training. Of course, I would like to also thank my previous office-mate, Dr. Jasper F. Kok, who showed me how to be a diligent and hard-working doctoral student. Other previous and present graduate and undergraduate students such as Dr. Tom Liu, Dr. Louis Musinski, Dr. Chris Deline, Amanda Brecht, Dr. Dave Pawlowski, Tami McDunn, Neal Rusche, Mark Pokora, Leslie Hall, Vijay Patel, Fernando Saca, Shaneen Braswell and Kristen Mihalka have helped me along the way. The research engineers of the University of Michigan's Space Physics Research Laboratory such as Robb Gillespie, Steve Rogacki and Ron Rizor provided immeasurable advice and support during the fabrication, implementation and operation of our experimental testbeds.

We also acknowledge the support of Dr. Ron Greeley and NASA's Planetary Geology and Geophysics Program for providing operational costs for the unique vacuum chamber facility critical to our investigation: The ASU-NASA Ames Planetary Aeolian Laboratory. This research was financially supported by the NASA GSRP Grant

NNX06AH56H, NASA, the Michigan Space Grant, and by Lockheed Martin Corporation.

The pillar through my doctoral training was my beloved wife Kasha E. Benton, who is aspiring to be a medical doctor by pursuing her education at Drexel University College of Medicine. She never stopped supporting my endeavors and always made sure that I strived to do the best work possible. Although this investigation required some time apart, she understood that this was for the betterment of my career. She has always been by my side in all my decisions and dreams. I now plan on wholeheartedly supporting her through her medical training.

I would also like to thank my father, Prem N. Mehta, and mother, Madhu Mehta, for bringing me up in understanding the importance of education. When I was younger, I may not have always valued learning, but they showed me all the opportunities that education brings. Lastly, I would not have gotten this far without the love and support of my little sister, Dr. Nidhi Mehta, who will be starting her fellowship training in Cardiology. She had the confidence that I would walk and finish this long educational journey. Many wonderful events took place during my PhD program and one of them was seeing my little sister marry a sincere and benevolent friend, Andrew E. Crooke, who is also pursuing his doctorate in English. Although I have suffered through some losses during these last 5 years, I could easily dub this the "Golden Era" of my life. I am truly grateful for such a loving and supporting family on both my side as well as my wife's side. My mother-in-law, Sally Flamer, never doubted my abilities and she left Connecticut to be with me while I was taking my qualifying exams and during my dissertation defense. Kasha's family including Polly Nugent, Al Flamer, and Tim and Amy Nugent have been a guiding light for me through this whole arduous process.

All of these individuals have played a role in helping me achieve my primary goal of applying fluid dynamics to understand a part of our solar system and technology for space exploration.

PREFACE

The best way to describe this dissertation thesis is a journey where scientific discoveries were made along the way. Not knowing what to expect or whether this research would provide new scientific insights, I set out a bold path to seek the truth. Hence, the chapters may seem disjointed, but they describe our investigations in detail and the exciting findings therein. It may be beneficial to briefly describe the sequence of events that led to the formation of my dissertation topic.

This research topic formulated from the inception of the 2007 Phoenix Mars Scout Mission in which Dr. Nilton O. Renno was a Co-Investigator. There were few concerns raised by Lockheed Martin (LM) due to rocket plume – surface interactions during the Phoenix landing phase in which they partnered with our research group to investigate, and this is presented in Chapter 2. I spear-headed this investigation and presented our results in numerous Technical Interchange Meeting reviews at LM during 2005 and 2006.

This investigation led our research group and the science and engineering teams to be concerned with rocket plume-induced dust lifting and cratering of the landing site and this is presented in Chapter 3. Although there were initially numerous obstacles to conduct this complex study such as funding and resources, I wrote proposals and discussed methodologies with my advisor and other engineers/scientists. We were then authorized to perform these studies with the support of NASA Jet Propulsion Laboratory (JPL) and NASA Ames Research Center (ARC) in which we presented our findings to both the Science and EDL teams as well as various science/engineering conferences in 2007 and 2008.

Perhaps, the most exciting moment of my doctoral training is to witness the successful landing of the Phoenix spacecraft on May of 2008 with all of my colleagues from the Phoenix Conference Center at JPL. After this momentous event, our research investigation was allowed to continue which led us to two exciting discoveries which

make the basis of both Chapters 3 and 4. As the reader will see, this investigation is quite diverse, but it provides important engineering and science insight into the final stages of a spacecraft landing on another planet and the possibility of life on Mars. Hence, this dissertation was truly a "journey" in every sense of the word.

We have submitted all three chapters for publication and these inspired further studies for future landing missions to planetary bodies such as the 2011 NASA Mars Science Laboratory (MSL) mission. Further work in collaboration with JPL for the MSL mission is documented in Appendix A and C.

TABLE OF CONTENTS

LIST OF FIGURES

LIST OF TABLES

LIST OF APPENDICES

ABSTRACT

Pulsed supersonic jets or rocket plumes have different surface flow physics than steady jets, in particular in tenuous atmospheres such as that of Mars where jets are collimated over large distances compared to their diameters. We show that plate shock formation and collapse during each cycle of pulsed jets impinging on a surface causes large pressure fluctuations capable of producing extensive erosion during spacecraft landings. Here, we study the pressure loads and erosion caused by pulsed jets of the Phoenix spacecraft on the surface of Mars and its implications to engineering and science.

While steady thruster jets caused only modest surface erosion during the landings of previous spacecraft on the moon and Mars, the pulsed jets from Phoenix led to extensive alteration of its landing site on the martian arctic, exposed a large fraction of the subsurface water ice under the lander, and led to the discovery of evidence for liquid saline water on Mars. We report the discovery of the 'explosive erosion' process that led to this extensive erosion and evidence for liquid water. We show that the impingement of supersonic pulsed jets fluidizes porous soils and forms cyclic shock waves that propagate through the soil producing erosion rates more than an order of magnitude larger than that of other jet-induced processes. The understanding of 'explosive erosion' allows the calculation of bulk physical properties of the soils altered by it, provides new insights into the behavior of granular flow at extreme conditions, and explains the alteration of the Phoenix landing site at the northern arctic plains of Mars.

We then show new photometric evidence that the Phoenix spacecraft imaged liquid saline water in the arctic, and that deliquescence causes liquid water to sporadically flow in the polar region. This finding also corroborates the hypothesis that the thermodynamics of freezing/thaw cycles leads to the seasonal formation of liquid saline water where ice and salts exist near the martian surface. Finally, we show broadband

spectral signature of liquid brines in flow-like and pond-like features on defrosting polar dunes. This has important implications for geology, geochemistry and the habitability of Mars.

CHAPTER 1

Introduction

1.1 Background

Mars is the planet most similar to Earth in the solar system. Earth and Mars have roughly the same land area. Both planets have large sustained polar caps and a 23 degree tilt in the axis of rotation, leading to seasonal variability. They both have large dust storms and atmospheres with some similar chemical species. However, the martian atmosphere is tenuous with surface pressure 1% of that of the Earth. Hence, Mars provides scientists with a simple comparative laboratory for studying terrestrial climate change, geophysics and perhaps the evolution of life in spite of being smaller with a lower gravitational field and much colder than Earth. One of the most compelling questions in space exploration is whether Mars ever had microbial life.

One of the necessary conditions for the existence of life is the presence of liquid water. Water is the medium for all biological processes on Earth and without it, life, as we know it, would not exist. Hence, we believe this molecule is vital for biological processes on Mars. Water is also the primary medium that shaped the geological landscapes on Earth and possibly on Mars as well. The first direct evidence of water on the Martian soil was found by the National Aeronautics and Space Administration (NASA) Mars Global Surveyor's (MGS) Gamma Ray Spectrometer [*Boynton et al*, 2002]. The evidence for water is the decrease in the epithermal neutron flux towards the poles as depicted in Figure 1.1. This discovery led to the development of the NASA 2007 Phoenix Mars Scout mission which first confirmed the existence of water ice at the northern polar region [*Smith et al*., 2009]. In addition, Phoenix discovered physical and thermodynamic evidence for liquid water on its landing site [*Renno et al.,* 2009].

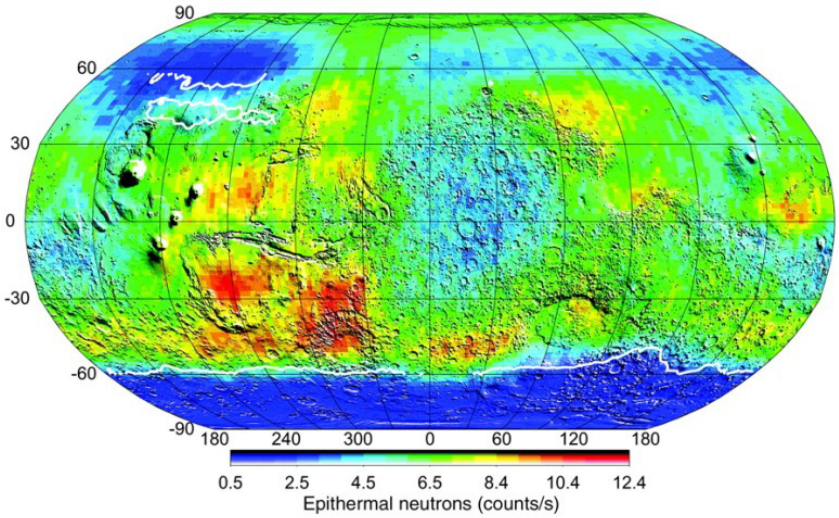

Figure 1.1 Epithural neutron flux of the entire surface of Mars. Minimum fluxes in the polar region suggest the presence of water ice [*Boynton et al.,* 2002].

One of the most important results of the Phoenix Mars mission was the potential discovery of present day liquid water at pressures and temperature below 1 kPa and 250 K, respectively. At these temperatures and pressures, pure water could only exist as either ice or vapor. Thermodynamically, liquid water could only be stable on the martian surface if it contained relatively high concentrations of salt ions. Surprisingly, after the discovery of evidence for liquid water, Hecht et al. [2009] and others found ~5% by mass of soluble salts in the martian soil. Consequently, the freeze/thaw cycles ranging from diurnal to geologic time-scales (T_{clim}) may lead to the formation of highly concentrated pockets of liquid brines as shown in Figure 1.2. Pure water ice precipitates when dilute mixtures are cooled and this leads to an increase in the salt concentration until the eutectic temperature (T_{eut}) is reached. When highly saline solutions exist, salts precipitate when concentrated mixtures are cooled until the eutectic solution is reached, and the solution freezes.

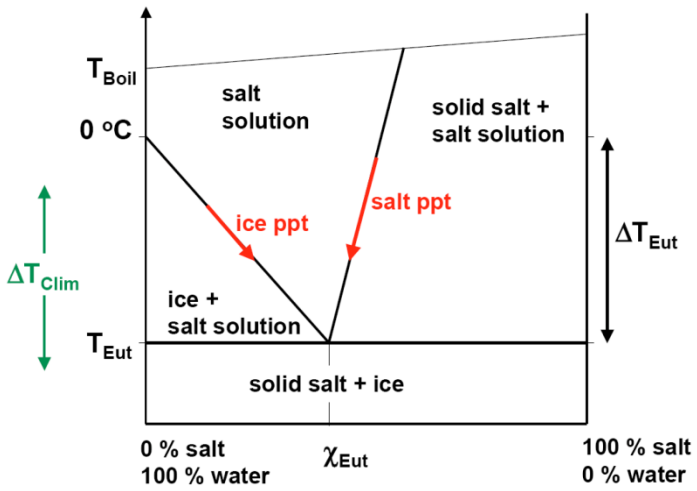

Figure 1.2. Sketch of the phase diagram of a brine solution [*Renno et al.,* 2009].

Renno et al. [2009] show that liquid saline water may form by deliquescence at the martian surface, a process in which a hygroscopic substance absorbs atmospheric water vapor until dissolution. The partial pressure of water vapor at the Phoenix landing site ranges from 0.3 to 2 Pa [*Renno et al.,* 2009; *Zent et al.*, 2009], which is higher than the deliquescence relative humidity (RH_D) of various salts seen at the landing site. Hence, this leads to absorption of water vapor and formation of brines. Since the polar regions of Mars possess water ice (ground ice and frost), salt and atmospheric water vapor [*Smith et al.*, 2009], interfacial liquid saline water should be convincingly ubiquitous. As a result of the similarities of Earth's sister planet and the increasing possibility of Mars harboring life, NASA developed its main theme for the robotic Mars Exploration Program, "follow-the-water".

As depicted in Figure 1.3, NASA successfully completed six surface robotic missions and five orbiting missions to the Red Planet since 1975. The NASA Viking 1 spacecraft was the first to successfully land on the martian surface, at western Chryse Planitia [*Shorthill et al.*, 1976]. The Viking spacecraft, the Mars Pathfinder and the Spirit and Opportunity Mars Exploration Rovers discovered hints of past liquid water on Mars. For example, Opportunity detected large concentrations of hematite at Eagle Crater, which most likely formed in the presence of liquid water [*Squyres et al*., 2004]. The high-resolution images from the MGS spacecraft detected gullies in the Newton Basin which have been hypothesized to be formed by trickling aqueous solutions of snow melt

[*Christensen*, 2003]. According to *Carter et al.* [2010] the Compact Reconnaissance Imaging Spectrometer (CRISM) and OMEGA spectrometers on-board the Mars Reconnaissance Orbiter (MRO) and Mars Express orbiters detected hydrated phyllosilicates on the northern plains of Mars. Chloride-bearing materials that form in aqueous solutions are found in localized regions less than 25 km^2, but are detected in small amounts in the southern highlands [*Osterloo et al.,* 2008]. The "follow the water" theme for space exploration resulted in the design and development of the MRO in 2005 and the Phoenix Mars Scout mission in 2007. The main goals of both of these missions were to confirm and characterize water and possibly organic compounds on the martian surface. Only the seventh and newest lander called Mars Science Laboratory (MSL), ready to depart Earth in 2011, is equipped with instruments to search for organics and signs of life [*Atreya et al*., 2007]. Unfortunately, many missions to the Red Planet failed either during the trip or during the treacherous landing phase.

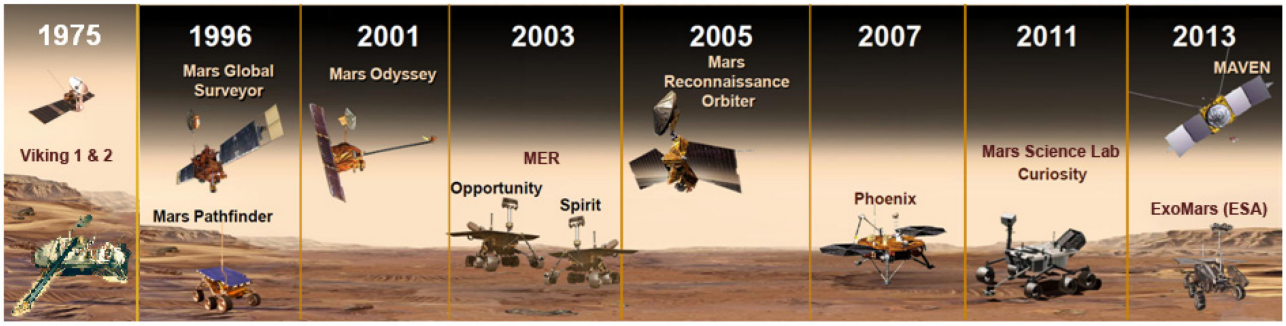

Figure 1.3 Robotic space exploration of Mars from 1975 to 2013 (ExoMars rover was delayed to 2018). *Courtesy of NASA/JPL-Caltech*

Spaceflight Mission	Year	Agency	Comments
Mars 2 & 3	1971	RFSA	Crashed on landing/ceased after 20 sec
Mars 6 & 7	1974	RFSA	Crashed on landing/entered heliocentric orbit
Phobos 1 & 2	1989	RFSA	Landing sequence was not initiated
Mars Polar Lander	1999	NASA	Crashed on landing
Beagle 2	2004	ESA	Lost contact after entry

Table 1.1. Eight failed spaceflight missions to Mars in the last four decades. RFSA = Russian Federal Space Agency; ESA = European Space Agency

1.2 Motivation

According to Table 1.1, more than 60% of surface missions to Mars failed with more than 50% of those failures occurring during the entry, descent and landing (EDL) phase. This landing sequence must remove more than 99% of the craft's kinetic energy

within seven minutes in an approximate distance of 3500 km. Hence, there are many engineering challenges during this sequence because: (a) the atmosphere is thick enough to cause significant dynamic loads and heating, but too thin to decelerate the spacecraft for soft landing; (b) the hazardous surface environment is either caused by landing-induced disturbances or pre-existing boulders, craters and variable atmospheric dust content; (c) it is difficult to simulate and test the end-to-end EDL sequence [*Braun and Manning*, 2006]; (d) the short landing phase makes it difficult to employ redundant systems; (e) accurate landing requires highly effective aerodynamic control over the flight path. To further elucidate the intricacies of landing a spacecraft on planetary bodies, the various phases of EDL are briefly described below and depicted in Movie D1, Appendix D.

Each EDL phase is described schematically in Figure 1.4 [*Grover and Desai*, 2004; *Bailey*, 2008]. The spacecraft first enters the martian atmosphere (entry phase) enclosed by the heat shield and back shell. During the hypersonic phase, there is maximum heat and deceleration loads as shown in Figure 1.4. Once the deceleration loads increase to a certain threshold value, the parachute is deployed (parachute phase), reducing the spacecraft to subsonic speeds. The heat shield is jettisoned and the radar locks onto the surface to accurately determine the spacecraft altitude. At pre-determined altitude, the lander separates from its backshell and parachute and descent rocket motors are warmed for the terminal descent phase. Radar locking is important before separation, because if the separation is too early there may not be enough fuel for a powered descent to the surface or if it is too late the spacecraft may impact the surface before stabilizing. Gravity turn aligns the spacecraft thrust vector with the velocity vector in the opposite direction. When thrust is applied, this reduces both the vertical and horizontal velocity components during terminal descent. Prior to the gravity turn, there may be an additional thrust applied off-nadir to prevent back shell recontact with the spacecraft (Backshell Avoidance Maneuver). Once gravity turn has been completed, the rocket motors are throttled or pulsed to achieve a constant descent velocity until touchdown. This spans the last ~50 m of flight. A single point failure in either of these phases could cause the spacecraft to crash on the surface. Hence, many simulations and adequate component testing is required for minimizing mission risk. The primary goal of the investigation

described in this thesis was to reduce the risks associated with the constant velocity phase of terminal descent of the Phoenix EDL sequence.

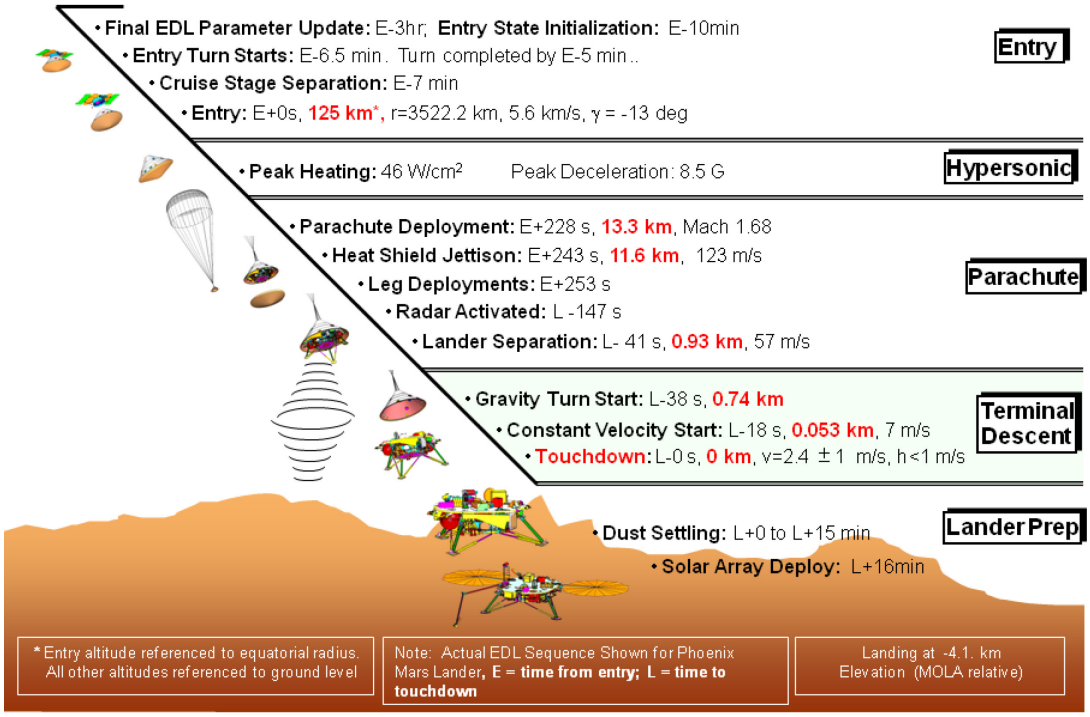

Figure 1.4. Phoenix entry, descent and landing (EDL) sequence. [*Bailey et al*., 2008]

During the constant velocity phase for a typical powered descent sequence, the rocket motors fire with ~2000 N of thrust for a ~ 350 kg lander. There are four main risks during the terminal descent phase as shown in Figure 1.5: (a) aerodynamic loads on the spacecraft, (b) site alteration, (c) ejecta accumulation and (d) surface contamination. All of these risks are dependent on the complex plume-surface interactions. During this phase, the spacecraft experiences large aerodynamic loads during the last 10 m of descent. For example, lift loss and ground effect forces, and asymmetric torques can destabilize the spacecraft. These effects are mainly the results of plume-surface interactions. These plumes can interact with each other, the surface and re-circulate back up into the lander base augmenting the thrust vector (ground effect) [*Gulick*, 2006]. For example, it was unexpectedly discovered by looking at archived and unsubstantiated results of numerical simulations that MPL suffered from high lander base pressures during descent. Jet entrainment causes a downward pressure force when the spacecraft approaches the surface, and this leads to lift loss [*Huseman and Bomba*, 2000]. This

effect can reduce thrust by about 60% close to the surface [*Krothopalli et al.*, 1999]. Hence, these two competing effects can lead to large instabilities prior to touchdown. According to the NASA JPL Special Review Board on the Loss of the Mars Polar Lander (MPL), "plume interactions should be modeled and verified by test for all future landers." According to the report, these complex interactions may have been one of the reasons for MPL failure [*Whetsel et al.*, 2000]. All of these areas are a potential concern for the Phoenix and MSL spacecrafts. However, the aerodynamic loads may not be a large issue for MSL due to a relatively large nozzle-to-surface height.

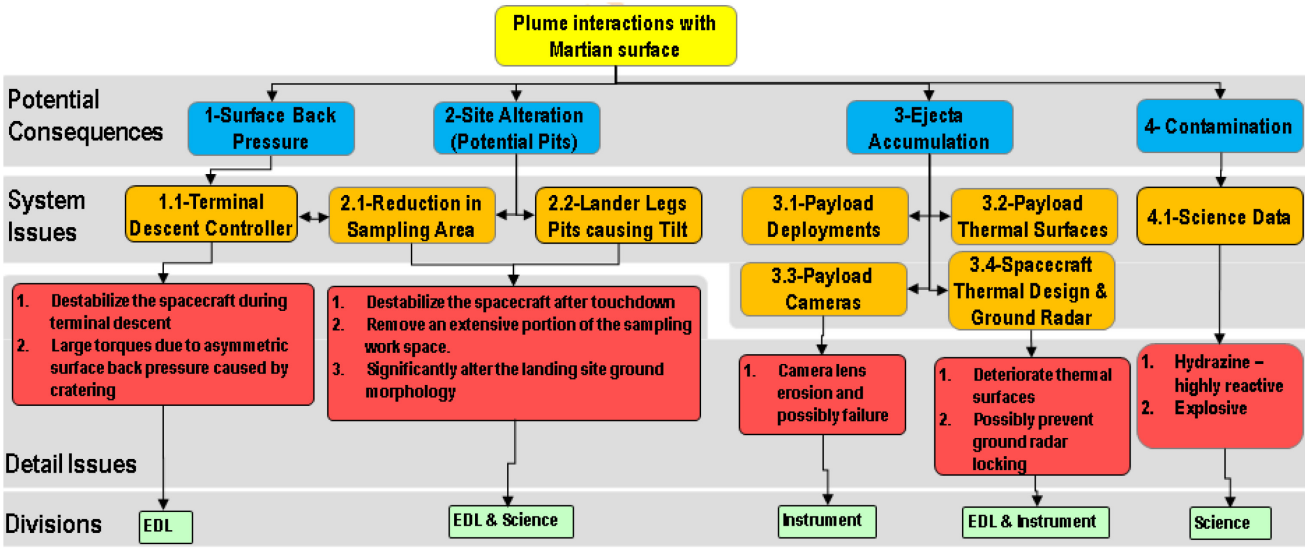

Figure 1.5. Risk assessment of a space mission due to plume-surface interactions

Cratering and erosion developed by high thrust and supersonic exhaust plume interactions has the potential to lead to the loss of planetary missions. Jet-induced cratering can lead to large trenches that can tilt or tip-over the spacecraft upon touching down [*Whetsel et al.*, 2000]. The craters formed during this process can lead to asymmetric deflection of the exhaust plumes, resulting in asymmetric torques on the base of the spacecraft. Another problem is that high-speed ejecta can impinge on the payload and the lander causing damage and destabilization during descent [*Gulick*, 2006]. Ejecta can lead to instrument and thermal hardware erosion and reduce visibility, preventing radar locking [*Sengupta et al.*, 2009]. Extensive ejecta on solar panels may reduce power

and lead to the loss of the spacecraft. Although plume-surface interactions can cause engineering problems, it is also a concern for science.

Predicting the extent of erosion and deposition at a landing site is of great benefit to science operations [*Arvidson et al*., 2009]. For example, static landers are able to sample and analyze areas that are not contaminated by the exhaust plumes. Knowledge of the altered ground morphology in conjunction with a good understanding of plume-soil interactions provide estimates of the mechanical properties of soil, as done by the NASA Surveyor [*Jaffe,* 1968] and Viking missions [*Shorthill et al.*, 1976]. Rocket plume induced cratering may uncover scientific clues within the deep subsurface of planetary bodies. In order to accurately predict cratering at landing sites, knowledge of the type of propulsion system used is imperative.

Liquid, solid and electric propulsion systems are used today for ascent, cruise and descent of launch vehicles and spacecrafts. However, the focus of this dissertation is the use of retro-propulsion for spacecraft landing architectures, and liquid propellant systems provide more diversity in operational modes and as a result are desired for landing spacecrafts. Liquid rocket propulsion systems are either pulsed or throttled [*Sutton and Biblarz*, 2009]. All space missions to Mars prior to 1998 used throttleable descent engines that allow continuous thrust modulation, forming steady-state supersonic exhaust plumes [*Romine et al.*, 1973; *Stitt,* 1967]. The 1998 NASA Mars Surveyor Mission and 2007 Phoenix Scout Mission used a new low cost pulse-modulated descent engine [*Martin et al.*, 1998]. Thrust is simply varied by dynamically controlling the duty cycle, the on-time within each pulse, and the pulse frequency. From water-hammer [*Martin et al.,* 1998] and cold start validation [*Frei et al.,* 2001] tests, this system proved to be robust with respect to the dynamic loads on the spacecraft and thrust ignition at atmospheric temperatures of 205 K. However, no studies of plume-surface interactions due to pulsed supersonic jets in tenuous atmospheres had been conducted [*Gulick*, 2006]. There was no knowledge on how impinging pulsed jets would affect the aerodynamic loads on a spacecraft or how a landing site would be altered by it [*Whetsel et al*., 2000]. The design and configuration of the Phoenix descent engine nozzles were considerably different from the Viking shower head nozzles as shown in Figure 1.6. Hence, scientists and engineers did not know if past studies conducted for the Viking missions would be

applicable to these pulsed engines. Because of the loss of MPL with a similar pulsed-modulated propulsion system, this was considered to be a significant mission risk. Thus, the Phoenix Project was encouraged to study plume-surface interactions [*NASA JPL (Phoenix CDR)*, 2004]. Our group at the University of Michigan proposed to conduct this research into two different phases: (a) plume-surface flow physics and (b) cratering dynamics. These investigations led to the third phase of our research: (c) evidence for water ice and liquid saline water on Mars. We will briefly discuss past research conducted in these three phases.

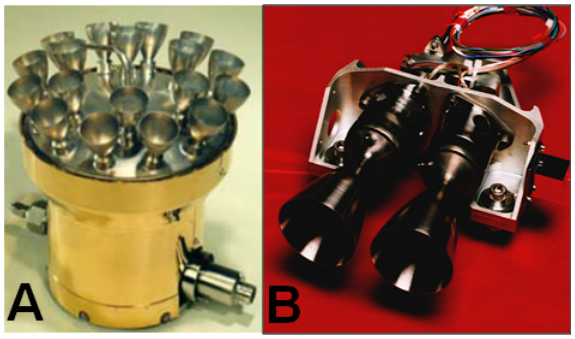

Figure 1.6. Terminal descent engines. (A) 18-nozzle Viking Rocket Engine Assembly [*Dawson et al*., 2008] and (B) MR-107 Phoenix Rocket Engine Motor (REM) [*Gulick*, 2006]

1.3 Prior research

Past work conducted for plume-surface flow physics were mainly done at low Mach numbers (<3), near field impingement distances (below 15 nozzle exit diameters, *d*) and at terrestrial atmospheric conditions of 101.3 kPa and 300 K. Although this provided valuable information with respect to acoustic and heat transfer applications, these conditions do not adequately simulate the flow physics of spacecraft landings on Mars. However, some insightful information into the flow physics was provided by these pioneering studies. It was determined that surface pressure is highly dependent on nozzle area ratio and nozzle contour geometry [*Romine et al.,* 1973]. *Vick and Andrews* [1966] first discovered that the surface pressure fields were highly dependent on the nozzle to surface distance. As discussed in detail in Section 2.6, three different shock structures of the supersonic thruster plumes were first observed by varying the nozzle-to-surface distance (4*d* to 400*d*) and nozzle exit to ambient pressure ratio (expansion ratio) [*Adamson and Nicholls*, 1967]. The first extensive characterization of these parameters in the tenuous martian atmosphere (<1 kPa) was done by Romine et al. [1973] during the

design phase of the Viking propulsion system. This provided important information such as the plume structure (Fig. 1.7A) and spatial ground pressure profiles (see Chapter 2) for steady supersonic jets. However these tests were limited because the ambient pressure would increase by a factor of two or three from martian conditions during the tests and they were constrained to altitudes of less than 35 nozzle exit diameters, where such interactions are observed up to a height of ~100*d*.

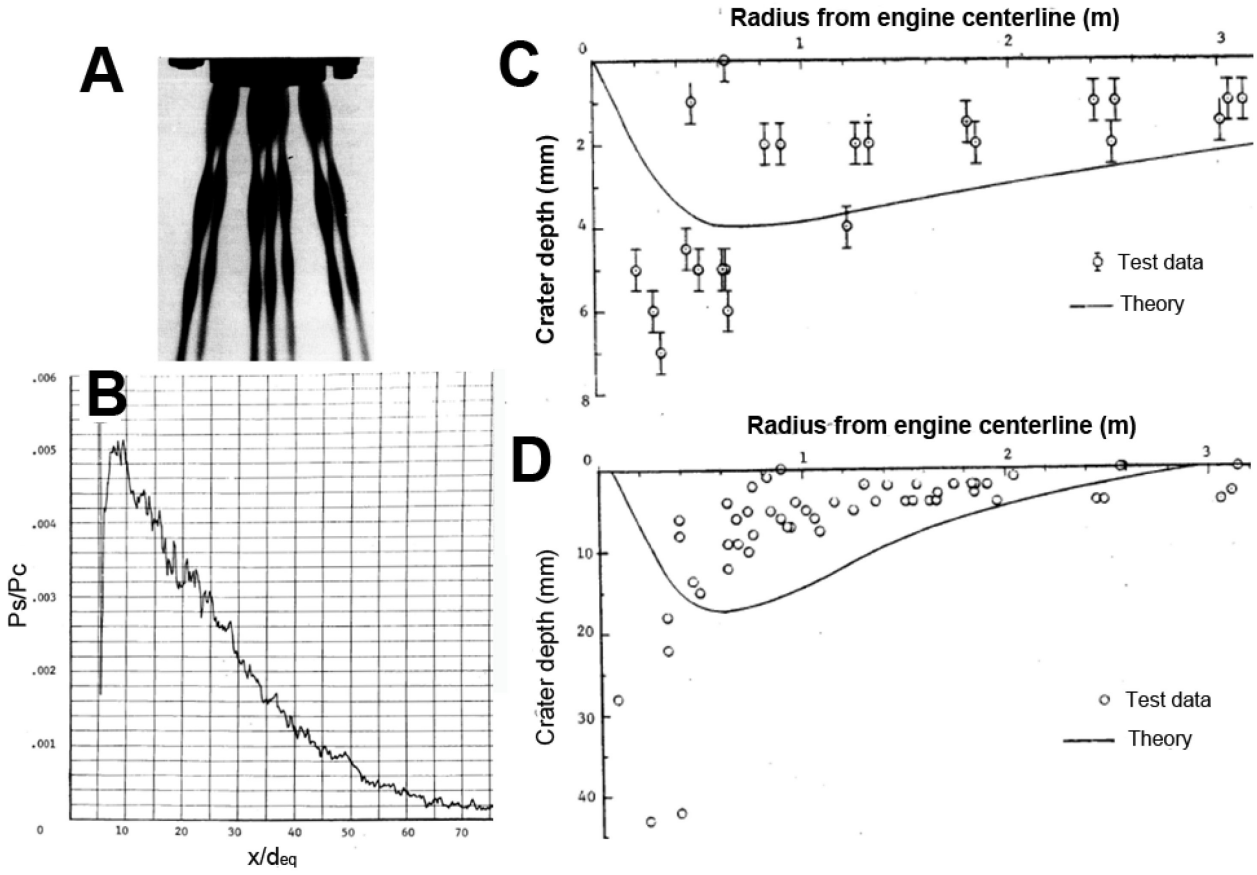

Figure 1.7. NASA Viking site-alteration test studies. (A) Shadowgraph image of the plume structure of cold gas N_2 supersonic jets with similar Viking showerhead nozzle configuration [*Romine et al.*, 1973]. (B) Normalized surface impingement pressure vs. normalized axial distance for prototype Viking rocket motor exhaust plume at Mars atmospheric pressure [*Romine et al*., 1973]. Crater depth and radius due to prototype Viking rocket motor exhausting into lunar nominal soil (C) and dune sand (D) at Mars atmosphere [*Romine et al.*, 1973].

There are only a few studies of cratering dynamics caused by steady supersonic jets in tenuous atmospheres. The main reasons for such limited tests are the fact that most partial vacuum chambers have to be clean for space hardware testing and hence, could not be used for these types of tests [*Greeley et al*., 1980]. Also, a significantly large

vacuum chamber (> 2000 m^3) was needed to perform relatively long duration tests to simulate spacecraft landings without large increases in the atmospheric pressure [*Braun and Manning*, 2006]. These full-scale experiments are also too expensive for typical spaceflight missions. Past studies were mainly done at either NASA Langley Research Center (LaRC) or NASA Lewis Research Center in the 1960s and 1970s [*Land and Scholl*, 1966; *Clark*, 1969; *Clark*, 1970]. Previous studies of jet-induced cratering dynamics in tenuous atmospheres in support of the Apollo, Surveyor and Viking missions were relatively rudimentary with limited documentation [*Romine et al.*, 1973; *Metzger et al.,* 2010]. Theories for predicting the crater dynamics by Alexander et al [1966] were not supported by visualization. Most of these studies only focused on the final crater morphology. The quarter-space and half-space techniques developed in 1976 for impact cratering studies first allowed an accurate visualization of both transient crater growth and ejecta trajectory. Unfortunately, such investigations were not conducted for the 1998 Mars Surveyor Mission. Hence, only limited analysis of the transient cratering process due to supersonic jet interactions exist.

However, these earlier and more recent studies did provide some insight into the various jet-induced erosion processes. There are four mechanisms which will be discussed in detail in Chapter 3 that lead to jet-induced erosion: (i) viscous shear erosion [*Shorthill et al*., 1976a]; (ii) bearing capacity failure [*Alexander et al.*, 1966]; (iii) diffusion-driven flow [*Metzger et al.*, 2009]; and (iv) diffuse gas erosion [*Scott and Ko*, 1968]. Earlier studies showed that underexpanded thruster plumes in lunar atmospheres leads to viscous shear erosion. The investigation conducted by Romine et al. [1973] at NASA White Sands Test Facility was the only in-depth theoretical and experimental study of the interactions of steady under-expanded jets with granular media at martian conditions. Their study led to the development of shower head nozzles in order to minimize cratering of the landing site (Fig. 1.7 B,C). This design was developed to substantially increase turbulent mixing between the jets and decrease the surface impingement pressure below the cratering threshold. This provided a wealth of knowledge that the Viking science and engineering teams used and formed the basis of our investigation. Currently, no robust numerical models or analytical solutions exist to simulate jet-induced cratering dynamics, but various academic and NASA centers are in

the process of developing them [*Metzger et al.*, 2009]. Before a robust model can be developed, extensive experimental tests at low (<1000 Pa) to vacuum pressures (~1 x 10^{-5} Pa) are needed. Theoretical and experimental investigations of the granular flow physics are the first steps in understanding cratering dynamics.

Granular media refers to any system composed of relatively macroscopic, discrete particles small in comparison with the length scale of the system. Granular flows are these particles set into motion. They are a subset of two-phase flows composed of solid particles and interstitial liquid or gas. Two types of general forces produce granular flows: pressure contact forces and interstitial fluid forces (e.g. cohesion, drag, lift, electrostatics etc.). Such flows lead to important natural phenomena such as sand dunes, impact craters, avalanches and landslides [*Pudsaini and Kroner*, 2008]. Granular flow physics are readily observed on Mars, because the martian surface is mainly covered with a centimeter to meter scale of basaltic sand. The particle size for martian regolith ranges from <15 μm to >1000 μm [*Shaw et al*., 2009].

Granular media can exist in distinct regimes analogous to the three phases of matter: solid, liquid and gas [*Jaeger, Nagel and Behringer*, 1996]. These regimes are dependent on how they are prepared and excited. There are many fluid dynamic structures observed for granular flows such as convective rolls [*Knight et al*., 1996], geyser-like excitations (oscillons) [*Umbanhowar et al.*, 2001], longitudinal vortices in chute flows [*Forterre and Pouliquen*, 2001], dead zones (regions of stationary deposits) [*Gray, Tai and Noelle*, 2003], particle-free regions and shock waves [*Amourechene and Kellay*, 2006]. The focus of this study is on shock waves within granular flows subject to jet impingement, but there are other applications where these structures are observed. The formation of shock wave features within rapid-granular flows around obstacles are readily observed from experiments and numerical simulations [*Gray, Tai and Noelle*, 2003; *Amourechene and Kellay*, 2006]. These flow structures are referred to as granular shock waves. Huang [2006] and Bougie et al. [2002] show that granular shock waves form and propagate in vibrofluidized granular media forced by oscillations of a solid plate. Experimental and numerical simulations show the propagation of a single granular shock wave results from the high-velocity impact of a projectile [*Schultz et al.*, 2007]. As further described in Chapter 3, shock waves are more commonly formed in granular

media than in gas because the sound speed is much lower in granular media [*Liu and Nagel*, 1992]. However, investigations of shock wave propagation in vibrofluidized granular media have only recently been investigated and are scarce [*Huang*, 2006]. In addition, investigations of the shock and flow physics of granular systems subject to interactions with supersonic jets are virtually non-existent.

Another focus of our research, which developed from site-alteration studies, is the search for water on Mars in both the liquid and ice phases. The consensus among planetary scientists is that Mars is a desolate and dry planet. Although only recently there were suggestions that large quantities of subsurface water ice likely existed in the polar region, this idea needed to be confirmed by in-situ analysis [*Boynton et al*., 2003]. Bandfield et al. [2003] found only trace amounts of magnesium carbonate (2-5% by weight) in the martian dust, supporting the idea that liquid water was not a major contributor to the geochemistry and geology of Mars. Also, olivine, which is easily transformed into other minerals in contact with liquid water, was widely detected at Nili Fossae by MGS's Thermal Emission Spectrometer, supporting the idea that Mars has been extremely dry on geological time scales [*Hoefen et al*., 2003]. Gullies found on Mars may not have developed by trickling aqueous solutions, but may be a direct result of landslides and wind erosion as seen on the moon [*Bart*, 2007] and observed by High Resolution Imaging Science Experiment (HiRISE) on board MRO [*McEwen et al*., 2009]. One of the goals of this dissertation is to test the idea that both ice and small amounts of liquid saline water exists on present-day Mars.

This research was a journey into unchartered realms that led to very interesting and exciting discoveries. The general methodology behind my dissertation topic is charted in Figure 1.8.

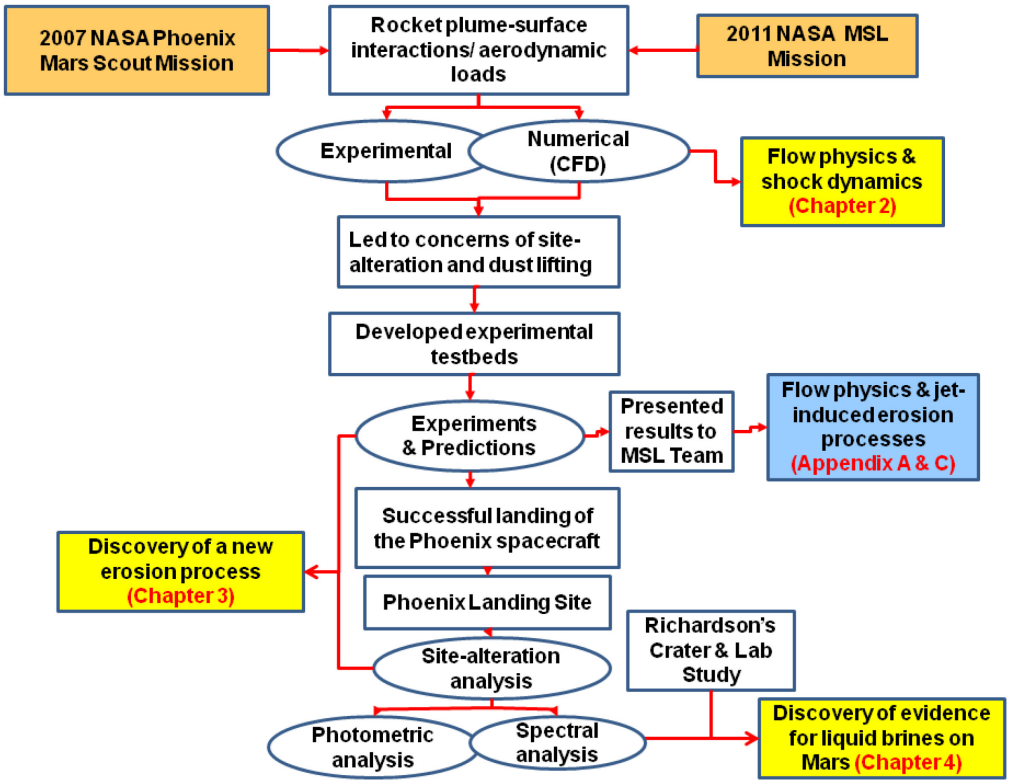

Figure 1.8. Flow chart of dissertation topic.

1.4 Central Research Themes

This dissertation seeks to provide a comprehensive understanding of plume-surface interactions caused by spacecraft landings and the various processes that led to the discovery of water on Mars. Although most of the results in the Chapters are either from or applied to the Phoenix Mars Scout Mission, we have also presented considerable research in the Appendices in support of the future Mars Science Laboratory (MSL) Mission.

What is the flow physics of impinging supersonic jets in tenuous atmospheres?

In order to address this question, we developed an experimental testbed and conducted various experiments at University of Michigan and NASA Ames Research Center. In Chapter 2, we analyze measurements of the exhaust plume composition for the full-scale Phoenix descent engine during tests at Aerojet Corporation in Redmond, Washington. This provides a detailed assessment of the potential contamination of the landing site during the Phoenix descent. We also analyze the interaction of the Phoenix plume with impermeable surfaces. We show that pulsed supersonic jets in tenuous (e.g.,

martian) atmospheres behave differently than steady jets. We compare the results of experiments with that of compressible computational fluid dynamic simulations from a few numerical codes and theory. Appendix A provides more details on the flow physics of steady supersonic jets for the purpose of simulating the plume effects due to the landing of MSL, the next NASA Mars mission.

What are the cratering dynamics associated with the impingement of pulsed jets into granular media and how does this compare to other jet-induced erosion processes?

We developed an experimental testbed at the University of Michigan and ran it in a large vacuum chamber at NASA Ames Research Center. We conducted various subscale site-alteration experiments for the Phoenix and MSL missions. In Chapter 3, we describe the results, physics and applications of jet-induced erosion processes and report the discovery of explosive erosion. Appendix B provides further calculations of this process. Appendix C provides a comprehensive analysis of erosion rates on planetary bodies due to spacecraft landings based on the results of previous spaceflight missions and our investigations for the Phoenix and MSL missions.

How water was discovered at the Phoenix landing site and what are its implications?

Through experimental and numerical simulations and the analysis of images taken by various spacecrafts described in Chapter 3, we show that the erosion dynamics due to the Phoenix landing phase led to a large exposure of water ice, extensive erosion and to the discovery of evidence for liquid brine at the landing site. Along with physical and thermodynamical evidence for liquid saline water, we show in Chapter 4 photometric and broadband spectral evidence for liquid brines on Mars.

We start this investigation by determining the rocket plume composition to ascertain the potential contamination at the Phoenix landing site, and then we embark on new studies of plume-surface interactions during Phoenix descent.

CHAPTER 2

Effects of the Phoenix Lander descent thruster plume on the Martian surface

Composition of the Phoenix descent thruster plume and the flow physics of impinging pulsed supersonic jets at Mars atmospheric pressure

This chapter describes an article published in the *Journal of Geophysical Research-Planets: Phoenix Special Issue* in 2008. The complete reference is: Plemmons, D. H., M. Mehta, B.C. Clark, S. P. Kounaves, L.L. Peach, N.O. Renno, L. Tamparri and S.M.M. Young (2008) Effects of the Phoenix Lander descent thruster plume on the Martian surface, *J. Geophys. Res.*,113, E00A11.

2.1 Introduction

The final descent and touchdown phase of the Phoenix Lander is controlled by twelve hydrazine (N_2H_4) monopropellant retro-rocket engines in pulsed mode, which could result in the impingement of some of the exhaust products onto the Martian regolith at the landing site. The Phoenix engines use pulse frequency and duty cycle control to dynamically throttle power during descent [*Wong et al*., 2002].

There was concern among the Phoenix Science Team that the exhaust products could interact with and alter the natural compounds in the Martian soil. There was also concern that unburned hydrazine and potential impurities in the fuel could contaminate the landing site. Finally, site-alteration and dust lifting by the interaction of the pulsed jets with the Martian regolith was also a concern. These same concerns are applicable for the MSL descent stage spacecraft.

To address these issues, the Phoenix Science Team performed extensive analysis of the hydrazine fuel, the thruster exhaust products, and the dynamical interaction of the exhaust plume with the surface. These efforts included: (1) selecting the cleanest, driest

propellant available for the Mission; (2) assaying and documentation of the Mission propellant; (3) conducting experimental plume signature identification during the hot-fire engine qualification testing of the flight motors using a batch of the Mission propellant; (4) capturing sample exhaust gases from these tests for use in future laboratory analysis; (5) extensive laboratory testing, computational modeling and analysis; and, (6) preserving a batch of the Mission propellant and a back-up rocket motor for potential future testing, should this be warranted. Computational and experimental studies have been performed on the products of the catalytic hydrazine decomposition in order to understand the potential physical interactions of the rocket plume with the Martian surface.

A very brief discussion of two of the Phoenix Lander primary scientific instruments that would benefit from the plume diagnostics data and analysis efforts is included in this section to provide context for the investigation. A more detailed description of these instruments is included in other manuscripts in this special issue [*Boynton et al.,* 2007*; Kounaves et al.,* 2007].

The Microscopy, Electrochemistry and Conductivity Analyzer (MECA) is a combination of scientific instruments including a wet chemistry laboratory (WCL), optical and atomic force microscopes, and a thermal and electrical conductivity probe. MECA determined acidity, salinity, and composition by mixing soil samples with small amounts of water. MECA examined the soil grains to provide information on mineralogy and origin.

The Thermal and Evolved Gas Analyzer (TEGA) is a combination of high-temperature ovens and a mass spectrometer that was used to perform chemical analysis of Martian soil and ice samples. TEGA was used to detect volatiles, soil mineralogy, and potential organics that may be resident on the Martian surface.

Understanding the physics of rocket plume impingement on planetary surfaces is important for the survivability of the spacecraft during terminal descent and touchdown phases of the Entry, Descent and Landing (EDL) sequence [*Whetsel et al.*, 2000]. Limited investigations of steady-state rocket plume interactions with the Martian soil surface were conducted for the Viking mission by NASA researchers in the 1970s [*Grover et al.*, 2005]. The dynamics of the interaction of an under-expanded jet plume flow field, where the nozzle exit pressure is greater than the ambient (back) pressure, with the surface is

quite complex. Indeed, instabilities in the flow occur because of the co-existence of subsonic, transonic, and supersonic regions within the flow [*Krothopalli et al.*, 1999]. For this reason, computational simulations must be tested with data from experiments [*Janos and Hoffman*, 1968].

This Chapter discusses the objectives of plume diagnostics and interaction research efforts and explains why they are important to the Phoenix science mission. We present the methodology and results from three research efforts: (1) spectral diagnostics of the rocket engine exhaust gases, (2) analysis of plume gases using gas chromatography and mass spectrometry, and (3) physical interactions of the rocket plume with an impermeable surface. We conclude with a brief discussion on planned future work and how these data will help with the scientific measurements on Mars.

2.2 Objectives

There are two main phases focused in this Chapter. The first phase is determining the composition of the rocket plume from the Phoenix descent engine. The second phase is the study of transient rocket plume interactions with a flat surface. First phase, the hydrazine fuel used in the Phoenix Lander is high purity grade (99% by weight) but still contains impurities such as water (< 1%), ammonia (< 0.3%), aniline (< 0.003%), and trace organics (< 0.005%). There was a significant level of uncertainty among the science team as to the exact composition of the exhaust products and it was decided to perform additional experimental and numerical studies on the Phoenix landing system rocket engines. Second phase, the understanding of the physical interaction of thruster plumes with the Martian surface is also crucial for assessments of dust lifting and spacecraft contamination. However, detailed experimental investigations of pulsed rocket plume interaction with the ground and the Martian regolith are currently not available [*Mehta et al.*, 2007]. We conducted computational simulations and laboratory experiments in conjunction with detailed scaling analysis to study these interactions and postulate their effects on dust lifting. We report such measurements here and show that they are consistent with numerical simulations.

2.2.1 Phoenix Descent Engine

These thrusters are classified as MR-107N and are designed and manufactured by the Aerojet Corporation. One engine has a maximum thrust of 300 N, a specific impulse of ~230 s and a mass of 0.7 kg as referred to in Table 1.1. Their rapid pulsing and high reliability with a life cycle of ~1500 pulses is accomplished by a Moog single seat valve. To provide a brief history, these thrusters were incorporated for the 2001 Mars Surveyor Program which was moth balled and re-installed for the Phoenix spacecraft, but some of the seat valves showed considerable deterioration upon hot-fire testing. Hence, new MR-107N engines were eventually employed. The Phoenix descent engines are paired in a package of two as shown in Figure 1.6. As we will describe in further detail below, these engines use hydrazine as the main propellant which spontaneously ignites with a catalyst. MR-107N engine specifications are provided below in Table 2.1.

Parameters	**MR-107N**
Catalyst	Iridium/rhodium
Propellant	Hydrazine
I_{SP} (s)	230
Combustion products	H_2, N_2, NH_3
Mass of engine (kg)	0.7
Total pressure at inlet (kPa)	1240
Total temperature at inlet (K)	1116
Maximum thrust (N)	~300
Nozzle area ratio (a.u.)	20.7
Plume Mach number at exit	4.7
Pulse frequency (Hz)	10
Pulse width (s)	~0.055
Jet firing duration (s)	<2.0
NH_3 exhaust mass fraction (a.u.)	0.49

Table 2.1. MR-107N (Phoenix) descent engine specifications

2.3 Analysis of the plume gases with Fourier transform infrared diagnostics

2.3.1 Chemical reaction modeling

The primary product of hydrazine decomposition is ammonia

$$3N_2H_4 \rightarrow \quad 4NH_3 + N_2. \qquad (2.1)$$

In the presence of sufficient heat, the ammonia will further decompose into N_2 and H_2

$$2NH_3 \rightarrow \quad N_2 + 3H_2. \qquad (2.2)$$

The catalyst beds in the Phoenix landing system engines are made of iridium and rhodium metals affixed to a porous ceramic alumina. The combustion temperature within the catalyst bed reaches ~1200 K. The decomposition of N_2H_4 with an iridium catalyst can be expressed by [*Lyon,* 1971]

$$N_2H_4 \rightarrow 4/3(1-x)NH_3 + 1/3(1+2x)N_2 + 2xH_2, \qquad (2.3)$$

where, x is the fraction of originally formed ammonia that has dissociated into N_2 and H_2. A rhodium catalyst produces nitrogen and hydrogen in equal quantities [*Sayer,* 1970]

$$2N_2H_4 \rightarrow 2NH_3 + N_2 + H_2. \qquad (2.4)$$

Chemical equilibrium modeling was performed to provide some insight on interpretation of Eqns. 2.1– 2.4. The predicted plume properties are shown in Table 2.2. The left column is the output from the NASA Gordon-McBride [*McBride and Gordon*, 1996] chemical equilibrium code. The right column is the results from similar calculation performed by the engine manufacturer. The manufacturer's code is a modified version of the Gordon-McBride code that allows for quenching the NH_3 decomposition inside the combustor. Eqns. 2.1–2.4 show that the products in hydrazine monopropellant rocket exhaust plume can significantly vary, with possible major species mole fractions of

NH_3: 10%–80%
H_2: 0%–67%
N_2: 20%–33%
N_2H_4: Unknown

Species	Equilibrium Model	Quenched Model
NH_3	9.1%	36%
N_2	32%	27%
H_2	59 %	36%

Table 2.2. Chemical equilibrium calculated mole percent at the rocket engine nozzle exit.

As mentioned in the Section 2.2, the hydrazine fuel used in the Phoenix Lander is high purity grade. A purity analysis was performed by the engine manufacturer to ensure that the fuel was in compliance with military specification MIL-P-26536. The results from the purity analysis are shown in Table 2.3.

Compound	Acceptable Values for High Purity Grade (by Weight)	Measured Values
N_2H_4	99.00 % min	99.69 %
H_2O	1.00 % max	0.25 %
NH_3	0.30 % max	0.06 %
Trace Organics (Excluding Aniline)	0.005 % max	0.001%
Aniline	0.003 % max	< 0.0006 %
Total Nonvolatiles	0.0010 % max	0.0004 %
Particulates	1 mg/L max	0.8 mg/L
Corrosivity	0.00125 % Fe max	0.00025 %
Chlorine	0.0005 % max	0.00017 %
CO_2	0.0030 % max	0.0003 %

Table 2.3. Hydrazine purity analysis results.

2.3.2 Test procedure

The thrusters exhaust products were characterized during the operational test phase of the engine manufacturing process. Three plume analysis systems were used (in addition to modeling and simulation) to ensure thorough characterization of the exhaust products. Exhaust gas samples were extracted through a heated sample line and analyzed using a Fourier transform infrared (FTIR) multigas analyzer (MGA) [*Markham et al.,* 2004]. A separate plume sample was extracted through the heated sample lines and stored in a passivated sample canister for off-site analysis using gas chromatography/mass spectrometry (GC/MS) methods. An additional gas sample was collected and stored for future analysis, if required. An instrumentation schematic is shown in Figure 2.1.

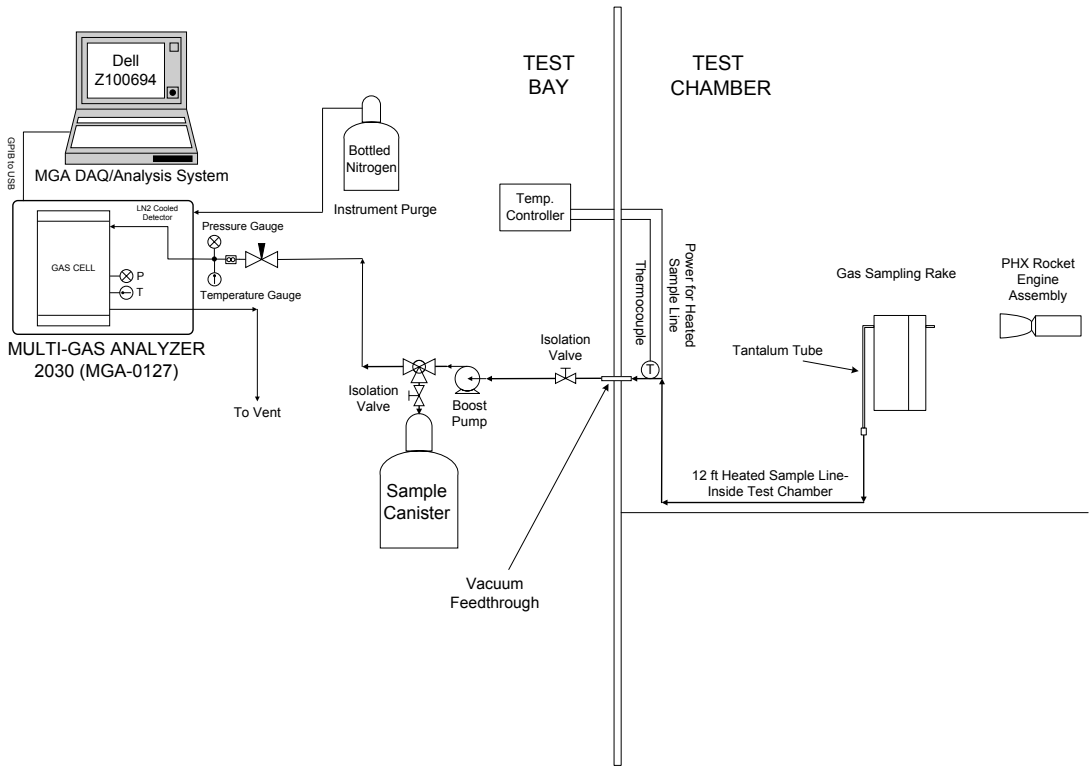

Figure 2.1. Schematic of the FTIR instrumentation installed on the rocket engine test cell.

As mentioned in the Introduction (Section 2.1), the same fuel lot as used on board the Phoenix Lander was used during the engine test firings. The results from the MGA analysis were previously reported by *Plemmons et al.* [2007] and are summarized below.

2.4 Plume gas analysis results

Based on the hydrazine decomposition analysis, the concern over unreacted hydrazine, and the results from the fuel purity analysis, the FTIR MGA was calibrated to measure high levels of NH_3, and low levels N_2H_4, and water vapor. Exhaust gas samples were acquired and analyzed for two separate engine firings. The MGA measured NH_3 concentrations in excess of 50% during engine start and settled to 45% after the engine reached operating temperature, which is 19% higher than the engine manufacturer's performance model and 5 times larger than the equilibrium model prediction. The measured water vapor levels are just under 0.25%, which is in agreement with the pretest fuel purity analysis shown in Table 2.2 and indicates that water does not participate significantly in the reaction.

Hydrazine was not observed in the thruster exhaust plume. However, the hydrazine FTIR absorption features on this instrument are coincident with the ammonia absorption spectra. Hence, the high ammonia concentration will mask low concentration hydrazine. Based on post-test analysis of the FTIR spectra where the spectra were manually searched for hydrazine absorption features, it is estimated that the unreacted hydrazine levels in the thruster plume is less than 0.2%.

The ammonia and water vapor concentration measured for one of the engine firings is shown in Figure 2.2. The engine was fired for approximately 40 seconds. At the end of the firing, the FTIR absorption cell was isolated and the MGA continued to analyze the final sample to obtain a baseline estimate on the instrument precision under test conditions. After approximately 2 minutes 40 seconds, the absorption cell was purged with high-purity nitrogen and the ammonia and water vapor concentration readings returned to zero.

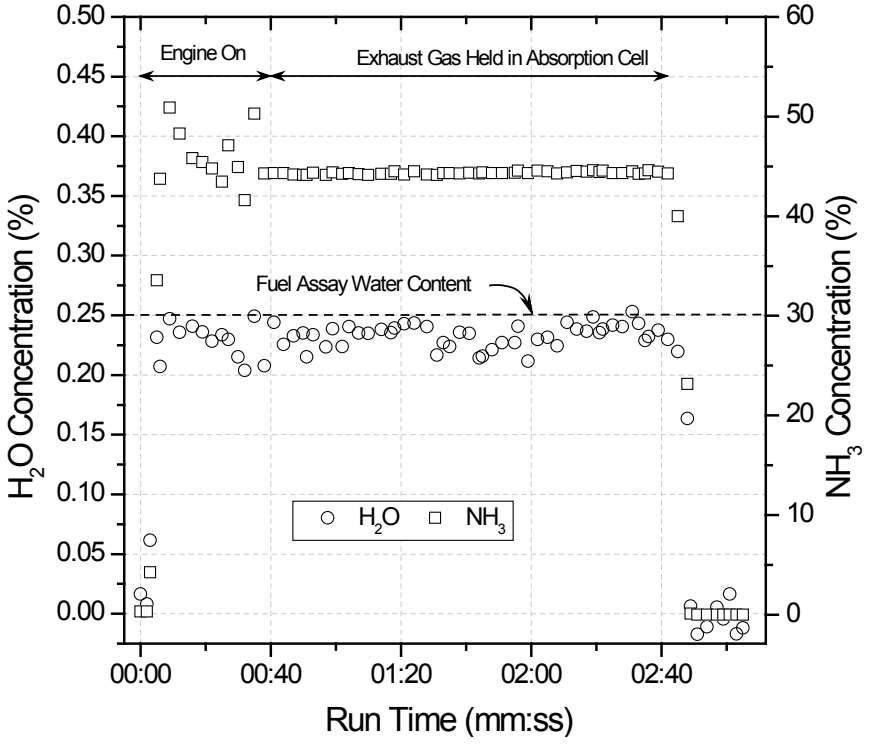

Figure 2.2. Multigas analyzer results for ammonia and water vapor.

Gas samples were extracted from the exhaust plume of two Phoenix retro-rocket thrusters during hot fire acceptance testing. Recirculation gas samples were taken from inside the test cell for two additional engine firings. The samples were analyzed for

ammonia, water vapor, and hydrazine concentrations using a FTIR absorption spectrometer. The measured ammonia and water vapor were in reasonable agreement with expected values. Using a value of $x = 0.3$ in Eqn. 3, yields 45% NH_3, 26% N_2, and 29% H_2, on a molar basis.

2.5 Analysis of the plume gases using gas chromatography-mass spectrometer

The purpose of this analysis was to corroborate the spectroscopic infrared gas analysis via the gas sample probe that was performed during the test firings. The samples were obtained during the test firings by diverting the plume gases into two passivated gas sample canisters. One was charged with the plume gases at 300 torr and the other at 1,277 torr, respectively. The analysis reported here was performed using the 1,277 torr sample. The analytical procedures for the instrumental analysis were developed for simple sample extraction, and used standard methods on a standard configuration GC-MS. The 300 torr sample and the remaining 1,170 torr sample have been stored for future testing should specific questions arise during surface measurements on Mars or should they arise regarding interpretation of the chemistry results.

2.5.1 Methodology

During two of the test firings, the stainless steel heated sample lines carrying hot rocket exhausted gases outside the test chamber, through a heated boost pump, delivered the gases to a sample canister rather than to the FTIR-MGA instrument. One of those sample containers collected only 300 torr of exhaust gases. Since this is below atmospheric pressure, the sample can only be accessed through complicated line work and was thus not analyzed in these tests. The other sample canister collected at a pressure of 1,277 torr, well above 760 torr (1 atm) was easily extracted and required no complicated processing.

A septum was attached to the canister outlet. The attachment included a rubber stopper plate through which a syringe could be inserted to extract samples. A small space of less than 0.25 mL volume was formed between the stopper and the closed-valve of the canister. The canister had to be opened and bled significantly (3 or 4 times for several seconds) to flush air out of the chamber. Samples were tested each time. The oxygen

peak reduced significantly with each flush. When the oxygen peak disappeared, it was assumed the chamber was emptied of air.

With the septum closed tight and the canister fully open, the small chamber was allowed to come to equilibrium with the gases in the canister. The canister was then fully closed off from the chamber. A 100 µL sample was extracted from the chamber, through the septum, with a 500 µL (Superco SGE) gas tight syringe. The sample was carried 15 feet and manually injected into the GC-MS (Shimaduz QP-5050A).

The injection temperature was 200 °C and interface temperature 280 °C. The instrument control mode was split because the samples were large and plentiful. The total flow rate was 21.7 mL/min under an inlet pressure of 100 kPa. The final reported analyses were run for 5 minutes at a steady oven temperature of 50 °C. Higher temperatures and ramped temperatures were unnecessary since the entire sample was gaseous and did not need to be volatilized. With significantly longer runs (>1 hour) only the peak at 1.25 minutes was observed in the gas chromatogram and thus a 5 minute run was more than sufficient.

Prior to the sample analysis, air was run by identical sample delivery and GC-MS method. The GC-MS method was also run without injection of any sample, and provided a true blank. After all plume analyses were complete, the GC-MS was baked out using a very slow temperature ramp of 50 °C to 470 °C. There were no indications of any less volatile substances remaining on the column.

2.5.2 GC-MS Results

Table 2.4 shows the results for the mass spectrum of the air blank and plume sample. The blank, containing approximately 77% N_2 and 21% O_2, displays a mass peaks at 28 m/z (14+14 atomic mass units (amu)) with a relative intensity (I_{rel}) of 100 and at 32 m/z (16+16 amu) with an I_{rel} = 40.4.

m/z	Air, I_{rel}	Sample, I_{rel}	Fragment
15	0.0	5.2	NH
16	3.1	88.8	NH_2
17	0.4	100.0	NH_3
18	0.8	3.8	? H_2O, NH_4
28	100.0	75.6	N_2
31	0.0	0.0	
32	40.4	1.2	O_2

Table 2.4. Results of GC-MS analysis.

The chromatogram for the 100 μL plume sample shows a single sharp peak with a retention time of 1.2 minutes. This peak in turn resulted in a mass spectrum with three major peaks at 16m/z (I_{rel} = 88.8), 17m/z (I_{rel} = 100), and 28 m/z (I_{rel} = 75.6). These peaks can be assigned to NH_2 (16 amu), NH_3 (17 amu), and N_2 (28m/z), respectively. Other very minor ammonia-related and water peaks are also present, probably for NH (15 amu) and H_2O (18 amu). It should be noted that detection and analysis of H_2 is extremely complex and requires special containers, handling, and procedures, thus no attempt was made to measure the H_2 content of the plume gases. It is also important to note that no standards were used to construct calibration curves and thus no quantitative results are provided for any of the other constituents.

2.5.3 Interpretation of the results

The most significant results of the GC-MS analysis are (1) that a major fraction of the thruster plume is composed of NH_3 and (2) that no hydrazine is present. As discussed above, the quenched equilibrium code for the Phoenix hydrazine thrusters predicts 36% NH_3, 36% H_2, and 27% N_2. The in situ plume gas analysis yielded 45% NH_3 and 0.23% H_2O. Using absolute intensities and setting the level of NH_3+NH_2+NH at 45%, we can calculate the levels of N_2 and H_2O, as 18% and 0.8%, respectively. Even though our results are not rigorously quantitative, these levels are reasonably close to those predicted by the model and performance criteria. Taking into account all these results, it is reasonable to estimate that the plume contains about 45% (±5%) NH_3.

The more significant result is that we found no indication in the mass spectrum, within our detection limits, of N_2H_4 (32 amu). If any is present it is <1%, however, given that there is no confirmation peak at 31amu for N_2H_3, the peak at 32 amu is most likely due to O_2 contamination from air not fully evacuated from the container.

The other major reaction product found in the plume sample is N_2 and this strongly influences the specific heat ratio. This is discussed in Section 2.6.2.2. This can typically range from 20% to 35% and the model predicts 27%. Our estimated result of 18% is low, but can be accounted for by the errors introduced if we allow for some

recombination of N_2 and H_2 fragments to give NH. Now, we will explore the second phase of this research investigation.

2.6 Flow physics of pulsed supersonic jet impingement at Mars pressure

An experimental testbed was developed to simulate the flow physics of the exhaust from a Phoenix pulsed rocket engine and its interaction with a flat surface. Indeed, all requirements for simulating these interactions were determined using non-dimensional scaling parameters. Numerical simulations were used to help the physical interpretation of the experimental results.

2.6.1 Introduction

Plume-surface flow physics in tenuous to vacuum atmospheres due to steady supersonic jets have been studied by researchers in preparation for the Apollo missions [*Roberts*, 1966]. The main methods of characterizing these flows are to spatially and temporally determine the pressure fields and density gradients (Schlieren). There are three types of supersonic free-jets that exhaust from nozzles. The jet or rocket plume can either be underexpanded, overexpanded or perfectly expanded [*Sutton and Biblarz*, 2009]. An underexpanded jet is when the jet pressure at the nozzle exit is larger than the ambient pressure. An overexpanded jet is when the ambient pressure is larger than the exit pressure, and perfect expansion of a jet occurs when both of these parameters are the same. The jet pressure tries to match the ambient pressure which leads to large differences in their shock structure.

For an underexpanded jet, the exit jet pressure (P_n) is larger than the ambient (P_b) and this leads to Prandtl-Meyer (PM) expansion waves, initiated at the lip of the nozzle (shown as blue lines in Figure 2.3A1), which reduces the jet pressure to match the ambient. Due to reflection of the PM expansion waves in region 2 shaded in grey, this leads to a jet pressure smaller than the ambient in region 3. Hence, this results in the reflection of these expansion waves from the ambient boundary, resulting in PM compression waves. The coalescing of the compression waves leads to oblique shocks shown as red lines. This results in the matching of the two competing pressures in region 4. When oblique shock reflection occurs, the jet pressure is larger than ambient in region

5 and the process starts again. These are known as “shock cells” which form as repeatable train-like structures as shown in Figure 2.3A1. They dissipate further downstream due to viscous losses and turbulent mixing with the ambient atmosphere. We show a planar-laser-induced-fluorescence (PLIF) spark image in Figure 2.3A2 and a contour image of the standard deviation of the mean velocity (standard deviation image) in Figure 2.3A3 of an underexpanded jet [*Inman et al*., 2009]. The standard deviation image correlates to turbulence intensity.

For an overexpanded jet, the exit pressure is smaller than the ambient and this leads to the formation of oblique shock waves at the nozzle lip shown in region 1 in Figure 2.3B1. The same dynamics as for the underexpanded jets are observed, but they are out-of-phase where it is now first compression and then expansion. The PLIF and standard deviation images are shown in Figures 2.3B2 and 2.3B3 respectively [*Inman et al.,* 2009]. Turbulence and unsteadiness are much more pronounced for overexpanded jets which may lead to instability and faster dissipation of the plume structure. According to [*Hagemann and Frey*, 2008], the diffusion rate of the entrained flow into the turbulent mixing region, the interface region between the jet shock and the ambient atmosphere, is larger than the underexpanded case and increases axially. Due to overexpansion of the plume, the free atmospheric boundary pinches the jet inward, leading to an increase in the turbulent mixing region and attenuation of the inviscid core. For perfectly expanded jet, the criteria for both pressures to be matched are met at the nozzle exit and hence, no expansion or compression waves are observed.

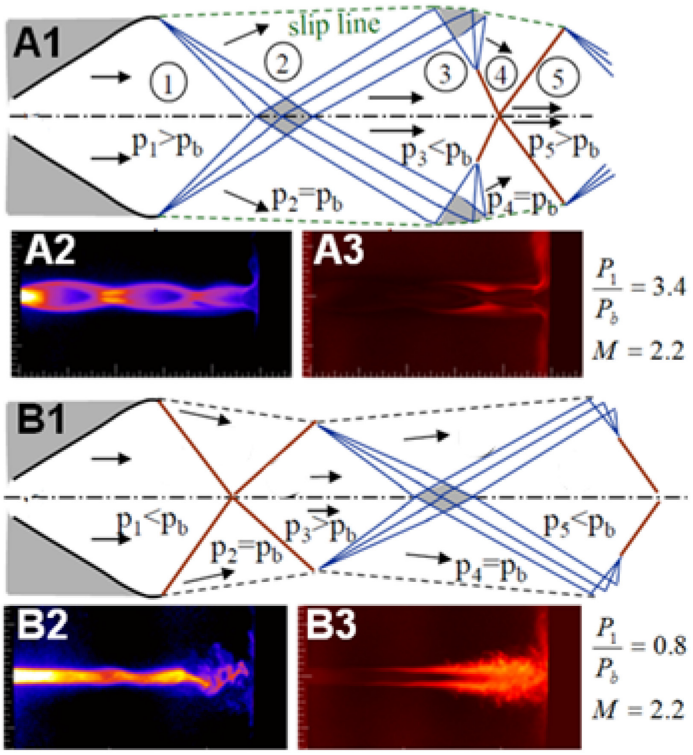

Figure 2.3. Plume shock structure of underexpanded and overexpanded supersonic jets. (A1) Schematic of an underexpanded supersonic jet. (A2) PLIF spark image and (A3) PLIF standard deviation image [*Inman et al*., 2009]. (B1) Schematic of an overexpanded supersonic jet. (B2) PLIF spark image and (B3) PLIF standard deviation image [*Inman et al*., 2009].

Most rocket plumes exhausting from a descent engine on Mars or the moon are underexpanded and this classification will be the prime focus of our studies. However, as discussed in Section 3.5.1 and Appendix A.5.5., the plume structure and their effects on the surface are considerably different between the two atmospheres. Flow structures due to impinging steady jets were separated into three regimes as discussed by Donaldson and Snedekar [1971]: (a) free-jet; (b) impingement zone and (c) wall jet. These structures are mainly characterized by pressure and density fields at steady-state as done by Stitt [1961] for preparation of the first landings on the moon. We will briefly discuss the flow structures within the impingement zone and wall jet which are considerably the most important for ground erosion [*Lamont and Hunt*, 1980]. The plate shock, tail shock and stagnation bubble below the plate shock as shown in Figure 2.4A are important flow structures which we show directly influences the ground pressure. Plate shock is a normal shock wave reflected from an impermeable surface. Tail shocks are oblique shock waves which are reflected from the plate shock and emanate from the triple point. The triple

point is the region where the incident, plate and tail shocks converge as depicted in Figure 2.4A. Since the total pressure loss is much greater for a plate shock than for oblique tail shocks, there is ring of relatively high surface pressure. A portion of the flow below the plate shock cannot overcome these relatively large pressure gradients on the outboard of the plate shock, resulting in the recirculation of gas (stagnation bubble) as depicted by Figure 2.4A [*Henderson et al.,* 2005]. For comparison, we depict the schematic and the Schlieren photograph (Figure 2.4B) of an underexpanded impinging jet. Past studies predominantly investigated these structures at steady-state conditions. Our main goal in this Chapter is to investigate the behavior of these structures in transient conditions.

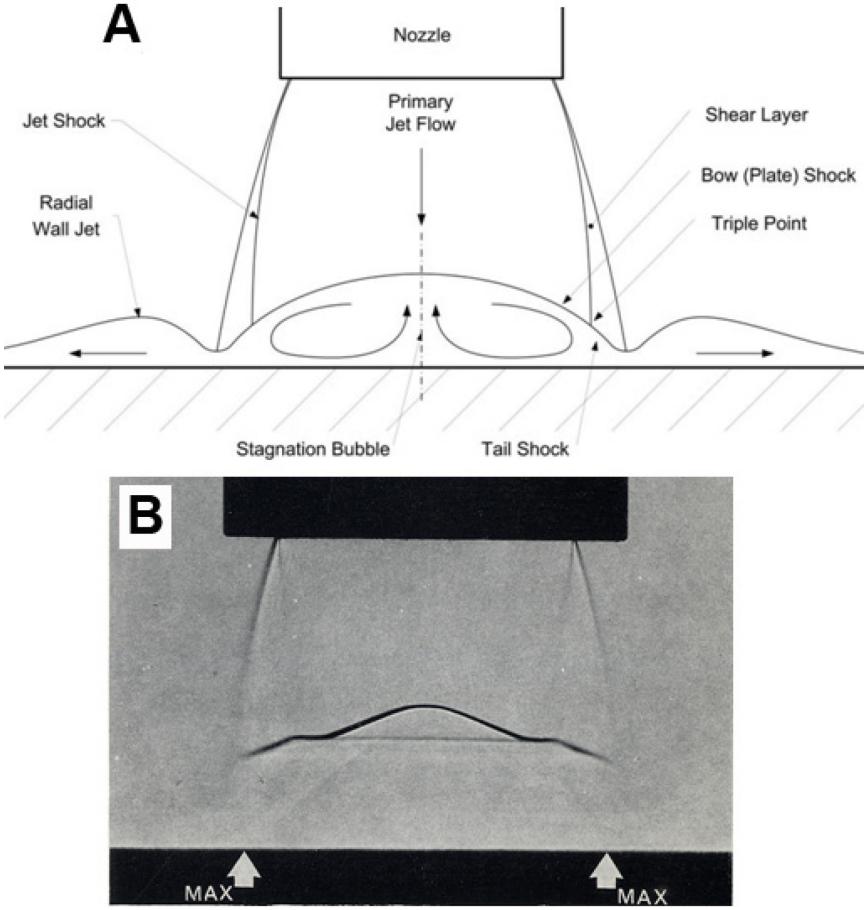

Figure 2.4. Plume shock structure within the impingement zone of an underexpanded jet. **(**A**)** Schematic of flow structures. [*Pattison et al.,* 2005]; (B) Schlieren image distinctly showing a curved plate shock [*Lamont and Hunt*, 1976]

2.6.2 Experimental and computational methodologies

2.6.2.1 Experimental methodology

A half-scale cold flow (non-heated jet) test-bed (CFTB) was developed to study the impingement of supersonic pulsed jets on a flat surface at Mars ambient pressure (Fig. 2.5). The thruster firing frequency, the duration of the pressure pulse, and the chamber pressure (P_C) were adjustable. Dry compressed nitrogen gas at room temperature was used to simulate hydrazine decomposition products because it has a similar specific heat capacity ratio. The importance of this parameter in scaling is discussed in the following section. Fast response absolute micro-electro-mechanical system (MEMS) pressure sensors were placed radially across the impingement plate at a spacing distance of 27.5 mm between sensors. A gauge pressure transducer was placed at the nozzle inlet which measured the stagnation pressure of the incoming flow. Both transducer and MEMS sensors each had a response time of 1 msec. One thermocouple was also placed at the plate's centerline. One ½ scale thruster with a similar nozzle contour profile as the Phoenix MR-107 descent engine nozzle was horizontally mounted inside a thermal-vacuum chamber, which was set to an ambient pressure of 690 Pa and ambient temperature of 290 K. The ambient pressure within the thermal-vacuum chamber was generated by a mechanical pump and monitored by a transducer with a response time of 1 msec at a maximum sensitivity of 1000 Pa. During the constant velocity descent phase of the Phoenix spacecraft, the rocket plumes are pulsed at a 10 Hz frequency, with a 55-45 msec pulse width, a maximum chamber pressure ($P_{C\text{-}max}$) of 1.24 MPa, and a chamber pressure (P_C) rate of change during engine startup/shutdown cycles of approximately 152 MPa/s. Our CFTB system generally met all these requirements as shown in Table 2.4, but it took many design iterations to obtain the required performance. The thruster chamber pressure and the ground impingement pressures (P_s) were measured at a sampling rate of 48 kHz. The thruster altitude (i.e., the distance of the thruster exit plane from the impingement plate) can be adjusted from 0.25 m (scaled touchdown altitude) to 1 m above the surface.

Parameters	MR-107N	½ scale
Total pressure at inlet (kPa)	1240	1240
Total temperature at inlet (K)	1116	300
Jet pressure at exit (kPa)	3.24	3.09
Jet density at exit (kg/m^3)	0.03	0.19
Jet velocity at exit (m/s)	1929	712
Jet mass flow rate (kg/s)	0.16	0.11
Pulse frequency (Hz)	10	10
Pulse width (s)	~0.055	~0.065
Firing duration (s)	<2.0	≤0.3
Nozzle diameter at exit (cm)	6.25	3.13
NH_3 exhaust mass fraction (a.u.)	0.49	0.0
Maximum thrust (N)	~300	~160
Exhaust plume products	N_2, H_2, NH_3	N_2

Table 2.5. Specifications of performance parameters between Phoenix rocket motor and ½ scale cold gas thruster.

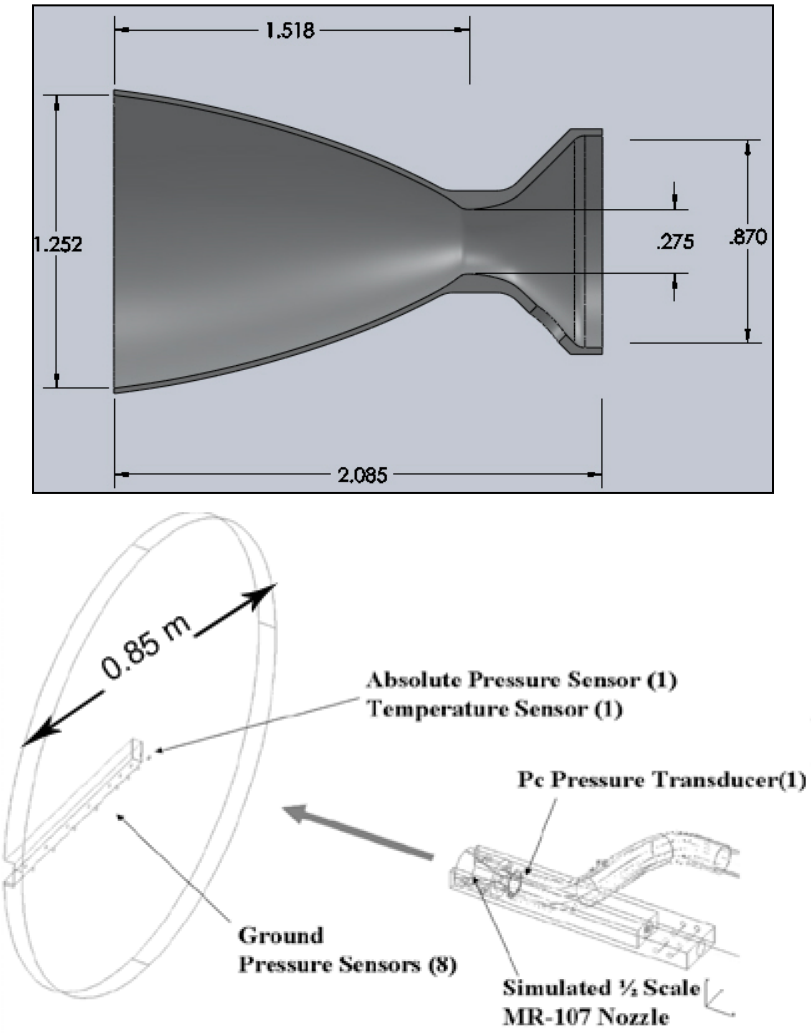

Figure 2.5. (Top) Schematic of ½ scale Phoenix nozzle contour. All dimensions are in inches. *Courtesy of Lockheed Martin.* (Bottom) Schematic of the CFTB experimental setup at University of Michigan [*Mehta et al.,* 2007].

2.6.2.2 Scaling laws for rocket plume flow physics

Theoretical scaling laws prove that subscale cold gas jets can simulate the shock structure and ground pressure values due to full-scale rocket plume interactions. This is proven through first principles by normalizing the conservation equations. The governing compressible Navier-Stokes equations (Eqns. 2.5 – 2.7) are presented in symbolic notation below [*Schlichting and Gersten,* 2001]:

$$\frac{D\rho}{Dt} = -\rho \nabla \cdot \vec{v} \tag{2.5}$$

$$\rho \frac{D\vec{v}}{Dt} = \vec{f} - \nabla p + \nabla \cdot [\vec{\tau}] \tag{2.6}$$

$$\rho c_p \frac{DT}{Dt} = \nabla \cdot (\lambda \nabla T) + \beta T \frac{Dp}{Dt} + \phi \tag{2.7}$$

Where T, p, ρ, v, λ, β, c_p, τ, t and ϕ are the plume temperature, pressure, density, velocity, thermal conductivity, coefficient of thermal expansion, isobaric specific heat capacity, the viscous stress tensor, time and the rate of viscous dissipation, respectively. The volumetric force is denoted by f. Arrows above the parameter denote that these terms are vectors. These compressible Navier-Stokes equations are normalized with the following parameters [*Schlichting and Gersten,* 2001]:

$$x' = x/D, \quad t' = tU_e/D, \quad \vec{v}' = \vec{u}/U_e, \quad p' = (p - p_e)/\rho_e U_e^{\,2}, \quad T' = T/T_e, \quad \rho' = \rho/\rho_e,$$
$$c_p{}' = c_p/c_{pe}, \quad \lambda' = \lambda/\lambda_e, \quad \beta' = \beta/\beta_e, \quad \nabla' = D\nabla, \quad \phi' = \phi D^2/\mu_e U_e^{\,2}, \quad \mu' = \mu/\mu_e \tag{2.8}$$

All the reference parameters are taken at the nozzle exit (denoted as a subscript e) with a diameter of D. The length scale and plume viscosity are denoted by x and μ, respectively. Upon substituting the reference parameters (Eqn. 2.8) into equations 2.5, 2.6 and 2.7, the normalized Navier-Stokes equations become:

$$\frac{D\rho'}{Dt'} = -\rho' \nabla' \cdot \vec{v}' \tag{2.9}$$

$$\rho' \frac{D\vec{v}'}{Dt'} = \frac{1}{\mathrm{Fr}^2} \rho' \vec{g} - \nabla' p' + \frac{1}{\mathrm{Re}} \nabla' \cdot [\vec{\tau}'] \tag{2.10}$$

$$\rho' c_p' \frac{DT'}{Dt'} = \frac{1}{\mathrm{Re}\,\mathrm{Pr}} \nabla' \cdot \left(\lambda' \nabla' T'\right) + \frac{U^2}{c_{pe} T_e} \beta' T' \frac{Dp'}{Dt'} + \frac{U^2}{c_{pe} T_e \,\mathrm{Re}} \phi' \tag{2.11}$$

$$\frac{U^2}{c_{pe} T_e} = \mathrm{Ma}^2 \frac{c_e^{\,2}}{c_{pe} T_e} = \mathrm{Ma}^2 (\gamma - 1) \tag{2.12}$$

The speed of sound at the nozzle exit is denoted by c_e. Substitute Eqn. 2.12 into Eqn. 2.11 for compressible ideal gas flow and equation 2.11 becomes:

$$\rho' c_p' \frac{DT'}{Dt'} = \frac{1}{\mathrm{Re}\,\mathrm{Pr}} \nabla' \cdot \left(\lambda' \nabla' T'\right) + \mathrm{Ma}^2 (\gamma - 1) \beta' T' \frac{Dp'}{Dt'} + \frac{\mathrm{Ma}^2 (\gamma - 1)}{\mathrm{Re}} \phi' \tag{2.13}$$

Where the following nondimensional terms are defined as:

$$\mathrm{Re} = \frac{\rho_e U_e D}{\mu_e}, \quad \mathrm{Fr} = \frac{U_e}{\sqrt{gD}}, \quad \mathrm{Ma} = \frac{U_e}{a_e}, \quad \mathrm{Pr} = \frac{\mu_e c_{pe}}{\lambda_e}, \quad \gamma = \frac{c_{pe}}{c_{ve}} \tag{2.14}$$

Hence, the flow physics of the rocket plume/supersonic jet is a function of the Reynolds number (Re), Froude number (Fr), Mach number (Ma), Prandtl number (Pr) and specific heat ratio capacity (γ). However, simplifications can be made due to the supersonic flow regime. For example as Fr $\rightarrow\infty$, the first term on the right hand side of Eqn. 2.10 tends to zero. Also as Re $\rightarrow\infty$ and applied to Eqns. 2.10 and 2.11, characteristic of supersonic flows, the flow can be considered inviscid. This is valid for supersonic jet interactions in all regions except at the viscous boundary layer. Here viscosity of the jet plays a role. However, the ground total pressure has a relatively minor dependence on the jet viscosity for large Reynolds number and this is known as the Barker effect [*Schlichting and Gersten*, 2001; *Barker*, 1922].

Alternatively another more simplified thermodynamics approach to Eqn. 2.11 is shown below:

$$E_t = IE + KE \tag{2.15}$$

$$E_t = c_v T_e + \frac{1}{2} U_e{}^2 \tag{2.16}$$

$$E_t' = 1 + \frac{\left(\frac{1}{2} U_e{}^2\right)}{c_v T_e} = \frac{U_e{}^2}{2\gamma R T_e}\left(\frac{\gamma R}{c_v}\right) \tag{2.17}$$

$$R = c_p - c_v, \tag{2.18}$$

$$c_e = \sqrt{\gamma R T_e} \tag{2.19}$$

Where E_t, *IE, KE,* c_v and R are the total energy (E_t), internal energy (*IE*), kinetic energy (*KE*), isovolumetric specific heat capacity (c_v) and gas constant (R) of the plume. By substituting the thermodynamic definition of the internal energy and kinetic energy of chemical specie, equation 2.15 becomes equation 2.16. Equation 2.17 results from normalizing equation 2.16 by the internal energy. Substitute equations 2.19 and 2.18 into 2.17 and apply the definitions of Mach number and specific heat ratios and the conservation of energy equation becomes:

$$E_t' = 1 + \frac{1}{2}\gamma\left(\gamma - 1\right)\mathrm{Ma}^2 \tag{2.20}$$

$$E_t' = 1 + k$$

Where k is known as the Mach similarity parameter and this is a function of both Mach number and specific heat ratios which is consistent with the normalization of the governing compressible Navier-Stokes equations (Eqn. 2.13) for the supersonic regime. To ensure dynamic similarity within the plumes between the supersonic jet and rocket plume, the Mach number and specific heat ratio need to be matched. Also, the Reynolds number must be within the turbulent regime ($>10^4$). Similar analyses need to be applied to the boundary conditions imposed by these flows.

There are two types of surface boundary conditions for this application: (a) free boundary and (b) solid boundary. The free surface boundary is defined as the infinitesimal interface between the exhaust plumes and the ambient atmosphere (P_∞). At this interface region near the nozzle exit, the entrained flow velocity and temperature are continuous to the plume. The solid surface boundary, intuitively, is defined as the solid surface where the jets interact. At the free boundary [*Schlichting and Gersten*, 2001]:

$$p_{fb} = P_\infty = P_{amb} \tag{2.21}$$

$$\vec{v}_{fb} = \vec{U}_e \tag{2.22}$$

$$T_{fb} = T_e \tag{2.23}$$

Substituting equations 2.21-2.23 into the normalized parameters shown in equation 2.8, these parameters become:

$$p'_{fb} = \frac{P_\infty - P_e}{\rho_e U_e^{\,2}} \tag{2.24}$$

$$v'_{fb} = 1.0 \tag{2.25}$$

$$T'_{fb} = 1.0 \tag{2.26}$$

Since the specific heat ratio and the nozzle area expansion ratio are similar for full-scale and subscale systems, the dynamic pressure at the nozzle exit, $\rho_e U_e^{\,2}$, will be similar from isentropic relations provided the stagnation pressure at the nozzle inlet, P_C are matched. The flow is isentropic at the nozzle exit, and this is a valid assumption due to the adiabatic and reversible nature of the flow through the diverging section of the nozzle [*Anderson*, 2006]. It should be noted that 1-D isentropic relations are only valid in regions of PM expansion and not throughout the exhaust plume. By manipulating equation 2.24, another nondimensional term named the jet expansion ratio (*e*), developed from the boundary conditions, needs to be satisfied:

$$p'_{fb} = \frac{P_\infty - P_e}{\rho_e U_e^{\,2}} = \frac{P_\infty\left[1 - \left(\frac{P_e}{P_\infty}\right)\right]}{\rho_e U_e^{\,2}} = \frac{P_\infty(1-e)}{\rho_e U_e^{\,2}} \tag{2.27}$$

P_C needs to be matched for both full-scale and subscale systems for equation 2.27 to be satisfied and this is defined as the nozzle pressure ratio (NPR), α. $P_{C\text{-max}}$ is defined

as the stagnation chamber pressure when maximum engine thrust is reached. The NPR and jet expansion ratio are defined as follows:

$$\alpha = \frac{P_{C-\max}}{P_\infty} \tag{2.28}$$

$$e = \frac{P_e}{P_\infty} \tag{2.29}$$

The normalized boundary conditions at the solid surface are the following:

$$p'_* = \frac{P_s - P_e}{\rho_e U_e^{\,2}} \tag{2.30}$$

$$T'_* = \frac{T_s}{T_e} \tag{2.31}$$

$$v'_* = 0 \tag{2.32}$$

The dimensional term, T_s, is the surface impingement temperature. *According to the governing Navier-Stokes equations and boundary conditions specific for supersonic jet interactions, there are five nondimensional numbers that need to be satisfied to ensure dynamic similarity:* ***γ*, Ma, Re, *e*, *α*.** From equation 2.30 and the matching of these required nondimensional numbers, the ground pressure is theoretically simulated. The ground temperature can also be calculated from this approach, but it is not of interest in these applications. Below is a description of each of these parameters.

The specific heat ratio for the gas mixture of hydrazine combustion products at the nozzle exit is not analytically straight-forward to determine. This parameter is numerically calculated throughout the internal nozzle using two-dimensional Method of Characteristics solutions fully coupled with finite-rate kinetics. From these numerical calculations, the specific heat ratio between the rocket plume and N_2 show good agreement as tabulated in Table 2.6. Using OVERFLOW CFD code, the specific heat ratio throughout the exhaust plume is ~1.4 [*Van Norman*, 2010] and hence, nitrogen test gas was used for our experiments.

The exit Mach number between the two flows is matched by simulating the nozzle expansion ratio, nozzle contour profile and the specific heat ratio. This ensures that the compressibility effects are simulated within the plume. This is also confirmed by numerical simulations. The Mach similarity parameter, as derived above, is a function of

the exit Mach number and specific heat ratio and is defined as the ratio of the kinetic energy of the plume to the internal energy of the plume at the nozzle exit [*Land and Scholl,* 1966],

$$k = \gamma(\gamma - 1)M^2 \qquad (2.33)$$

There are four flow regimes determined by the Reynolds number in increasing order: (a) Stokes or creeping (<1), (b) laminar (10^0-10^3), (c) transition (10^{3}-10^4) and (d) turbulent (>10^4) flows. For rocket plumes and supersonic jets used in the experiments, the flow is fully-turbulent. It can be seen from Table 2.6 that the rocket exhaust plume and supersonic jet are within the same flow regime.

The other parameter, as derived above, used to scale our CFTB is the jet expansion ratio of the exhaust plume at the nozzle exit. This term has important physical interpretations as well. The pressure force ratio of the rocket plume at the nozzle exit (F_e) relative to the atmosphere (F_∞) is important in determining both the jet expansion angle of the plume with respect to the centerline [*Clark,* 1971] and shock structure of the plume as described in Section 2.6.1. This parameter described the effects of the ambient atmosphere on the exhaust plume. Its' far-field effects are described in more detail in Section A.5.5, Appendix A. This in turn is determined by the ratio of nozzle exit pressure (P_e) to ambient pressure (P_∞) [*Clark and Conner,* 1969],

$$e = \frac{F_e}{F_\infty} = \frac{P_e A_e}{P_\infty A_e} = \frac{P_e}{P_\infty}. \qquad (2.34)$$

The final scaling parameter used is the nozzle pressure ratio (Eqn. 2.28). This parameter is obtained by normalizing the maximum stagnation pressure of the nozzle inlet ($P_{C\text{-}max}$) with respect to the ambient atmospheric pressure. NPR is an important parameter in ensuring that the CFTB has ground pressure profiles similar to the full-scale case of the real size and performance of the rocket motor. Simulation of the thruster plume temperature is not critical in understanding the force loads on the surface [*Roberts et al.,* 1982]. This is further corroborated by normalization of the conservation of energy (Eqn. 2.13) which is only a function of the Mach similarity parameter for supersonic turbulent flows.

By matching these nondimensional numbers and the geometric length scaling with respect to the nozzle diameter, the ground pressure profiles and the plume and

impingement flow structures produced by the CFTB theoretically simulates those produced by the rocket exhaust. This is further confirmed by comparing full-scale and subscale numerical analyses as described in Sections 2.6.5.3 and A.5.8 (Appendix A). Table 2.6 quantitatively compares non-dimensional plume parameters between the experimental setup and full-scale. Based on the similarity of the nondimensional parameters shown in Table 2.6, the subscale CFTB theoretically simulates the interactions of the Phoenix rocket plume with the impermeable surface. The rocket exhaust parameters may vary slightly depending on the extent of ammonia disassociation during the hydrazine decomposition reaction described in Section 2.3.1.

Parameters	Full-Scale	Experiment
k	11.4	12.7
e	3.8	4.4
α	~1500	1550
Ma	4.7	4.8
γ	1.38	1.4
Re	3.4×10^5	12.7×10^5

Table 2.6. Exhaust plume non-dimensional scaling parameters.

2.6.2.3 Computational methodology

In addition to the experimental study, we also used 3-D and axisymmetric computational fluid dynamics (CFD) models to study the transient impingement of the Phoenix thruster plume on the surface. The full Navier-Stokes equations were solved over the entire domain including the nozzle internal flow, where a total temperature, total pressure boundary condition was used to satisfy inlet conditions. Unsteady, compressible inviscid and turbulent numerical solvers of the finite volume based ANSYS Inc. FLUENT code were used. Structured mesh generation was developed for the flow domain using ANSYS Gambit. Grid adaption and an iterative time stepping size of 1 μsec were applied to the computational models to resolve shocks and capture small transient events. This CFD study was done in collaboration with Lockheed Martin's Aerophysics Department where they ran the Aerosoft GASP numerical code. Time series of thruster chamber pressure measured during hot fire (rocket engine testing) and cold flow tests were used to force the CFD models [*Huseman and Bomba*, 2000]. More details

regarding the flow domain and boundary conditions for these numerical codes are described in Appendix A (see section A.4.2).

2.6.3 Experimental results

The main data obtained from our experiments were the time-series of both the ambient pressure and P_C profiles and ground pressure time series and spatial profiles. All pressure profiles were normalized with respect to the average maximum P_C value and all dimensions were normalized with respect to the nozzle exit diameter. From temporal ground pressure profiles at touchdown altitude (Fig. 2.6) and Mars atmospheric pressure, the centerline peak pressures at the ground vary between 35 and 20 kPa (non-dimensional ground pressure values of 0.028 and 0.014, respectively). These surface overpressures last between 10 and 18 msec (Fig. 2.6), which is repeatable for the two 100 msec pulse firing sequences. The P_C pulse firing sequence is comprised of: 10-12 msec P_C ramp up; 40 - 50 msec of relatively constant maximum P_C value known as the quasi-steady state regime; and 30 msec P_C ramp down (Fig. 2.6). The pressure amplitude is largest at the centerline and it decreases nonlinearly with nozzle-to-surface distance as discussed in Section 2.6.6. During the quasi-steady state regime, at a non-dimensional altitude of $h/D_e = 8.4$, the pressure amplitude is about 5 kPa ($P_s/P_{C\text{-}max} = 0.005$) for about 40 to 50 msec into each power cycle. The quasi-steady state regime is defined to be when the ground pressure is relatively constant with time during the full-thrust duration. Only two thruster firing cycles were captured due to a significant increase in the vacuum chamber ambient pressure by 500% which alters the ground pressure due to change in the jet shock structure [*Mehta et al.*, 2007]. These repetitive and transient ground overpressures illustrated in Figure 2.6 do not occur in experiments with steady-state (non-pulsating) supersonic jets at Mars atmosphere as illustrated in Figure A3 (Appendix A.5.7) or pulsating supersonic jets at Earth atmosphere. The physical reason of this difference is explained in more detail below.

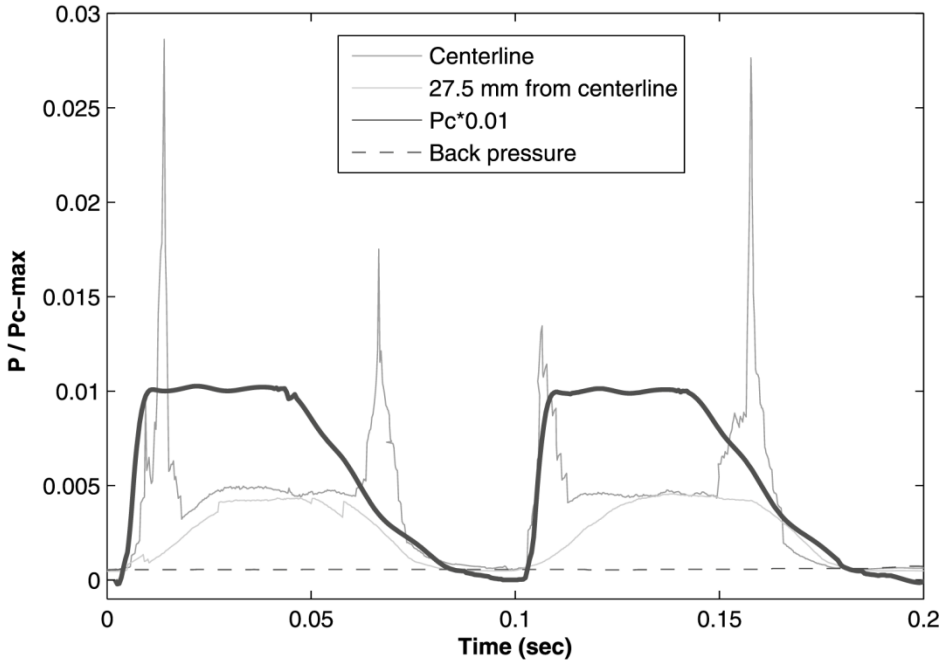

Figure 2.6. Non-dimensional thruster chamber pressure (P_C) and ground pressure (P_s) time series during two complete ~50 msec pulse width thruster firing cycles at the Phoenix touchdown altitude (h/D_e = 8.4). The thin dark line is the centerline ground pressure profile as a function of time. The thin light line is the ground pressure profile at 27.5 mm from the centerline. The dashed and thick dark lines are the back (ambient) pressure and P_C time series profiles, respectively. The quasi-steady state regime occurs between 25 and 70 msec for the first firing cycle and between 115 and 155 msec for the second firing cycle. For the first engine cycle, plate shock formation occurs between 10 and 20 msec and approximately between 60 and 75 msec during plate shock collapse. Measurement error of ground pressure is 2.5% of full-scale value and measurement error of P_C is 1% of full-scale value.

Further evidence of ground overpressure are seen in the spatial ground pressure profiles presented in Figure 2.7. At t = 112 msec, around the time of the first overpressure during the second firing cycle, the centerline pressure amplitude is 16 kPa ($P_s/P_{C\text{-}max}$ = 0.013) and that during the quasi-steady state phase at t = 136 msec the pressure amplitude decreases to 5 kPa ($P_s/P_{C\text{-}max}$ = 0.0042). It can be seen that during the quasi-steady state regime, the ground pressure is relatively constant up to approximately r/D_e of 0.9 and then it decreases monotonically.

For pulsed jets at an e = 0.02 at touchdown altitude, transient overpressures were not observed and a maximum normalized pressure of less than 0.003 was measured. Between moderately underexpanded and highly overexpanded jets, we observe approximately up to two orders of magnitude increase in the maximum ground pressure.

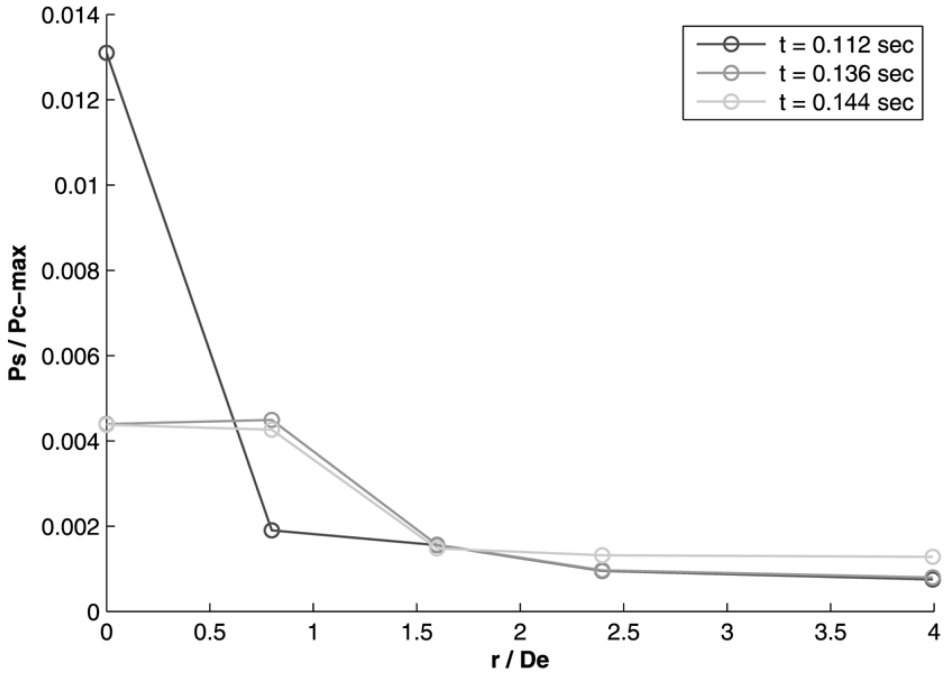

Figure 2.7. Ground pressure profile (P_s) non-dimensionalized with the maximum chamber pressure ($P_{c\text{-}max}$), as a function of non-dimensional distance from the centerline at the ground in two phases of the thruster firing cycle at an altitude of h/D_e = 8.4: before (112 msec) and during (136 msec; 144 msec) fully developed plate shock formation. Measurement error of ground pressure is 2.5% of full-scale value.

2.6.4 Numerical results

Figure 2.8 shows the Mach contour – time sequence profiles of a pulsed supersonic jet impinging on a flat surface at an altitude of $h/D_e = 25$. These calculations were done at Mars ambient pressure conditions and ambient temperature of 298 K. The plume properties were those of dry nitrogen at temperature of approximately 300 K, similar to the experimental conditions. Similar characteristic transient ground overpressures were observed with a maximum centerline pressure of 40 kPa ($P_s/P_{C\text{-}max}$ = 0.032) with a duration between 10 and 15 milliseconds. This also developed during P_C ramp up and ramp down phases [*Mehta et al.,* 2007].

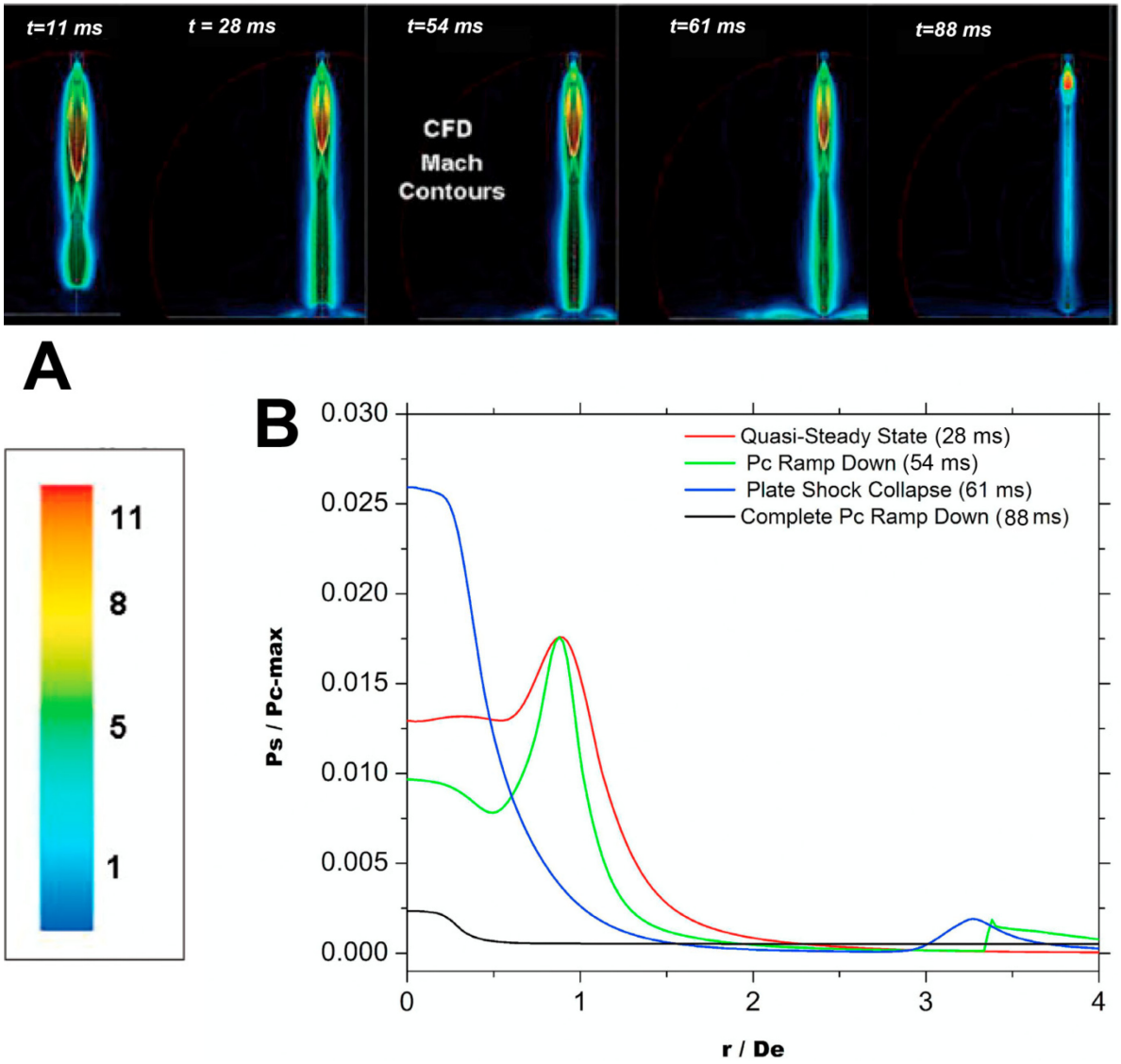

Figure 2.8. Plate shock formation and collapse process at h/D_e = 25 from axisymmetric, compressible, unsteady numerical simulations. (A) Mach contours profiles of the plate shock dynamics. Mach contour range is from Mach 0 to 11 and a legend is provided in the figure. (B) Non-dimensional ground pressure profiles as a function of non-dimensional distance from the centerline during four stages of the plate shock collapse process: quasi-steady state regime (28 msec); P_C ramp down (54 msec); Plate shock collapse (61 msec); and complete P_C ramp down (88 msec). The Pc profile for this case has a pulse-width of ~50 msec representative of the Phoenix pulse-modulated engines during the terminal descent phase of EDL.

Figure 2.8B shows the spatial ground pressure profiles at varying stages of the plume impingement process. It indicates that the ground pressure peak of 21 kPa ($P_s/P_{C\text{-}max}$ = 0.017) at r/D_e = 0.9 is observed during the quasi-steady state regime. Minor pressure perturbations of approximately 2.1 – 3.8 kHz were also observed during this regime [*Mehta et al.*, 2007]. During the ground overpressure regime when P_C ramp down occurs, a monotonic spatial increase in centerline pressure is observed with a

maximum of 35 kPa ($P_s/P_{C\text{-}max}$ = 0.028) at t = 61 msec. As qualitatively observed in our experimental results, the spatial ground pressure is relatively constant in the quasi-steady state regime at ~16 kPa ($P_s/P_{C\text{-}max}$ = 0.013) up to a non-dimensional radial distance of approximately r/D_e = 0.8 at t = 28 msec. During the start of P_C ramp down, the centerline pressure decreases to ~12.4 kPa ($P_s/P_{C\text{-}max}$ = 0.01) at t = 54 msec with a similar spatial profile. During complete P_C ramp down, where the thruster inlet stagnation pressure is below 20% of its' maximum value, there is a small monotonic pressure profile with a maximum non-dimensional ground pressure of 0.002 at the centerline.

Another important feature of these jets at Mars atmospheric pressure is their tightly collimated plume structure as shown in Figure 2.8. We observe minimal dissipation of the structure and jet pressure for large axial lengths. This is characteristic of moderately underexpanded jets and as discussed in Appendix A, this is not observed for highly overexpanded or underexpanded jets.

2.6.5 Interpretation of experimental and numerical results

Results of the cold flow testbed and numerical simulations, described above, show qualitative and quantitative similarity. Both of these studies suggest that a highly unstable normal plate (bow) shock (Fig. 2.4A) and possibly stagnation bubble form and collapse at the ground during the engine startup and shutdown portions of each power cycle, respectively. However, the large overpressures at the ground are primarily associated with the formation and collapse of this plate shock. The amplitude of the largest overpressures depends on the stagnation pressure rise and fall rates, atmospheric density or jet expansion ratio, and most importantly, the strength or Mach number of the plate shock. A relatively constant spatial ground pressure profile along the span of the plate shock diameter as observed in Figures 2.7 and 2.8B is indicative that a fully developed shock has formed near the surface. It can also be seen for a ½ scale thruster, the fully developed plate shock diameter is ~5 cm. We also note that during P_c ramp down the plate shock diameter decreases and eventually collapse.

From Figure 2.4A, the other flow features directly related to this interaction during the quasi-steady state regime are symmetric oblique tail shocks that emanate from the triple point and may impinge on the surface [*Krothapalli et al.,* 1999]. The triple

point region is where the reflected incident, plate and tail shocks converge. The relatively small ground pressure peak of 21 kPa ($P_s/P_{C\text{-}max}$ = 0.017) observed at r/D_e ~0.9 in Figure 2.8B probably result from flow passing through the oblique tail shock boundary which has a higher pressure recovery than a normal shock [*Krothopalli et al.,* 1999].

The wall jet, the last flow feature of interest, was not discernable from our temporal or spatial pressure profiles due to low spatial resolution. From the Mach contours, the plume impingement at the surface creates a supersonic wall jet that propagates along the ground at Mach 2 (Fig. 2.8). This is further supported by small secondary pressure peaks at r/D_e=3.5 in which the flow went through a compression wave. The wall jet can cause considerable soil erosion and dust lifting. These successive overpressures and the associated ground shock vibrations may lead to site alteration and this is further discussed in Section 2.6.6.

Although the ground pressure values are different due to different h/D_e cases, an important finding is that the qualitative temporal and spatial ground pressure profiles are the same for two different altitudes. However, the GASP numerical solver was used to provide a more accurate quantitative comparison between the experimental measurements and numerical simulations. Both temporal (Fig. 2.9A) and spatial (Fig. 2.9B) ground pressure profiles of the cold flow testbed measurements and numerical simulations are consistent with each other [*Mehta et al.,* 2007]. There are some discrepancies, but the general flow physics can be extrapolated from this analysis. For example, the onset of the overpressure is delayed for the experimental measurements by ~5 ms and its' magnitude is less than those recorded numerically. The discrepancies can be attributed to limitations to both the hardware sampling frequency and numerical model assumptions. The Pc profile used for the numerical simulation has a slightly larger pulse-width than for the experiments. Some of these inconsistencies could be attributed to the high instabilities within the plate shock and as discussed in the following section, as being more likely.

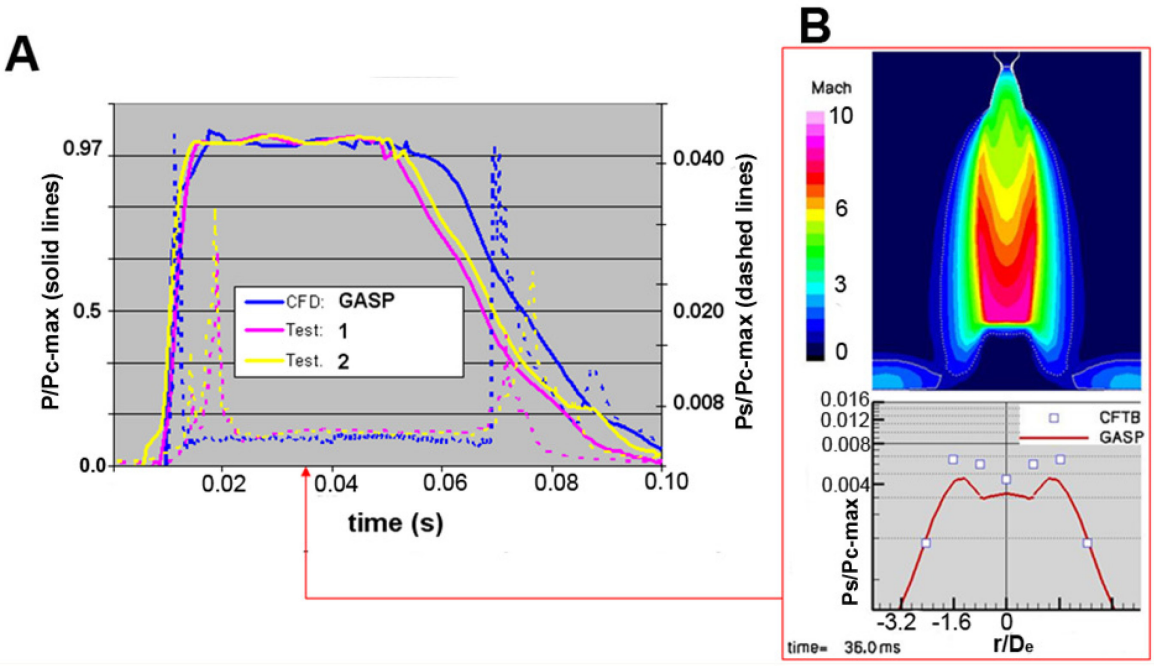

Figure 2.9. Comparison of axisymmetric numerical simulations and experimental measurements of pulsed supersonic N_2 jet interactions at $h/D_e = 8.4$. (A) Temporal centerline ground pressure (dashed lines) and P_c (solid line) profiles; (B) Spatial ground pressure profiles and Mach contour. [*Gulick*, 2006]

2.6.5.1 Plate shock dynamics

The dynamics of the impingement of a pulsed rocket plume with the surface at low ambient pressure is illustrated in Figure 2.8A and can be seen by a transient numerical simulation (Movie D2, Appendix D). From numerical and experimental results, we deduced the following mechanism for this complex interaction. At the start of the engine duty cycle, P_C ramp up, isentropic expansion waves coalesce into accelerating shock waves, which propagate downward from the converging-diverging nozzle and impinge on the ground [*Courant and Friedrich,* 1999]. This sudden compression causes an increase in the flow momentum and ground pressure, which is defined as the pre-plate shock formation stage. An irreversible and detached normal shock forms when compression/oblique shock waves are reflected by the ground and coalesce at a particular distance upstream from the flat surface (shock stand-off distance) [*Lamont and Hunt,* 1980]. The non-isentropic behavior and viscous dissipation across this normal shock boundary causes a decrease in ground total pressure, attributed to a sudden decrease in plume velocity across the boundary [*Anderson,* 2004]. The loss in the total pressure or

pressure recovery across the normal shock is directly a function of the shock strength (Mach number) and orientation (oblique or normal) [*Lamont and Hunt,* 1980].

Additional ground pressure perturbations are caused by instabilities at the boundaries of a stagnation bubble and plate shock that forms during the quasi-steady portion of the duty cycle (25 to 70 msec during the first cycle and 115 to 155 msec during the second cycle all illustrated in Figure 2.6). Plate shock fluctuations normal to the surface also contribute to the ground pressure perturbations [*Henderson et al.,* 2005]. These fluctuations during the quasi-steady regime are not readily observed in the experimental data because of the limited sampling rate, but are observable in numerical simulations. Theoretically, as the shock stand-off distance decreases, the ground pressure increases due to smaller gas expansion over a smaller plume volume below the plate shock. When, on the other hand, the stand-off distance increases, the ground pressure decreases because of an increase in the plume volume below this shock which facilitates expansion and momentum dissipation. Henderson et al [2009] shows that the axial oscillations of the plate shock are due to the motion of both the contact surface, which separates shock driven flow and stagnant ambient flow, and the stagnation bubble. These pressure fluctuations due to normal shock oscillations are also observed during its' formation and collapse as shown by an axisymmetric transient simulation (Movie D3, Appendix D).

Once the thruster inlet stagnation pressure to ambient pressure ratio is not large enough to support a normal shock at the surface during P_C ramp down phase, the plate shock and/or stagnation bubble collapses, leading to the propagation and impingement of weak shock waves. Through gas compression, this considerably increases the ground pressure similar to the mechanisms described above [*Mehta et al.*, 2007]. Once the plate shock is absent during complete P_C ramp down, the ground pressure monotonically decreases with decreasing thruster inlet stagnation pressure as would be seen for subsonic jet impingement (Fig. 2.8B) [*Donaldson et al.,* 1971]. From our results, this mechanism causes large pressure spikes observed at the beginning and end of each engine power cycle (Figs. 2.6 and 2.9A). Numerous tests confirmed that the overpressures correlated to engine thrust cycling. The plate shock acts to decelerate the impinging jet flow and

increase pressure loss which leads to a relative decrease in the ground pressure and the observed overpressure peaks.

The plate shock dynamics can also be seen by spatial ground pressure profiles (Figures 2.7 and 2.8B). As described above, once a plate shock is fully developed, the ground pressure at the centerline drops and remains relatively constant along the plate shock diameter. Once pre-plate shock formation or post-collapse occur, a monotonic increase in spatial ground pressure is observed due to direct impingement of compression waves. This further validates the dynamic process of the normal stand-off shock due to pulsed underexpanded jet impingement.

By applying this proposed mechanism and the lack of large pressure gradients and characteristic overpressure peaks, pulsed supersonic jets at Earth atmosphere at an h/D_e = 8.4 and e = 0.02 never developed a plate shock at the surface. This is described in more detail in Appendix A, Section A.5.5

2.6.5.2 Asymmetries due to adjacent plume interactions

Although most of the studies presented thus far are primarily concerned with single jet interactions, we will briefly discuss the ground pressure and shear stress (tau) behavior due to two adjacent underexpanded N_2 jets with a nozzle spacing of x/D_e = 0.1, similar in geometric configuration as adjacent Phoenix descent engines. A 3-D steady state numerical simulation was developed to understand possible asymmetries at the surface. In contrast to the radial symmetry of single subsonic and supersonic jet interactions [*Phares et al*, 2000], adjacent jets develop large asymmetries in both ground pressure and wall shear stress parameters as shown in Figure 2.10. There are no symmetric ring-like contour profiles, but rather asymmetric semi-circular high pressure and shear stress regions. This may be attributed to shock-shock Riemann interactions [*Menikoff and Plohr*, 1989] which develop a merged shock with higher strength at both the near-field and far-field regimes. Hence, the plate shock is almost twice in diameter as observed for a single jet case. This merging could lead to a noncoplanar development of the normal shock, resulting in asymmetry in ground pressure. This may also affect both the tail shock and the flow behavior of the supersonic wall jets, leading to asymmetry in the wall shear stress. These wall jets are caused by flow expansion, developing mainly

from flow across the tail shock and propagating along the surface (Fig. 2.8A) [*Carling and Hunt*, 1974]. Hence, these results demonstrated the need for 3-D numerical simulations of the six pairs of Phoenix REM plume interacting at the surface.

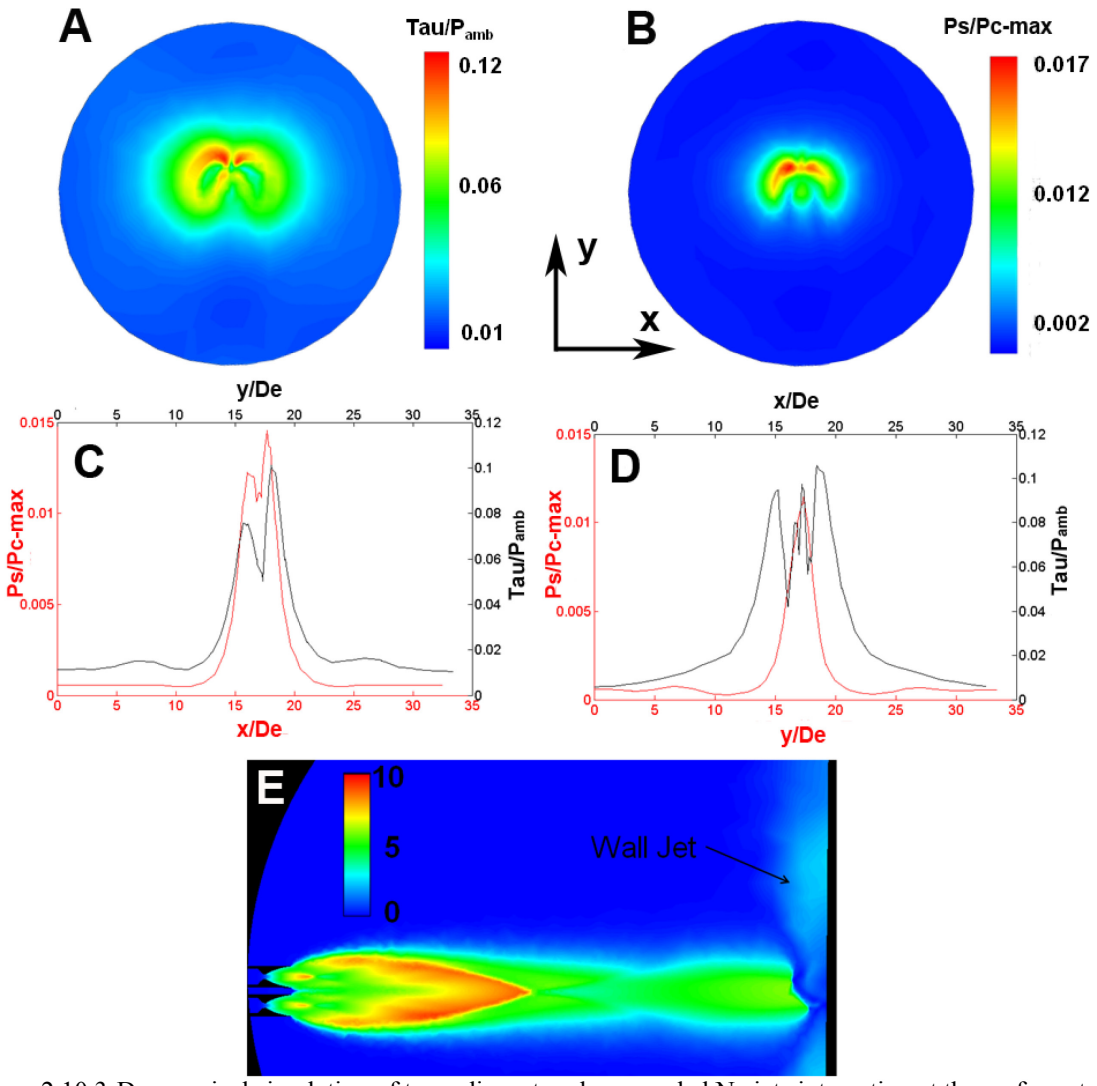

Figure 2.10 3-D numerical simulation of two adjacent underexpanded N_2 jets interacting at the surface at $h/D_e = 25$. Contour s of (A) wall shear stress normalized by ambient pressure and (B) normalized ground pressure; (C,D) Tau and ground pressure profiles along the *x* and *y* centerlines. (E) Mach contour

2.6.5.3 Comparison of full-scale and subscale analyses

First, a single full-scale descent engine was numerically modeled and we observed good agreement with data from subscale experiments. This profile is shown in Figure A16, Appendix A. This was an important result, because it partially confirmed the validity of our scaling laws. Full-scale rocket test firing at simulated martian conditions

that record both temporal and spatial ground pressures are needed to fully validate these laws.

Once numerical and experimental results showed relatively good temporal and spatial agreement, the numerical code GASP was used to model full-scale three-dimensional cases for adjacent thruster plumes impinging at the surface. The computational domain spans a 60° wedge where two engines are modeled and is bounded by symmetry planes [*Gulick*, 2006]. This domain is then extrapolated to obtain the Mach and pressure contour profile of the full 360° Phoenix Lander as shown in Figure 2.11. More details in regards to the development of the flow domain and boundary conditions are described in Appendix A.4.2. Due to adjacent plume interactions and non-linear shock/shock interactions as described in the previous section, the plate shock demonstrates noncoplanarity and oscillates in three-axes, leading to both asymmetric high pressure regions (Fig. 2.11A) and ground pressure fluctuations (Fig. 2.11B) during the quasi-steady regime. Most importantly, characteristic overpressure peaks are observed during rapid engine start-up and shut down, suggesting the mechanism of plate shock formation and collapse. These numerical simulations show that the spatial ground pressure profiles between the full-scale (Fig. 2.11) and subscale (Fig. 2.10) systems show good agreement and further confirm the use of these scaling laws.

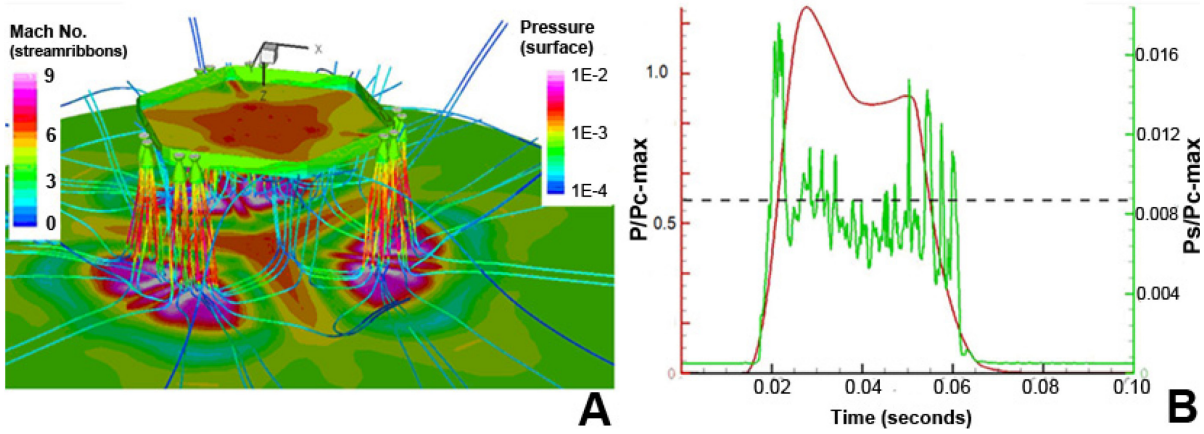

Figure 2.11. Three-dimensional numerical simulation of full-scale interacting REM plumes exhausting into a martian atmosphere. (A) Mach and normalized pressure contours of steady REM plumes interacting at the surface at an altitude of h/D_e = 8.4 and 0° slope [*Gulick*, 2006] (B) Centerline ground pressure (green curve) and P_c (red curve) temporal profiles due to 0.1 s jet pulse at an altitude of h/D_e = 21.9 and 0° slope. The dashed line is the centerline ground pressure solution for steady-state numerical simulation. [*Gulick*, 2006]

2.6.6 Site-alteration and dust lifting

Various mechanisms due to the pulsed rocket plume scheme can lead to significant soil erosion and dust lifting. The overpressures described above and the high surface shear stress associated with the supersonic wall jets can lead to soil erosion and dust lifting. Large and rapid pressure fluctuations might cause soil liquefaction [*Youd,* 2001]. Soil liquefaction is defined as the fluid-like state of granular media. Ground shock vibrations caused by these large transient overpressures super-imposed by the pulsing quasi-steady state overpressure regions may disrupt the soil and break the particle-to-particle cohesive forces. This can decrease the bearing capacity, maximum average contact pressure between the foundation and the soil to prevent shear failure, and increase the fluidization of the soil, possibly leading to lateral ground failure and crater formation [*Vitton et al.,* 1990]. This similar mechanism provides a hydraulic mining pulsed water jet to excavate heavy granular and rock material [*Kolle*, 1994]. The extent of ground failure depends on the soil properties, surface impingement pressure, ground shear stress [*Romine et al*., 1973] and the dynamic interactions between the thruster plume and the ground [*Youd*, 2001]. The minimum ground pressure threshold before erosion takes place at a simulated martian environment is approximately ~2 kPa for soil similar to dune sand or lunar nominal [*Romine et al.,* 1973].

Also, depending on whether the shock cell is within the compression or expansion zone near the surface results in a non-linear behavior of ground pressure with altitude, which presents itself differently than for the asymptotic profiles of subsonic jets [*White*, 1996]. These pressures are relatively independent of altitude and oscillate around a mean value for small h/D_e (< 40). The overpressure and quasi-steady state ground pressure can significantly change in magnitude as can be seen for the two non-dimensional altitude cases presented here: h/D_e = 8.4 and 25. This high variability is further shown in Figure 2.12. We see good qualitative agreement between experimental observations of cold gas simulations [*Romine et al*., 1973] and 3-D numerical results of full-scale systems [*Gulick*, 2006]. This variability may also lead to further disturbance of soil during spacecraft descent.

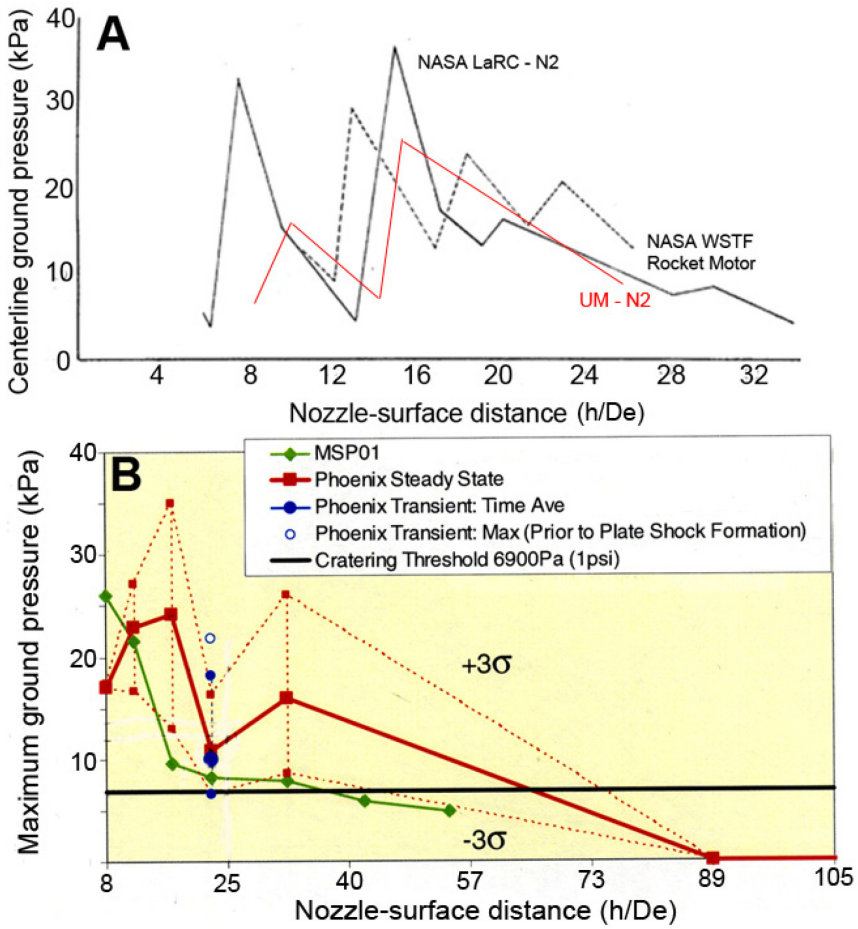

Figure 2.12 High variability of ground pressure vs. altitude profiles due to shock wave interactions. (A) Limited experimental results (red profile) compared to NASA WSTF and NASA LaRC studies using a single nozzle [*Romine et al.,* 1973]; (B) Numerical result for full-scale Phoenix REM plume interactions at both steady state and transient conditions. Green curve - earlier numerical solution in support of the Mars Surveyor Program (MSP) [*Gulick*, 2006].

According to Romine et al [1973], there are three main mechanisms that lead to site-alteration and dust lifting: (a) bearing capacity failure; (b) viscous erosion and (c) diffused gas erosion. Through extensively developed scaling laws which address these three mechanisms, we can properly scale earth-gravity based tests for Mars conditions (Chapter 3). All three mechanisms may play a significant role in site-alteration and dust lifting due to Phoenix's pulsed thrust impact on the surface. Also, the recent discovery that Mars northern polar region surface has extensive soil-depth variability, ranging from 5 cm to greater than 20 cm [*Bandfield,* 2007], has made understanding site-alteration and dust lifting important for Phoenix science operations. Due to the importance of understanding ground pressure profiles of thruster plume interactions, further studies were conducted in support NASA's new Mars mission.

The main parameter that is used to determine the extent of jet-induced soil erosion is the surface pressure profile of the impinging jet or rocket plume [*Romine et al*., 1973]. As discussed in Chapter 3, soil pore pressure and soil properties are directly dependent on the surface pressure. However, this investigation shows that along with surface pressure magnitude and spatial profiles, the temporal pressure profile is also a critical parameter in determining the flow physics of the exhaust gas within the granular media.

2.6.7 Flow physics of steady supersonic jet impingement at varying atmospheric regimes

Numerical and experimental investigations of both far-field and near-field supersonic steady jet interactions with a flat surface at various atmospheric pressures are presented in Appendix A. These studies were done in support of the NASA Mars Science Laboratory mission. Temporal and spatial ground pressure measurements in conjunction with numerical solutions at altitudes of 35*d* and jet expansion ratios between 0.02 and 100 are used. Data from steady nitrogen jets are compared to both pulsed jets and rocket exhaust plumes at Mach ~5. Due to engine cycling, overpressures and the plate shock dynamics are different between pulsed and steady supersonic impinging jets. In contrast to highly over-expanded and underexpanded exhaust plumes, results show that there is a relative ground pressure load maximum for moderately underexpanded (e ~2-5) jets which demonstrate a long collimated plume shock structure. For plumes with e >>5 (lunar atmospheric regime), the ground pressure is minimal due the development of a highly expansive shock structure. This is dependent on the stability of the plate shock, the length of the supersonic core and plume decay due to shear layer instability which are all a function of the jet expansion ratio. Asymmetry and large gradients in the spatial ground pressure profile and large transient overpressures are predominantly linked to the dynamics of the plate shock as discussed in this Chapter. Results also show that subscale supersonic cold gas jets adequately simulate the flow field and loads due to rocket plume impingement provided important scaling parameters are in agreement. More importantly, this study shows that thruster plumes exhausting into martian environments possess the largest surface pressure loads and can occur at high spacecraft altitudes in contrast to the jet interactions at terrestrial and lunar atmospheres.

2.7 Conclusions and future work

The FTIR and GC-MS analysis of the thruster plume gases show no detectable hydrazine. This is the primary result of the FTIR and GC/MS analysis, since the presence of hydrazine has the potential to significantly complicate the interpretation of the in-situ analysis of the Martian soil. The analysis however did show significant amounts of NH_3 and N_2. The N_2 posses no problem for the Phoenix wet chemistry, but the presence of NH_3 in the plume must be further investigated and a good understanding of the possible reactions obtained.

Experiments and numerical simulations suggest that the ground impingement pressure of the pulsed thruster plumes at the surface of Mars generates large transient overpressures which correlate to a ground shock frequency of approximately 20 Hz and a 10 Hz quasi-steady state ground pressure perturbation. These large ground overpressures occur due to the formation and collapse of the plate shock near the surface due to high instability in the plate shock dynamics during P_C start up and shutdown cycles. This, in conjunction with surface asymmetry and altitude effects, may have the potential to significantly increase soil erosion and uplifting. The amount of cratering and soil uplifting depends on the soil properties, ambient pressure and engine thrust to be discussed in Chapter 3.

We plan to use the data presented here to test the effects of NH_3 adsorption on a cross section of Mars simulant soils. The experiments are designed to provide information as to what effects such adsorption may have on the chemical analyses that will be performed by the Wet Chemistry Laboratory (WCL) on Phoenix.

Significant insight and information have been obtained in understanding the flow field of pulsed underexpanded jets and its dynamics on the surface. However, high-speed Schlieren imaging at a minimum of 1000 frames per second is needed to confirm our theory. This should be compared to numerical simulations performed. In particular, Schlieren with Particle Image Velocimetry will also provide information on the behavior of stagnation bubbles subject to the described plate shock dynamics and may shed some light on acoustics.

The next approach is to conduct experiments with the CFTB at the NASA Ames Research Center's Planetary Aeolian Laboratory (PAL), Aeolian wind tunnel facility at

martian environments, to quantify soil erosion and uplifting during spacecraft landing on Mars. Our main goal is to understand the flow physics and its' effects of pulsed under-expanded jets impinging on granular systems in tenuous atmospheres. Scaling laws (see section 3.2.1) are used to relate experimental results to the site-alteration measurements at the landing site.

These experimental results described in Chapter 3 provided the Phoenix Science Team with an approximation of the crater contour as well as the crater depth and dust deposition at the landing site. Results from the tests were primarily used for scientific interest and assessment of spacecraft stability, providing information about possible dust contamination in the vicinity of sample ingestation areas for MECA and TEGA, on calibration targets, and general albedo-induced changes to the thermal properties of the science deck [*Marshall et al.*, 2007]. Subsequently, these tests were used to provide information of erosion or deposition at the digging location, solar panels and landing deck. Provided that MECA only has four sample analysis opportunities for the wet cells, it was important that we understood soil disturbance in the digging area, both its lateral and vertical extent. These top few centimeters were also the zone of chemical contamination from the plumes that could potentially influence TEGA results. Results from these tests lead to mitigation strategies. Our research group worked closely with both the Phoenix engineering and science teams to implement these strategies. For example, the solar panels were controlled to deploy much later than originally planned and the robotic arm avoided regions of high contamination.

CHAPTER 3

Explosive erosion during the Phoenix landing exposes subsurface water on Mars

Cratering dynamics due to impinging supersonic jets

This chapter describes an article submitted and revised to *Icarus* in 2010.

3.1 Introduction

On May 25th 2008, the Phoenix spacecraft landed on the martian arctic to study the local environment and its potential for sustaining life [*Smith et al.*, 2009]. The search for water has been an important goal of the mission because liquid water is an essential ingredient for life as we know it [*Renno et al.*, 2009]. Here, we report the discovery of the erosion process that rapidly removed 5 to 18 cm thick layers of soil [*Smith et al.*, 2009; *Sizemore et al.*, 2009], first exposing water ice at the landing site [*Renno et al*., 2009], and leading to the discovery of evidence for liquid saline water on Mars [*Renno et al.*, 2009]. The understanding of this process allowed the calculation of bulk physical properties of the soil at the Phoenix landing site. This study also provides information on site contamination that may have occurred during the landing phase. Along with new developments in granular flow, the discovery of the 'explosive erosion' process reported here has important implications for engineering and science.

Brief interactions of the jets from three non-pulsed engines of the Viking landers (with 2230 Newtons of thrust) with the martian soil caused only modest surface erosion during landing [*Shorthill et al.*, 1976a, 1976b]. However, Phoenix's twelve engines (with 30% less total thrust) pulsating at 10 Hz with an average impingement pressure of only 1/10 of the Earth's sea level pressure [*Renno et al.*, 2009], caused extensive erosion of the

landing site, and exposed the subsurface ice under the lander over a radius between 75 and 85 cm from its centerline (Appendix B.1) [*Smith et al.*, 2009]. The Phoenix inertial measurement unit indicates that lift loss started when the spacecraft was 5 m above the surface, while descending at ~2.6 m/s, followed by ground effects and a slight reduction in the spacecraft descent velocity (see Section 3.8) [*Desai et al.*, 2008]. This suggests that the jets interacted with the soil for less than 2 s. Although unlikely, minor incipient erosion may have occurred while the spacecraft was above 5 m [*Clark*, 1970]. To provide more contexts to our investigation, the aerodynamic loads and rates during the Phoenix spacecraft entry, descent and landing sequence is presented in Section 3.8.

It has been known that jet impingement produces soil erosion and craters through four distinct physical processes: **(i)** The dragging of surface soil particles by viscous shear erosion (VSE) when the forces caused by the jet's shear stress exceed the cohesive and frictional forces between particles, as occurred during previous landings on Mars and the moon [*Shorthill et al*., 1976a, 1976b; *Christensen et al.*, 1967]; The formation of transient craters with steep walls occurs by a combination of two distinct processes termed **(ii)** bearing capacity failure (BCF) and **(iii)** diffusion-driven flow (DDF) when the jet's ground pressure exceeds the shear strength of the soil [*Metzger et al*., 2009]; **(iv)** The removal of soil when gases from the thruster jets rapidly escape from the granular pore space causing diffuse gas erosion (DGE), a single eruption event when the engines shut down [*Metzger et al.*, 2009; *Scott and Ko*, 1968]. Here, we report the discovery of a fifth process **(v)**, which we name diffusive gas explosive erosion (DGEE) or 'explosive erosion' that dominates the erosion process when supersonic pulsed jets impinge into porous soils which generate high pore pressure gradient forces to soil weight ratios, ΔP^*. These processes are described in further detail in Section 3.4.

3.2 Experimental methods

Here, scaling analysis of laboratory experiments and numerical simulations are used to study the erosion caused by the Phoenix landing on Mars. Scaling of the thruster jet-soil system indicates that the erosion dynamics due to spacecraft landings on Mars can be simulated by laboratory experiments on Earth. Hence, the terms "experiments" and "laboratory simulations" are used interchangeably in the Chapter. Similarity can be

achieved by matching the nondimensional numbers that scale gravitational (F_g), interparticle (F_σ), pore pressure gradient (F_p) and aerodynamic (F_{aero}) forces on the granular media (Fig. 3.1) [*Balme and Hagermann*, 2006; *Neakrase et al*., 2009; *Greeley and Iversen*, 1985] or by simulating these forces in the absolute scale. F_{aero} on the particle is dependent on the jet's shear stress and it has two components: the lift force which is perpendicular to the jet and drag force which is parallel to the flow. The interparticle forces which are a function of the particle size include cohesion, van der Waals, electrostatics and moisture [*Neakrase et al*., 2009]. The Magnus lifting force due to particle rotation and Saffman force due to shearing flow is less than a percent of the particle weight [*Kok and Renno*, 2010] and has been neglected in our scaling laws. It is also important to ensure that the jet impingement dynamics such as the pulse width, frequency and jet orientation (cant angle with respect to nozzle centerline) are simulated. These parameters are tabulated in Table 3.1.

Parameters	**MR-107N**	**½ scale**
Total pressure at inlet (kPa)	1240	1240
Total temperature at inlet (K)	1116	300
Jet pressure at exit (kPa)	3.24	3.09
Jet density at exit (kg/m^3)	0.03	0.19
Jet velocity at exit (m/s)	1929	712
Jet mass flow rate (kg/s)	0.32	0.22
Pulse frequency (Hz)	10	10
Pulse width (s)	~0.055	~0.065
Firing duration (s)	<2.0	≤3.0
Nozzle diameter at exit (cm)	6.25	3.13
NH_3 exhaust mass fraction (a.u.)	0.49	0.0
Maximum thrust (N)	~600	~160
Cant angle (deg)	0	0

Table 3.1 Specifications of the performance parameters between dual Phoenix rocket motors and ½ scale cold gas thrusters.

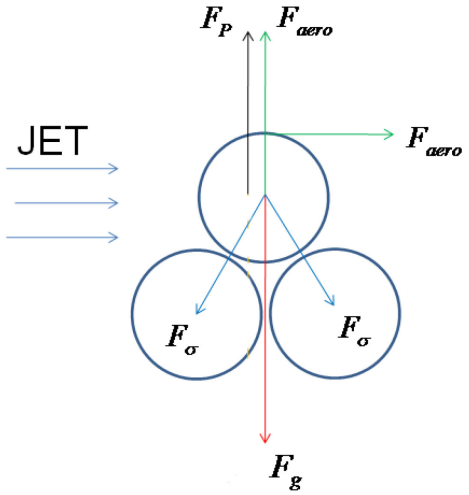

Figure 3.1. Sketch of the main forces acting on soil particles during jet-induced erosion. Although depicted that the jet is incoming from left to right, it can be in any direction.

A duration of 0.75 to 3.00 s long interactions of dry N_2 jets from a pair of subscale Phoenix engine nozzles with a granular bed of martian simulant was studied using various particle size distributions in a pressure-controlled chamber. The criterion to use nitrogen as the test gas is described in Section 3.2.1. Brief plume-soil interactions of steady and 10 Hz pulsed jets at ~300 K with a ~65 msec pulse width (Fig. 3.2) at various static altitudes are studied in a ~4000 m^3 chamber at NASA Ames Research Center's Planetary Aeolian Laboratory (PAL). The vacuum chamber was set to atmospheric pressures between martian and terrestrial near-surface ambient conditions. All jets impinge normally with respect to the soil bed. The contours of the pair of Phoenix descent rocket engine motor (REM) nozzles and the spacecraft configuration including the lander deck and nozzle orientation and spacing are all ½ scale models as depicted along the $+z$ and $-x$ directions in Figure 3.3A,B and Figure 2.5 (Chapter 2).

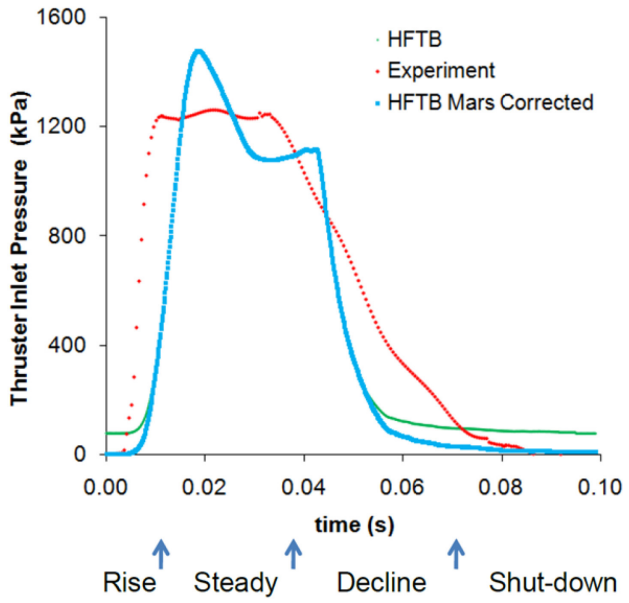

Figure 3.2. ½ scale Phoenix descent engine simulators pulsating at 10 Hz with a ~65 msec pulse width are used in our laboratory simulations (experiment). Data from a single thrust cycle of our laboratory simulation is compared with that from the Phoenix REM thrusters hot fire testbed (HFTB) performed at Earth atmospheric pressure and corrected for Mars atmosphere conditions.

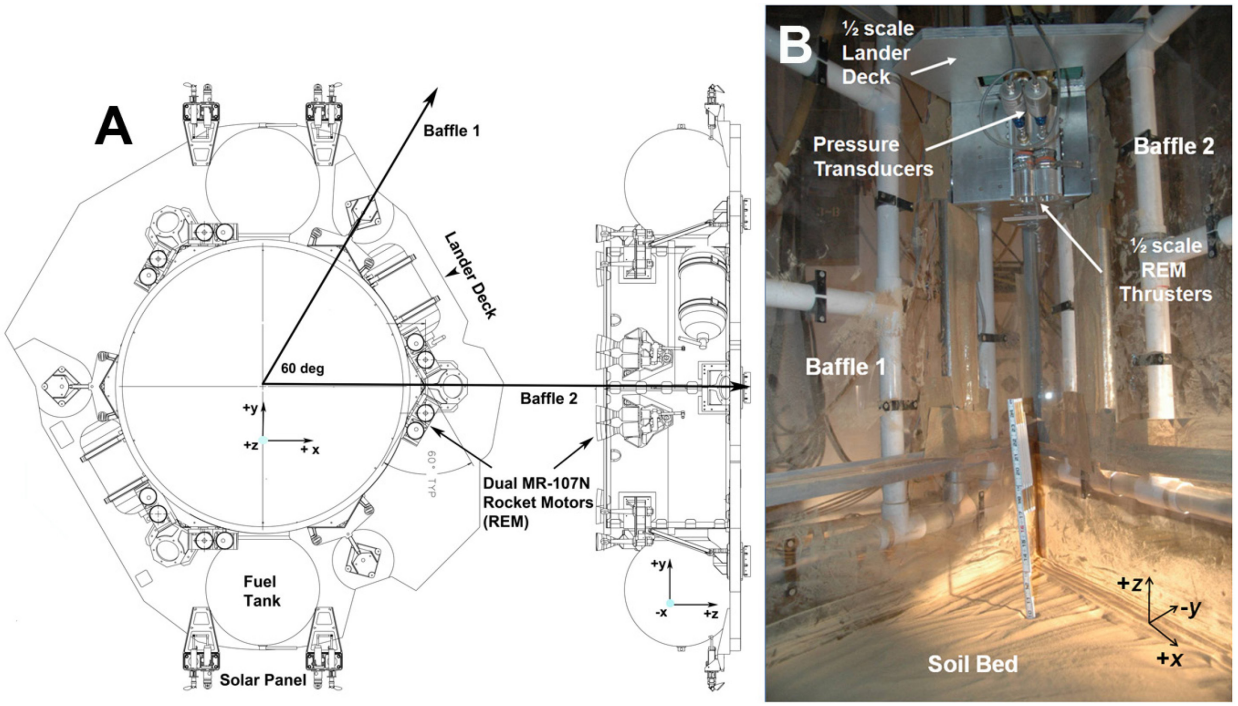

Figure 3.3. (A) Top-down schematic along the +*z* axis and side (along the -*x*-axis) views of the Phoenix spacecraft which shows the placement of the transparent baffles 1 and 2 and thrusters. *Courtesy of NASA/JPL-Caltech/Lockheed Martin*. (B) An isometric photograph of the laboratory simulations at NASA Ames Research Center - PAL.

Pressure transducers installed in the nozzle inlets were used to monitor the stagnation pressure in the thruster simulator and assure that its' magnitude and temporal profile were similar to that in the combustion chamber of the Phoenix descent engines during the landing phase. The nozzle pressure ratio (NPR) was identical between subscale and full-scale systems. The thruster inlet stagnation pressure vs. time graph known as a thrust cycle for a 10 Hz pulsed jet is shown in Figure 3.2. There are four regimes for each cycle which spans 0.1 s: thrust rise, 'steady' thrust, thrust decline and thrust shut-down For all tests, the maximum thruster chamber pressure and temperature are 1.2 MPa and 300 K, respectively.

Transparent plexiglass baffles (baffles 1 and 2) were used to simulate the planes of symmetry between neighboring pairs of thruster jets as shown in Figure 3.3A [*Romine et al.*, 1973; *Huseman and Bomba*, 2000] and to visualize the erosion process through still and hi-speed imaging [*Schultz et al.*, 2007; *Metzger et al*., 2009]. When multiple jets impinge on the surface, stagnation planes develop between groups of thrusters [*Huseman and Bomba*, 2000; *Romine et al.*, 1973]. The trajectories of fine soil particles loosely follow these planes. Therefore, a sixty-degree test section was developed to simulate the fluid dynamic effects of the outboard REM thrusters. This approach was further confirmed by computational fluid dynamic simulations as discussed in section A.4.2.

The quarter-space technique [*Schultz et al.*, 2007] described below is used in all PAL experiments to approximately visualize the axisymmetric crater growth process. All high speed images are taken along the *x-z* plane (baffle 2) in the direction of the +*y* axis which is directed into the page and the origin is at the apex of the wedge as depicted in Figure 3.4A,B. These images at full resolution of 1280 x 1024 pixels are taken normal to baffle 2 at a frame rate of 500 images per second and shutter speed of 1 msec. The high speed camera is located 30 cm from the baffle plane (Fig. 3.4C) and focused on the impingement region's *x-y-z* coordinates of: (30 cm, 0 cm, 20 or 5 cm). The test section which shows a 2-D layer of granular media is illuminated with 750 W lamps on either side of the camera. The high speed camera operates with a wide angle lens which allows a coverage width of 75 cm. Based on test setup configuration, the impingement centerline point on the granular media is at an *x-y-z* coordinate of: (30.0 cm, 5.6 cm, 20.0 or 5.0 cm). In cylindrical coordinates, the *r-θ-z* values are: (30.0 cm, 10.6º, 20.0 or 5.0 cm). All

data extrapolated from high speed images are taken along the *x*-*z* plane at $\theta = 0^{o}$ (baffle 2). Post site alteration data is taken from still images along the *x*-*z* plane at $\theta = 0^{o}$ and $\theta = 60^{o}$ (baffle 1) and isometric images and measurements.

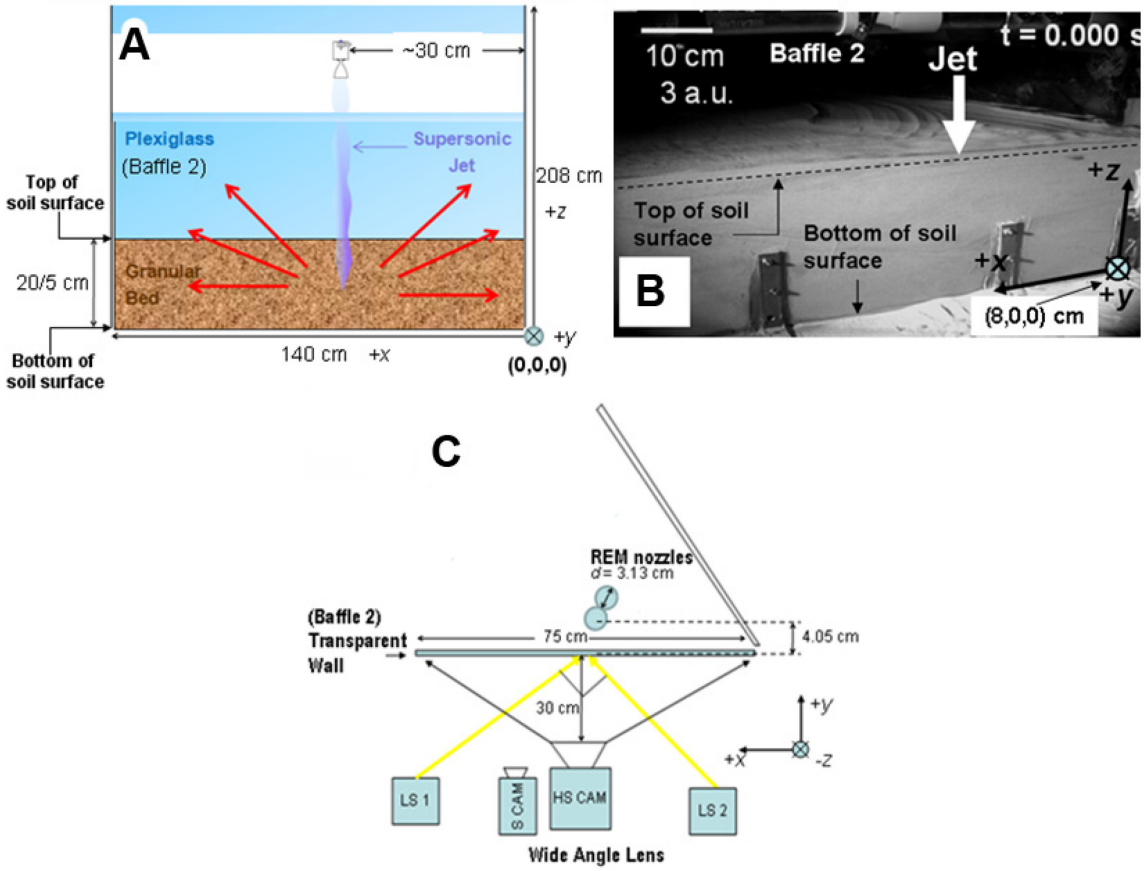

Figure 3.4. (A) A side-view schematic of the impingement of supersonic pulsed jets on porous soils. The quarter space technique [*Schultz et al*., 2007] with the high-speed camera viewing along the positive *y*-axis and focusing on the plexiglass symmetry-plane (*x*-*z* plane) is used to analyze the jet-soil interaction. (B) An annotated monochromatic image of the side-view of the test section along the *x*-*z* plane at pre-jet impact conditions (t = 0.0 s). (C) A top-view schematic of the experimental setup looking along the –*z* axis. Shows the positioning of the test section, high speed (HS CAM) and still (S CAM) cameras and focused lights sources (LS) depicted by yellow arrows.

In order to account for the effects of lower martian gravity, low-density crushed walnut shells were used to simulate the gravitational forces of soil particles on Mars [*Greeley et al*., 1980]. These martian stimulants, partitioned into four different particle size distributions, were used in the experiments: (i) poorly sorted fine sand (S) (diameter, d ~160μm), (ii) fine silt/dust (F) (d < 15 μm), (iii) large coarse sand (C) (d = 850 to 2500 μm), and (iv) bimodal mixture of fine silt/dust with fine sand (B) (Table 3.2). The

simulants were sieved to resemble the various size distributions of basaltic sand found on Mars [*Shaw et al.*, 2009] to accurately simulate interparticle forces. The simulant properties were determined by direct shear, constant/variable head permeability and relative density tests performed in controlled laboratory conditions at 300 K and 5-20% relative humidity which was representative conditions of the NASA Ames vacuum chamber facility.

Soil stimulant	Particle diameter (μm)	Mean diameter (μm)*	Cohesive strength (kPa)	Permeability coefficient (cm/s)	Porosity (a.u.)	Angle of friction (deg)	Crater volume ratio (a.u.)
Fine silt/fine sand (B)	2 – 200	~BI	5.0 (±1.5)	0.0003 (±2e-5)	0.45(±0.05)	31 (±2.0)	0.16
Fine sand (S)	2 – 200	~160	1.3 (±0.3)	0.0021 (±0.001)	0.50(±0.05)	33 (±2.5)	0.20
Coarse grain (C)	850-2500	~1500	0.0 (±0.25)	0.3000 (±0.1)	0.30(±0.03)	35 (±2.0)	0.01
Fine silt (F)	2 – 25	<15	7.5 (±1.0)	0.0002 (±3e-5)	0.73(±0.10)	28 (±2.0)	0.65

* BI – 50% fine silt and 50% fine sand by volume

Table 3.2. Measurements of the physical properties of the martian soil simulant (crushed walnut shells) used in the laboratory simulations

3.2.1 Scaling analysis

Erosion rates and dynamics depend on the forces acting on the granular media (Fig. 3.1) and modes (Fig. 3.2) of the impinging jets. It follows from nondimensional analysis that the forces caused by the impinging jets on the soil are scaled by matching the ratio of the kinetic with the internal energy (hypersonic similarity parameter) of the plume (k, Eqn. 3.1), the jet expansion ratio (e, Eqn. 3.2), and the plume's exit Mach number and Reynolds number (Re, Eqn. 3.3) as discussed in Chapter 2. Along with matching the jet dynamics, the erosion dynamics are scaled (Appendix B.2) by matching the densimetric Froude number (Fr_d, Eqn. 3.4) [*Mazurek and Rajaratnam*, 2005; *Greeley and Iversen*, 1985], the soil strength scaling parameter (β, Eqn. 3.5) [*Holsapple*, 1993], the nondimensional threshold friction velocity (u_{*t}/u_*, Eqn. 3.6) [*Greeley and Iversen*, 1985], the ratio of the characteristic diffusion time in the vertical component with jet pulse period (τ/t_{imp}, Eqn. 3.7) and the normalized pressure gradient within the soil (ΔP^*, Eqn. 3.8) [*Balme and Hagermann*, 2006]. From dimensional analysis (Appendix B.2), the important scaling laws are tabulated in Table 3.3 and defined as follows:

(3.1)
$$\frac{KE}{IE} = \gamma(\gamma - 1)M_e{}^2$$

(3.2)
$$e = \frac{P_e}{P_{amb}}$$

(3.3)
$$\mathrm{Re} = \frac{\rho_a D U_e}{\mu}$$

(3.4)
$$Fr_d = \frac{U_e}{\sqrt{\frac{\rho_p}{\rho_a} g\bar{d}}}$$

(3.5)
$$\beta = \frac{Y}{\rho_a U_e{}^2}$$

(3.6)
$$\frac{u_{*_t}}{u_*} = \sqrt{\frac{A_N\left(\frac{\rho_p}{\rho_a} g\bar{d} + \frac{\kappa}{\rho_a \bar{d}}\right)}{u_*{}^2}}$$

(3.7)
$$\frac{\tau}{t_{imp}} = \left(\frac{2l^2 n\mu}{kP_{imp}}\right)\frac{1}{t_{imp}}$$

(3.8)
$$\Delta P^* = \frac{3\left(P_p - P_{amb}\right)}{2\rho_p g\bar{d}} = \frac{3\Delta P}{2\rho_p g\bar{d}}$$

where γ is the specific heat ratio, M_e and M_g are the Mach numbers (= U/c_s) of the exhaust jet at the nozzle exit and granular shock waves and c_s is the speed of sound of its respective medium, P_e, P_{amb}, and P_{imp} are the nozzle exit, ambient and steady impingement pressures, ΔP is the pressure differential between the soil pore space, P_p, and the surrounding atmosphere [*Balme and Hagermann*, 2006], U_e is the nozzle exit jet velocity, $\bar{d}$ is the average particle diameter, D is the nozzle exit diameter, g is gravitational acceleration, τ is the gas diffusion characteristic time-scale, t_{imp} is jet impingement pulse period, ρ_a is the jet density, ρ_p is the particle density, l is soil depth, μ is jet viscosity, k is soil permeability, n is soil porosity, u_{*t} is the threshold friction velocity [*Shao and Lu*, 2000], u_* is the friction velocity, A_N ($=\sqrt{f(\mathrm{Re}_{*_t})}$; dimensionless) [*Shao and Lu*, 2000], and κ which is proportional to the interparticle forces (dimensional) [*Shao and Lu*, 2000] are relatively constants, and Y is soil strength which is dependent on cohesive strength (c), effective normal stress and angle of internal friction (θ_i) [*Terzaghi*, 1943]. A_N is weakly dependent on Re_{*t} for particle sizes between 30 μm and 1300 μm. The scaling parameters highlighted in red in Table 3.3 are most important for simulating soil particle forces and plume dynamics due to DGEE.

Normalized parameters	**Full scale**[†]	**½ scale**[ɣ]
Expansion ratio (e)	3.8	3.7
Exit Mach number (M_e)	4.7	4.8
Nondimensional threshold friction velocity	~0.015	0.014
Nozzle pressure ratio	~1500	1550
Densimetric Froude number (Fr_d)	250	230
Gas Reynolds number (Re_g)	3.4×10^5	12.7×10^5
Particle Re number (Re_p)[‡]	0.7×10^3	2×10^3
Strength scaling parameter (β)	~0.4	~0.3
KE/IE plume	11.4	12.7
Diffusion time scale (τ/t_{imp})[‡]	~330 – 10	200 - 6
Gamma (γ)	~1.38	1.40
Nozzle area ratio (A_e/A_*)	20.7	20.7
Knudsen number (Kn)	0.03	0.05
Altitude (h/D)	8 – 80	8 - 60
Normalized pressure gradient (ΔP^*)[‡]	>2500	>1800

[†]Data obtained from fine basaltic sand at Viking 2 Landing Site on Mars [*Shaw et al.*, 2009]
[‡]Properties significantly change from pre-jet impact conditions during DGEE
[ɣ]Data obtained for simulant-type S

Table 3.3. Normalized parameters at pre-jet impact conditions based on scaling relations

We briefly discuss our assumptions and add further detail in the usage of these scaling laws. For these jets which are in the turbulent regime (Table 3.3), the gas Reynolds number (Re_g) has a small effect on aerodynamic forces due to the Reynolds Number Similarity [*Townsend*, 1956]. The aerodynamic forces are dependent on the lift and drag coefficients, the dynamic pressure and the particles cross sectional area. These aerodynamic coefficients are relatively constant and independent of Re_g within the turbulent regime. The bulk particle Reynolds number (Re_p) for packed granular beds which is dependent on particle size and porosity (Eqn. B7, Appendix B.2), for both full-scale and subscale simulations indicate that the flow is near or within the turbulent regime (Table 3.3). According to the Burke-Plummer equation for $Re_p \geq 1000$ [*Bird*, 1996], the friction factor (C_d) is relatively constant and independent of Re_p for average particle sizes tested and adequately simulates the viscous forces. Independently, neither the Fr nor the density ratio (Eqn. B5, Appendix B.2) accurately describe sediment transport due to jet interactions, but the combination of the two parameters (Eqn. 3.4) show good correlation with erosion rates and crater profiles as proven by previous researchers [*Greeley and Iversen*, 1985; *Mazurek and Rajaratnam*, 2005; *Neakrase et al*., 2009]. The β parameter, a function of cohesion and angle of internal friction, is not important for low cohesive and low bulk weight soils as observed on Mars and in our experiments. The nondimensional threshold friction velocity (u_{*t}/u_*) is an important parameter because it determines whether the jet's viscous shear stress is capable of eroding soil grains when $u_{*t}/u_* < 1$. The numerator of Eqn. 3.6 determines the required friction velocity to lift spherical particles by taking the summation of the aerodynamic, interparticle and gravitational forces and moments on a grain [*Shao and Lu*, 2000]. The denominator of Eqn. 3.6 is the friction velocity of the exhaust plume along the granular media which is calculated from Eqn. B34 (Appendix B.5) at a normalized radius of ~4 from the plume centerline. Here, the velocity and density profiles were similar to the nozzle exit conditions and were obtained from computational fluid dynamic simulations of both full-scale and subscale jets. Since the particle size distribution is approximately equal between the simulant and martian soil [*Goetz et al*., 2009], we use the same aerodynamic roughness length, z_0, (Eqn. B34, Appendix B.5) when calculating the friction velocity (Eqn. 3.6) [*Greeley et al*., 2000]. Eqn. 3.7 is the ratio of time needed for

diffusion of the exhaust plume to reach steady state to a soil depth of l (diffusion time) with respect to the jet's pulse period, t_{imp}. The $\frac{D}{\bar{d}}$ scale is orders of magnitude larger than unity which proves that microscopic effects due to gas diffusion on individual grains can be neglected [*Mazurek and Rajaratnam*, 2005] and the dynamics are governed by bulk properties.

The scaling analysis of cratering described above demonstrates similarity in the absolute forces and force ratios on the granular system between the laboratory simulations and the full-scale process of spacecraft landings on Mars (Table 3.3). Hence, this satisfies our main goal of simulating the dynamics of the exhaust plume and soil particles during cratering. As a result and noted in Chapter 2, similar transient pressure distributions on the surface, similar shock structure profiles, shear strength soil properties and soil weight occur in the laboratory experiments and full-scale system on Mars. In Section 3.6, we show that the normalized crater and deposition profiles and normalized erosion rates are similar in both our experimental results and observations at the Phoenix landing site. This similarity in the dynamic forces is critical for the quantitative simulation of the erosion and cratering dynamics caused during the Phoenix landing [*Holsapple*, 1993; *Greeley et al*., 1980]. Certain scaling parameters can be neglected depending on which erosion process is dominant. For example, the normalized shear strength (Eqn. 3.5), pore pressure gradient (Eqn. 3.8) and diffusion time-scale (Eqn. 3.7) parameters can be neglected for VSE dominant processes.

There are some limitations to these tests due to the fact that they were conducted at Earth's gravity and used exhaust jets composed of N_2 at room temperature. Dynamic descent of thrusters during test firing was not pursued because of adding unknown complexity to the physics. However, static testing at various altitudes allowed us to integrate this function and obtain a representative mean value for erosion rates and crater dimensions. Due to the lighter weight of walnut shells, the soil simulant particles accelerate faster by a factor of ~2.2 than soil particles on Mars, but the initial trajectories of the ejecta are adequately simulated because the inertial forces are similar in both at the near-field crater regime (near and within the crater). Hence, complete similarity of the kinematics is difficult to achieve. Within this regime, the drag (D) and lift forces (Eqn.

3.9) are independent of the particle velocity, u_p, due to the valid assumption that the gas velocity, U_∞, is much larger than the particle velocity. This is also supported by experimental observations.

$$(3.9) \qquad D = \frac{1}{8} C_d \rho_a \left(U_\infty - u_p\right)^2 \pi \bar{d}^2 = \frac{1}{8} C_d \rho_a \pi \bar{d}^2 U_\infty{}^2 \left[1 - 2\frac{u_p}{U_\infty} + \left(\frac{u_p}{U_\infty}\right)^2\right] \sim \frac{1}{8} C_d \rho_a \pi \bar{d}^2 U_\infty{}^2;\ U_\infty >> u_p$$

This is partly due to high particle collision frequencies which inhibit large increases in the particle acceleration relative to the exhaust plume. At far-field regimes, this assumption may not be valid for certain cases and further studies are needed to assess the lift and drag forces on the ejecta. Particle Reynolds number presents a large disparity between experiment and full-scale processes for clay-size particles (~1 μm) due to differences in exhaust plume viscosity. More importantly, we have not quantified here how each scaling parameter affects the erosion rates. This has been started in a study described in Appendix C. Although these scaling laws described above prove to be theoretically valid, we conclude that this application needs to be confirmed by additional experimental and numerical simulations.

3.2.2 Determining average jet-induced erosion rates

The average erosion rates were calculated by measuring the radius and depth of the final crater developed in each experiment. The error associated with these in-situ measurements was less than 5%. The total crater volume (V_c) was calculated assuming that it is a paraboloid with a volume:

$$(3.10) \qquad V_c = \frac{1}{2} \pi\, r^2\, h$$

where r is the radius of the crater and h is its depth. Knowing the duration of the jet impingement, t_L, the bulk density of the martian simulant, and the crater volume, the average rate of mass ejected by the jets can be calculated. Some crater volumes (e.g., exposed surface) were geometrically calculated from a derivative of the paraboloid. This approach shows good agreement to the method of integrating infinitesimal parabolic contours. Physical dimensions and erosion rates are normalized by the pair of subscale thrusters' exit diameter (3.125 cm), and mass flow rate (0.22 kg/s), respectively, and therefore expressed as adimensional units (a.u.). The normalized crater dimensions such

as depth and exposed and crater radii are recorded in Table B1, Appendix B.3. We use a mass correction term to estimate the erosion rate expected at the Phoenix landing site from our experimental data. This term is the density ratio between simulant and basaltic sand (factor of 2) and this mass scaling approach was confirmed by Greeley et al. [1982] using wind tunnel simulations to estimate the sediment flux due to dust devils on Mars.

3.3 Observations

There were four general experimental cases performed in this study: (i) pulsed and (ii) steady jets at mars atmospheric pressure and (iii) pulsed and (iv) steady jets at Earth atmospheric pressure. The main goal of this study was to determine the effects of pulsed jets on granular media in tenuous atmospheres. These cases were selected to provide a range of data sets applicable to various spacecraft landing architectures on planetary bodies. These 24 experiments tabulated in Table 3.4 would also provide a diverse range of erosion mechanisms observed by impinging jets.

Test	Jet height (m)	Soil depth (cm)	Soil simulant	Jet mode	Pulse frequency (Hz)	Test duration* (s)	P_{amb} (kPa)	P_{imp} (kPa)	T_{amb} (K)	Dominant mechanism
1	0.26	20	B	pulsed	10	1.50	0.800	18	287	DGEE
2	0.26	5	B	pulsed	10	1.50	0.800	18	288	DGEE
3	0.26	5	B	pulsed	10	3.00	0.864	18	288	DGEE
4	0.26	20	S	pulsed	10	3.00	0.864	18	285	DGEE
5	0.41	20	S	pulsed	10	3.00	0.864	22	288	DGEE
6	0.41	20	S	pulsed	10	3.00	0.800	22	286	DGEE
7	0.74	20	S	pulsed	10	3.00	0.864	11	285	DGEE
8	1.88	20	S	pulsed	10	3.00	0.864	8	285	DGEE
9	0.26	20	S	pulsed	10	1.50	0.800	18	287	DGEE
10	1.88	20	S	pulsed	10	1.50	0.800	8	286	DGEE
11	0.26	5	S	pulsed	10	1.50	0.800	18	287	DGEE
12	0.41	20	S	pulsed	10	3.00	101.3	--	290	VSE
13	1.56	20	S	pulsed	10	3.00	101.3	--	290	VSE
14	0.26	20	S	pulsed	10	3.00	101.3	3	291	VSE
15	0.74	20	S	pulsed	10	3.00	101.3	--	290	VSE
16	0.26	20	S	steady	0	0.75	101.3	--	290	VSE
17	0.26	20	S	pulsed	10	1.50	101.3	--	285	VSE
18	0.26	20	S	steady	0	0.75	0.800	18	288	BCF/DDF
19	1.05	20	S	steady	0	0.75	0.800	--	284	BCF/DDF
20	1.56	20	S	steady	0	0.75	0.864	--	290	BCF/DDF
21	0.26	5	F	pulsed	10	1.50	0.800	18	287	DGEE
22	0.26	20	F	pulsed	10	1.50	0.800	18	288	DGEE
23	0.26	5	C	pulsed	10	1.50	0.864	18	285	VSE
24	0.26	20	C	pulsed	10	1.50	0.800	18	288	VSE

Table 3.4.Test matrix

Here, we will briefly discuss the various observations noted from the experiments conducted at the PAL facility. For all of the cases of pulsed jet impingement into simulant at martian atmospheric pressure, the soil was rapidly excavated to the hard surface and moved granular media outward in a radial fan reaching mean heights of ~3 m (~100 a.u.) and radial distances of ~10 m (~300 a.u.) as observed by real-time imaging. Highly dynamic granular structures within the soil bed were only observed with high-speed imaging. For example, bright radial granular fronts which originated below the thruster were seen propagating within the soil along the transparent baffle 2 plane, but not along baffle 1. Also, bubbling and semi-stratification of the soil below the thrusters were observed during the thrust shut-down phase. Upon complete excavation of the granular media before four thrust cycles (0.4 s), the ordered granular structures disappear and turbulent movement of soil is observed. These highly dynamic granular structures, the associated explosive energy and substantial rapid removal of soil were not seen for the impingement of pulsed and steady jets at earth atmosphere or steady jets at mars atmosphere.

For all cases at Earth atmosphere, the erosion was highly localized and resulted in the surficial removal of less than 5 cm of soil, leading to characteristic parabolic craters. The trajectories of the soil particles were mainly vertical with a maximum height of ~0.6 m which did not extend outward beyond 0.5 m from the jet centerline. For pulsed jets during thrust shutdown phase, the crater slope would exceed the angle of internal friction leading to re-deposition of the crater. For steady jets at Mars atmosphere, the soil was temporarily excavated to the hard surface within ~0.7 s, forming a steep cylindrical crater which quickly re-deposited during the thrust shut-down phase. The soil trajectory was mainly vertical but a modest amount of simulant did extend outward to a radial distance from jet centerline and height of ~2 m.

No signs of crater disturbances were noted due to the filling of the vacuum chamber to terrestrial atmospheres after each tests was completed. The suspension time of C-type, S-type, and F-type simulant within the martian atmosphere after test completion was less than 1 s, 300 s and 11000 s, respectively. Distinct characteristic observations were noted for the four general cases by both high-speed and real-time

imaging, and this led us to believe that different mechanisms and dynamics were involved as will be discussed in the following sections.

3.4. Diffusive gas explosive erosion

3.4.1 Results

To compare the various jet-induced erosion and crater growth processes observed in the experiments, we developed normalized erosion rate vs. normalized altitude profiles from the numerous test cases as shown in Figure 3.5. These comparisons are made with the thrust duration being equivalent for all cratering processes studied which is approximately similar to the spacecraft descent time within the last 5 m prior to landing (Table 3.4). The average crater growth rate caused by DGEE, depicted by blue and red data points in Figure 3.5 (Tests 1-11, 21,22), is approximately five times greater than that caused by BCF/DDF, the dominant cratering mechanisms caused by steady (non-pulsed) jets at Mars atmospheric conditions illustrated by the green curve (Tests 18-20). DGEE occurs for thruster altitudes ranging from 0.26 to 2 m above the surface for all soil simulants tested, except coarse sand/granules (Tests 23-24). Indeed, our laboratory experiments also show that DGEE at Mars atmospheric conditions removes 10 to 20 times more soil particles per unit thrust time than VSE either at Mars [*Shorthill et al*., 1976a, 1976b; *Romine et al*., 1973], or at Earth's atmospheric conditions, where VSE dominates illustrated by the yellow curve (Tests 12-15,17). DGE was not observed in our tests.

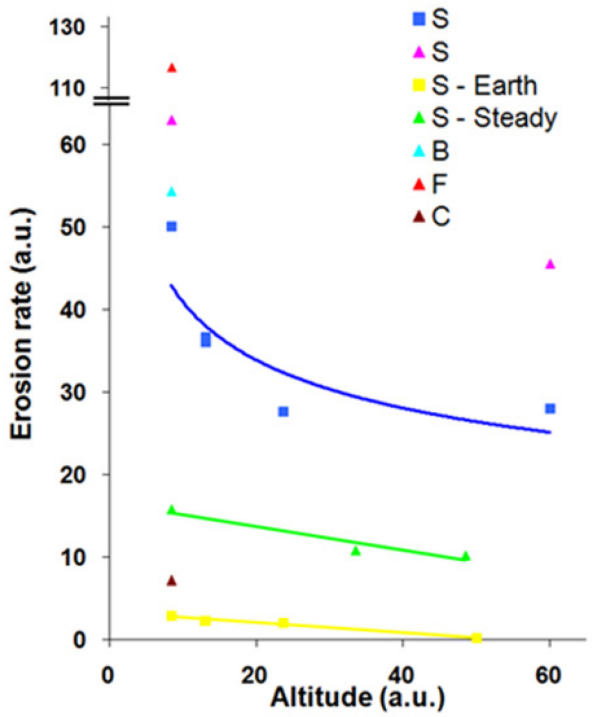

Figure 3.5. Normalized erosion rate vs. normalized altitude for laboratory simulations with various soil simulants at Mars and Earth atmosphere conditions. The erosion rate is normalized by the jet's mass flow rate and the altitude is normalized by the nozzle exit diameter. All data points are for pulsed impinging jets at Mars atmosphere at 20 cm soil depth unless specified. Square and triangle box symbols denote 3 s and 1.5 s test durations, respectively; 0.75 s test duration for steady jets; The blue curve fitting line for the fine sand (S) experiments (Tests 4-8) is a power law polynomial, and the green (Tests 18-20) and yellow fitting lines (Tests 12-15) are linear.

The final crater morphology, calculated from isometric images such as in Figure 3.6A, is shown in Figures 3.6B, 3.7 and 3.8 as contour plots to depict the extent of erosion and cratering that occurred in each test case. The colorbar denotes the normalized soil depth where negative and positive values correlate to depth of soil either eroded (shaded in blue) or deposited (shaded in red), respectively. A quarter section of the spacecraft is superimposed onto these contour plots. Also included in these contour plots is the 90° sweep of the Robotic Arm which is depicted in a darker shade. All length scales (x, y, z and l) in these figures are normalized by the nozzle exit diameter, D. All values reported within this article and figures are obtained from the experiments (exp), and the full-scale (fs) length quantities are calculated by Eqn. 3.11 and denoted in parenthesis or otherwise stated.

(3.11)

$$[x]_{fs} = \frac{D_{fs}}{D_{\exp}}[x]_{\exp}$$

$$[x] = \text{length scale quantity}$$

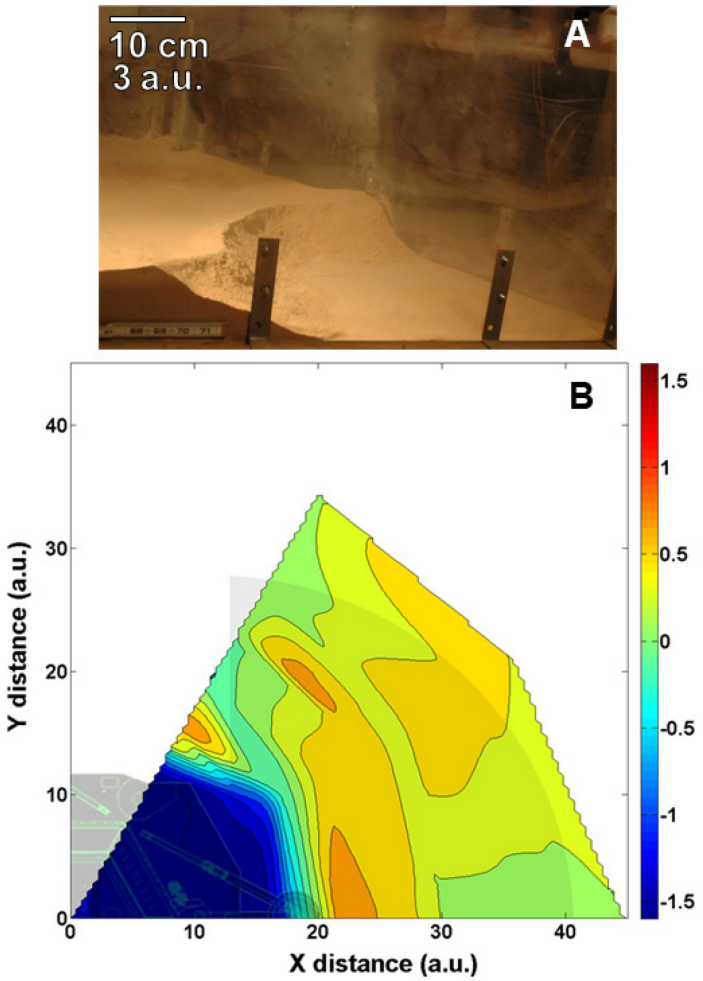

Figure 3.6. Diffusive gas explosive erosion. (A) Image of the crater caused by Test 2 (Table 3.4); (B) Normalized erosion/deposition contour plot for crater shown in the above figure; similar contours observed for Test 1. Color bar indicates the normalized depth of soil in which zero a.u. is the reference value prior to jet impingement. Scaled 90° section of the lander and RA coverage area is indicated in dark shading within the figure.

These contour plots indicate that layers of mixtures of fine silt and sand of 5 cm of thickness are completely removed in less than 1 s at the scaled Phoenix touchdown altitude of 0.26 m (0.5 m at full-scale), leaving a completely exposed impermeable subsurface with radius of ~42 cm (85 cm at full-scale) as illustrated in Figure 3.6B (Test 2). In contrast to BCF, DDF and VSE processes, this rapid and broad excavation to the surface occurred in experiments at Mars atmosphere with fine sand (Test 9, Fig. 3.7A),

silt (Test 22, Fig. 3.8) and their mixtures (Test 1) with depths ranging from 5 to 20 cm. In many cases, the final crater radius exceeded 85 cm in tests with the largest soil depths.

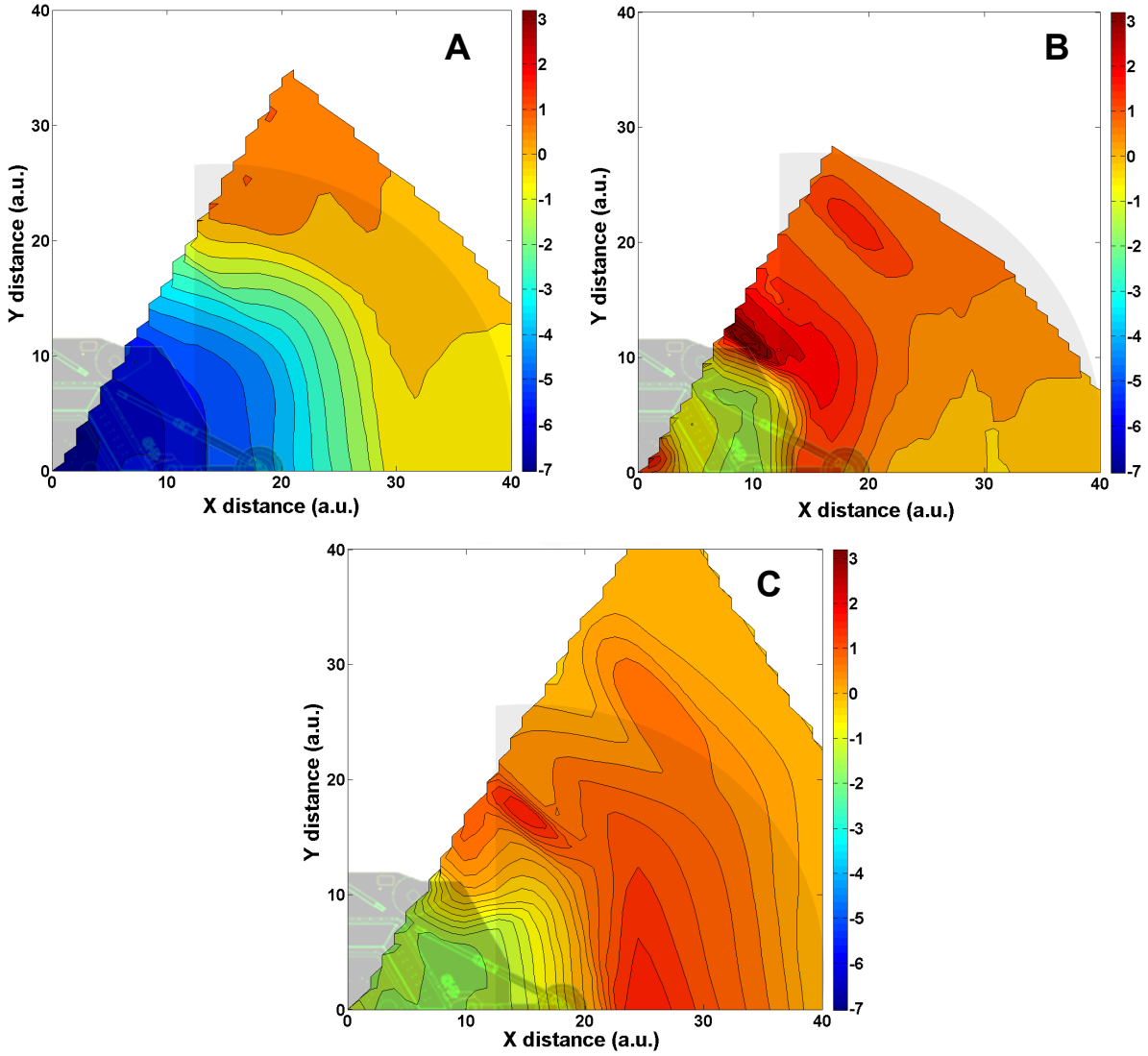

Figure 3.7. Normalized erosion/deposition contour plots of laboratory simulations with a 20 cm thick layer of simulant for (A) Test 9, (B) Test 17 and (C) Test 18 (Table 3.4).

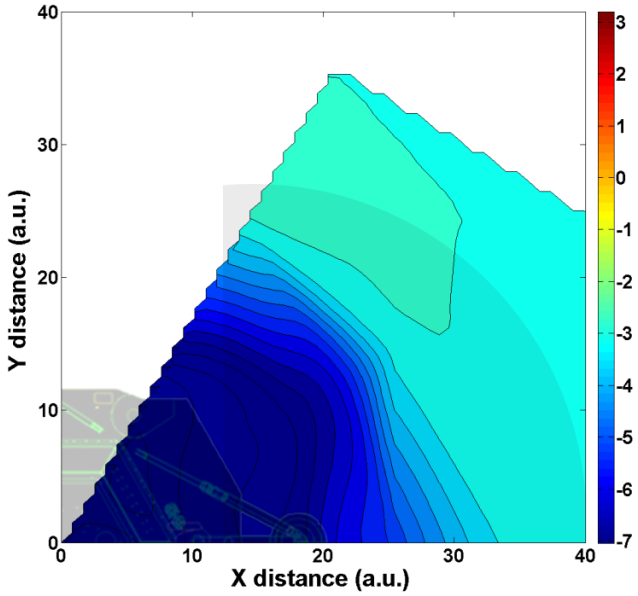

Figure 3.8. Normalized erosion/deposition contour plot of laboratory simulation for Test 22 (Table 3.4).

3.4.2 Predictions at the Phoenix Landing Site

Through these analyses, we predicted prior to Phoenix touching down on the martian arctic that the subsurface ice could be extensively exposed by this erosion process due to pulsed rocket plume-soil interactions. As a result, from heat transfer analysis, the subsequent hot jet impingement on the subsurface water ice at the Phoenix landing site would melt ~1 mm of its top layer, and could splash mud with salt under the lander [*Renno et al.*, 2009]. This process led to the first direct observation of deliquescence on Mars [*Renno et al.*, 2009]. Deliquescence is the absorption of atmospheric water vapor by hygroscopic materials (salts) to form a liquid brine solution. From the calculations shown in Appendix B.1 and the understanding of the rocket combustion process, a total of ~0.37 kg of ammonia may have interacted with the subsurface ice during landing.

The ability of DGEE to remove large quantities of soil in a very short time interval could result in the widespread exposure of subsurface ice at the Phoenix landing site as shown by two bright elliptical surface features in the center of Fig. 3.9. Furthermore, our results indicate that the 'explosive erosion' caused by the Phoenix thrusters could remove soil layers with depths in excess of 15 cm, producing a large blast

zone by ejecting soil particles meters from the jet impingement point. It also indicates that soil particles removed from below the lander could cover the entire Phoenix work area and beyond with a cm-thick or less layer of loose soil particles as shown in Figure 3.6B (Test 2 in Table 3.4). Our laboratory simulations indicate that if VSE (Fig. 3.7B is an example of Test 17) or BCF/DDF (Fig. 3.7C is an example of Test 18) were the dominant erosion mechanisms during Phoenix's short landing phase, the cratering would be minimal and the subsurface ice would not have been exposed. These claims are further supported by the dynamics of 'explosive erosion' and other cratering mechanisms which are presented below.

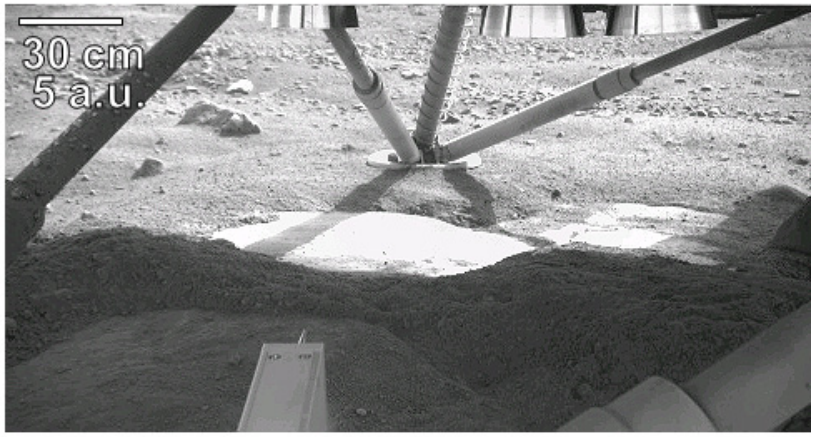

Figure 3.9. RAC Sol 5 image (RS005EFF896663219_11730MDM1) of the extensively exposed ice under the lander near the southern footpad ("Holy Cow"). *Courtesy of NASA/JPL-Caltech/U. of Arizona/Max Planck Inst.*

3.4.3 Dynamics

Characteristic shock wave structures are readily observed in granular media such as in soil and snow. Granular shock waves occur in nature during avalanches and landslides [*Pudsaini and Kroner*, 2008]. They occur when high-speed granular flow impinges on obstacles and present similar structure to shock waves in air [*Amarouchene et al.*, 2001]. These granular structures also play an important role in DGEE.

The erosion rate of DGEE is much larger than that caused by other erosion mechanisms because it locally fluidizes the soil and produces cyclic granular shock waves as depicted in Movie D4 (Appendix D) and Fig. 3.10 (Test 9). These two processes are intimately linked because soil fluidization below the jet plays an important role in the formation and propagation of shock waves. Both of these processes are caused

by the short pulse period of the jet relative to the time-scale for gas diffusion through the soil ($\tau / t_{imp} > 1$). The 'explosive erosion' process is forced by the large pressure variations caused by the partial reflection and collapse of normal shock waves produced by the interaction of pulsed supersonic jets with the surface. Pressure variations at the surface ranging from ~0.8 to 40 kPa forces exhaust gases to penetrate into the porous soil and rapidly diffuse outward because of the low atmospheric pressure, $\Delta P^* \geq 1$. The collapse of normal shock waves and the significant decrease in the impingement pressure near the end of each engine thrust cycle results in pressure gradients within the soil that causes soil fluidization shown in Figures 3.10A3 and 3.10A5 as dark mottled bands within the granular media below the jet.

From Movie D4, we observe the separation of many granular particles from each other along the $+z$ and $\pm x$ directions which can lead to the loss of shear strength. This fluidization results in large increases in soil porosity and reduces the speed of sound in it from ~280 to ~0.3 m/s (Fig. 3.13, see Section 3.4.4) [*Huang et al*., 2006; *Amarouchene and Kellay*, 2006; *Liu and Nagel*, 1992]. From classical continuum-kinetic theory, the speed of sound of granular mediums is dependent on granular temperature and soil volume fraction (porosity). The granular temperature for these systems is much smaller than for gas mediums due to inelastic collisions. The methodology of calculating the sound speed and granular temperature for our application is given in Section 3.4.4.

Cyclic variations in soil porosity create large soil density gradients that produce large variations in the speed of sound [*Huang et al.*, 2006; *Amarouchene and Kellay*, 2006]. This creates supersonic and subsonic granular flow regimes when the gas from a subsequent thrust cycle penetrates into the fluidized soil. Granular shock waves, produced during the power rise of each thrust cycle, develop from large pressure gradients between the impingement zone (epicenter) in the fluidized soil interior and its' surroundings at ~800 Pa. These shock waves, shown as bright radial granular structures in Figures 3.10A2, 3.10A4 and 3.10A6, form and propagate in regions of significantly reduced granular sound speed. Such regions have a low particle density (fluidized) and are shown by Figures 3.10A3 and 3.10A5 to be relatively darker than the undisturbed areas and semi-stratified.

During the ‘steady power phase’ of the thrust cycle , the pressure of the impinging jet reach high uniform values, compresses the soil, and reduces the pressure gradient between the soil pores in the impingement area and surrounding regions. This increases the speed of sound in the soil and inhibits the formation of shocks fronts [*Huang et al*., 2006; *Amarouchene and Kellay*, 2006]. As a result, granular shock waves are produced in a cyclic pattern, as indicated by the propagation of high particle density fronts shown in Figure 3.10. High speed images show that radial shock waves propagate with an average speed of Mach 12 in relatively high permeability soils. These shock fronts eject a large mass of particles of fine sand and silt ballistically and supersonically with respect to the granular sound speed to ~3 m above the surface and at distances greater than ~4 m (fine sand) and 15 m (silt) from the wave front. As a result of ejecta with high-kinetic energy, soil deposition occurs over a large area and large accumulations do not occur close to the crater. A schematic in Figure 3.10 further elucidates the ‘explosive erosion’ dynamics described above.

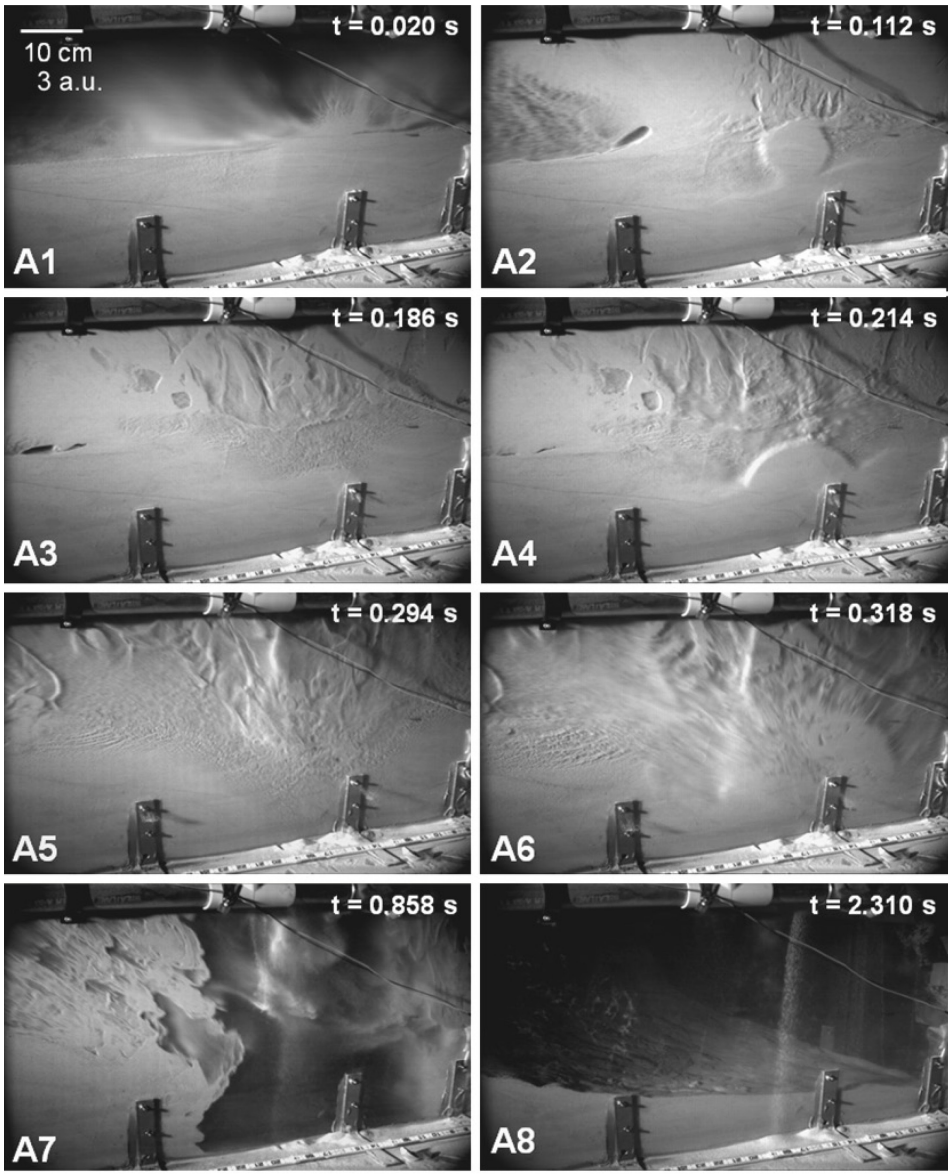
10 cm
3 a.u.
t = 0.020 s
A1
t = 0.112 s
A2
t = 0.186 s
A3
t = 0.214 s
A4
t = 0.294 s
A5
t = 0.318 s
A6
t = 0.858 s
A7
t = 2.310 s
A8

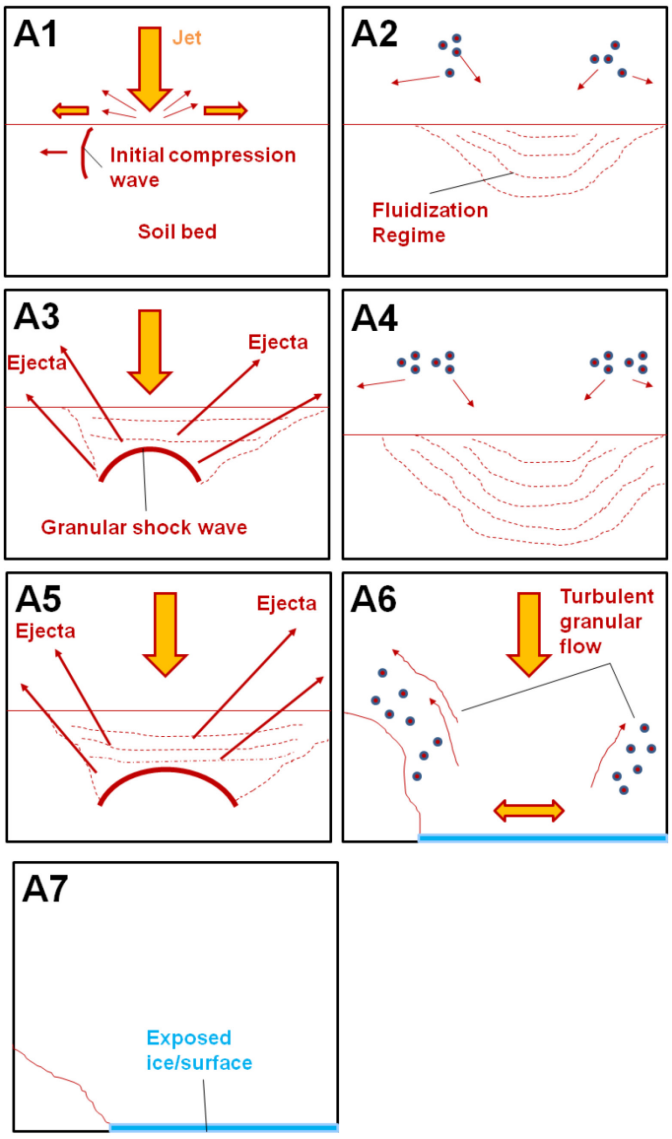

Figure 3.10. (Top) High speed images of the 'explosive erosion' dynamics observed in Test 9 (Table 3.4). The duration of this test spans a time constant, t/t_{imp}, of 0.2 to 23.1. Images along the *x-z* plane (baffle 2) were taken at 500 frames per second using the quarter space technique. At A2, A4 and A6, three granular shock waves (shown as bright curved granular structures) are observed propagating outward from the impact centerline (epicenter). At A3 and A5, localized soil fluidization (shown as dark semi-stratified regions below the jet) is observed during the thrust shut-down phase. At A7, the exposed surface can be seen, and at A8, minor crater re-deposition occurs. Similar dynamics observed in fine silt/sand simulants (Test 1). This spans a t/t_{imp} between 0.2 to 23.1 See Movie D4. (Bottom) Schematic of the 'explosive erosion' dynamics. Speed of sound in granular media decreases by three orders of magnitude in the fluidization regime.

High velocity ejecta blankets are produced during the impingement of each jet pulse, until the soil below the thrusters is completely removed. Since the volume of fluidized soil increases with each engine thrust cycle, the radius of the shock waves also

expands, leading to increases in the outward flux of ejecta with time. The soil is being ejected and partially re-deposited into the transient crater from surrounding regions during the first four thrust cycles. During the fifth thrust cycle, much of the soil has been excavated and redeposition is minimal, enabling the fluidization depth to extend to the impermeable subsurface. Turbulent entrainment of the granular flow removes the remaining soil. Once the surface is exposed and the nearly final crater has formed, the more benign VSE mechanism begins to dominate the erosion process and removes surface particles along the periphery of the crater and ground topography, producing erosion striations. These dynamics are noted for soil depths between 5 cm and 20 cm, and the number of granular shock waves observed is dependent on the soil depth.

Similar dynamics were observed in experiments with the three soil simulants used in our laboratory experiments: fine sand (Tests 4-11), fine silt (Tests 21, 22) and fine sand/silt mixture (Tests 1-3). In the experiments with the course sand model (Tests 23, 24), the dominant erosion mechanism observed was VSE with the formation of a large transient crater and turbulent granular flow. However, in experiments with silt, soil fluidization is more expansive and plays a more important role in the erosion process than in other experiments. Also, the initial radial shock front leads to the ejection of large clumps of silt and turbulent particle entrainment, and as a result subsequent granular shock waves are either less visible or possess smaller amplitudes. Localized soil fluidization and granular shock waves do not occur in the VSE and BCF/DDF processes as depicted by Figures 3.11 and 3.12, respectively, and therefore they produce much smaller and shallower craters. Although diffuse gas erosion (DGE) was not observed for any of the test cases, DGE dynamics are presented as a schematic in Figure X.X for completeness.

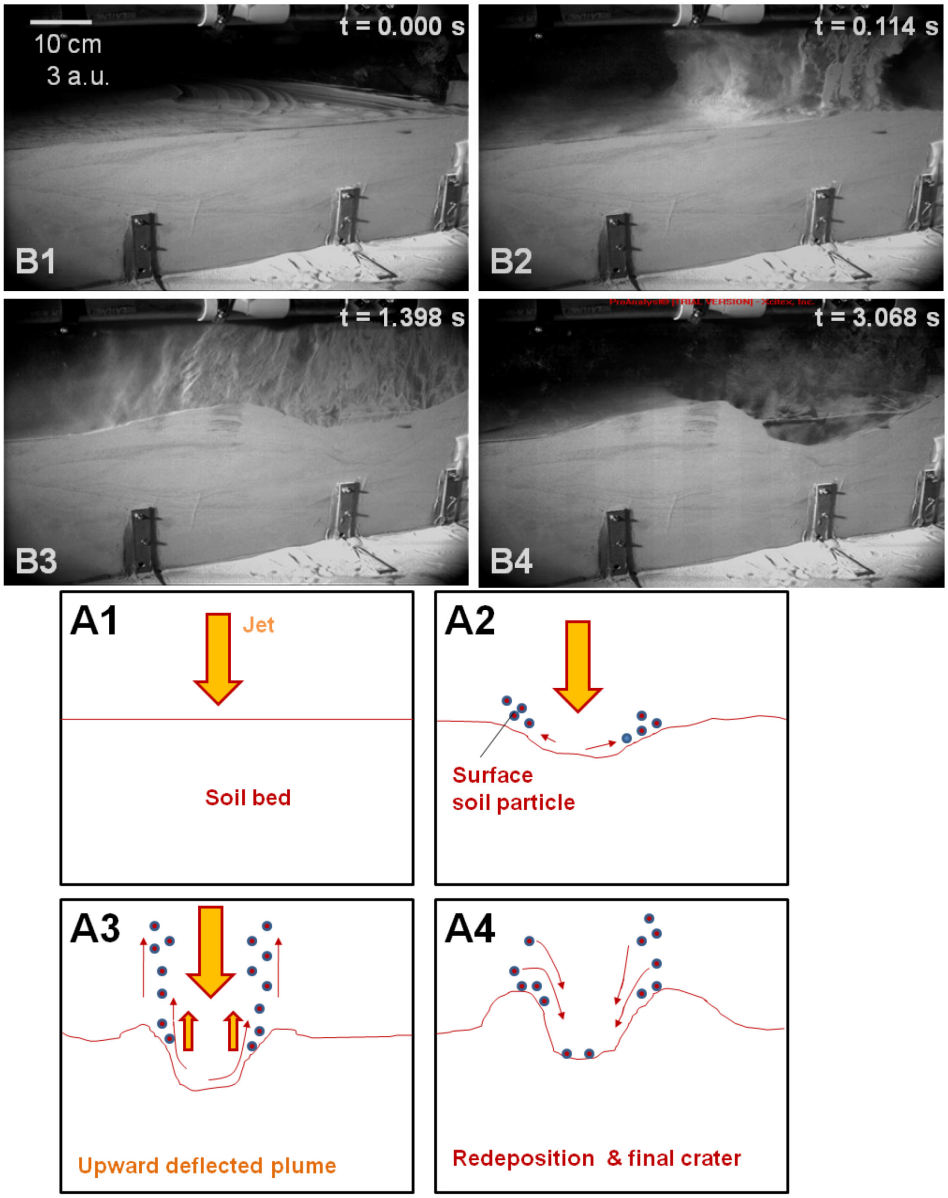

Figure 3.11. (Top) High speed images of the viscous shear erosion dynamics observed in Test 17 (Table 3.4). See Movie D5. (Bottom) Schematic of the VSE dynamics.

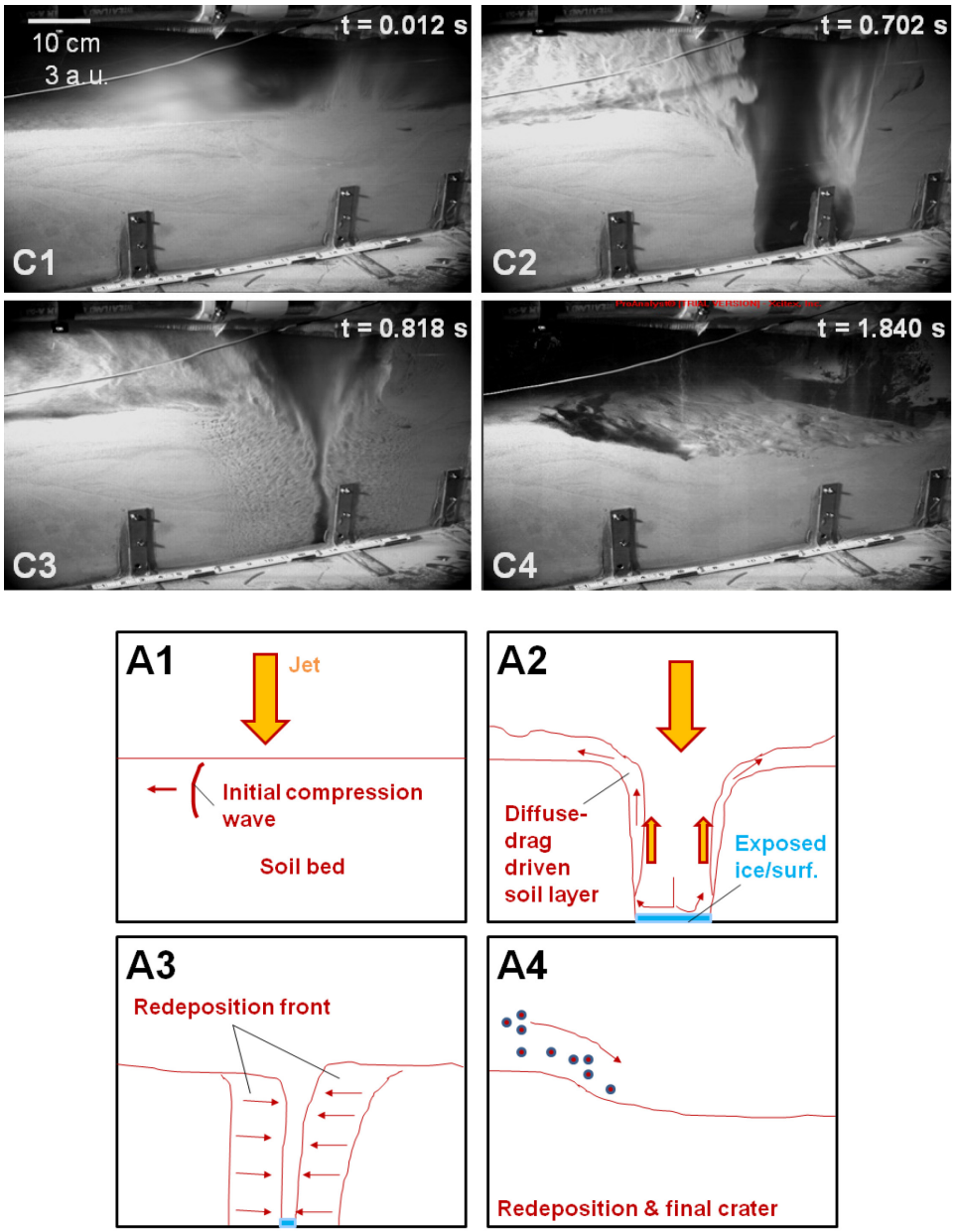

Figure 3.12. (Top) High speed images of bearing capacity failure/diffusion-driven flow dynamics observed in Test 18 (Table 3.4). See Movie D6. (Bottom) Schematic of the BCF/DDF dynamics.

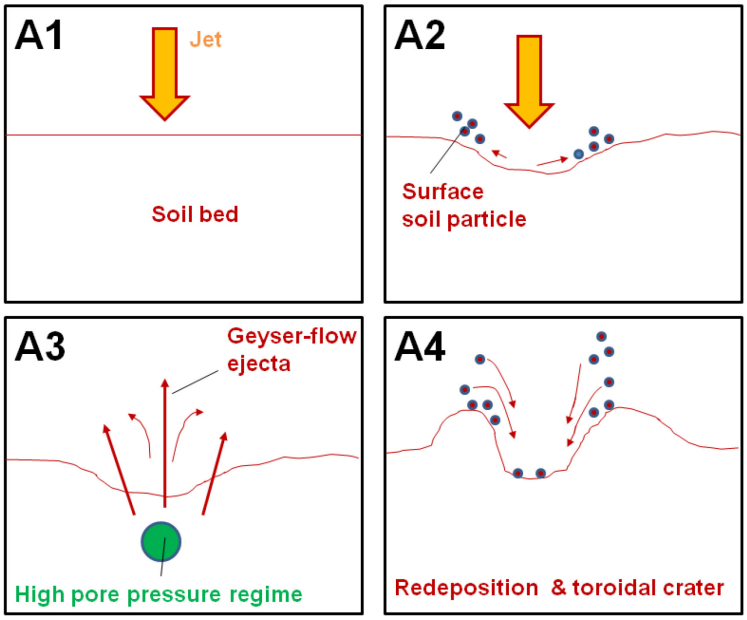

Figure 3.13. Schematic of DGE dynamics.

3.4.4 Calculations of granular temperature and speed of sound from high speed imaging

To determine whether our flow of interest is within the subsonic, transonic or supersonic regime, we calculated the temperature and sound speed of the granular system from high-speed imaging. Granular temperature is defined as the collisional velocity fluctuations of granular particles within the system and they continually dissipate energy due to its inelasticity. However, granular flows may be excited or perturbed to increase or maintain this temperature. The temperature of the fluidized granular regions prior to granular shock formation is calculated from Eqn. 3.12 [*Huang et al.*, 2006]. These calculations were done for Tests 4 and 9. The granular temperature, T_g, is defined as the following:

$$T_g = \sum_{n=1}^{N} \frac{1}{2} \left| \vec{v}_n(i,j) - \vec{v}_b(i,j) \right|^2 / N \qquad (3.12)$$

The v_n and v_b are the velocity vectors of the n particle and background velocity, respectively. N is the number of particles. These parameters were calculated using the high-speed imaging of 2-D high resolution images and a simple particle tracking software. Each image was analyzed every 2 ms. Each pixel which is ~400 μm in size in the x-z plane (Fig. 3.4) was tracked in both space and time. This was recorded for

multiple particles along the fluidized domain during the thrust shut-down phase. Background velocity is defined as the following [*Huang et al*., 2006]:

$$\vec{\mathrm{v}}_{\mathrm{b}}(i,j) = \sum_{n=1}^{N} \vec{\mathrm{v}}_{\mathrm{n}}(i,j)/N \qquad (3.13)$$

The granular temperature increased during each thrust cycle, and the average value during four thrust cycles is ~0.016 m^2/s^2. This trend is consistent with previous studies of high-speed granular flow such as those reported by Amarouchene and Kellay [2006] and Huang et al. [2006]. The speed of sound (c_s) in the granular medium is calculated from continuum-kinetic theory (Eqns. 3.14 – 3.16) [*Bougie et al.*, 2002], and this approach shows good qualitative agreement with experimental results [*Amarouchene and Kellay*, 2006].

Here, we briefly discuss the derivation of the granular sound speed which is important in understanding the flow regime of interest. The conservation equations of mass, momentum and energy for granular flows have the following forms [*Savage et al.*, 1988]:

$$\frac{\partial \rho}{\partial t} = -\rho \nabla \cdot \vec{u} \qquad (3.14)$$

$$\rho = \rho_{\mathrm{p}} \nu \qquad (3.14a)$$

$$\rho \frac{\partial \vec{u}}{\partial t} = \rho \vec{g} - \nabla \cdot \vec{p} \qquad (3.15)$$

$$\rho \frac{3}{2} \frac{\partial T}{\partial t} = -\vec{p} : \nabla \vec{u} - \nabla \cdot \vec{q} - \gamma_{\mathrm{c}} \qquad (3.16)$$

where $\vec{u}$ is the bulk velocity of the granular particles, ρ_{p} is the particle density, ν is the solid volume fraction, $\vec{p}$ is the pressure tensor which has a kinetic and collisional component, $\vec{q}$ is the flux of fluctuation energy which is also composed of a kinetic and collisional component, $\vec{g}$ is the gravitational acceleration, γ_{c} is the collisional rate of dissipation per unit volume and t is time. For moderate concentrations of particles where binary collisions are dominant, it is a valid assumption to neglected the kinetic components of the equations. However at higher concentrations where collisions significantly increase, the assumptions of binary collision do not hold and rate-independent and collisional rate-dependent stresses occur.

The total stress tensor is then assumed to be the sum of collisional momentum flux and rate-independent stresses as shown by

$$\vec{p} \approx \vec{p}_c + \vec{p}_s = \left[p_{so} + f(\kappa)\right]\vec{I} - g(\kappa) \qquad (3.17)$$

where κ is analogous to viscosity and defined by Savage et al. [1988].

To obtain an approximate estimate of the "sound speed" of granular media, we neglect the dissipation and flux of fluctuation energy terms and Eqn. 3.16 simplifies to

$$\rho \frac{3}{2} \frac{\partial T}{\partial t} = -\vec{p}_c : \nabla \vec{u} \qquad (3.18)$$

Neglecting analogous terms for viscosity from Eqn. 3.17, the collisional stress tensor is

$$\vec{p}_c = p_0 \vec{I}. \qquad (3.19)$$

The normal stress is defined by

$$p_0 = 2(1+\varepsilon)\,\nu\, g(\nu)\rho\, T = \chi(\nu)\rho\, T \qquad (3.20)$$

Where ε is defined as the particle's coefficient of restitution and this determines the efficiency of energy dissipation. For values near one, the energy of the system is relatively conserved. The term *g(ν)* is the radial distribution function at contact and is defined as follows:

$$g(\nu) = \left[1 - \left(\frac{\nu}{\nu_m}\right)^{\frac{4\nu_m}{3}}\right]^{-1} \qquad (3.21)$$

Then, substitute Eqn. 3.19 into Eqn. 3.18 to obtain

$$\vec{p}_c : \nabla\vec{u} = p_0 \nabla \cdot \vec{u} \qquad (3.22)$$

Using the conservation of mass equation (Eqn. 3.14) and Eqn. 3.22, we substitute these relations into the modified conservation of energy equation (Eqn. 3.18). By differentiating the granular pressure with respect to the bulk density of soil, we obtain the granular sound speed [*Savage et al.,* 1988] as shown

$$c_s = \sqrt{\frac{\partial p}{\partial \rho}} = \sqrt{T_g \chi \left[1 + \frac{2}{3}\chi + \left(\frac{\nu}{\chi} \right) \frac{\partial \chi}{\partial \nu} \right]} \qquad (3.23)$$

$$\chi = 2(1+\varepsilon)\nu\, g(\nu) \qquad (3.24)$$

As can be seen in Figure 3.14, the sound speed is a non-linear function of porosity, volume fraction. From this derivation, it can be seen that the speed of sound within the granular media is not directly dependent of the plume temperature. Fundamentally, the granular sound speed is a function of the granular temperature (particle velocities) which is dependent on the applied and simulated particle forces. The plume temperature indirectly contributes to these particle forces. Hence, Eqn. 3.23 applies to both hot and cold gas flows.

Analytical calculations based on continuum-kinetic theory indicate that the sound speed within the fluidized bed is approximately 0.3 m/s at a soil volume fraction of 0.2 for our experiments dominated by DGEE (Fig. 3.13). This is well below the speed of sound in gas and can support supersonic flow. This is predominantly due to soil particle inelastic collisions which significantly reduces the granular temperature. These calculations were used to determine the Mach number and granular flow regime. Experiments supported by Particle Image Velocimetry (PIV) are needed to directly measure the particle velocities, obtain the granular temperature and test our calculations and data interpretation.

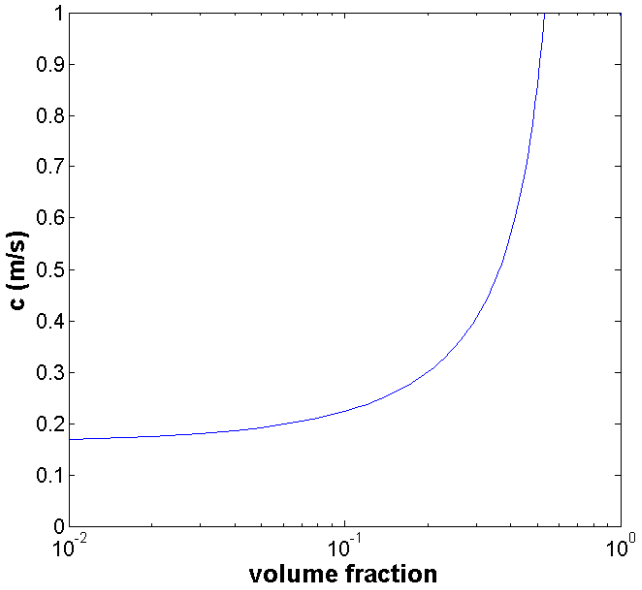

Figure 3.14. Speed of sound in the granular media (c) vs. soil volume fraction for laboratory simulations with fine sand simulant composed of crushed walnut shells.

3.4.5 Quantitative analysis

Next, we quantify the sudden increase in soil density across the shock fronts and the DGEE granular flow physics presented above, using the light reflectance photometry technique [*Lee et al*., 2007; *Caesar Ton-That et al*., 2008; *Hapke,* 2008]. The soil volume fraction is calculated from reflectance intensity data provided by the high speed images (Appendix B.4). A calibration curve is developed, where relatively black and white pixels with a pixel length of ~400 μm represents 0 and ~1 soil volume fractions (relative density), respectively [*Caesar Ton-That et al*., 2008]. A calibration curve is specific to different granular media or particle sizes. For Fig. 3.14 (Test 9), the soil volume fraction data is obtained along the +x-axis on the x-z plane (baffle 2) from the granular shock wave epicenter (x = 28.2 cm) to a radial distance of 15.6 cm (x = 45.6 cm). Similar analyses were conducted for the fluidization regimes within an area band of $z = \pm 0.1$ cm. The x-coordinate is fixed at the epicenter for each time interval, but the z-coordinate decreases during the erosion process from z = 17.2 cm at t = 0.112 s to z = 13.2 cm at t = 0.214 s. These profiles of soil volume fraction vs. normalized x-distance are calculated at various stages of DGEE along the +x axis.

Analysis (Appendix B.4) of sequence of images of the DGEE process in fine sand simulant indicates that the soil volume fraction jumps from ~0.2 to ~0.8 at the beginning of each thrust cycle as shown by the orange and black profiles in Figure 3.15, suggesting the formation of a strong shock wave. The images also show that when the soil becomes fluidized near the end of each thrust cycle, the soil volume fraction at the origin decreases from ~0.5 to below 0.2 (granular gas), as illustrated by the red, blue and green curves, substantially reducing the speed of sound in it. It is difficult to quantify subsequent shock waves because of the increased fluctuations in the soil volume fraction (reflectance intensity). With each pulse cycle, the shock strength increases and fluidization further decreases the soil volume fraction and expands its domain. Large increases/decreases in the soil volume fraction (density) are not observed in experiments dominated by either BCF/DDF or VSE as illustrated in Figures 3.11 and 3.12.

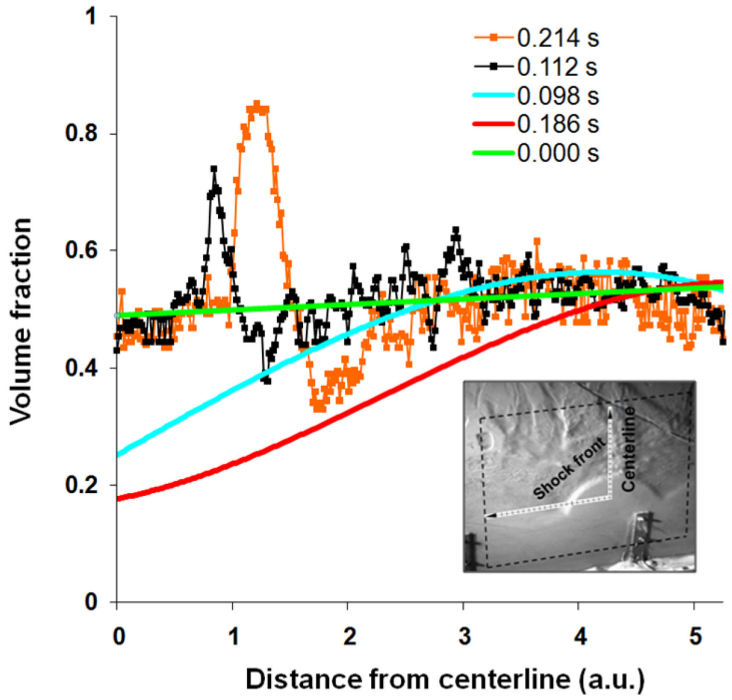

Figure 3.15. Soil volume fraction as a function of normalized *x*-distance from the epicenter of a granular shock wave, at the times indicated in Fig. 3.10, during the 'explosive erosion' process (Test 9). These profiles are calculated from reflectance intensity data. Third order polynomial fitting was used for experimental data at times t = 0.098 s (t/t_{imp} = 0.98) and 0.186 s (t/t_{imp} = 1.86) and linear fitting was used at t = 0.00 s.

Our analysis suggests that the uncertainty in the volume fraction value for fine sand simulant [*Lee et al*., 2008; *Caesar Ton-That*, 2009] is approximately ±0.05. In order to account for small asymmetries in the light illumination angle (leading to small localized bright and dark zones away from the area of interest), we determined the average soil volume fraction profile prior to jet impingement along an area band of z = ± 5 cm as seen by the green curve in Fig. 3.14. This analysis suggests a mean volume fraction of ~0.5, which agrees with density measurements for fine sand (Test 9). Light oversaturation of the complementary metal-oxide-semiconductor (CMOS) sensors may record higher reflectance values for the brightest pixels within the image, known as the blooming effect, and result in larger uncertainty values

The qualitative assessment of granular shock waves shown in Figure 3.10 indicates that it also has similar characteristics to shock waves observed in supersonic gas media (Fig. B5, Appendix B.7). Dark and bright bands of the shock structure within gas and granular media are observed in all images. Although reflectance intensity profiles and qualitative observations support localized soil fluidization which led to the formation

of these shock waves, we numerically and analytically investigate this dominant mechanism caused by DGEE.

3.4.6 Gas diffusion induced fluidization within granular media due to DGEE

Through analytical calculations, and numerical and laboratory simulations, we show that DGEE can cause gas diffusion to extend to large depths in short time intervals and lead to localized soil fluidization. The characteristic diffusion time-scale, τ, and characteristic one-dimensional diffusion velocity (= l/τ) to depth l can be calculated from Eqn. 3.7. As described in Sections 3.4.2 and 3.4.3, DGEE is not a static process. Indeed, it causes many jet and soil parameters to change by orders of magnitude in short time scales. For example in Figure 3.15, the soil volume fraction decreases by a factor of ~3 within 0.2 s during this process, significantly increasing the average soil porosity (n). According to the Kozeny-Carman equation (Eqn. 3.25) and the assumption of Darcian flow within the granular micro-pore space [*Costa*, 2006], an increase in n increases the soil permeability by orders of magnitude. This equation is derived by applying the Navier-Stokes equations within an assembly of capillary tubes representing the pore spaces of the granular media. Eqn. 3.25 and the parameter C, a function of particle diameter, tortuosity of the pores and shape factor, assumes homogeneous semi-spherical fine sand particles with the same $\bar{d}$ used in Test 9. This particle size is also similar to the effective particle diameter calculated from Carrier [2003].

$$k = C\frac{n^3}{(1-n)^2};\ C = \frac{\bar{d}^2}{180} \qquad (3.25)$$

Due to DGEE, the characteristic diffusion time-scale decreases by a factor of greater than 50 from the maximum values recorded in Table 3.3 which results in a 1-D diffusion velocity of ~1 m/s. Along with large changes in the soil properties responsible for gas diffusion, the ground pressure values significantly change due to the interaction of pulsed jets with the surface. Ground pressure values can transiently increase by a factor of 3 to 5 times the value at steady-state due to partial plate shock formation and collapse at the surface. This could further increase the characteristic diffusion velocity to ~2 m/s.

From Figure 3.10, granular shock wave epicenters originate from z = 17 cm at t = 0.112 s down to z = 7 cm at t = 0.318 s. The shock wave epicenters occur at an average

soil depth of ~4 cm per thrust cycle. Gas diffusion and large pressure gradients need to develop to these soil depths in order for granular shock wave propagation to initiate at these locations. Hence, the experimental results for Tests 4 and 9 show an average lower bound value of the characteristic gas diffusion velocity to be 0.4 m/s.

Along with the results from the analytical calculations and experimental observations presented above, an axisymmetric time-varying numerical simulation which is more quantitatively accurate shows that gas diffusion by the exhaust plume during the thrust rise phase has the potential to reach large depths within the granular bed in short time scales and initiate soil fluidization due to DGEE. The localized fluidization process that occurs during DGEE is dependent on ΔP^* and large variations in soil properties. The numerical simulation is conducted with an axisymmetric explicit finite-difference code [*Scott and Ko*, 1968] based on a second-order non-linear differential equation (Eqn. 3.26*a*) with a time-dependent impingement pressure profile. This is developed using MATLAB. The numerical code is derived from the Navier-Stokes equations using homogenization mathematical techniques. We make the assumption that isothermal transient flow within the porous medium obeys Darcy's Law (Eqn. 3.26*a*) [*Scott and Ko*, 1968]. This transient numerical model simulates normalized pore pressure contours in a granular bed due to jet interactions with soil depth (z) of 15D and radial domain of 15D with a time step of $1\text{x}10^{-7}$ s. The pore pressure (p) values are normalized with respect to the steady-state jet impingement pressure (P_{imp}). The outer walls of the simulations at z = 0 and x = 15D are modeled as impermeable surfaces where $x = r$ is the radial component. The axis at r = 0 is defined as the axisymmetric line. For simplicity, we model the pulsed jet from a pair of thruster nozzles as a sine pressure wave (Eqn. 3.26*b*) with a pulse width, T_{PW}, for a single thrust cycle that interacts with a static granular bed with constant permeability and porosity. Hence, the removal of sand grains is not simulated. Prior to jet impact and during the thrust shut-down phase, the model assumes a constant pore surface pressure in equilibrium with the martian atmosphere (Eqn. 3.26*b*). Exhaust plume and soil properties used within the simulation shown in Figure 3.16 are generally representative of the experiment conditions.

$$\frac{\partial^2 p^2}{\partial z^2}+\frac{1}{r}\frac{\partial}{\partial r}\left(r\frac{\partial p^2}{\partial r}\right)=\frac{2n\mu}{k}\frac{\partial p}{\partial t} \qquad (3.26a)$$

$$\frac{p(t)}{P_{imp}}=1.0\sin\left(\frac{\pi t}{T_{PW}}\right)+\frac{P_{amb}}{P_{imp}};\ \ 0\le t \le T_{PW} \qquad (3.26b)$$

$$\frac{p(t)}{P_{imp}}=\frac{P_{amb}}{P_{imp}}=\text{constant};\qquad t > T_{PW}$$

The dimensionless form of Eqn. 3.26*a* can be written in explicit finite difference form as:

$$\frac{P_{0,T+\Delta T}-P_{0,T}}{\Delta T}=\frac{1}{(\Delta Z)^2}\left[P_{2,T}{}^2+P_{4,T}{}^2-2P_{0,T}{}^2\right]+ \frac{1}{(\Delta R)^2}\left[\left(1+\frac{\Delta R}{2R_0}\right)P_{1,T}{}^2+\left(1-\frac{\Delta R}{2R_0}\right)P_{3,T}{}^2-2P_{0,T}{}^2\right] \qquad (3.27)$$

Where $P = p/P_{imp}$, $R = r/r_0$, $Z = z/r_0$, $T = (kP_{imp}/2\mu n r_0^2)t$, numerical value subscripts (i.e. 0,1,2, etc.) are vertex points on the mesh developed with 0 at the origin and r_0 is the radius of the dual nozzles.

DGEE is a highly dynamic process and as a result, soil permeability and porosity significantly change during a single thrust cycle, but even more so from one cycle to another. Figure 3.16 shows the pressure contours within the fine sand simulant (S) at times t = 0.015 s, t = 0.030 s and t = 0.085 s for soil porosities of n = 0.50 and n = 0.78. This soil porosity implemented in the code simulates the average bounds observed during the DGEE process in the experiments (Test 4-11) noted in Figure 3.15. We observe that the pressure contours can extend to a soil depth of ~11 cm with an average soil pore pressure greater than 3.0 kPa at t = 0.015 s (thrust rise phase) for a soil porosity of n = 0.78. Maximum gas diffusion depth of ~17 cm is reached at 0.0325 s when maximum thrust is reached. Hence, this leads to the formation of granular shock waves at martian atmospheric pressures. The pressure contours dissipate to less than ~2.4 kPa and expand to a soil depth of ~34 cm during the thrust shut-down phase (t = 0.085 s). Higher pore

pressure contours of ~5 kPa are observed at the start of the thrust shut-down phase (t = 0.065 s). This leads to the pressure gradient forces on the soil particles exceeding the normal atmospheric pressure and cohesive forces. Hence, this process is more readily observed at low atmospheric pressure environments (Mars) than at terrestrial atmospheres.

Once these gradients break minor cohesive bonds, the only restraining force is the cumulative weight of the sand grains. For the particle sizes studied, the pressure gradient force is slightly larger than the particles' gravitational force during the thrust shut-down phase (t = 0.065 s to 0.1 s), causing the effective stress to be zero and the soil to enter a fluidized state as observed experimentally. For porosities between n = 0.5 and n = 0.78, the potential fluidization depth, z_f, which results in soil instability ranges from 10 cm to 16 cm per thrust cycle. This calculation from Eqn. 3.28 takes into consideration the gravitational weight and cohesive strength (c) of a column of sand of cross sectional area $\overline{d}^2$ which extends from the surface to a depth z_f where the gas diffusion pore pressure can lead to such instabilities. It should be noted that the pressure contours show relatively good agreement with the fluidization spatial profile shown in Figures 3.10A3 and 3.10A5.

$$z_f \leq \frac{\frac{3}{2}\left[p(r,z,t) - P_{amb} - c\,(t)\,\right]}{\rho_p g} \qquad (3.28)$$

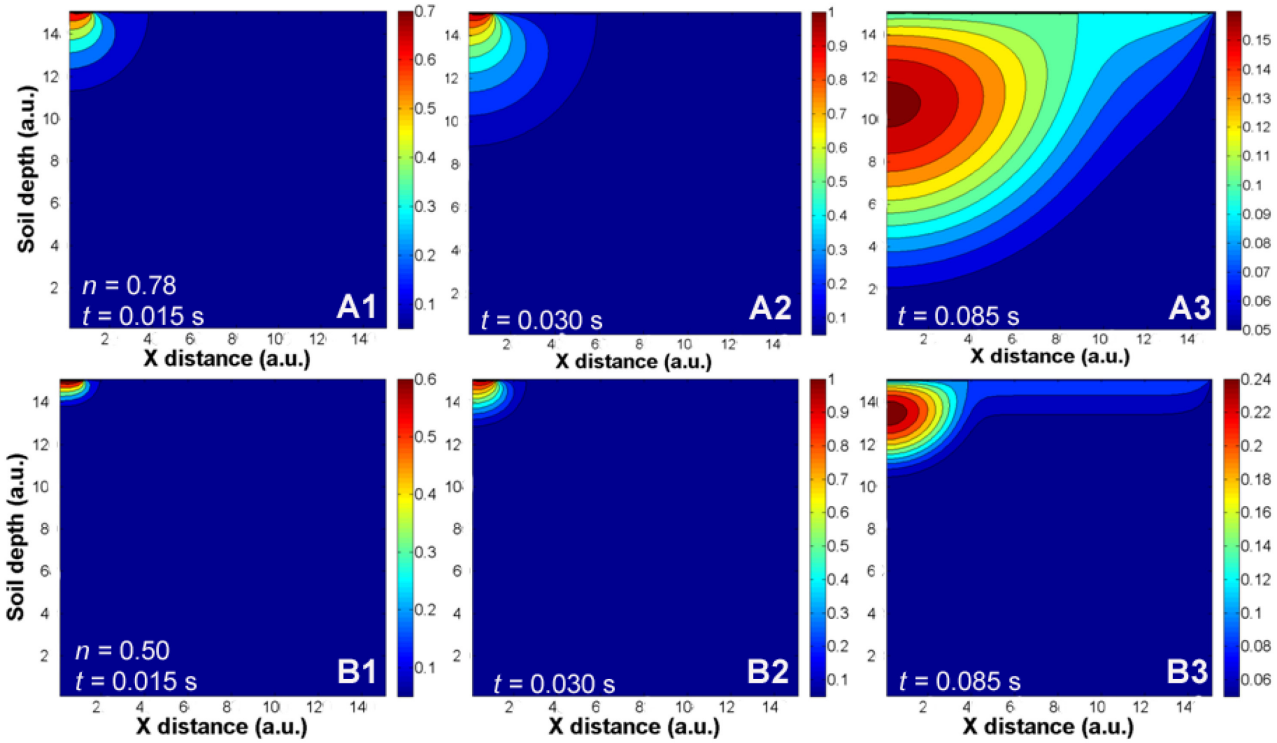

Figure 3.16. Results of numerical simulations of the time-varying pressure wave propagating within the fine sand simulant for a single thrust cycle at Mars atmospheric pressure for the laboratory simulations (Tests 4-10). All length scales are normalized by the nozzle exit diameter and the colorbar depicts the pore pressure values within the soil which are normalized by the average steady state impingement pressure, P_{imp}. We show these pressure contours at t = 0.015 s, t = 0.030 s and t = 0.085 s for two average bounds in soil porosity observed experimentally: n = 0.50 and n = 0.78.

As a comparison, we show that for a constant soil porosity of n = 0.5 during the thrust rise phase, gas diffusion extends to a soil depth of 4 cm with an average pore pressure of 6.4 kPa and expands to a depth of ~13 cm with a pore pressure less than 4 kPa during the thrust shut-down phase. Hence, the average characteristic diffusion velocity from these numerical simulations is between 1 and 3 m/s. This is also observed experimentally, where the depth of fluidization and resulting shockwave epicenter are much smaller for the first thrust cycle where the initial porosity is 0.5 as opposed to subsequent cycles. The duration when maximum penetration depth is reached is most likely smaller in our laboratory simulations due to a shorter thrust rise phase than numerically simulated. From conducting a series of numerical simulations with slight variations in permeability and porosity (sensitivity tests), we find that a decrease in soil permeability by a factor of 10 from theoretical values at pre-jet impact conditions has a

relatively minor effect on the pressure contour profiles and decreases the calculated depth of gas penetration and fluidization by a factor of ~0.7.

As a further comparison, the numerical model was applied to input conditions from the full-scale Phoenix REM thrusters and soil properties typical of Mars as shown in Table 3.5. Hot fire test data of the REM motors were used to bound the simulations shown in Figure 3.17. Here, the maximum diffusion depth reaches ~16 cm at n = 0.78 and t = 0.030 s and then expands to ~32 cm during the thrust shut-down phase. Good agreement with numerical simulation results for the subscale experiment was observed for the absolute values of the depth of gas penetration and pressure contours. Normalized jet penetration radius during thrust rise show good agreement between full-scale and subscale results. Inconsistencies in the normalized radius and depth between the two cases are observed during the fluidization regime at the thrust shut-down phase. Slightly higher pore pressure values were predicted for the full-scale case, but it should be noted that the pulse width for the Phoenix REM motors are shorter than for the experiments (Table 3.5). Gas diffusion depth does not necessarily scale with nozzle diameter as observed for the penetration radius. This predominately scales with known soil properties and the impingement pressure magnitude and temporal profile.

Overall, the numerical simulations and analytical calculations support the observations seen in Tests 4-10 and that the 'explosive erosion' process leads to soil fluidization, granular shock waves and large penetrations of the exhaust plumes into relatively fine grained and low cohesive granular media within short time scales. The full-scale numerical simulation also supports that 'explosive erosion' was likely the governing mechanism during the Phoenix landing. The smaller grain and higher porosity of the fine silt simulant (Tests 21-22) may explain the expansive fluidization during thrust shut-down phases. Another possible but an unlikely mechanism that could have assisted liquefaction is vibro-fluidization, a process in which large surface vibrations could lead to extensive soil fluidization.

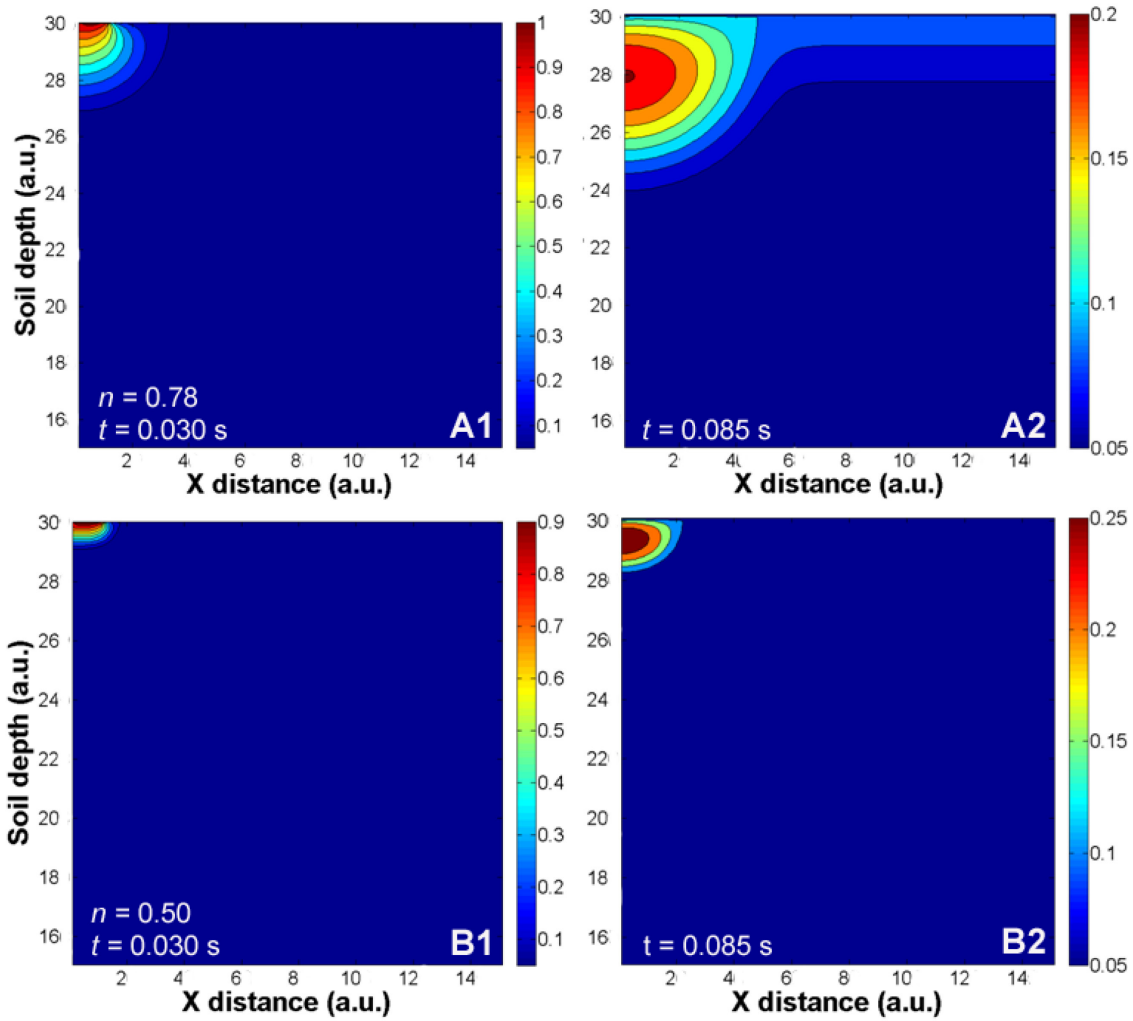

Figure 3.17. Results of the numerical simulations of the time-varying pressure wave propagating within fine basaltic sand at 160 µm for a single thrust cycle at Mars atmospheric pressure. The input and boundary conditions correspond to the full-scale Phoenix REM thrusters firing during descent.

Parameters	**Full scale**[†]	**½ scale**[ᵞ]
Friction velocity (m/s)	~88.9	~35.6
Threshold friction velocity (m/s)	1.3	0.5
A_N (a.u.)	0.0123	0.0123
K (m^4/kg-s^2)	3 x 10^{-4}	3 x 10^{-4}
Gas diffusion time (s)[‡]	~33 – 1	~20 - 1
Soil depth (cm)	5 – 18	5 - 20
Porosity (%)[‡]	~50	50
Gas viscosity at exit (kg/m-s)	9.4 x 10^{-6}	3.5 x 10^{-6}
Permeability (m^2)[‡]	7.1 – 0.2 x 10^{-11}	7.1 – 0.2 x 10^{-11}
Cohesion (kPa)	0.3 – 1.9	1.3
Angle of internal friction (deg)	~30	33
Soil particle density (kg/m^3)	3000 – 2650	1300
Particle size (µm)	~160	~160
Impingement pressure (kPa)[‡]	~15	~15
Gravitational acceleration (m/s^2)	3.71	9.8
Atmospheric pressure (Pa)	~858	~832

Atmospheric temperature (K)	~243	~280
Maximum thrust (N)	~600	~160

[†]Data obtained from fine basaltic sand at Viking 2 Landing Site on Mars [*Shaw et al.*, 2009]
[‡]Properties significantly change from pre-jet impact conditions during DGEE
[ɣ]Data obtained for simulant-type S

Table 3.5. Dimensional parameters at pre-jet impact conditions based on scaling relations

Although the assumption that viscous dominant flow within the micro-pore space is reasonable, especially during the thrust shut-down phase and deeper within the soil, there may be times within the thrust-cycle and regions within the granular media where inertial effects become important. This increases complexity of the problem, but Teruel and Rizwaan-uddin [2009] show that the permeability for turbulent flows, determined numerically, also increases with soil porosity, $k = f(n^3/1\text{-}n)$. Also, modeling of turbulent flow in porous media is limited and there is currently no consistent well founded methodology [*Teruel and Rizwaan-uddin*, 2009]. The Kozeny-Carman equation is well established for applications with granular media larger than clays, but more accurate calculations of the permeability may be obtained by measuring the sphericity factor and tortuosity of the granular media, rigorously accounting for permeability anisotropy and varied particle size distributions, and assuring complete steady flow and saturated soil specimen during the permeability tests.

3.5. Relatively benign jet-induced erosion processes at Earth and Mars atmospheric pressure

3.5.1 Viscous shear erosion

Viscous shear erosion dominates during the impingement of the pulsed thruster jets into soils composed of fine sand and silt at Earth atmospheric conditions depicted in Movie D5 (Appendix D) and Figure 3.11 which are examples of Test 17. It can be seen that VSE mainly acts by removing surface layers of soil particles. The radius and depth of the craters developed by VSE shown by Figure 3.7B (Test 17) were three to four times smaller than that caused by 'explosive erosion' shown by Figure 3.7A (Test 9). After pulsed jet impingement for 3 s or less, the crater developed is less than 5 cm deep and had a diameter less than 20 cm. Similar crater profiles were also observed for VSE at Mars atmospheric conditions [*Shorthill et al.*, 1976a, 1976b, *Romine et al*., 1973]. The crater contour profiles showed relatively little difference between soil simulants tested.

The large coarse sand/granules (~1500 μm) have more massive particles which also inhibits the 'explosive erosion' process. No localized soil fluidization or granular shock waves were observed in VSE dominated processes.

Dust lifting is considerably more localized in VSE dominated experiments at Earth and Mars atmospheric conditions than DGEE [*Romine et al*., 1973]. However, soil deposition due to VSE at Mars atmosphere is less. At Earth atmosphere, Figure 3.7B shows a contour plot of a distinct crater rim of ~15 to 30 cm in width (~30 to 60 cm at full-scale) and a deposition of 7 to 10 cm layers of soil near the lander footpad. The soil was ejected vertically at a steady rate due to the formation of a parabolic crater as shown in Figure 3.11, in contrast to 'explosive erosion' which led to sudden dynamic events which ejected granular media outward from the shock wave epicenter. The area covered by ejecta is considerably larger in experiments dominated by 'explosive erosion' and this correlates well with what is observed at the Phoenix landing site. In these experiments, many soil particles are ejected well beyond the testbed area.

From particle tracking data, we deduce that there are two reasons for the large differences in the deposition location between the two mechanisms. First, the drag on particles or bulk flow at Earth atmospheric pressures is hundred times larger than for the cases at Mars. Second, the mean velocity of shock-induced bulk media is five to seven times larger than for viscous shear-induced flows at martian atmosphere. For example, on the moon in a vacuum atmosphere, jet-propelled particles can reach supersonic speeds and travel distances greater than 160 m due to negligible drag forces. This was recorded by the Apollo 12 crew when they noticed microscopic craters on the Surveyor 3 hardware due the sandblasting effects during their lunar landing [*Jaffe*, 1971].

The other main difference between the site-alteration characteristics on Mars and Earth, at a similar thruster inlet pressure, is caused by the fact that the impingement pressure is significantly larger at Mars atmosphere conditions than on Earth conditions as discussed in Chapter 2. This occurs because the thruster jet is underexpanded and collimated at Mars conditions and forces the development of a plate shock at the surface. A highly overexpanded shock structure which rapidly develops into a subsonic turbulent plume is observed in experiments at Earth atmospheric conditions, leading to the inability of a plate shock to develop at the surface. The surface impingement pressures at lunar

atmosphere have modest values as well due to a highly expansive plume shock structure [*Clark*, 1971], characteristic of highly underexpanded jets (e > 100). This forms a large areal plate shock which distributes the thrust load over a larger area, significantly decreasing the ground pressure and producing minimal site-alteration as observed for previous Apollo and Surveyor missions [*Christensen,* 1967; *Mason*, 1970].

3.5.2 Bearing capacity failure and diffusion-driven flow

Bearing capacity failure and diffusion-driven flow dominate the erosion process in experiments with steady jets at Mars atmospheric conditions depicted in Movie D6 (Appendix D) and Figure 3.12 which are examples of Test 18. In this case shown in Figure 3.12, a partially reflected plate shock developed at the surface, and the soil composed of fine sand simulant was excavated down to the impermeable subsurface in less than a second. Minor eroded soil was ejected away and upwards by flow deflected by the steep parabolic crater with a diameter of ~10 cm.

Diffusion-driven flow (DDF) drives the soil in a tangential direction and bearing capacity failure (BCF) forces the soil in a perpendicular direction to the crater surface [*Metzger et al.,* 2009]. DDF occurs when the exhaust plume diffuses into the soil layer and through viscous drag removes a uniform soil layer along the periphery of the crater wall. In contrast to DDF, the BCF mechanism alone does not erode soil layers. The pressure force of the jet mechanically compresses the soil, forming a cup-like crater. Majority of the soil is seen to be compressed along the cavity by bearing capacity failure similar to that observed during initial simulations of the Viking and Mars Science Laboratory (Appendix C) landings on Mars [*Romine et al*., 1973]. The distinction between which erosion process dominates is determined by the ratio of simulant particle to plume diffusion velocity. If the plume diffuses faster than the movement of simulant grains, DDF prevails and vice-versa for BCF [*Metzger et al*., 2009]. We have not assessed in this Chapter which distinct process between DDF and BCF is governing, but we believe that both processes play a role in erosion by steady jets. For experiments with the S-type simulant, the exhaust plumes diffuse into the soil layer and removes soil along the crater periphery as shown in the schematic of Figure 3.12. Small amounts of surface viscous erosion were also observed at the outer areas of the crater.

After engine shut-down, most of the eroded and compressed soil rapidly refills the cavity and hence, we hypothesize that BCF was dominant. The final crater was less than 5 cm deep with a diameter of 50 cm shown in Figure 3.7C. Although soil deposition thickness was greater for VSE, loose soil deposition also surrounds the crater rim for the BCF/DDF process. Similar erosion dynamics and crater profile were observed for the fine silt/dust simulant and this was also recorded for pre-Viking site alteration experiments conducted with lunar nominal soil (d < 20 μm) [*Romine et al*., 1973]. No localized soil fluidization or granular shock waves were observed in experiments dominated by BCF/DDF.

3.6 'Explosive erosion' at the Phoenix Landing Site

The idea that DGEE occurred during the landing of the Phoenix spacecraft is supported by images from the Surface Stereo Imager (SSI) and Robotic Arm Camera (RAC) [*Smith et al*., 2009]. These images shown by Figures 3.9 and 3.18 suggest that the erosion removed layers of regolith, rapidly exposing the subsurface ice over a large area [*Smith et al*., 2009] of ~2 m^2 and ejecting ~300-120 kg of soil in less than 2 s, as predicted by DGEE. The calculated normalized erosion rates $\left(\frac{\dot{m}_c}{\dot{m}}\right)$ for type B and S simulants with depths between 5 cm and 20 cm at various altitudes (Tests 1-11) range from 20 to 65 for DGEE dominant processes, 40 to 130 when including the mass correction term discussed in Section 3.2.2. In contrast, these average erosion rates are below 10 (20 by including the mass correction term) for BCF, DDF and VSE processes (Tests 12-20). The range of normalized erosion rates calculated from RAC images of the Phoenix landing site (Appendix B.1) are between 35 and 100 which are in good quantitative agreement with the laboratory simulations governed by DGEE.

Furthermore, the exposed ice table seen at the southern footpad in Figure 3.9 extends to a radius between 75 and 85 cm from the spacecraft centerline with a width of ~1.1 m, similarly observed by the 'explosive erosion' process through normalization in applying Eqn. 3.11. In Figure 3.9, there are three large patches of the exposed subsurface where two exposed surfaces are bright and the third is much darker. Mellon et al [2009] indicates that the two bright features are either lighter-toned water ice or ice-saturated

soil observed at a high phase angle. They are separated with a modest amount of dark soil deposit. Figure 3.18A shows that the ice table was also extensively exposed near the eastern footpad.

In contrast to VSE and BCF/DDF, DGEE produces poorly defined and narrow crater rims with minor fluidized deposition, similar to those observed below the Phoenix lander. Loose soil particles are observed along stagnation planes between the three groups of thrusters and at the spacecraft centerline, in agreement with the design and results of our experiments. Modest amounts of particle deposition are observed around the crater rim, seen by the ejecta covered rocks near the footpad (Fig. 3.17D). Our experiments suggest that a layer of loose soil of ~1 to 2 cm of thickness was deposited in this region located in the work area as indicated in Figures 3.6B and 3.7A. This agrees with the fact that the forces on the robotic arm indicate less cohesive top soil near the crater rim than in places farther away [*Arvidson et al*.,2009]. Most importantly, these erosion characteristics are further corroborated by our experiments which simulates the dynamic pulsed nature of the impinging jets on soil at Mars atmospheric pressure as observed during the Phoenix landing.

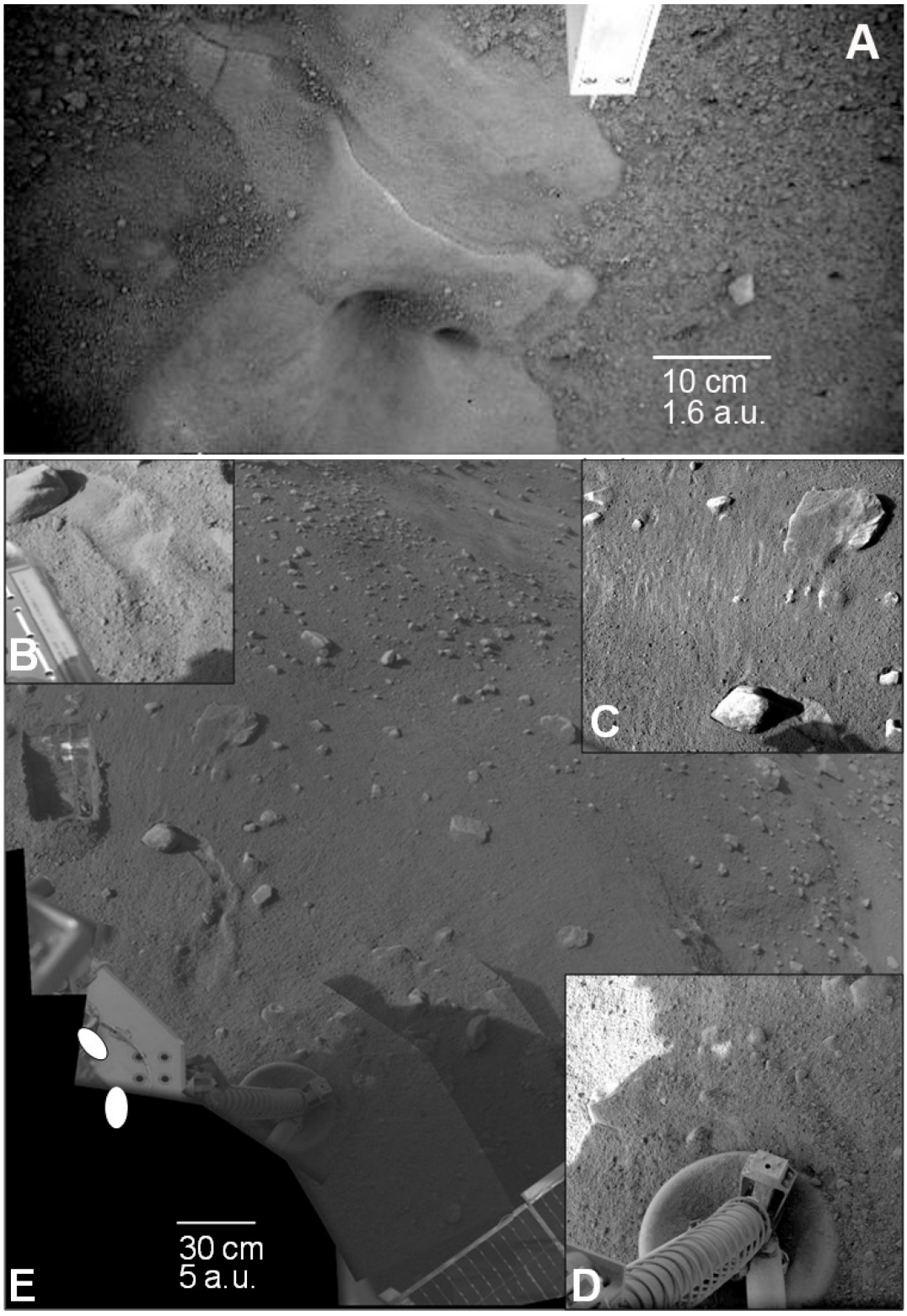

Figure 3.18. Images of erosion and deposition areas at the Phoenix landing site. (A) A partial close-up view of the exposed ice table, "Snow Queen" which is approximately ~55 cm in diameter (RS006EFF896752928_117A6MDM1). (B) Sol 7 SSI image (SS007EFF896839472_117FER1M1) of a rock (of ~12 cm of diameter) that was dragged for ~35 cm due to the shear force of the exhaust plume; (C) Sol 6 SSI image (SS006EFF896755404_1179ER1M1) of striations, ejected pebbles, and ejecta-covered

rocks out to ~3 m from the spacecraft centerline; (D) Sol 0 SSI image (SS000EFF896228288_10C96R1M1) of loose fluidized regolith is observed near the lander footpad. (E) Sol 5 SSI mosaic of the site alteration features seen with respect to the thrusters (marked in white ovals). *Courtesy of NASA/JPL-Caltech/U. of Arizona/Texas A&M*

Both local and macroscopic effects were observed due to the erosion caused by the landing phase. Displaced and ejected pebbles/rocks (Fig. 3.17B), ejecta covered rocks (Fig. 3.17C), and radial erosion striations all up to 3 m away from the lander centerline (Fig. 3.17 C, E), soil disturbance at a diameter of more than 40 m around the lander [*Smith et al*., 2009] (Fig. 3.18) and ejecta deposition even near the top of the legs struts [*Renno et al*., 2009] are all consistent with the explosive nature of DGEE. Some embedded rocks were dislodged from the ice table [*Sizemore et al*., 2009] due to the jets rapid, violent and broad excavation process and high surface impingement pressure loads. These soil disturbances are much larger in scale than those from the Viking, Surveyor and Apollo landings [*Shorthill et al*., 1976a, 1976b; *Christensen*, 1967; *Mason*, 1970), and experiments governed by either the VSE or BCF/DDF mechanisms which produced less intense, more localized erosion. Landing site images of previous spaceflight missions are shown in Appendix B.6 to provide a qualitative comparison of rocket plume-induced cratering.

VSE at the Phoenix landing conditions would lift soil particles less than 7 m away from the lander as shown by analytical calculations presented in Appendix B.5. However, Mars Reconnaissance Orbiter (MRO) High Resolution Imaging Science Experiment (HiRISE) image in Figure 3.19 shows a dark symmetric halo extending more than 20 m away from the lander, probably caused by surface erosion due to the impact of sand grains ejected by 'explosive erosion' [*Smith et al*., 2009; *Greeley*, 2002; *Greeley et al*., 1974]. Another interpretation of this halo is that the high-energy ejecta composed mainly of silty-sand and aggregates could have been deposited over these distances [*Markiewicz et al.*, 2009; *Greeley et al*., 1974] as observed experimentally. It should be noted that this dark halo was not observed at the landing site prior to Phoenix touching down. Both interpretations support the idea that 'explosive erosion' was dominant. Relatively much smaller in scale, asymmetric erosion was observed by the backshell and heatshield's oblique impact with the martian surface, which may imply that the dark halo around Phoenix is characteristic of the "erosion-supported" hypothesis.

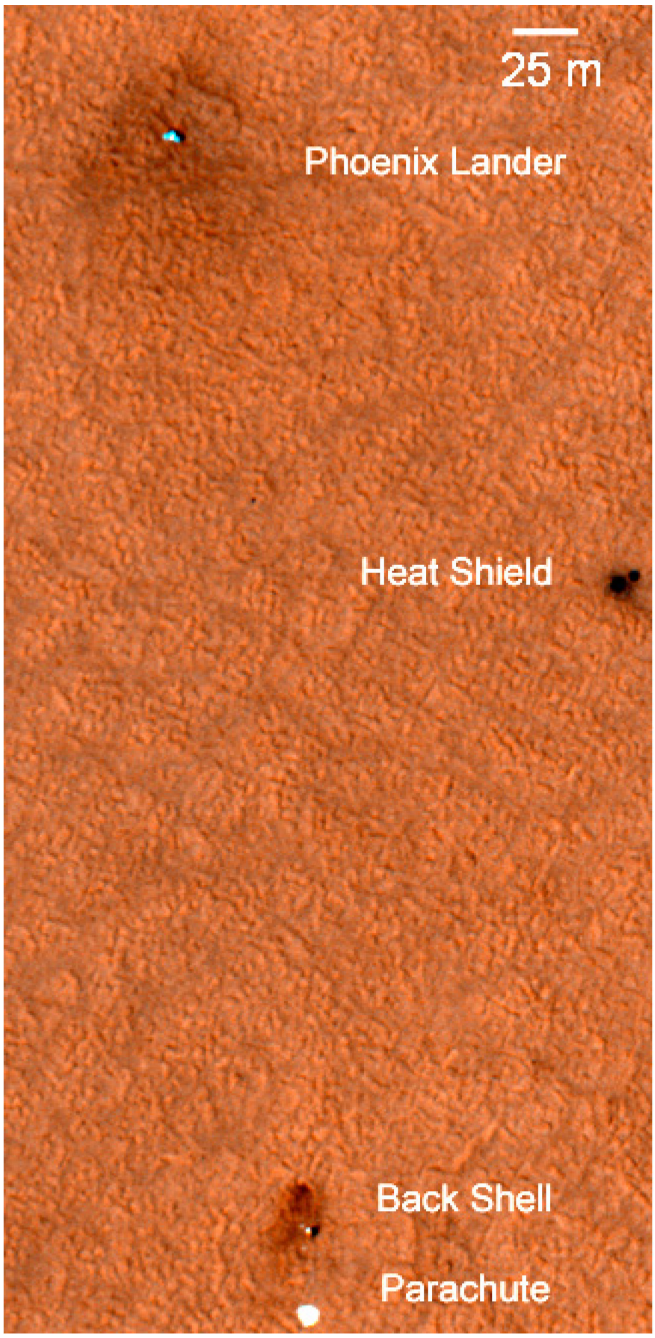

Figure 3.19. Sol 0 MRO HiRISE image (PSP_008591_2485) of the Phoenix landing site taken 22 hours after landing. A dark halo of more than 20 m in radius can be seen around the spacecraft depicted by a blue dot. Contrast applied to image. *Courtesy of NASA/JPL-Caltech/U. of Arizona/Ball Aerospace.*

Slight discrepancies in the normalized erosion rates and crater profiles between spacecraft observations and laboratory simulation may be due to the assumptions made in our analyses of the Phoenix data. Calculation of the soil removal from Phoenix data

(Appendix B.1) is under the assumption that the soil media has a relatively constant bulk density and the third group of thrusters exposed a similar fraction of subsurface ice. Since a digital elevation map has not been created under the lander, this value is only an approximation based on limited images taken from Phoenix's RAC. Also, complete similarity between subscale terrestrial and full-scale planetary processes is difficult to achieve for granular processes and this may lead to some inconsistencies.

3.7. Bulk physical soil properties derived from DGEE

The erosion processes described above can be used to determine approximate bulk physical properties of the soil at the landing site because crater morphology depends strongly on soil porosity, permeability and cohesion [*Shorthill et al*., 1976a, 1976b; *Hutton et al*., 1980]. Thus, the value of these important soil parameters can be determined by the analysis of images of the area below the lander and its surroundings [*Shorthill et al*., 1976a, 1976b; *Hutton et al*., 1980]. Our analysis in Appendix B.5 compares the ratio of average volume eroded with that of unaltered soil up to a distance of 40*D* from the lander centerline between experiments (Tests 1-11, 21-22, 23-24) and observations at the workspace region of the Phoenix landing site. This eroded volume fraction has been defined as the crater volume ratio.

The average crater volume ratio caused by the Phoenix landing is ~0.10. These calculations based on Figures 3.7A, 3.8 and 3.20 were averaged between soil depths of 5 cm and 20 cm. DGEE on soils composed solely of fine silt (Tests 21-22), which has the highest porosity and lowest permeability of all soil simulants used, predicted to remove greater than six times the volume eroded during the Phoenix landing, corresponding to an exposed area of ice six times larger than observed under the spacecraft (Table 3.2). Relatively incompressible simulant such as large coarse sand/granules (Tests 23-24) or heavily cemented soils are not subject to DGEE and therefore cannot produce the alteration observed at the landing site (Table 3.2). A mixture of approximate equal parts of fine sand and silt simulant by volume (type B) produces erosion similar to that caused by Phoenix (Tests 1-2, Table 3.2).

First order comparison of the crater volume ratio from our laboratory simulations and that calculated with the Phoenix data suggests that the permeability coefficient and

porosity of the soil of the Phoenix landing site are within the range of ~3 x 10^{-4} cm/s and ~0.45, respectively. The martian arctic regolith seems to possess high compressibility at relatively high pressure loads as discussed in Section 3.4. These values and general properties can be used to constrain models of hydrological and vapor diffusion processes and therefore provide insights into the deposition and mobilization of water ice on the martian arctic [*Hannah and Phillips*, 2005; *Sizemore and Mellon*; 2006].

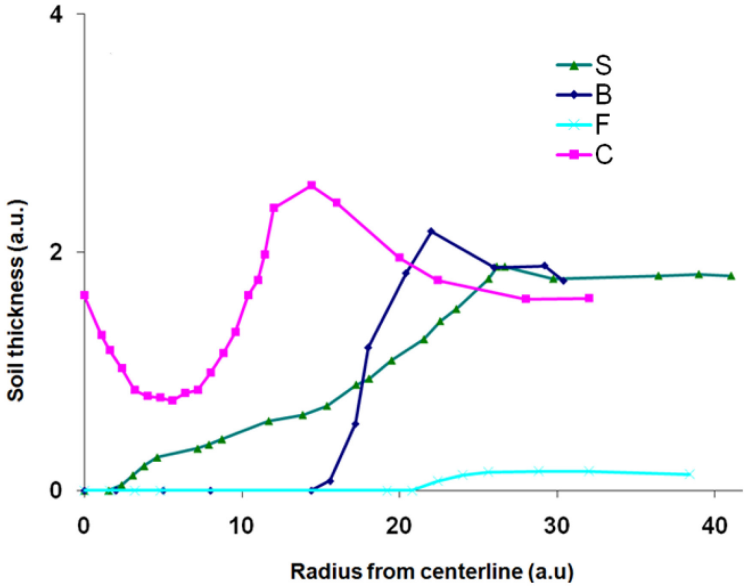

Figure 3.20. Crater profiles for 5 cm soil depth cases for Tests 2, 11, 21 and 23 (Table 3.4).

From our experimental results and RAC and SSI imaging, the large volume of exposed subsurface water ice, the lack of soil deposition within the crater, and the steep crater walls indicates that the soil at the landing site is a cohesive mixture of fine silt and sand. Since the average crater volume ratio at the landing site is smaller than that observed in our laboratory simulations for type-B simulant, the soil cohesive strength may be larger than 3.5 kPa. We hypothesize that duricrust formed by liquid brines may be a source for the higher cohesion [*Renno et al*., 2009].

As an alternative or in conjunction hypothesis, the crater volume ratio (Table 3.2) which shows a general increase with decreasing particle size may also imply a larger presence by volume of fine sand (d > 200 μm) at the Phoenix landing site than estimated previously by the Microscopy, Electrochemistry and Conductivity Analyzer's (MECA) Optical Microscope (OM) [*Goetz et al*., 2009]. The MECA OM shows two main particle size distributions at the landing site: ~70-100 μm and <15 μm. However, caution must be

taken in this comparison because the OM does not sample particles larger than 200 μm in diameter, and therefore its analysis is biased towards a smaller size distribution [*Goetz et al*., 2009]. The presence of a dark halo around the lander (Fig. 3.18) may also suggest a larger fraction of sand, coarser than the surface deposit which has a higher albedo [*Smith et al*., 2009; *Greeley et al*., 1974].

3.8. Spacecraft aerodynamic loads and rates during the Phoenix EDL sequence

This section is included to provide context to the research investigation described above. Data from inertial measurement units (IMU) and gyros sampled at 200 Hz, located at the base of the lander, measures the three-dimensional accelerations and angle rates of the spacecraft. The radar provides 10 Hz altitude and spectra data. The altitude is measured from the lander footpad to the surface. Entry state such as flight path angle, speed, azimuth, time, latitude and longitude are provided from the Navigation Team. These figures were generated by applying the data file provided by NASA JPL/LaRC: phx_tlm.traj.grnd_up.lla.alt_abv_LS

Figure 3.21 shows the three-axis acceleration on the spacecraft during the EDL sequence. The *x*-direction is depicted along the vertical direction relative to the spacecraft. It shows maximum gravitational (*g*)-loads at Hypersonic 4 regime and parachute deployment. Maximum *g*-loads on the spacecraft occurs when we obtain maximum dynamic pressure on the heat-shield. As designed, it can be seen that immediately after backshell separation, the pulsed thrusters are firing until touchdown.

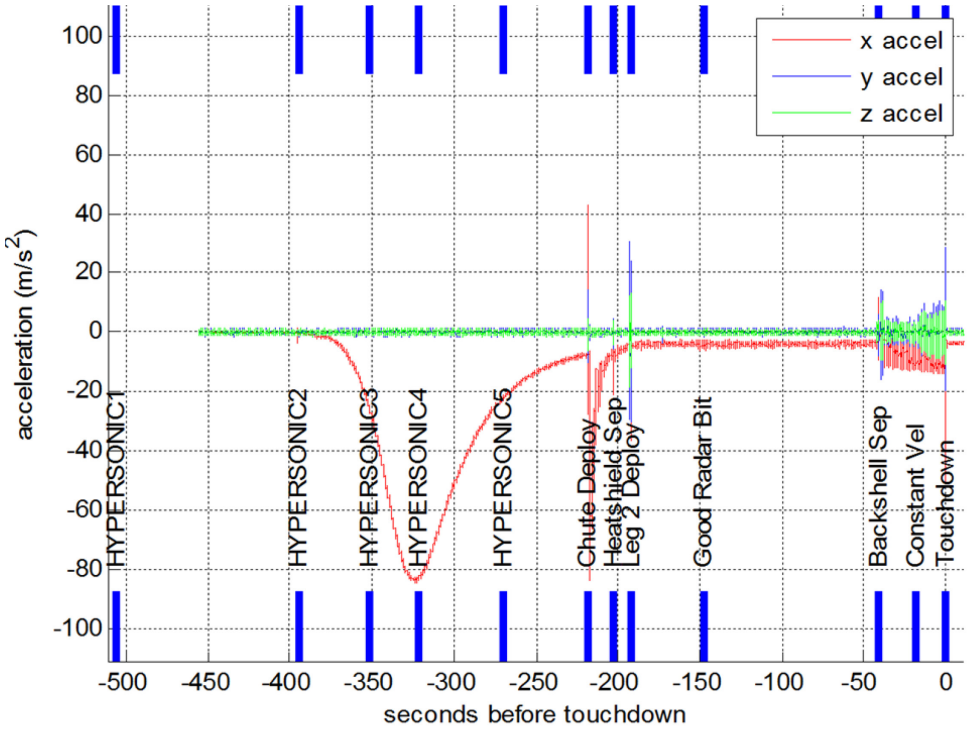

Figure 3.21 Three-axis acceleration vs. time of the Phoenix spacecraft during the EDL sequence.

The figures below in Fig. 3.22 focus on the last 6 m of descent. From this data, lift loss due to plume-surface interactions spans an altitude from 4.5 m to ~3.5 m, causing an increase of ~0.25 m/s in the descent velocity. Then, ground effects due to plume-surface interactions starts and decreases the descent velocity from 2.65 m/s to 2.4 m/s (Fig. 3.21). These figures support that the duration of plume-surface interactions was indeed quite brief on the order of ~1.7 s. The onset of ground effect is delayed as compared to simulations and this may be attributed to the fact that reflected plumes start interacting with the base of the lander closer to the ground (h/d ~60) than predicted.

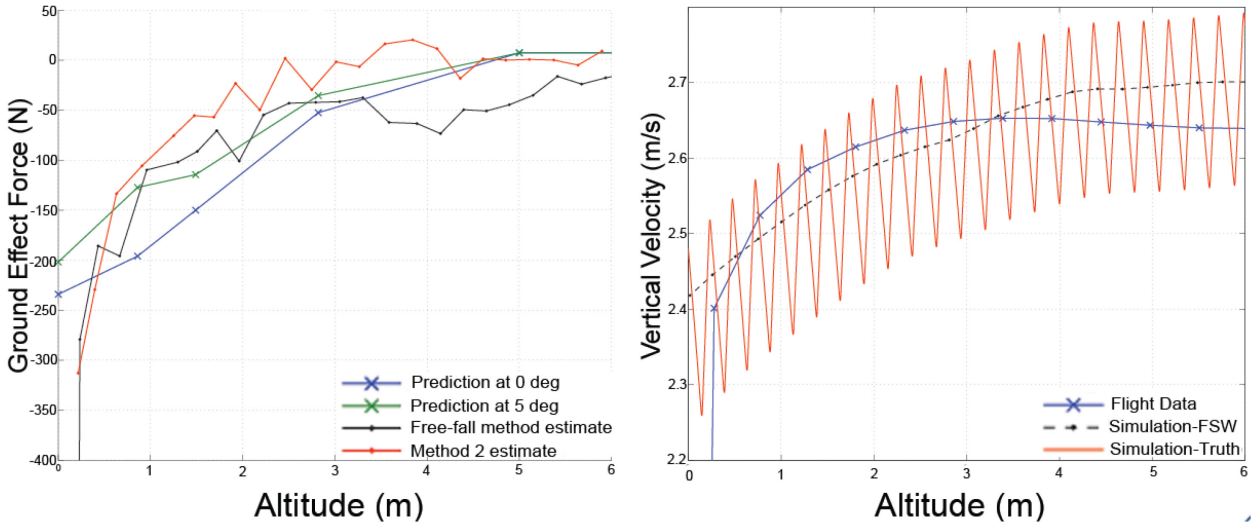

Figure 3.22**.** Ground effect force vs. altitude (left) and vertical descent velocity vs. altitude (right) during the Phoenix landing. The force and vertical velocity were calculated with data from the lander's inertial measurement unit (IMU) and numerical simulations. *Courtesy of Lockheed Martin/NASA/JPL-Caltech.*

Figure 3.23 shows the aerodynamic acceleration and angle rates in all three axis during the last 2.5 second prior to touchdown. It shows the successful thrusters firings at 10 Hz which results in transient acceleration peaks in all directions, but most prevalently within the *x*-direction. It can also be seen there was a slight bounce upon touchdown impact. Hence, a single decceleration peak is observed at ~0.3 s after touchdown. The unexpected bounce could have resulted from an additional 25 msec of pulsed thrusting upon initial contact. During the last 6 m, there was no mean roll rate, but a slight pitch and yaw rate within the last ~1.8 m which may be attributed to reflected plume interactions.

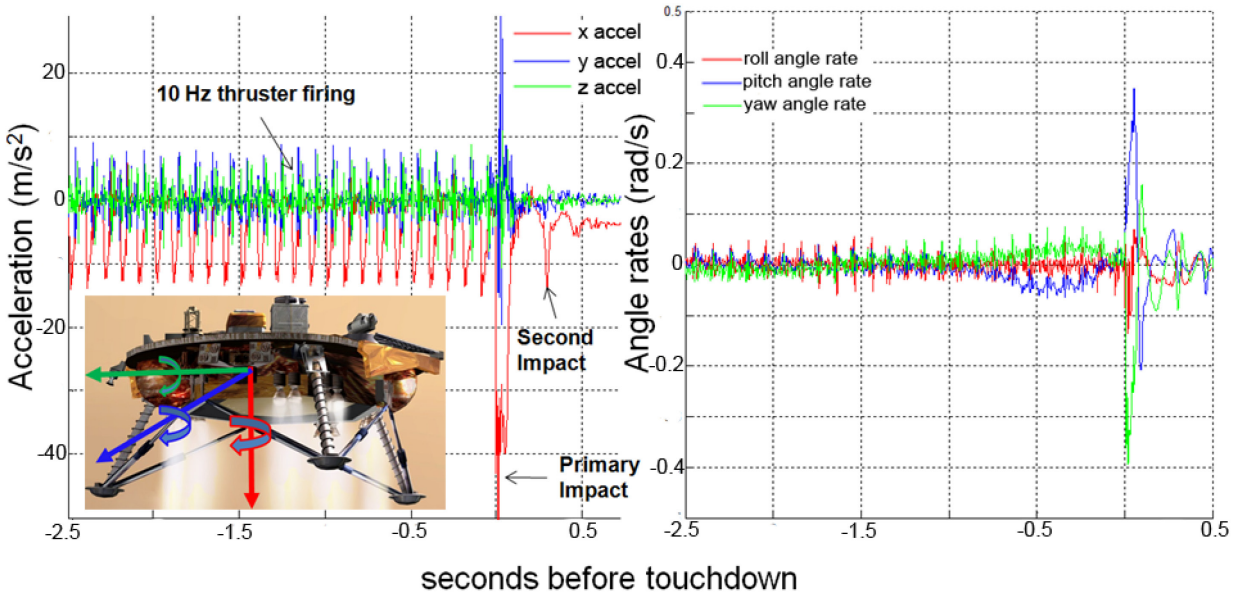

Figure 3.23. Three-axes spacecraft acceleration (left) and angle rates (right) vs time before touchdown.

From 3-D CFD steady-state simulations developed by the Aerosoft GASP code, the ground effect forces starts increasing below ~3 m as shown in Figure 3.24A. This is consistent with the flight data shown above in Figure 3.22. It can also be seen that lift loss occurs at 5 m or greater. Figure 3.24B suggests a large destabilizing torque in the z-direction at a ground slope of ±10 degrees. Both destabilizing functions are maximized at touchdown altitude.

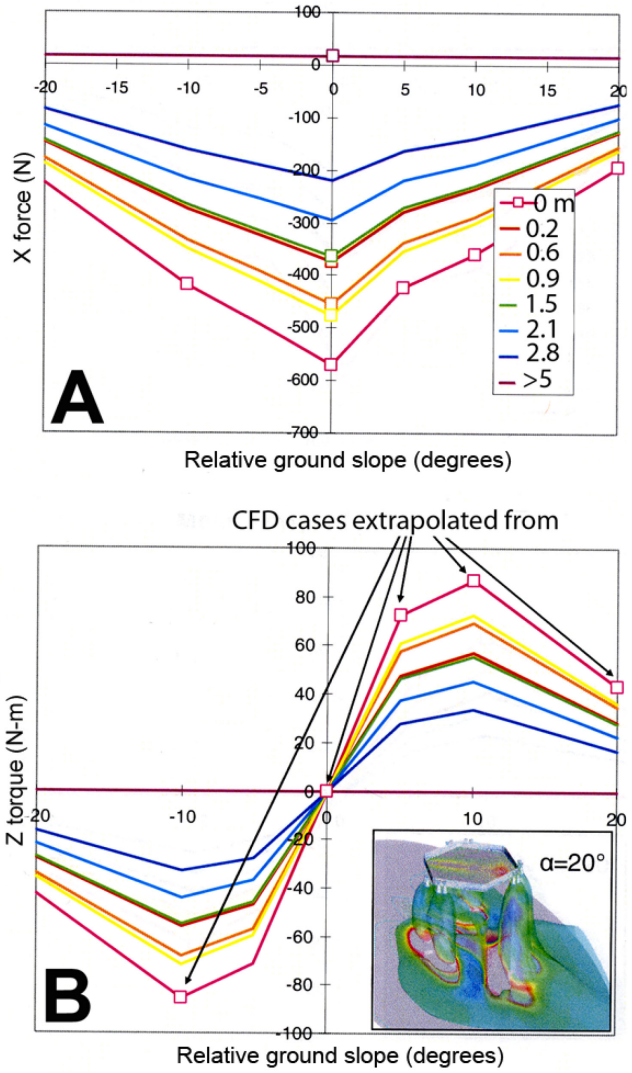

Figure 3.24. Three-dimensional steady-state numerical simulations for full-scale maximum torques and forces on the Phoenix Lander during descent. Force in the *x*-direction (top) and torque in the *z*-direction on the spacecraft vs. relative ground slope and altitude. [*Gulick*, 2006]

3.9 Further experimental studies of cratering physics due to supersonic jet interactions in tenuous atmospheres

As a follow-up to this research investigation, a detailed experimental study of the interactions of steady supersonic jets with granular systems at altitudes greater than 35*d* was conducted at Mars atmospheric pressure. The research was done in support of the future NASA Mars Science Laboratory mission and described in Appendix C. Key findings include BCF/DDF as the primary erosion mechanisms which lead to a semi-linear dependence of erosion with throttle level, ground slope and particle size. These test

programs in conjunction with spaceflight data were used to determine the dependency of nondimensional parameters on erosion rates. We find that the densimetric Froude number – erosion rate profiles are distinct between three jet-induced cratering processes: VSE, BCF/DDF and DGEE. Maximum cratering is observed at Mars atmospheric regimes relative to lunar and terrestrial environments.

3.10 Conclusions and future work

This study used Phoenix spacecraft data and experimental and numerical simulations to investigate the dynamics of erosion caused by the thruster plume interactions with soil during the Phoenix spacecraft landing on the martian arctic. Its main results are:

(1) A new erosion process termed diffusive gas explosive erosion (DGEE) is discovered. DGEE is caused by supersonic pulsed jets impinging in porous soils at martian (low) atmospheric pressure. The explosive nature of this erosion process is caused by the localized fluidization of soil and the formation and propagation of strong cyclic and radial granular shock waves. This leads to erosion rates which are 5 to 20 times greater than that of previously known processes caused by impinging jets. From theoretical calculations, numerical simulations, high speed imaging and photometry techniques, we are able to qualitatively and quantitatively determine the formation and effects of fluidization and granular shock waves on the surrounding granular media at extreme conditions.

(2) RAC, SSI and HiRISE images of the landing site, together with our results suggests that DGEE is responsible for the removal of 5 to 18 cm thick layers of soil, the first discovery of the expansive exposed ice table under the lander and an altered ground morphology that extends to 40 m in diameter which all occurred during the Phoenix landing. The more interesting observation is that this excavation took place in very short time scales of less than a second. This violent erosion process led to the discovery of the first direct evidence of liquid saline water on Mars [*Renno et al.*, 2009] and provided information in regards to site contamination. While surface erosion during previous soft landings on Mars was dominated by VSE [*Shorthill et al.*, 1976a, 1976b; *Hutton et al.,* 1980], we show the erosion during the Phoenix landing was dominated by DGEE.

(3) Through experimental findings and spacecraft imaging of the altered landing site, we are able to approximately quantify through interpolation the various soil properties of the martian arctic plains that can be determined through jet-induced erosion.

The main goals of this research are to provide insights into the behavior of granular media subject to thruster jet interactions during spacecraft landings on Mars. Based on past studies on scaling laws, this Chapter takes a fresh look at the scaling of jet-soil interactions. Accurately simulating the dynamics of granular flow as attempted here should be paramount and a first step in understanding these interactions. Most importantly, the physics described in this Chapter sheds light into the dynamic behavior of granular media subject to jet impingement at extreme conditions of low atmospheric pressure and low gravitational acceleration.

This study may also provide important information into in-situ resource utilization (ISRU) technology. This highly efficient and extremely rapid erosion process could be used to excavate the soil and extract resources from it. Pulsed cold gas thrusters on the spacecraft can be used as a low cost instrument to effectively sample martian soils. Hence, further studies, as briefly outlined below, are needed of soil transport in planetary environments.

Additional controlled experiments at low atmospheric pressure environments with large variations in particle sizes and densities and plume velocities are necessary to validate our scaling laws and further corroborate our theories of jet-induced erosion processes at extreme conditions. Along with additional terrestrial experiments, it would be beneficial to conduct a series of controlled experiments on Mars, of the effect of supersonic jets on granular soil. This can provide us with the ground truth to both our scaling laws and more importantly to numerical models being developed. Although limited, similar tests in the 1960s were conducted using NASA Surveyor V's liquid propulsion system on the moon.

Additionally, all future planetary surface missions should obtain detailed images and digital elevation maps of the site-alteration regions. Also, a camera on-board the spacecraft should take a time sequence and high-resolution images of dust lifting and erosion during the spacecraft descent and ascent phases. Limited observations were made during the Apollo lift-off and landings on the Moon. Moreover, Mars Science Laboratory

Mars Descent Imager (MARDI) will document its descent and may provide science and engineering teams with a further understanding of the erosion process due to spacecraft landings on Mars, for the first time. Numerical models and laboratory simulations in conjunction with ground truth are essential in fully characterizing these complex interactions. For future manned and robotic missions to Mars and other celestial planets, the understanding of these interactions is critical for the safety and survivability of the crew and spacecraft. Although the engineering aspects of 'explosive erosion' as described above are important, this discovery led to revolutionary thinking in the search for life on Mars.

Due to the physics and effects of the newly discovered erosion process at the Phoenix landing site and high relative humidity above the sublimating and exposed ice table, we looked for signs of liquid water below the lander. Shortly after, Renno et al [2009] first discovered possible signs of liquid brines on Mars. In Chapter 4, we further investigate this discovery by photometric and broadband spectral analyses of images taken by the Phoenix and MRO spacecrafts and controlled laboratory experiments.

CHAPTER 4

Photometric and spectral evidence for deliquescence and liquid saline water on Mars

This chapter describes an article submitted and under review by *Nature* in 2010.

4.1 Introduction

Determining if life ever existed on another planet is one of the main goals of space exploration. Since it is believed that liquid water is a basic ingredient for life, an important step in the search for extraterrestrial life is to determine if liquid water exists in other planets [*Space Studies Board,* 2002]. Mars is the most Earth-like planet in the solar system and there is evidence that it had liquid water in the past [*Squyres et al.*, 2004]. Therefore, Mars is an excellent candidate for searching for signs of past microbial life. The recent discoveries of evidence for interfacial water [*Kereszturi et al.*, 2009; *Mohlmann et al.*, 2010] for liquid saline water or brines [*Renno et al.*, 2009], and for methane [*Mumma et al.*, 2003] on Mars have excited the science community by reviving the possibility of extant microbial life in a nearby planet. Here we show photometric and broadband spectral evidence that liquid saline water exists on Mars. In addition, we show that this finding indicates that deliquescence occurs seasonally on Mars' polar region. These discoveries support the hypothesis that freezing/thaw cycles lead to the formation of brine pockets where ice and salts coexist in the shallow martian subsurface [*Renno et al.*, 2009]. This has important implications for the search for extraterrestrial life because a diverse array of terrestrial microorganisms thrives in brines [*Boetius et al.*, 2009].

The water vapor pressure at the triple point of water is below the atmospheric pressure on the lowest regions of Mars, but the low surface temperature and dry atmosphere inhibits the presence of pure liquid water on them. However, liquid water can

exist as brines because salts can lower the freezing temperature to Mars like temperatures [*Renno et al.*, 2009; *Haberle et al.*, 2009; *Hecht et al.*, 2009; *Chevrier et al.*, 2009]. The lowest temperature at which brines freeze, known as their eutectic temperature, can be lower than 200 K for single salts found on Mars, and mixtures of different salts can have even lower eutectic temperatures [*Renno et al.*, 2009]. The eutectic temperature depends mainly on the solutions' ion concentration and composition. Salts absorb water when the relative humidity over them is above the deliquescence relative humidity. This humidity value can be lower than a tenth of the saturation value over pure water, depending on the salts composition and the temperature of their solutions [*Renno et al.*, 2009; *Seinfeld et al.*, 2006].

It has been postulated that eutectic solutions form where salts are present near water ice and their temperatures oscillate around the eutectic value [*Renno et al.*, 2009]. These solutions form because salts deliquesce and ice precipitates from their diluted solutions when they are cooled, until the solution reaches the eutectic concentration and freezes, at the eutectic temperature [*Renno et al.*, 2009]. The eutectic temperature of solutions of some salts found on Mars is low enough that they could be liquid even in the polar region [*Renno et al.*, 2009; *Hecht et al.*, 2009; *Chevrier et al.*, 2009; *Seinfeld et al.*, 2006; *Pestova et al.*, 2005]. The Phoenix Lander found physical and thermodynamical evidence for liquid brines on its landing site in the Mars Arctic [*Renno et al.*, 2009]. This was first investigated due to the nature of the altered site and extensive exposure of subsurface water ice under the lander by the explosive erosion process described in Chapter 3. Hence, it was hypothesized by Renno et al. [2009] that the saline mud was easily splashed onto the lander struts and a few of these deposits dried upon cooling and formed distinct spheroids. Here we report the discovery of photometric evidence that liquid saline water is present at the Phoenix landing site. In addition, we report the discovery of photometric and broadband spectral evidence that liquid brines seasonally flows in some areas of Mars polar region, when they start to defrost early in the spring. These results have important implications for the habitability of Mars [*Boetius et al.*, 2009].

4.2 Methodology

The reflectance at wavelength λ is defined [*Rees,* 2001] as

$$R_\lambda = \frac{\pi I_\lambda}{F_\lambda}, \tag{4.1}$$

where F_λ and I_λ are the radiances at wavelength λ incident at the surface and reflected by it. The reflected radiance can be calculated using the measured brightness intensity, or instrument digital number (*DN*), with the aid of the instrument calibration function [*Delamere et al.,* 2010]

$$I_\lambda + I_\lambda^{path} = aDN + b, \tag{4.2}$$

where I_λ^{path} is the net source of radiance (emission plus scattering, minus absorption) at wavelength λ integrated along the surface-instrument path, and *a* and *b* are the instrument gain and offset. Taking the radiance reflected from the darkest pixels on shadows to be $I_\lambda \cong 0$, it follows from Eqn (4.2) that

$$I_\lambda = a\left(DN - DN_{dark}\right). \tag{4.3}$$

Substituting Eqn (4.2) into (4.1), we get

$$R_\lambda = \frac{\pi}{F_\lambda}\left(aDN + b - I_\lambda^{path}\right). \tag{4.4}$$

Thus, the reflectance of pixels dominated by ice is

$$R_\lambda^{ice} = \frac{\pi}{F_\lambda}(aDN_{ice} + b - I_\lambda^{path}), \tag{4.4a}$$

and the reflectance of dark pixels dominated by shadows is

$$R_\lambda^{dark} = \frac{\pi}{F_\lambda}(aDN_{dark} + b - I_\lambda^{path}). \tag{4.4b}$$

Subtracting Eqn (4.4b) from (4.4a), we get

$$R_\lambda^{ice} - R_\lambda^{dark} = \frac{\pi}{F_\lambda}(aDN_{ice} - aDN_{dark})$$

$$\frac{\pi}{F_\lambda} = \frac{R_\lambda^{ice} - R_\lambda^{dark}}{a}\left(\frac{1}{DN_{ice} - DN_{dark}}\right).$$

Multiplying both sides by I_λ, we get

$$\frac{\pi I_\lambda}{F_\lambda} = R_\lambda^{ice} - R_\lambda^{dark}\left(\frac{1}{DN_{ice} - DN_{dark}}\right)\frac{I_\lambda}{a}.$$

Taking $R_\lambda^{dark} \cong 0$, it follows from the above and Eqn (4.3) that

$$R_\lambda = R_\lambda^{ice}\left(\frac{DN - DN_{dark}}{DN_{ice} - DN_{dark}}\right). \qquad (4.5)$$

Eqn (4.5) is used to adjust the reflectance of each pixel of the images analyzed in this Chapter. Reflectances of ice, at the spectral bands in consideration, measured in the laboratory [*Clark*, 1981; *Painter et al.,* 1998] are used in our calculations. The error in the reflectance calculation is estimated in Section 4.5.

Images of brines of laboratory experiments at Mars conditions [*Zorzano et al.,* 2009], of Phoenix spheroids [*Renno et al.,* 2009], and of flow-like and pond-like features on Richardson crater's dunes [*Kereszturi et al.,* 2010; *Kereszturi et al.,* 2009; *Mohlmann and Kereszturi,* 2010] are analyzed by visually finding the brightest 25-50 pixels indicating frost/snow, the 25-50 darkest pixels in the darkest shadows, and adjusting the reflectance of each pixel with the aid of Eqn (4.5). Important parameters in regards to these three studies are tabulated in Table 4.1.

Table 4.1 gives the spectral band covered by each image analyzed in this Chapter. The presence of the liquid phase and ice in the laboratory experiments was verified by infrared spectroscopy [*Zorzano et al.,* 2009]. The controlled laboratory experiments at similar Phoenix landing site conditions were conducted at the Planetary Environment Simulation Chamber (PESC) at Centro de Astriobiologia (Spain). Both laboratory and Phoenix images are in the visible (VIS) portion of the spectra spanning from 400 to 750 nm (Table 4.1). The DN_{ice} values for these images were obtained from the brightest locations where frost was detected [*Zorzano et al.,* 2009; *Renno et al.,* 2009], while the DN_{dark} values were from the darkest shadows on the edge of the sample holder and where the diameter of the Phoenix strut changes.

† Albedo of the liquid phase derived from field measurements of terrestrial sea ice[*Perovich,* 1996]

Studies	P_{atm} (Pa)	T (K)	Atmospheric Composition	Camera Sensitivity (nm)	Pixel Resolution (μm)	Albedo†
PESC	~800-700	~220-240	~95% CO_2	400-750	~150	< 0.3
Phoenix RAC	~840-800	~225	~95% CO_2	400-750	~200	< 0.3
MRO HiRISE (BG)*	~850-720	~140-260	~95% CO_2	400-600	25 x 10^4	< 0.4
MRO HiRISE (VIS)	~850-720	~140-260	~95% CO_2	550-850	25 x 10^4	< 0.1
MRO HiRISE (NIR)	~850-720	~140-260	~95% CO_2	780-1060	25 x 10^4	< 0.05

Table 4.1. Albedo of liquid brines at Mars atmospheric pressure (P_{atm}) and temperature (T) at the spectral bands (Camera Sensitivity) of the various images analyzed in this article.

The value of DN_{dark} of Mars Reconnaissance Orbiter (MRO) HiRISE images are from pixels located on the darkest shadows casted by boulders and dune edges on low albedo areas. The DN_{ice} values of these images were found on locations where the Compact Reconnaissance Imaging Spectrometer **(**CRISM) detected surface frost [*Kereszturi et al.,* 2010]. CRISM detected both carbon dioxide and water ice frost in this area, in particular on dune crests and slopes [*Kereszturi et al.,* 2010; *Kereszturi et al.,* 2009]. The presence of ice is also confirmed by the spectral analysis reported later.

Table 4.1 indicates that HiRISE images in the blue green (400-600 nm), visible with red filter (550-850 nm), and near infra-red (780-1060 nm) portions of the spectra were analyzed. The HiRISE images were analyzed using both USGS ISIS 3.2 [*USGS,* 2009] and ITT Visual Information Solutions IAS Viewer 3.2.1 [*ITT Visual Inf. Sys.,* 2009]. Only radiometrically calibrated images were used, and no additional dynamic range adjustments were applied to them.

4.3 Photometric and broadband spectral analysis

The diffuse component of light scattered from wet surfaces is reduced by an amount proportional to the inverse of the square of the index of refraction [*Jezek et al*., 1987]. Since the index of refraction of liquid water is larger than that of water ice, liquefaction darkens water substance. Because liquid brines have larger index of refraction than liquid water, they enhance the darkening [*Renno et al.*, 2009]. Scattering is reduced because changing the medium covering the surface from air to water decreases the relative index of refraction between the surface and its surroundings. This increases forward scattering and produces reflections at the liquid-air interface, causing the wet

surface to absorb more light than the dry [*Lekner et al.*,1988; *Twomey et al.*, 1986]. These effects have been studied extensively in sea ice (a mixture of ice, brines, and salts) because changes in its albedo play an important role on climate [*Perovich et al.*, 1996]. The albedo of sea ice decreases when it starts to melt in the summer, causing increases in the absorption of solar radiation that accelerates the melting [*Perovich et al.*, 1996]. Simple quantitative relationships between the physical and optical properties of sea ice do not exist. However, it is well established that spectral variations in the optical properties of sea ice are dominated by absorption [*Perovich et al.*, 1996]. Because ice is highly scattering, its reflectance is approximately constant with wavelength. On the contrary, the reflectance of sea ice with melt (brine) ponds decreases strongly with wavelength (Fig. 4.1) [*Perovich et al.*, 1996]. Except for an increase of the order of 30% at the angle of reflection of the solar beam, the reflectance of sea ice is approximately constant in all directions (it is Lambertian) [*Perovich et al.*, 1996]. Therefore, the albedo of sea ice is approximately equal to its reflectance.

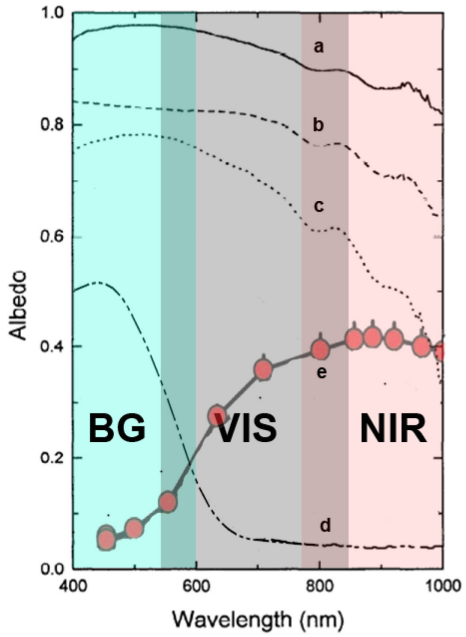

Figure 4.1. Albedo of ice, frost/snow, liquid water/brines and Mars soil as a function of wavelength. Albedo of (a) snow-covered sea ice [*Perovich*, 1996], (b) glazed-snow over sea ice [*Perovich*, 1996] , (c) bare sea ice [*Perovich*, 1996], (d) melt ponds [*Perovich*, 1996] , and (e) Mars polar soil [*Smith et al.*, 2009], . The colors represent HiRISE blue-green (BG), visible (VIS), and near-infrared (NIR) spectral bands [*Delamere et al.*, 1996].

A schematic diagram of the relationship between the physical conditions of sea ice and its albedo in the visible portion (400-750 nm) of the spectrum is shown in Figure

4.2. Measurements between the blue green (400-600 nm) and near infrared (780-1060 nm) portions of the spectrum show that the albedo of glazed ice and snow covered ice is approximately constant with wavelength and that the albedo of melt ponds in sea ice peaks at approximately 400-500 nm and decreases by almost an order of magnitude beyond 600 nm (Fig. 4.1). The albedo of snow covered sea ice (snow or frost covered soils on Mars) and melts ponds (liquid brines on Mars) at various portions of the spectrum, at which images from Mars are available, can be used to fingerprint liquid brines because it distinguishes them from frost/snow, ice and soil (Table 4.2) [*Perovich et al.*, 1996; *Smith et al.*, 2009].

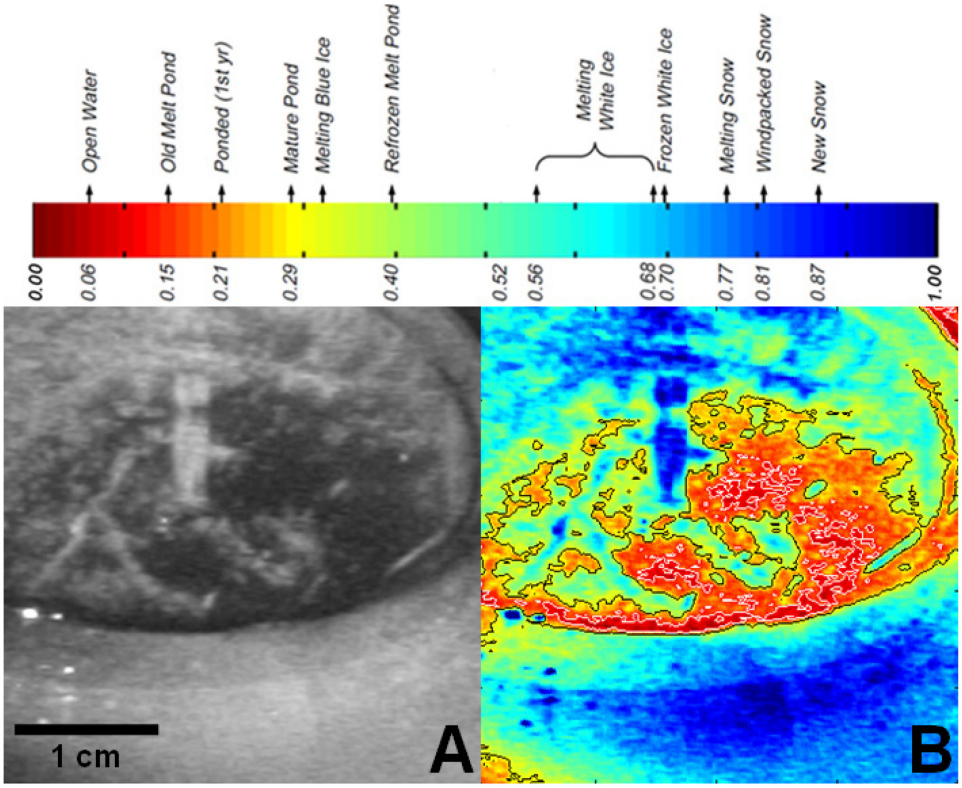

Figure 4.2. Photometric relationship between the albedo and the physical conditions of brines. (Top) Schematic diagram of the relationship between the albedo and the physical condition of sea ice. It shows that albedo (in the visible) smaller than ~0.3 indicates the presence of the liquid phase (Fig. 4.1). This color scale is used in all photometric analysis of this article. (A) Image of a sample of sodium perchlorate brine in a laboratory chamber at Mars conditions (Table 4.1) [*Zorzano et al.*, 2009]. The bright area inside the sample holder is a mixture of ice and frozen brine, the dark area is liquid brine, and the bright area outside the sample holder is frost [*Zorzano et al.*, 1996]. (B) Albedo calculated with Eqn (4.5), from the image on the left. Isolines at 0.1 are in white and at 0.3 in black. Frost and frozen brines have high albedo (similar to fresh or new snow) and areas containing liquid brines have albedo smaller than 0.3. Albedo uncertainties are ~10% (Section 4.5).

Material	Spectral Window	Wavelength (nm)	Mean albedo
Frost/Snow	Blue-Green (BG)	400 – 600	0.9
Melt Pond			0.4
Mars Soil			0.08
Frost/Snow	Visible (VIS)	550 – 850	0.9
Melt Pond			0.1
Mars Soil			0.3
Frost/Snow	Near Infra-red (NIR)	780-1060	0.75
Melt Pond			0.05
Mars Soil			0.4

Table 4.2. Mean albedo of snow-covered sea ice (frost/snow) [*Perovich*, 1996], melt pond on sea ice (melt pond) [*Perovich*, 1996], and Mars polar soil (Mars soil) [*Smith et al.*, 2009], on the blue-green, visible with red-filter, and near infra-red portions of the spectra. The mean albedo values are calculated from the data presented in Fig. 4.1.

Images of brines from the studies described in Table 4.1 are analyzed by finding the brightest pixels indicating ice, the darkest pixels on shadows indicating reflected radiance $I_\lambda \cong 0$, and by adjusting the reflectance of each pixel [*Smith et al*., 2005] as

$$R = R_{ice}\frac{DN - DN_{dark}}{DN_{ice} - DN_{dark}},$$

(shown in Eq. 4.5) where R_{ice} is the reflectance of ice measured in the laboratory (Table 4.3) [*Clark et al*., 1981]. We refer to the resulting images as reflectance adjusted images, or simply "albedo images."

Spectral Window (λ)	HiRISE	Phoenix RAC & Lab Experiment
Blue – Green (BG)	1.00 – 0.90	--
Visible (VIS)	0.95 – 0.85	0.95 – 0.85
Near – infrared (NIR)	0.95 – 0.70	--

Table 4.3. Reflectance of water frost (R_λ^{ice}) at martian conditions at the spectral windows [*Clark*, 1981] of the images analyzed in this letter. The range of values covers possible frost grain sizes [*Clark*, 1981; *Painter et al.,* 1998].

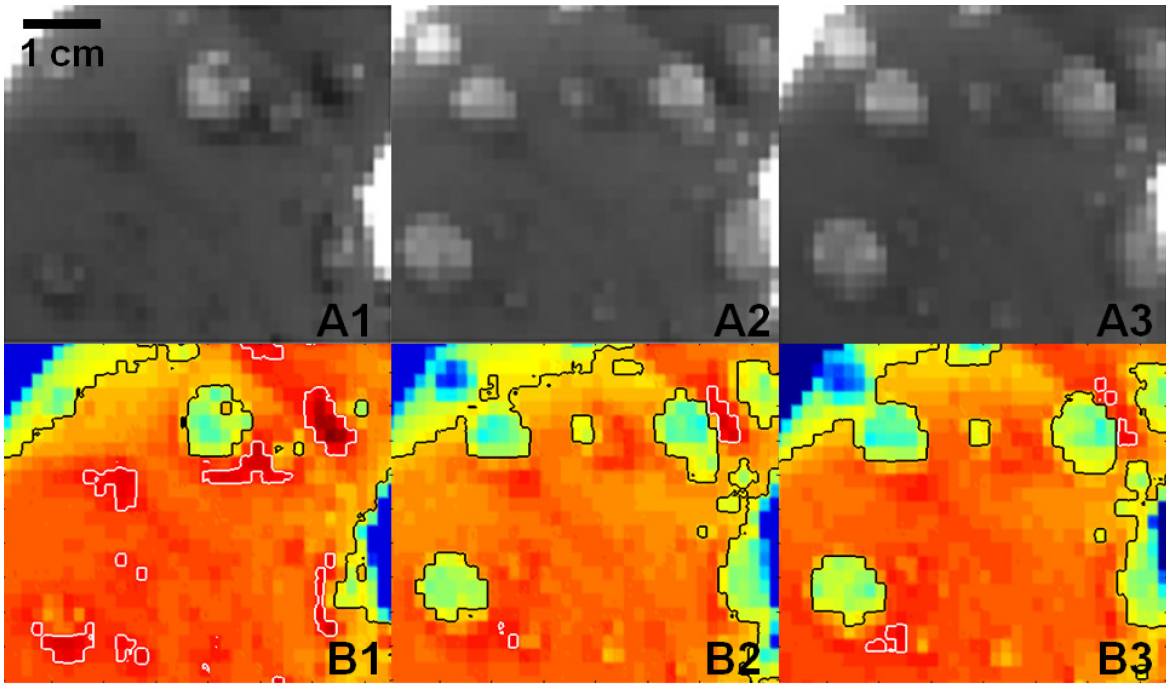

Figure 4.3. Photometric analysis of images of spheroids on a strut of the Phoenix Lander. (A1-A3) Raw images (Table 4.1) of spheroids on a strut of the Phoenix Lander on martian days or Sols 8 (A1), 31 (A2) and 44 (A3) [*Renno et al.*, 2009]. *Courtesy of NASA/JPL-Caltech/U. of Arizona/Max Planck Inst.* (B1-B3) Albedo of the images A1-A3 with isolines at 0.1 in white and 0.3 in black. The color code presented in Fig. 4.2 is used here. The white isolines enclose areas of low albedo associated with growth and motion of spheroids, suggesting deliquescence. None of the spheroids have albedo high enough to correspond to frost. The spheroids albedo values indicate the presence of both liquid phase (albedo ~0.1) and refrozen liquid (albedo ~0.45).

Comparison of images of brines at Mars laboratory conditions and the schematic diagram at the top of Figure 4.2 indicates that the knowledge acquired in studies of terrestrial sea ice can be used to search for liquid brines on Mars, even when only images at visible wavelengths are available. Indeed, it indicates that significant amounts of liquid brines decrease the albedo of ice (frost or snow) and martian soils to values below 0.3, and that albedo smaller than 0.1 indicates areas dominated by the liquid phase. It has been argued that the darkening of spheroids on a strut of the Phoenix Lander indicates melting [*Renno et al.*, 2009]. Figure 4.3 shows quantitative photometric evidence that the Phoenix spheroids are composed of liquid saline water. It shows that the area of the Phoenix strut where a spheroid appears to liquefy and drip [*Renno et al.*, 2009] has the low albedo of liquid brines. The albedo of other areas where spheroids grow is similarly low, supporting the idea that they grow and move by deliquescence. Both spheroid darkening (melting) and spheroid growth near dark albedo regions (<0.1) can be seen. This growth rate is also analytically predicted by the deliquescence process. These

spheroids are also observed and measured to either stop growing or shrink towards the end of the mission where the atmospheric temperatures are much colder. This is caused by dilution of the spheroids which leads to both freezing and sublimation. The quantitative photometric analysis here presented adds to the physical and thermodynamical evidence for liquid saline water discovered by Phoenix.

It is highly unlikely that these spheroids are dominated by polar soil or frost. Polar soil exhibits a much higher albedo of ~0.25 to ~0.3 due to a large fraction of atmospheric dust and they would not show large changes in albedo as a function of time or the observed spheroid dynamics described above. Although thermodynamics does not support that these spheroids are dominated by frost, we further show that they have moderate to low albedo, are spherical in shape and are more importantly highly localized. Frost is bright ice crystals which form from solid deposition of atmospheric saturated water vapor on solid surfaces. It can be seen from Figure 4.4 that surface frost at martian conditions exhibits high and uniform albedo along the sample holder. This also shows good agreement with both the optical and physical behavior of frost/snow in terrestrial and martian environments (Phoenix Landing Site) [*Searls et al.,* 2009].

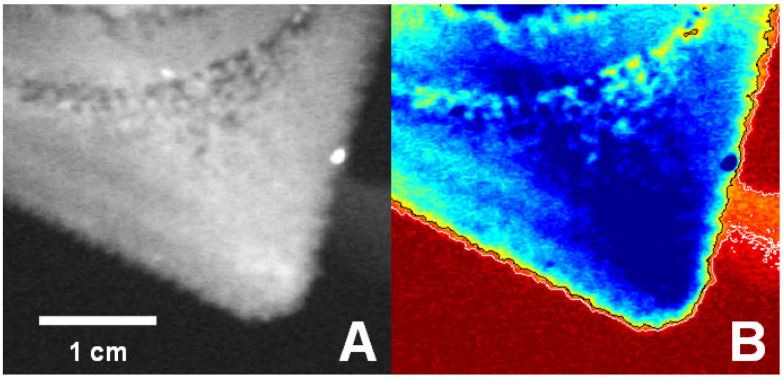

Figure 4.4. Photometric analysis of a laboratory image of frost at visible wavelengths. Photometric analysis of new frost evenly deposited along the sample holder of laboratory experiments at Mars conditions (Table 4.1) [*Zorzano et al.,* 2009]. It indicates that new frost that never melted has albedo > 0.8. If the Phoenix spheroids were frost, they would have similarly high and uniform albedo values. Ice with lower albedo indicates that it is refrozen.

Figure 4.5 images of isocontour albedo profiles further support that deliquescence was responsible for the growth and movement of these spheroids. Higher albedo gradients show higher concentration of pixel filling. Hence, these images adequately separate the spheroids and dark albedo regions from the uniform, low gradient, albedo of the lander strut.

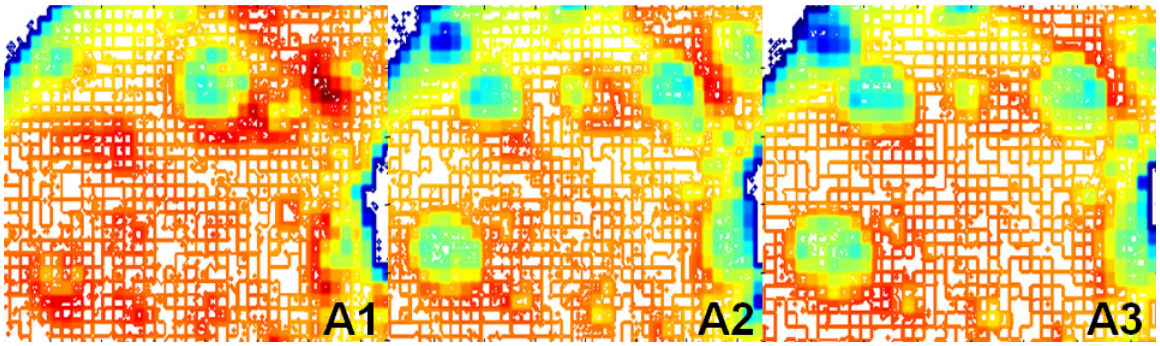

Figure 4.5. Albedo isocontour images of spheroids on a strut of the Phoenix Lander (A1-A3). The colorscale in Fig. 4.2 is used. Higher filled regions depict higher albedo gradients and lower filled regions depict lower albedo gradients.

Material	η
Melt Ponds	-8 to -6
Frost/Snow	-1.5 to 0
Mars Soil	0.5 to 1

Table 4.4. Broadband spectral signature of frost/snow [*Perovich*, 1996], melt ponds [*Perovich*, 1996], and Mars soil [*Smith et al.*, 2009; *McCord and Elias*, 1971], . The calculations of η and their uncertainties are discussed in Section 4.5.

Table 4.4 indicates that the broadband spectral parameter

$$\eta \equiv \frac{a_{NIR} - a_{BG}}{a_{NIR}}, \tag{4.6}$$

where a_{NIR} and a_{BG} are the albedo at near-infrared (NIR) and blue-green (BG), can be used to distinguish liquid brines from frost/snow and soil. Indeed, $\eta \cong$ -6 to -8 would be a fingerprint of liquid brines because none of the substances likely to be present on the martian surface have this low value.

Figure 4.6 shows the spectral fingerprint of liquid brines on pond-like and flow-like features on polar dunes starting to defrost in the spring [*Kereszturi et al.*, 2009; *Mohlmann et al.*, 2010] (Figs. 4.7 and 4.8 show photometric evidence for liquid brines in this and nearby areas), confirming suggestions that significant amounts of liquid saline water form seasonally on Mars surface [*Kereszturi et al.*, 2009; *Mohlmann et al.*, 2010]. As expected, the flow front is dominated by liquid. Furthermore, it can be seen from Figure 4.7 that the slow moving and narrow dark albedo front abruptly terminates at L_s= 238°. This is an important result, because debris flows due to dry-ice evaporation leads to fan-shaped formations at the down slope regions [*Blair and McPherson*, 1994]. Possibly,

the components within the dark albedo region are either being absorbed by the surface or evaporating into the atmosphere. Our analysis also indicates the presence of bulk amounts of liquid brines (Fig. 4.7 A1-A2) that evaporates as it gets warmer, leaving bright salts at the surface (Fig. 4.7 A3-A4). Eqn. (4.5) is applied to each image, and then the value of η is calculated for each pixel. Radiometrically calibrated blue green and near infra-red HiRISE images [*Delamere*, 2010] are used in the analysis. This analysis does not provide details to the depth or concentration of brines in these regions.

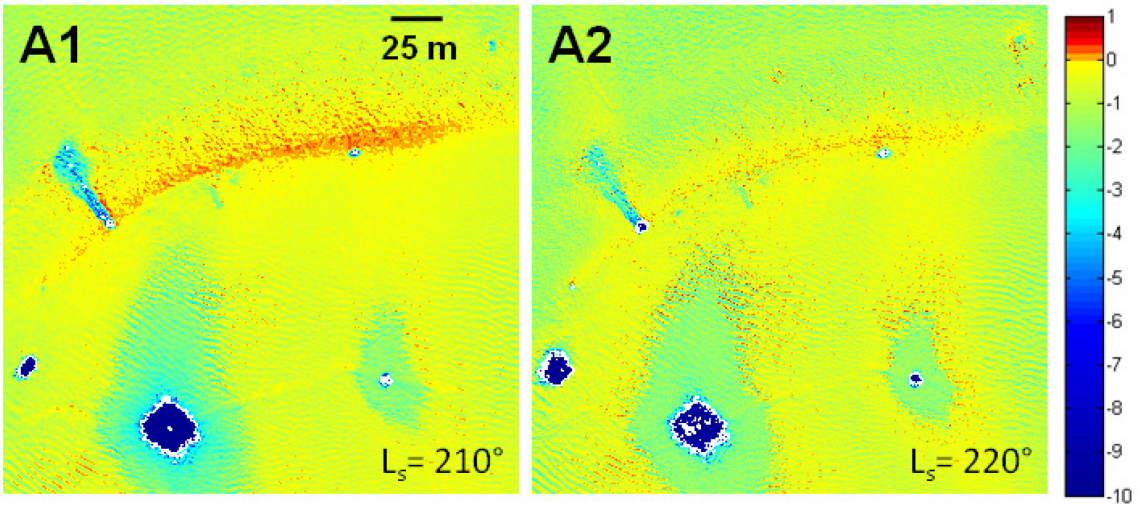

Figure 4.6. Broadband spectral analysis of flow-like and pond-like features on a sand dune on Richardson crater at Mars' south polar region (north is on the right)**.** The image depicts the values of the parameter η, with white isolines at -6 enclosing areas containing liquid brines. As expected from deliquescence, flow-like and pond-like features are surrounded by frost. A combination of frost and soil dominates the rest of the images. The time difference between the two images is 19 Sols. CRISM measurements indicate that water and CO_2 surface frost are present in this area, supporting our analysis. Color images and photometric analysis of this area are presented in Fig. 4.8.

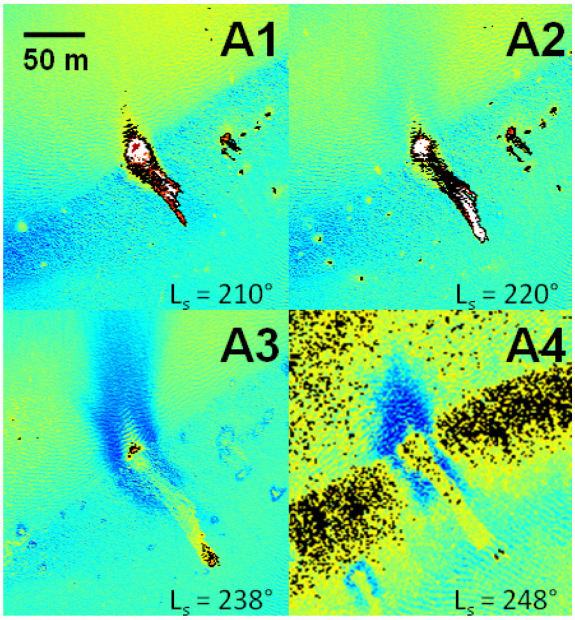

Figure 4.7. Photometric analysis of images (in the visible) of flow on a slope (north is on the right) of Richardson crater at Mars south polar region [*Kereszturi et al.*, 2010; *Kereszturi et al*., 2009; *Mohlmann and Kereszturi*, 2009]. The images span a period of 72 Sols. White isolines at 0.1 indicate areas dominated by the liquid phase. Black isolines enclose areas with albedo 0.3. This does not necessarily indicates the presence of liquid in visible HiRISE images because the images are biased towards red (Table 4.1) and smaller albedo values are necessary to indicate the liquid phase (Fig. 4.2). The color scale shown in Figure 4.2 of the main text is also used in these images. The mean ground temperature at A1, A2, A3 and A4 are 164 K, 185 K, 255 K and 262 K. However, the local temperature at the flow-like features can be higher because the dark flow-like features absorb more solar radiation than the surrounding areas and the deliquescence of many salts is a highly exothermic reaction. It has been suggested that liquid films of water or brines cause these flows [*Kereszturi et al.*, 2010; *Kereszturi et al*., 2009; *Mohlmann and Kereszturi*, 2009].

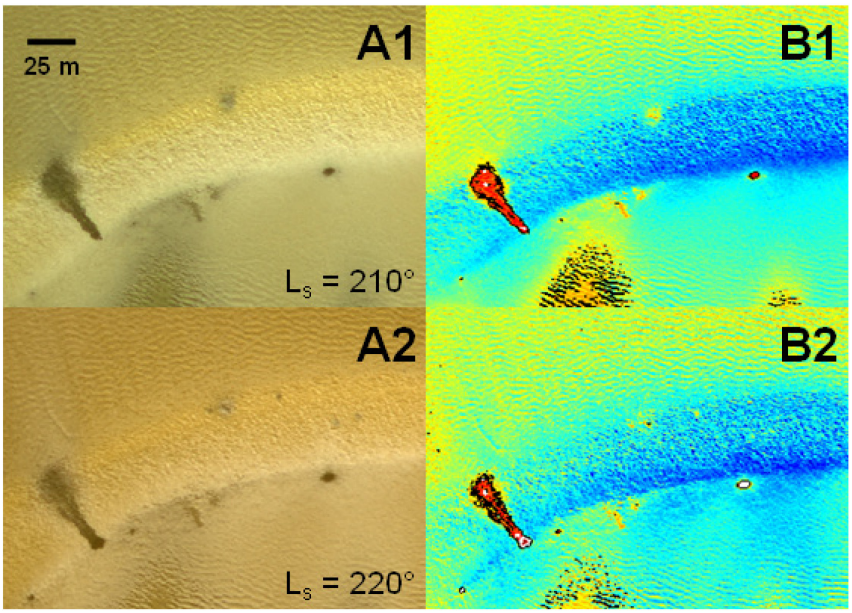

Figure 4.8. Color images and photometric analyses of the flow-like feature shown in Fig. 4.6. *Courtesy of NASA/U. of Arizona/Ball Aerospace.* (Left) False color HiRISE image of the flow-like feature showing that

it is darker than the light-brown sand mainly covered by frost. The image suggests the presence of frost on the dune crest and slope, and this is confirmed by CRISM measurements [*Kereszturi et al.*, 2010]. (Right) Photometric analysis indicates that the flow-like feature has the low albedo of liquid. Isolines at 0.1 in white enclose areas dominated by liquid. Isolines at 0.3 in black does not necessary enclose liquid because HiRISE visible images are biased towards red (Table 4.1) and therefore a smaller albedo value is required to indicate the presence of the liquid phase (Fig. 4.2).

4.4 Deliquescence and the potential for life on Mars

Salts in contact with ice are subject to water vapor pressures equal to that of the saturation value over the ice, and therefore deliquesce if the ice is warmed above the eutectic temperature of their saline solutions. During fall/winter, frost accumulates uniformly on the ground of the polar region. As the ground temperature increases early in the spring, water frost becomes warm enough for some of the salts in contact with it to deliquesce before the frost sublimates. Therefore, deliquescence occurs in frost-covered areas at which the temperature exceeds the eutectic temperature of salts in contact with it, before the frost sublimates. This implies the existence of an optimum zone between the polar cap and mid latitudes where deliquescence occurs seasonally at the surface. The location and extent of this zone is discussed next.

Phoenix found significant amounts of perchlorates, sulfates, sodium, and magnesium ions in the martian soil, likely from magnesium and sodium perchlorate hydrates [*Hecht et al.*, 2009; *Smith P. H. et al.*, 2009; *Kounaves et al.,* 2010]. The deliquescence relative humidity of magnesium perchlorate 8-hydrate is about 0.5 and its eutectic temperature is ~200 K. At this temperature, a water vapor partial pressure of ~0.1 Pa is sufficient to cause deliquescence [*Renno et al.*, 2009]. Humidity measurements and the detection of the formation of fogs and clouds at temperatures of ~210 K indicate that the mean diurnal value of the water vapor pressure at the Phoenix landing site was ~1 Pa. This is further corroborated by observing sublimation of the extensively exposed water ice table below the lander ("Holy Cow") which is near the landing strut of interest. This value is consistent with satellite measurements indicating total atmospheric column water vapor of ~50 pr-μm if the water vapor is assumed to be well mixed in the planetary boundary layer [*Whiteway et al.*, 2009]. Thus, deliquescence of magnesium perchlorate can occur in areas of the polar region at which the peak ground temperature reaches values between 200 K and 210 K. Since the efflorescence temperature can be substantially lower than the eutectic temperature [*Renno et al.*, 2009], the hydration of

perchlorate is an exothermic reaction, and local (e.g., inside valleys and depressions such as craters) humidity values can be larger than regional, liquid water can be present poleward of the 200 K maximum ground temperature isotherm and equatorward of the 210 K isotherm.

Deliquescence is also likely to occur in the shallow subsurface of Mars, where salts and ice are present and the temperature exceeds the eutectic value, because the topsoil would inhibit sublimation. Therefore, liquid brines should be common on Mars. This testable hypothesis has important implications for the habitability of Mars because microbes thrive in terrestrial brines [*Boetius et al.*, 2009; *Mikucki et al.*, 2009; *Junge et al.*, 2001]. Traces of methane and formaldehyde discovered in the martian atmosphere could be the products of microbial reactions, such as methanogenesis and incomplete oxidation of methane [*Moran et al.*, 2005]. Analyses of martian soil samples indicate the presence of calcium carbonate, possibly magnesium carbonate, iron oxyhydroxides, smectites, iron sulfate, magnesium sulfate, and serpentine. Together with the evidence for liquid brines, this suggests that Mars could be habitable today.

To continue this search for liquid brines on Mars, more in-depth multi-spectral analyses of the polar regions should be done. Cross correlation between HiRISE and CRISM spectra data can provide further support to these findings and improve the accuracy. Instruments that can detect liquid phases with very high sensitivity should be incorporated in future missions to regions between the polar caps and mid-latitudes of Mars.

4.5 Error analysis

The error or uncertainty in the reflectance calculation is estimated by differentiating Eqn (4.5). Neglecting the smallest terms, we find that the error is

$$\delta R_\lambda \sim R_\lambda^{ice}\left(\frac{\delta DN_{dark}}{DN_{ice}-DN_{dark}}\right). \qquad (4.7)$$

It follows from the DN_{dark} and DN_{ice} values of each image analyzed in this Chapter that the uncertainty of the reflectance calculation is at most $\delta R_\lambda / R_\lambda \sim$ 10% for all images, except the HiRISE blue-green image that has an error of ~20%. Other important sources of errors are the assumptions that $I_\lambda \cong 0$ on the darkest pixels on shadows, and that $R_\lambda^{dark} \cong 0$. We estimate that these assumptions produce errors much smaller than ~10%. This estimation is based on the fact that the darkest shadows have a fraction of the brightness of liquid brines, which according to Figure 4.2 have albedo or reflectance of ~0.1. Therefore, the overall uncertainty of the reflectivity analysis is ~10%.

The error in the calculation of the broadband spectral parameter defined by Eqn (4.6) of the main text can be estimated by differentiating it. Neglecting the smallest terms, we find that the error is

$$\delta\eta \sim \frac{\delta a_{NIR}}{a_{NIR}} + \frac{\delta a_{BG}}{a_{NIR}} . \qquad (4.8)$$

Since $a_\lambda \cong R_\lambda$, it follows from Eqn (4.7) that $\delta\eta/\eta \sim 20\%$.

4.6 Spacecraft images used

The images of the Phoenix spheroids and the laboratory experiments used in this Chapter are full resolution raw images. The RAC raw monochromatic images are obtained from the Max Planck Institute for Solar System Research, Lindau, Germany. The HiRISE images are radiometrically calibrated images downloaded from the NASA Planetary Data System (PDS). Figures 4.6 and 4.8 uses HiRISE color images PSP_003175_1080.COLOR.JP2 and PSP_003386_1080.COLOR.JP2, and visible with red filter images PSP_003175_1080.RED.JP2 and PSP_003386_1080.RED.JP2. Figure 4.7 uses HiRISE images number PSP_003175_1080, PSP_003386_1080, PSP_003742_1080, and PSP_003953_1080.

CHAPTER 5

Summary

This dissertation provides a detailed exploratory study of supersonic plume-surface interactions and its applications to engineering and planetary science. We divide the problem into three steps by investigating: (i) the flow physics of jets impinging on impermeable surfaces, discussed in Chapter 2; (ii) jet-induced cratering dynamics within granular systems, discussed in Chapter 3; and (iii) the discovery of water on Mars, discussed in both Chapters 3 and 4. The physics of supersonic jet interactions, in particular pulsed jets, with both impermeable surfaces and granular systems is discussed in detail by analyzing results from theoretical calculations, laboratory experiments and numerical simulations. These results uncovered three unique processes: (i) plate shock dynamics due to pulsed jets, (ii) diffusive gas explosive erosion and (iii) deliquescence on Mars. The main highlights of this research were the discovery of a new erosion process, named "explosive erosion", the accurate predictions of erosion at the Phoenix landing site, and the discovery of liquid saline water on present-day Mars. Photometric and broadband spectral analysis using data from both the MRO HiRISE camera and the Phoenix RAC and SSI cameras were used to confirm these findings. Our experimental and numerical results were used by NASA to assess the risks associated with the landing phases of both the Phoenix and Mars Science Laboratory missions. Moreover, they enabled the Phoenix science team to determine the contamination of its landing site. This study is only the first step into investigations of granular flow physics in extreme environments and the search for liquid brines on present-day Mars.

Although much of the future work has been discussed within each individual chapter, the need for further studies of jet-induced soil erosion in various planetary

environments is overwhelming. The behavior of granular media is quite different in these extreme conditions, low atmospheric and gravitational regimes. It is critical to understand for the development of landing and launching architectures, propulsion systems and sample acquisition systems, for survivability of crew and spacecraft and to further planetary science. This area of research can significantly benefit from NASA's future proposed plan for robotic space exploration with emphasis in technology development.

The discovery of evidence for liquid brines as presented in Chapter 4 and the confirmation of water ice on the northern polar region as discussed in Chapter 3 has made a strong case for liquid water to sporadically exist on Mars. These discoveries have recently led to many other investigations that support the existence of liquid brines on Mars [*Kereszturi et al.*, 2009; *Mohlmann et al.,* 2010a; *Mohlmann et al*., 2010b; *Davila et al*., 2010]. These findings in conjunction with methane emissions from the martian surface [*Mumma et al*., 2003] have excited the public and made a viable case for astrobiological microbial life.

APPENDICES

APPENDIX A

Underexpanded supersonic plume surface interactions: applications for spacecraft landings on planetary bodies

A.1 Introduction

Supersonic jet interactions with the ground or flat surface are a complex fluid dynamics problem with many nonlinearities. These nonlinearities arise from shock-wave surface interactions, stagnation bubble formation and the propagation of wall jets along the surface. Lamont and Hunt [1980] studied the flow field and surface interactions due to axisymmetric underexpanded supersonic nitrogen jets at distances between one and three nozzle exit diameters. Steady state numerical simulations, conducted by Wu et al [2002] at these distances, show good agreement with Lamont and Hunt's experimental results. Most of literature concentrates on studies where the nozzle pressure ratios (NPR) are below 10 [*Lamont and Hunt*, 1980; *Carling*, 1974]. NPR is the ratio of nozzle chamber pressure to ambient pressure.

By applying Schlieren imaging and ground pressure sensors along with numerical simulations, important shock structures such as the plate shock and stagnation bubble were identified. A plate shock is a reflected and detached shock wave from a surface due to the impingement of a supersonic jet [*Lamont and Hunt*, 1980] and this is observed in many applications such as solar wind forming a curved bow shock reflection from the Earth's surface [*Vergin et al*., 2001] to a planar bow shock formed during an Apollo capsule reentry into the Earth's atmosphere [*Mehta*, 2008]. Stagnation bubble (recirculation zones) can form below the plate shock and has only recently received more attention due to its effects on acoustic noise production [*Henderson et al*, 2005; *Carling and Hunt*, 1974]. The third structure of importance is the propagating wall jet which can reach supersonic speeds, demonstrate compression and expansion regimes and decay as a function of axial distance from the impingement point [*Carling and Hunt*, 1974]. These flow features are within the far-field or shock wave interaction regime, and are considerably different than the flow structures observed in the near-field regime.

The near-field regime is within the first nozzle exit diameter from the nozzle exit plane. Near-field supersonic jet characteristics are dependent on the nozzle chamber stagnation pressure, nozzle area ratio and atmospheric pressure as discussed in Section 2.6.1. There are three types of flow characteristics which are first observed at this regime: overexpansion, underexpansion and perfect expansion of the jet [*Scroggs and Settles*, 1996]. All three flow characteristics which are described in more detail in Section 2.6.1 are observed when rockets launch into space and as discussed in this Appendix lead to different far-field surface interactions.

The main focus of this study is to investigate the flow physics of plume ground interactions from exhaust plumes of rocket motor engines during planetary landings, specifically for environments of Mars. For appropriate simulations, this requires different flow requirements than observed for past studies conducted by Lamont and Hunt [1974], Krothapalli et a [1999], Henderson et al. [2005] and other researchers focused on the acoustic nature of impinging jets. Rocket plumes exhausting into near-vacuum planetary environments demonstrate higher exit Mach numbers on the order Mach ~5 with nozzle pressure ratios greater than 1000, an order three times larger in magnitude for those observed in acoustic studies [*Henderson et al*., 2005]. Rocket plumes interact with the surface at much higher altitudes between ~100d and ~5d, where d is the nozzle exit diameter [*Clark*, 1971], to decelerate the spacecraft and to ensure a successful soft landing. In contrast to previous studies, all of our tests were conducted at reduced atmospheric pressures which spanned from the martian to terrestrial environments. The largest difference between previous jet impingement studies is the engine mode can be either pulsed or steady during landings and attitude corrections (Chapter 2). Comparative studies between these two modes are limited.

This Appendix will look at numerical and experimental ground interaction data between pulsed and steady underexpanded supersonic jets exhausting from simulated Phoenix Rocket Engine Module (REM) and Mars Science Laboratory Main Landing Engine (MLE) nozzles. More importantly, this Appendix will focus on these interactions associated with jets exhausting from high altitudes of $h > 20d$. We will then compare our experimental sub-scale temporal and spatial results with numerical simulations at full-scale to provide further insight in the complex flow physics and to ascertain the reliability

of our scaling laws. This study was performed to reduce mission risk for both of NASA's recent Mars missions.

A.2 Scaling Laws

To adequately simulate room-temperature underexpanded supersonic gas jets and satisfy the flow physics and shock structure of rocket plume impingement, scaling laws are necessary to develop. Although derived and first introduced in Section 2.6.2.2, here we provide further insight into these parameters. These scaling relations can be applied to various experimental tests performed in understanding rocket plume effects on soil erosion and flat surface features. The first parameter is the exit Mach number ($M_e = U_e/a_e$) of the plume where U_e and a_e are the jet velocity and sound speed, respectively. This parameter is a function of the nozzle area ratio and specific heat ratio of the propellant. The exit Mach number determines the compressibility flow regime, the strength of the shock structure and influences the supersonic core length [*Scroggs and Settles*, 1996]. Given the nozzle area expansion ratio, the exit Mach number is calculated from the 1-D isentropic area-Mach relation (Eqn. A1). The second scaling law is the hypersonic similarity parameter (Eqn. A2), which is the ratio of kinetic (*KE*) to internal energy (*IE*) of the plume, determines the specific energy density of the plume. The derivation of this scaling law is presented from basic calorically perfect thermodynamics (Eqns. 2.14-2.19, Chapter 2). The third parameter is the jet expansion ratio (ϵ), which is the ratio of the plume exit pressure to the ambient pressure (Eqn. A3), and this parameter determines the near-field flow physics and expansion of the exhausting jet. This parameter is derived from considering the ratio of pressure forces between the exhaust plume and atmosphere at the nozzle exit. For $\epsilon < 1$, the jet is over-expanded and for $\epsilon > 1$, the jet is underexpanded which also directly corresponds to the expansion angle of the jet boundary with respect to the normal [*Clark*, 1971]. For $\epsilon = 1$, the jet is perfectly expanded which rarely occurs in our applications due to changing atmospheric pressures during launch and landings of rockets and spacecrafts. The fourth parameter is the Reynolds number of the jet (Eqn. A4), which is determined from its nozzle exit conditions. This is the ratio of inertial to viscous forces that determines the flow regime. Most rocket plumes and supersonic jets are within the turbulent regime. The fifth

parameter is the Strouhal number, which is the ratio of the inertial force associated with unsteady flow characteristics to the inertial force due to the velocity gradient (Eqn. A5). This nondimensional number is applied for pulsed jets [*Chotaupalli et al*., 2009]. These parameters for both the full-scale and subscale analysis are tabulated in Table A1. The dimensional quantities used to calculate these scaling parameters are tabulated in Table A2. We will discuss how these various parameters, in particular the jet expansion ratio and Strouhal number, change the flow physics at the far-field/interaction regime. The following scaling laws (Eqns. A2-A5) theoretically define the plume structure and ground interactions:

$$\frac{A_e}{A^*} = \left(\frac{\gamma+1}{2}\right)^{-\frac{(\gamma+1)}{2(\gamma-1)}} \frac{\left(1+M_e{}^2\right)^{\frac{\gamma+1}{2(\gamma-1)}}}{M_e} \qquad \text{(A1)}$$

$$\frac{KE}{IE} = \frac{1}{2}\gamma(\gamma-1)M_e{}^2 \qquad \text{(A2)}$$

$$e = \frac{P_e A_e}{P_{amb} A_e} = \frac{P_e}{P_{amb}} \qquad \text{(A3)}$$

$$\mathrm{Re} = \frac{\rho D U_e}{\mu} \qquad \text{(A4)}$$

$$\mathrm{St} = \frac{fD}{U_e} \qquad \text{(A5)}$$

Where γ is the specific heat ratio of the propellant, P_e and P_{amb} are nozzle exit and atmospheric pressures, U_e is the jet velocity at the nozzle exit, D or d is the nozzle exit diameter, A_e and A_* are the nozzle exit area and throat area, m is the molecular mass of the exhaust products, T_e is the exhaust temperature at the nozzle exit, C_p and C_v are the constant pressure and volume specific heats of the plume, R is the plume gas constant, μ is the jet viscosity and ρ is the jet density, and f is the pulse frequency.

		MSL MLE		Phoenix REM	
		¼ scale	full-scale	½ scale	full-scale
Hypersonic similarity	k	14.8	14.0	12.7	11.4
Jet expansion ratio	e	2.9 – 2.1 - exp 3.5 - num	6.8 – 2.2 - flt 6.8 – 4.1 - num	~4.4 - exp 4.5 - num	3.8 - flt 4.7 – num
Reynolds Number	Re	24.5 – 14.7 x 10^5 -exp 23.3 x 10^5 - num	8.4 – 5.0 x 10^5 - flt	12.7 x 10^5	3.4 x 10^5
Mach Number	M_e	5.14	5.08	4.77	4.67
Strouhal Number	St	0	0	4.4 x 10^{-4}	3.3 x 10^{-4}

Table A1. Scaling parameters; exp-experiment; num-numerical simulation; flt-spaceflight conditions

		Phoenix REM:100% throttle		MSL MLE:100% throttle	
		½ scale	full-scale	¼ scale	full-scale
Min area (m^2)	A^*	3.83 x 10^{-5}	15.3 x 10^{-5}	6.9 x 10^{-5}	110.3 x 10^{-5}
Exit area (m^2)	A_e	0.00079	0.00318	0.00193	0.03089
Expansion ratio	A_e/A^*	20.7	20.7	28.0	28.0
Mass flow rate (kg/s)	$\dot{m}$	0.11	0.16	0.28	1.52
Chamber temp. (K)	T_c	300	1114	300.0	1218.2
Chamber press. (kPa)	P_c	1240	1240	1765	1765
Exit density (kg/m^3)	ρ_e	0.194	0.026	0.202	0.023
Exit pressure (Pa)	P_e	3091	3241	2837	2927
Exit temperature (K)	T_e	54	217	47	202
Exit Mach	M_e	4.8	4.7	5.1	5.1
Exit velocity (m/s)	v_e	713	1929	721	2123
Thrust (N)	F	80	321	206	3313
Time (s)	t	0.75,1.5,3.0	< 2.0	1	~ 6
Pulse frequency (Hz)	f	10	10	N/A	N/A
Pulse width (ms)	PW	~65	55	N/A	N/A
Altitude (m)	h/d	8.4-25	8.4-80	34.5	34.5 – 50.0
Slope (deg)	Φ	0	~0	0.0, 22.5	0.0, 22.5
Specific heat ratio	γ	1.40	1.38	1.40	1.38

TABLE A2. Dimensional parameters.

A.3 Experimental Methods

A.3.1 Jet-ground interactions due to the subscale MSL MLE thruster plumes

The experiments were conducted at NASA Ames Research Center in a 4000 m^3 vacuum test chamber at the Planetary Aeolian Laboratory (PAL) which is directed by Arizona State University. The vacuum chamber has a height of 30 m and a diameter of ~15 m and it can be evacuated to 350 Pa by a steam ejector driven vacuum system. The chamber was backfilled with air for all tests conducted. Its' average temperature was approximately 280 K with an average relative humidity of 5-10%. For our tests, we varied the atmospheric pressure within the vacuum chamber between 0.7 kPa and 101.3

kPa. Due to the steam ejectors and large chamber volume, atmospheric pressure and temperature were constant during the entire test duration.

Dry nitrogen flows from the 14 MPa high pressure supply cylinder which is controlled by a regulator to two reservoir tanks in parallel that are set to a specified total pressure dependent on the throttle levels to be simulated (Fig. A1). The total pressure in the reservoir tanks are set to ~1850 kPa for 100% MLE throttle setting. The other two settings used are 60% and 30% throttle. To minimize the loss of total pressure as a function of time, the regulator supplies the needed flow rate to prevent premature choking (Fig. A1). We can remotely set the controls for operating the jet such as duration, pulse width, pulse frequency and total pressure within the nozzle chamber (P_c). The flow then passes through a solenoid valve, which is remotely activated, and into a converging-diverging nozzle. The solenoid valve and propellant system performance was tested to ensure a relatively constant P_c that simulates the profiles from the MLE hot-fire tests. A schematic of the experimental setup is shown in Figure A1.

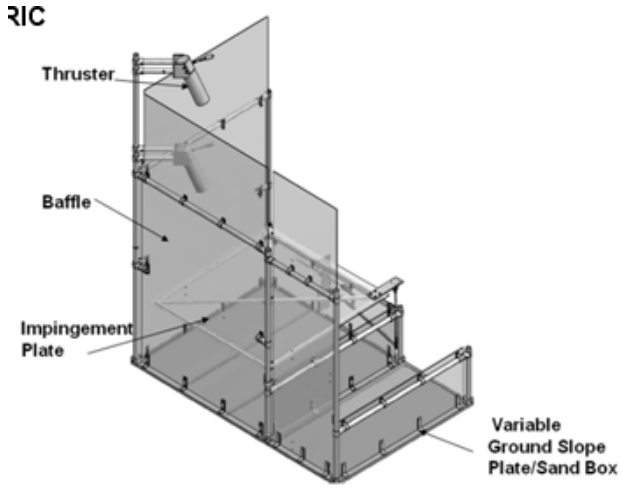

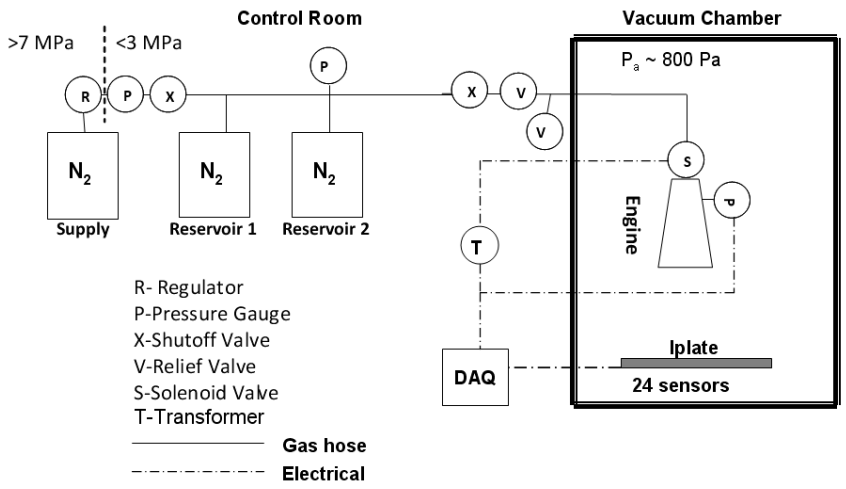

Figure A1 . Isometric view (top) and general plumbing and electrical schematic (bottom) of MSL MLE plume impingement test setup at the NASA Ames Research Center.

A converging-diverging nozzle with an area ratio of 28 was used to match the nozzle contours on the main landing engines (MLE) of the Mars Science Laboratory (MSL) Descent Stage spacecraft [*Sengupta et al*., 2009]. The subscale nozzle was canted to 22.5º to accurately simulate the nozzle orientation and configuration on the MSL Descent Stage (Fig. A2). The experimental nozzle is ¼ scale of the MLE flight system with an exit Mach number of 5. The parameters that we varied are the nozzle pressure ratio (NPR) or the jet expansion ratio (e), and ground slope. The NPR ranged from 12 to 1200 and the jet expansion ratio spanned between 0.02 and 3.00. The MLE simulations are operated at an altitude of 35*d* with ground slopes of 0º and 22.5º. The test matrix is included in Table A3. This simulates the lowest altitude the MSL descent stage approaches the surface prior to separation of the MSL rover [*Sengupta et al*., 2009]. Other important nozzle and test specifications, such as area ratio, exit diameter, etc are tabulated in Table A2. The exhausting jet impinges onto a 1.2 m x 1.8 m aluminum plate (iplate) of which 24 surficial fast responsive piezoresistive pressure sensors are located (Fig. A1). These sensors are then recorded at 1 kHz by a simultaneous sampling data acquisition system. These pressure sensors are scattered in high concentration near the expected impingement point, denoted as an "x", with lower concentration outward from this point. The ground pressure contour plots use linear interpolation between sensor data points. The stagnation pressure within the inlet nozzle chamber (P_c) is recorded by a fast responsive pressure transducer at 1 kHz.

Test	Atmos.(Pa)	Ground (deg)	Height (m)	Throttle Level (%)
1	800	0.0	1.73	60.00
2	733	0.0	1.73	60.00
3	933	0.0	1.73	100.00
4	1470	0.0	1.73	100.00
5	1530	22.5	1.73	96.67
6	1610	22.5	1.73	91.67
7	1730	22.5	1.73	86.67
8	1730	22.5	1.73	80.00
9	1800	22.5	1.73	73.33
10	1840	22.5	1.73	68.33
11	1870	22.5	1.73	63.16
12	1880	22.5	1.73	56.84
13	1930	22.5	1.73	53.68
14	2000	22.5	1.73	47.37
15	2000	22.5	1.73	44.21
16	2030	22.5	1.73	41.05
17	2070	22.5	1.73	37.89
18	2110	22.5	1.73	34.74
19	2470	1.9	1.73	31.58
20	2530	1.9	1.73	28.42
21	101325	22.5	1.73	100.00
22	101325	0.0	1.73	100.00

Table A3. Test Matrix

Two transparent baffle planes at 90º as seen in Figure A1 (Plexiglass) are used in our experiments to simulate the effects of the outboard thrusters shown in Figure A2 as done for the Phoenix-based experiments [*Romine et al.*, 1973; *Huseman and Bomba*, 2000]. Only one MLE per quadrant is firing during descent. The jets from symmetrically opposing thrusters stagnate at the midline between the two engines. These planes were also used to minimize the complexity of the experiment.

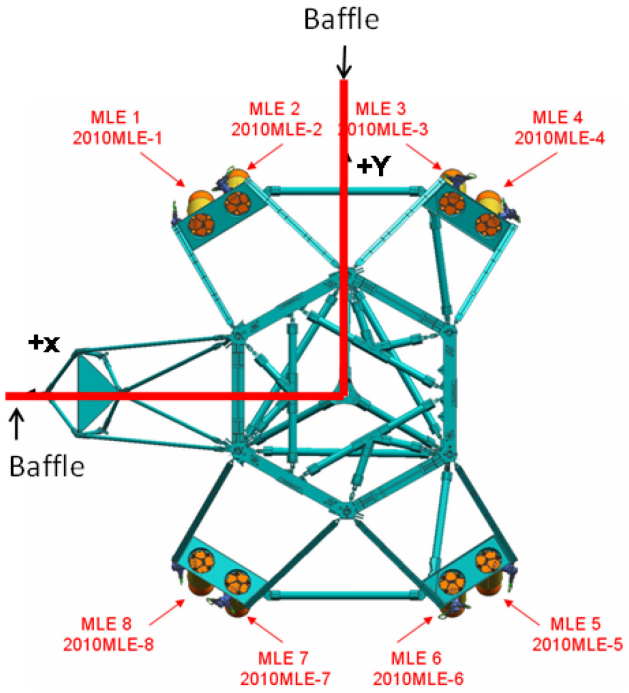

Figure A2.Top-down schematic of the Mars Science Laboratory Descent Stage with superimposed baffles to simulate outboard thrusters as implemented in experimental testbed. *Courtesy of NASA/JPL-Caltech*

A.3.2 Jet-ground interactions due to the subscale Phoenix REM thruster plumes

For the full-scale and subscale Phoenix REM nozzles, the jets were pulsed with similar initial conditions described in Table A2. Although during Phoenix descent, where twelve engines were firing, we used a single nozzle to validate the numerical solutions at University of Michigan. The plume interactions with the surface at a 0º slope for the Phoenix spacecraft lasted less than 2 s which decreased in altitude from ~60*d* to 8.4*d*, touchdown altitude (as discussed in Section 3.8) [*Desai et al.*, 2009]. The parameters that we varied were the jet expansion ratio and the altitude from 8.4*d* to 25*d*. Similar impingement plate and diagnostic pressure sensors were used as described in the previous section. A more detailed experimental setup for the subscale Phoenix cases is presented in Chapter 2, Section 2.6.2.1.

A.4 Numerical Methods

A.4.1 Jet-ground interactions due to MSL MLE thruster plumes

Computations were carried out using the OVERFLOW 2.1 code, a three-dimensional time-marching implicit code that uses structured overset grid systems

[*Buning*, 1999]. The full Navier-Stokes equations were solved over the entire domain including the nozzle internal flow, where a total temperature, total pressure boundary condition was used to satisfy inlet conditions. Nozzle interior, nozzle enclosure, jet plume, and far-field domain grids of ~12 million cells were generated to encompass the experimental setup with viscous spacing at solid wall surfaces. A shear stress turbulence (SST) model with compressibility correction was used for all computations, as it has been shown to preserve jet plume velocity profiles better than other models available in the solver [*Nichols*, 2000]. All simulations for full-scale and sub-scale studies were steady-state solutions.

A.4.2 Jet-ground interactions due to Phoenix REM thruster plumes

Two flow solvers were used to obtain numerical solutions for both full-scale and subscale flow physics of the interaction of the underexpanded supersonic thruster plumes from the Phoenix REM nozzle with the flat surface. Transient and steady-state solutions were developed from these numerical solvers. Both 3-D and axisymmetric solutions were developed. The two numerical codes used were Aerosoft GASP [*Walters et al*., 1990] and ANSYS FLUENT [*ANSYS Inc*., 2009]. GASP was used to model both full-scale and subscale cases.

Transient and steady state Reynolds averaged Navier-Stokes equations were solved by the GASP code, using both axisymmetric and 3-D density based solver. To resolve the shock waves, the Van Leer flux splitting scheme is used which is dissipative and leads to the smearing of shocks [*Van Leer et al.,* 1990]. A Reynolds Stress turbulence model was used. To obtain time accurate results, a dual implicit time stepping derived solution is selected. A single species frozen flow model is assumed. Total pressure and temperature are the inlet boundary conditions and the outlet is a Riemann subsonic inflow/outflow which takes into consideration the potential entrainment of exhaust near the nozzle. The pressure inlet boundary condition for the transient simulations was forced by using test data from both the hot-fire rocket motor tests and cold flow experimental tests. Grid independence is applied to both axisymmetric and 3-d meshes. Internal nozzle flow solution was calculated as well as external to the nozzle. For the 3-d models, a symmetry plane is developed between the pair of thrusters to obtain the solution for a 60°

wedge of the spacecraft [*Huseman and Bomba*, 2000; *Gulick et al*., 2005]. This was done because 180° and 60° wedges showed very similar flow fields and ground pressure results due to the development of stagnation planes formed by the exhaust plume interactions of the two pairs of descent thrusters [*Gulick et al.,* 2005]. This also decreased the complexity of the flow domain. Four million grid cells were generated for the fine mesh 3-D models.

Another numerical solver called ANSYS FLUENT was applied to further confirm the results of the experimental test data. The turbulence model used was the renormalization group (RNG) of *k-ε* [*Papp and Ghia*, 1998] and to confirm that dissipation did not significantly affect the shock wave profiles, an inviscid case was also run. Transient axisymmetric and 3-D solutions with a 1 μs dual implicit time stepping scheme with adaptive grid meshing was applied to resolve the shock waves in the flow domain. Pressure inlet and outlet were the applied boundary conditions. Convergence was observed for 2nd order upwind discretization schemes for all state parameters.

A.5 Results and discussion

Spatial and temporal ground pressure profiles along with Mach contours are used to analyze the flow physics of supersonic impinging jets by mainly varying the jet expansion ratios and Strouhal numbers. Correlation of this data with temporal P_c profiles and other initial conditions such as nozzle exit pressure (Eqn. A6), mass flow rate (Eqn. A7) and thrust (*T)* (Eqn. A8) added insight into the physics where T_C, $\dot{m}$ and R are the nozzle chamber stagnation temperature, mass flow rate and propellant gas constant, respectively. These values are tabulated in Table A2. All ground pressure values (P_g) are normalized by P_c and physical dimensions are normalized by the nozzle exit diameter, d.

$$P_e = P_C\left(1+\frac{\gamma-1}{2}M_e{}^2\right)^{-\frac{\gamma}{\gamma-1}} \qquad \text{(A6)}$$

$$\dot{m} = \frac{A^* P_C}{\sqrt{T_C}}\sqrt{\frac{\gamma}{R}}\left(\frac{\gamma+1}{2}\right)^{\frac{-\gamma+1}{2(\gamma-1)}} \qquad \text{(A7)}$$

$$T = \dot{m}U_e + (P_e - P_{amb})A_e \qquad \text{(A8)}$$

A.5.1 Experimental results due to subscale MSL MLE thruster plumes

For the temporal ground pressure profiles, we record the ground pressure rise and settling times, maximum and steady state pressure values, atmospheric pressure (vacuum chamber) and P_c profiles. All these steady tests were performed for one second duration. We observe transient ground overpressures on the order of 100% to 30% increase from its' steady state values for $e > 2$ (Fig. A3, solid line). However, no repetitive ground shock frequencies were observed for these cases. These overpressures span from 0.1 s to ~0.3 s during the P_c rise due to engine start-up as observed in Figure A3 (dashed line). There is a steady-state ground pressure regime that lasts from 0.3 s to ~1.0 s. After this point, there is a simultaneous rapid ground pressure decline with a sudden decrease in the P_c due to engine shut-down. For $e < 2$, there are no characteristic overpressure and exhibits relatively steady and much smaller pressure amplitudes as seen from Figure A3 A,B. At $e = 0.02$ (Earth atmospheric pressure), the ground pressure maximum is well below 0.001.

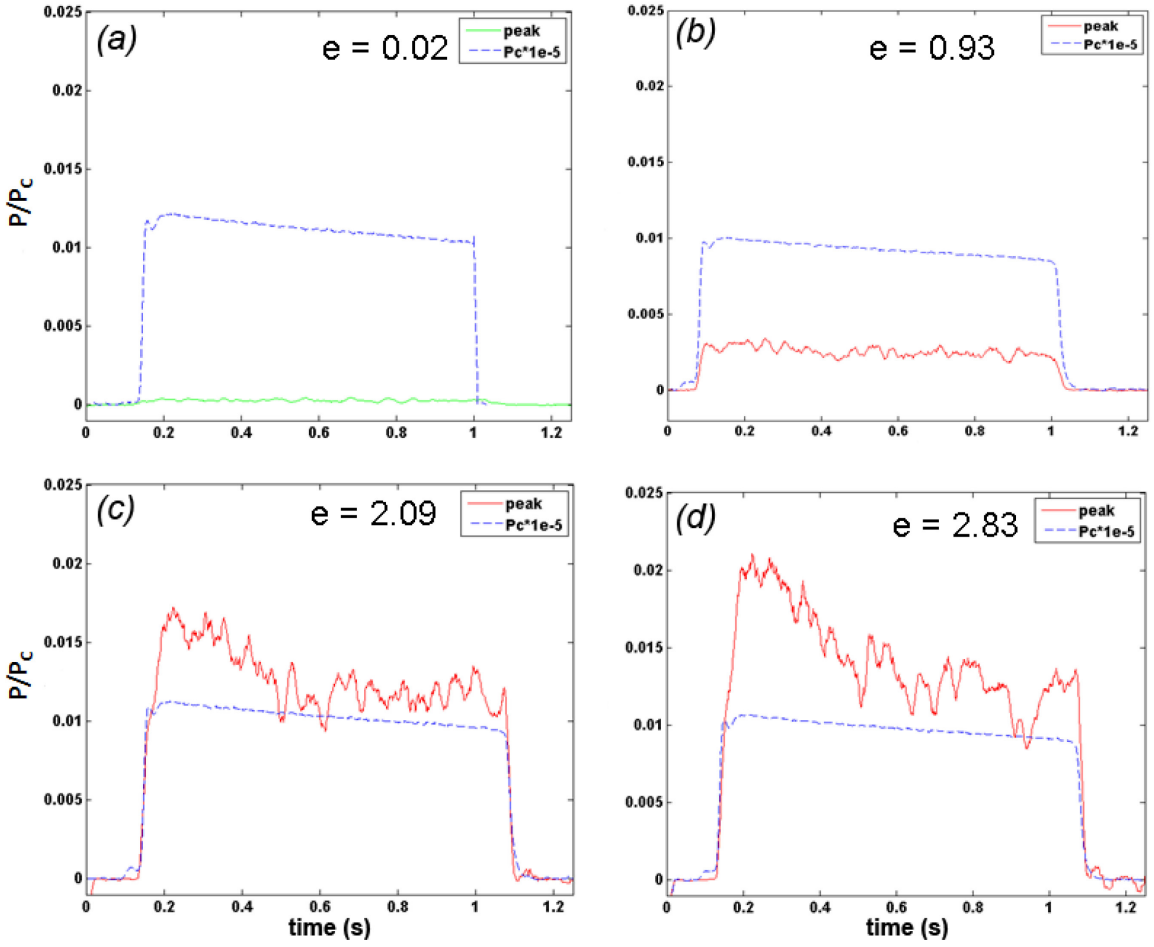

Figure A3. Temporal maximum ground pressure (peak) and P_C profiles of steady impinging jets at an altitude of ~35*d* for varying jet expansion ratios of Test 22 (A), Test 11 (B), Test 1 (C) and Test 2 (D). See Movie D7 and D8 for Test 2 and Test 22, respectively.

For the spatial ground pressure profiles, we developed ground pressure contour maps at the maximum overpressure value at $t = 0.25$ s (Fig. A4) and steady-state values at $t = 0.45$ s. From these contour maps, we observe that at $e = 2.09$ and $e = 2.83$, there is a radial pressure footprint which is bounded by the sensors and it is ~2*d* in diameter (Fig. A4 C,D). There is a large normalized pressure gradient, ∇, (Eqn. A9) of 0.017 at $e = 2.83$ determined from the periphery of the footprint. For $e = 0.02$, we do not observe these large pressure gradients ($\nabla < 0.001$) and there is a modest increase in pressure that spans a distance of ~7*d* as seen in Figure A4A. For $e = 0.93$ and less, the pressure gradient is much smaller in magnitude ($\nabla < 0.0025$) and more gradual, typical of a Gaussian distribution. The normalized pressure gradient is defined as follows:

$$\nabla = \frac{\Delta P_g}{P_C}\frac{d}{\Delta x} \qquad \text{(A9)}$$

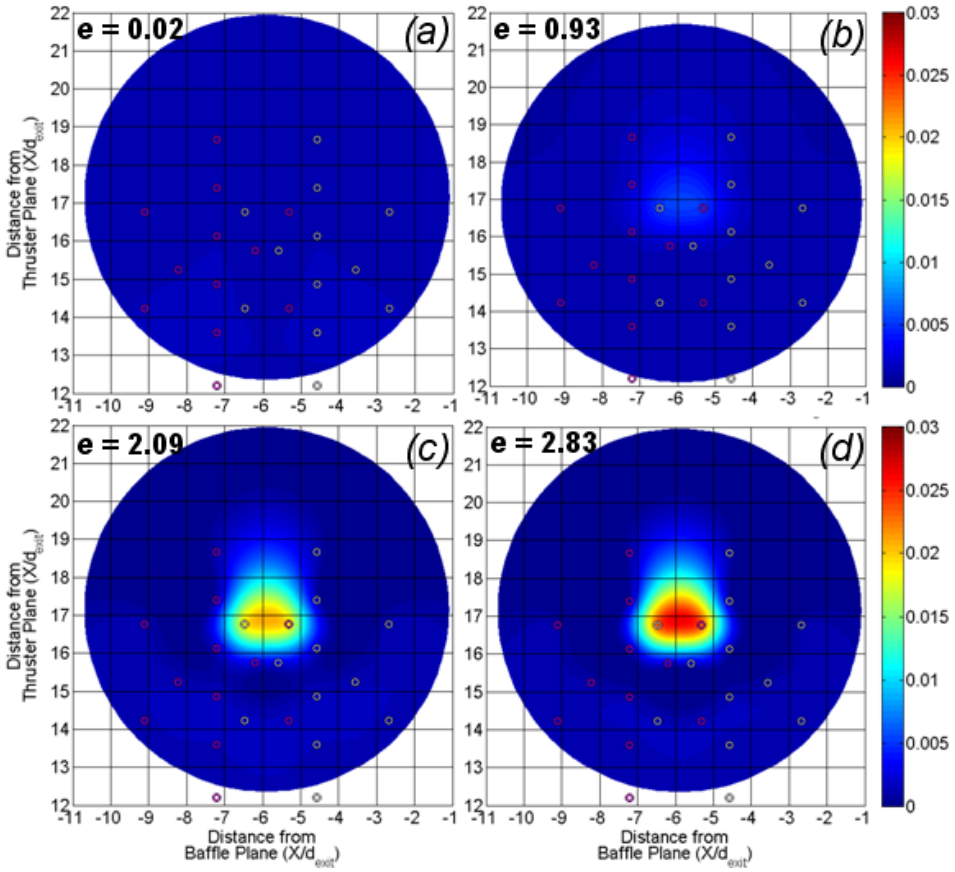

Figure A4. Ground spatial pressure profiles of steady impinging jets at an altitude of 35*d* for varying jet expansion ratios for test cases presented in Fig. A3. The colorbar depicts the normalized ground pressure values.

Figure A5 shows how the jet expansion ratio affects normalized impingement pressure (P_g/P_c) from our experiments. We observe for our tests that there is a maximum for overpressure ($P_g/P_c = 0.005$) and steady ground pressure ($P_g/P_c = 0.015$) values for $e > 2$. The overpressure is defined as the difference between maximum and steady-state ground pressure values. This is an increase by a factor of 5 compared to amplitudes at $e < 2$. These amplitudes are relatively constant between $e = 2$ to $e = 0.25$ with a slight increase in the steady ground pressure magnitude (P_g/P_c). We notice a minimum in steady and overpressures at $e = 0.02$.

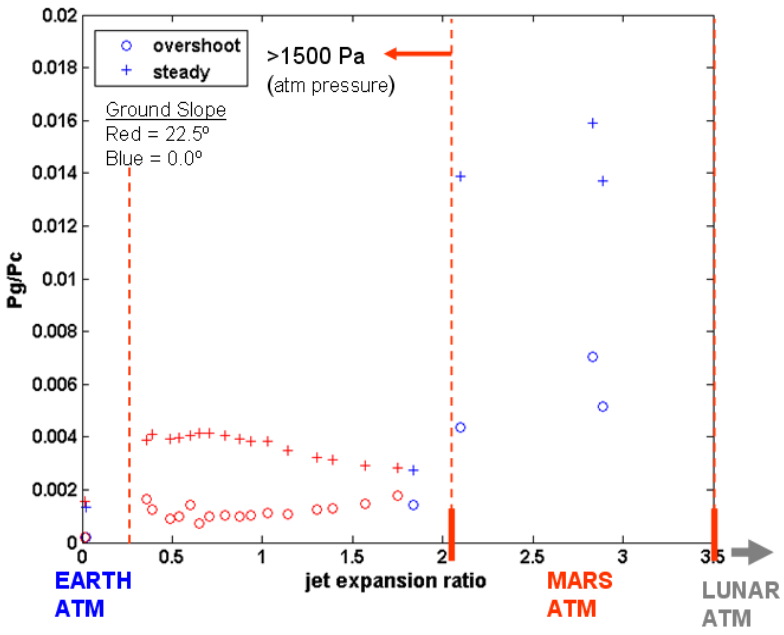

Figure A5. Normalized maximum ground pressure vs. jet expansion ratio curve at an altitude of ~35*d*.

Normalized ground pressure rise rates are how quickly the normalized ground pressure values rise to the maximum amplitude due to engine start-up. Figure A6 shows the rise rates (1/s) as a function of the jet expansion ratio. We observe a linear increase in the pressure rise rate with increasing jet expansion ratio for $e > 0.5$. We observe the largest rise rates for $e > 2$ with an increase by a factor of ~4 from the values compared to $e < 1.5$. The normalized settling rates, which determine how quickly the ground overpressure values settle to its' steady-state values, do not show a characteristic trend with respect to the jet expansion ratio.

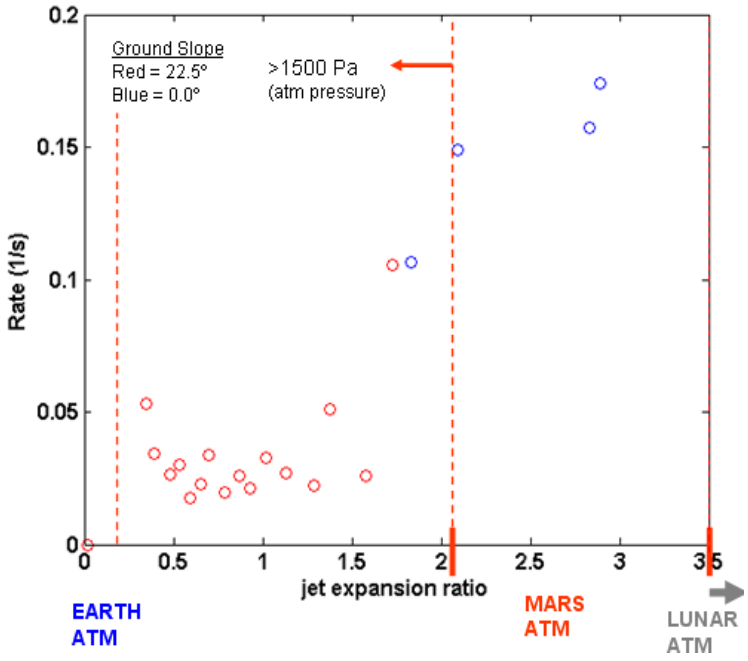

Figure A6. Rise rate vs. jet expansion ratio curve at an altitude of ~35*d*.

A.5.2 Experimental results due to Phoenix REM thruster plumes

For experimental results in understanding pulsed jet effects on ground pressure (non-zero Strouhal numbers), we used two different jet expansion ratios: *e* ~4.5 – 3.8 (moderately underexpanded) and *e* = 0.02 (highly over-expanded) at an altitude of 8.4*d*. The most interesting feature in the temporal pressure profiles analysis at *e* = 4.4 are the transient overpressures observed during engine start-up and shut-down phases as described in detail in Section 2.6.5. These peaks demonstrated normalized rise rates on the order of 6.0. These overpressures were repeatable and did not demonstrate hysteresis.

The spatial ground pressure profile for *e* = 4.4 were also radial with a pressure footprint diameter of ~3.2*d*. As noted for the MSL experimental measurements, for highly over-expanded jets, the pressure footprint was more diffuse with a smaller magnitude and a Gaussian distribution and did not indicate large pressure gradients as observed for moderately under-expanded jets. As discussed in Section 2.6.5, the spatial pressure profile for moderately underexpanded jets is non-Gaussian and there is minor pressure peaks observed at ± 1.6*d* due to the effects of oblique tail shocks.

A.5.3 Numerical results due to MSL MLE thruster plumes

Numerical results are first used to compare subscale ground pressure spatial and temporal profiles and near-field plume structure with measured quantities. Once in similar agreement, Mach contours can be used in conjunction with ground pressure profiles to understand the flow physics. This approach was used to obtain an understanding of our observations.

The Mach contours for the MLE plumes have a maximum Mach number of ~10 with a shock cell length of 14*d*. Approximately 2.5 shock cells are formed within the plume. As can be seen from Figure A7, the plumes are highly collimated even to distances greater than 35*d*. This is a very important characteristic that will be discussed in a later section. We observe characteristic flow features such as a plate shock with a diameter of ~2*d* and wall jet as observed by Lamont and Hunt [1968]. Due to an oblique jet interaction, the wall jet predominantly propagates in a +x direction as shown in Figure A7.

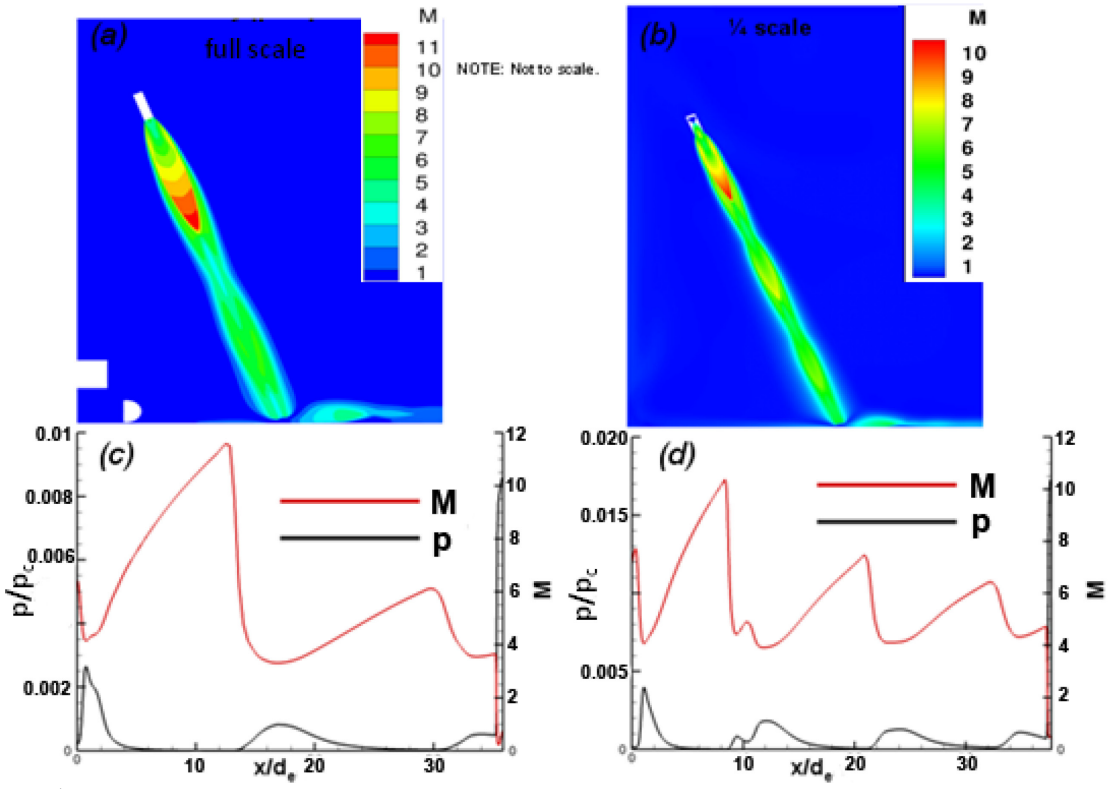

Figure A7. Full-scale and subscale MLE plume shock structure and axial static pressure profiles. *(a,b)*, Full-scale and subscale numerical solutions of the Mach contour at an altitude of ~35*d* for MLE plumes at 100% throttle; *(c,d)*, Full-scale and subscale numerical solutions of Mach (red line) and static pressure (black line) profiles as a function of x/d_e (axial distance along the plume).

All solutions were for steady-state conditions and hence only steady ground spatial pressure profiles are recorded (Fig. A8). This exhibits a radial pressure footprint with high pressure gradients of 0.026 and a diameter of 1.75*d*. There is an asymmetry in the profile and the highest pressure regions reach a nondimensional value of 0.028, which is approximately 0.5*d* from the plume centerline. The average ground pressure value within the footprint area is within the range of 0.018.

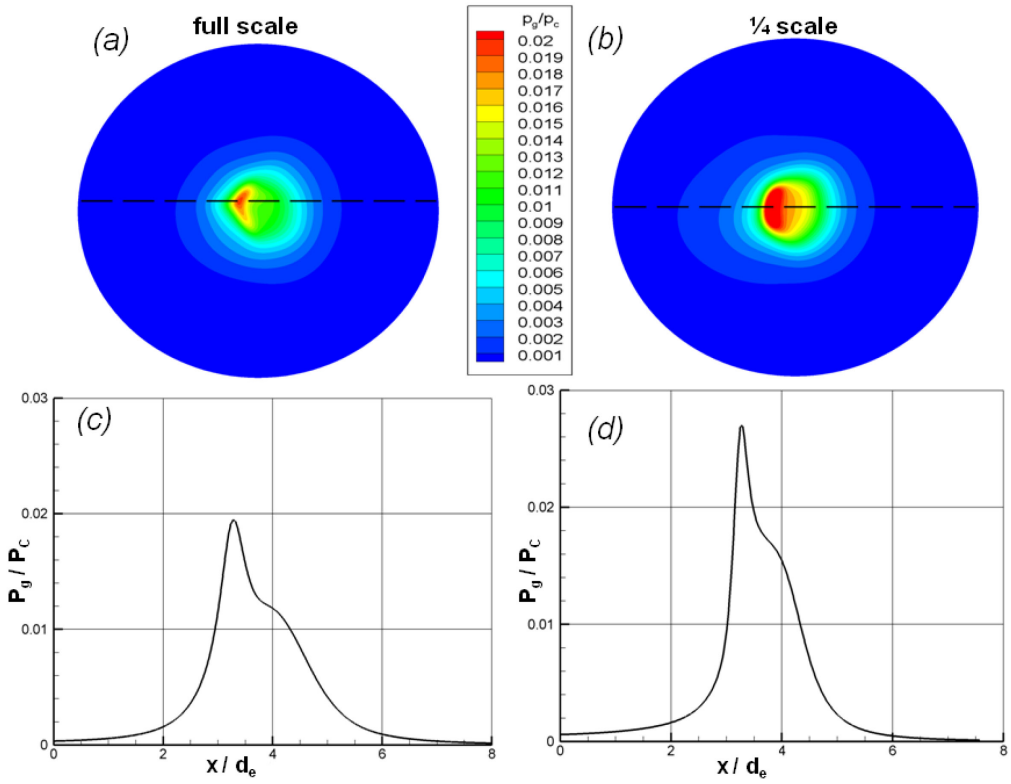

Figure A8. Numerical solutions between *(b,d)* subscale and *(a,c)* full-scale spatial ground pressure profiles of MLE plume interactions at 35*d* at 100% throttle. Subscale and full-scale numerical solutions of normalized ground pressure profiles (P_g/P_c) as a function of x/d_e along the dotted lines shown in the a and b panels.

From Figure A9, we observe good agreement between numerical solutions and experimental measurements for normalized spatial ground pressure profiles at *e* ~3. The pressure footprint diameter, normalized maximum ground pressure values and pressure gradients are similar for both simulation and measurements. The numerical solution show a slightly smaller pressure footprint (see Results section). There are some minor discrepancies in the features such as the lack of capturing the high pressure asymmetry region which is due to lower measurement resolution than the numerical simulation and sensitivity in turbulence modeling.

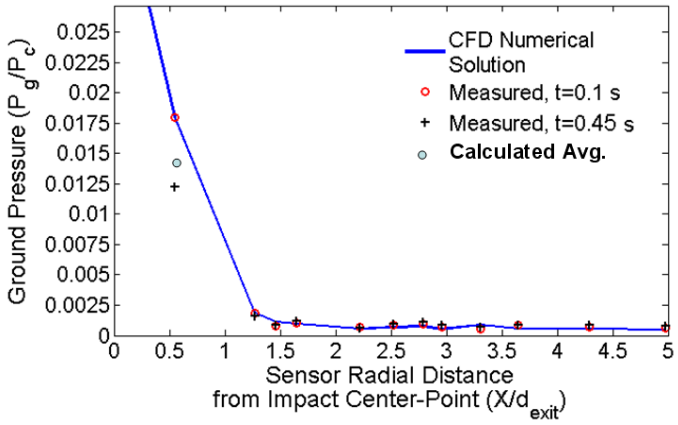

Figure A9. Numerical solution compared to measured quantities at t = 0.1 s and t = 0.45 s for steady underexpanded N_2 jet impingement at e ~3 at an altitude of 35d (Test 3).

A.5.4 Numerical results due to Phoenix REM thruster plumes

Transient and steady state solutions were developed for the pulsed supersonic jets impinging at the surface at various altitudes. Simulations at two altitudes are presented here: 8.4d and 25d. Numerical simulations show that an underexpanded supersonic jet with an e = 4.4 at an altitude of 25d results in the development of a normal plate shock with a diameter of ~2d and wall jets that propagate in the ±x direction (see Chapter 2, Fig. 2.8). Two shock cells are observed with a length of ~12d within the plume structure at an altitude of 25d. Here, once again, the plume structure is collimated as observed for the MLE thruster plume numerical simulations.

According to Chapter 2, Section 2.6.5, the numerical simulations and experimental measurements at an altitude of 8.4d show good agreement in both temporal and spatial ground pressure profiles at the far-field and near-field regimes for underexpanded jet at e ~4.4. They both show ground overpressures at a 20 Hz frequency and similar quasi-steady ground pressure magnitude, footprint area and pressure gradients. We also observe good agreement between numerical simulation and shadowgraph imaging in the plume shock structure at the near-field regime (Fig. A10). The numerical simulation exhibits a plume expansion angle from the nozzle exit plane of approximately 25º. This also shows good agreement with the findings from Clark et al., [1971]. This value is somewhat less for our shadowgraph images which show an expansion angle of 22º. However, there are a few discrepancies described in Section 2.6.5

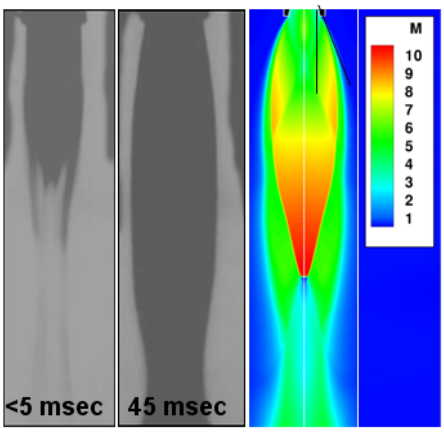

Figure A10. *(a)* Shadowgraph image of a near-field underexpanded jet (e ~4.4) at < 5 ms during engine start-up and *(b)* during full-throttle and *(c)* numerical solution during full-throttle

A.5.5 Jet expansion ratio

The jet expansion ratio is one of the most important factors in determining ground pressure profiles at high altitudes ($h > 5d$). The jet expansion ratio influences the near-field and far-field plume structure as discussed in Section 2.6.1. For $e > 1$ (underexpanded jets) the plume nozzle exit pressure is greater than the ambient pressure. This leads to the formation of expansion fans at the lip of the nozzle, causing the plume to expand outward with respect to the normal increasing the plume expansion angle ($\theta > 0^o$). For $e < 1$ (overexpanded jets), the plume nozzle exit pressure is less than the ambient pressure. This leads to the formation of reflected oblique shock waves that cause a decrease in the plume expansion angle with respect to the normal ($\theta < 0^o$). For $e = 1$ (perfectly expanded), the plume nozzle exit pressure is similar to the ambient pressure. This prevents the formation of expansion and shock waves and the plume expansion angle is zero. As a result of the low planetary atmospheric pressure on Mars and the moon, most of the thruster jets observed during spacecraft landings on these celestial bodies is underexpanded.

From Figure A5, it can be seen that the normalized ground pressure value increases by a factor of five for jet expansion ratio greater than 2. It can also be seen that for very low e on the order of 0.02 the ground pressure was minimal. Numerical simulations that were validated by experimental tests show in Figure A11 that the Mach contours and plume structure are also considerably different between e ~4.5 and $e = 0.02$.

For moderately underexpanded jets (e ~4.5), the plume structure has compressed and collimated shock cells that are formed until a downstream distance is reached when plume and ambient static pressure are in equilibrium. This downstream distance, supersonic core length (x), is considerably larger for moderately underexpanded jets as compared to highly over-expanded jets (e ~0.02) as shown in Figure A11. This classification of jets may develop a stable plate shock at the surface and a propagating wall jet.

The relatively larger ambient pressure for highly over-expanded jets ($e << 1$) leads to the formation of reflected oblique and normal shock waves which may occur at the diverging section of the nozzle. Boundary-layer separation at the diverging section can lead to attenuation of the jet [*Shimshi et al*., 2009]. Once a strong normal shock wave forms at the diverging section (Fig. A11), this results in the propagation of very weak shock waves which leads to flow separation and shock wave instability. The shock wave is further attenuated by the interaction and mixing of the shock with the dense shear layer at the jet boundary which leads to Kelvin-Helmholtz instabilities. Due to overexpansion, the atmospheric free surface boundary pinches the jet inward, leading to an axial increase in the turbulent mixing layer. This decreases x and results in the rapid decay of the plume structure to a fully turbulent subsonic jet with a linear spreading profile (b = const*L), where L is the axial plume length that is both turbulent and subsonic [*White*, 1991]. As a result of the spreading profile, large altitudes and subsonic flow field, normal plate shocks are not developed above the surface. This prevents the formation of large pressure gradients at the surface as well as the formation of supersonic wall jets.

For $e >> 1$, highly underexpanded jets shown in Figure A12, we also observe a decrease in normalized ground pressure profiles and this is due to a large plume expansion angle. The shock propagation of a large expansion plume results in a large areal plate shock as observed by Clark et al. [1971] which significantly reduces the normalized ground pressure since pressure is inversely dependent on area. Another mechanism may be due to the increased pressure losses due to a normal shock wave or a Mach disk formed within the near-field regime at high e as opposed to the unsteady oblique shock waves developed in the far-field regime at lower jet expansion ratios.

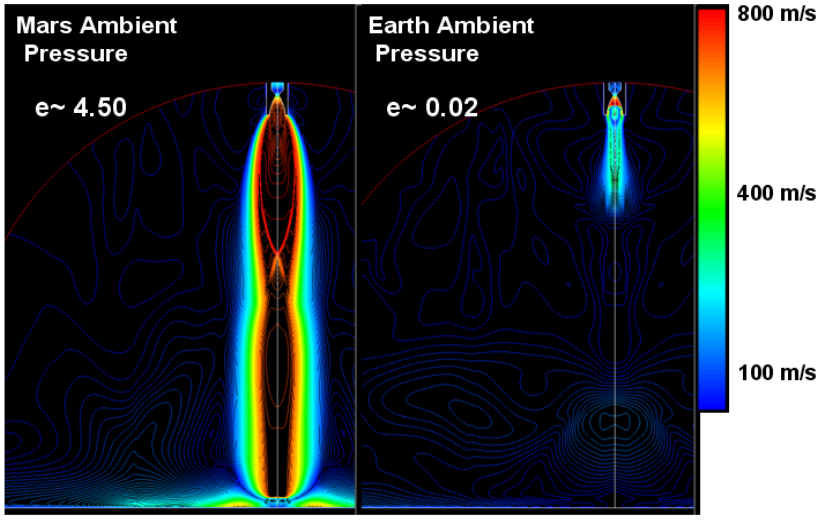

Figure A11. Numerical solution of velocity contour comparison between steady underexpanded (Mars) and highly overexpanded (Earth) supersonic jets at an altitude of 25*d*.

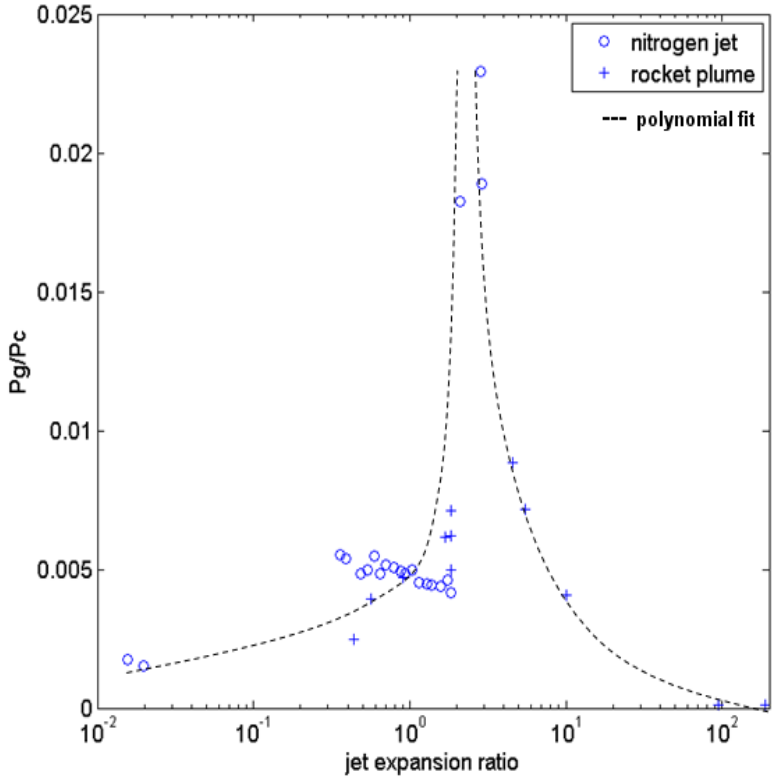

Figure A12. Normalized centerline ground pressure vs. jet expansion ratio for nitrogen jets and rocket plumes at an altitude of ~35*d*.

We presented data of the comparison of supersonic nitrogen jets and rocket plumes from monopropellant and bi-propellant rocket motors at an altitude of ~35*d* (Fig. A12). All nitrogen jets and rocket plumes demonstrate an exit Mach number of ~5

[*Clark*, 1971; *Romine et al*., 1973; *Stitt and Latto*, 1963]. The monopropellant rocket motors use hydrazine as the fuel which combusts at a T_C of greater than 1000 K, releasing N_2, H_2 and NH_3 as low density exhaust species (Chapter 2). The bi-propellant uses methyl hydrazine as the fuel and nitric oxides as the oxidizer [*Clark*, 1971]. We show good agreement in the trend between nitrogen jets and rocket plumes in which the highest normalized ground pressure values have jet expansion ratios between 2 and 5 as observed in our studies (Fig. A12). Rocket plumes also exhibit minimal normalized ground pressure values for highly over-expanded ($e < 0.5$) and underexpanded jets ($e >> 5$). Hence, to obtain accurate risk assessment of spacecraft landings on Mars and the moon without changing the thrust conditions, it is critical to study these interactions at the appropriate atmospheric environments so that the jet expansion ratio is accurately simulated.

This analysis of jet expansion ratio is quite important to consider, because these values are dependent on the propulsion system and atmospheric density of the planets for our application. We can decrease the effects of thruster plumes on the surface by changing the propulsion system requirements or by landing at a different latitude and longitude on planets. For example, the atmospheric pressure on Mars can change from ~350 Pa to 1000 Pa depending on the location and time of day [*Taylor et al*., 2009].

A.5.6 Supersonic core length

Supersonic core length can be inferred from ground pressure profiles. An indirect approach in measuring the supersonic core length is by varying the distance from a flat surface and monitoring the ground pressure. Supersonic core that propagates to the flat surface results in the formation of a plate shock which leads to steep pressure gradients as observed in Figure A4. We conclude that there are large differences in the supersonic core length and spatial ground pressure profiles for highly overexpanded and moderately underexpanded jets at an altitude of 35*d*. In contrast to moderately underexpanded jets, we observe a very diffuse and Gaussian pressure profile for highly overexpanded jets (e = 0.02) as depicted in Figure A4 and this leads to rapid decay of the plume structure which demonstrates a core length of less than ~5*d* as shown in Figure A11. The experiments indicate that the supersonic core length developed by MLE plumes (e ~3) propagate to at

least a distance of 37*d*. This is also supported by Mach contours generated by the numerical simulations (Fig. A7). Numerical solutions show that REM plumes (e ~4.4) have a supersonic core length of at least 25*d* (Fig. A13). This is further supported by Inman et al. [2009] which shows with Planar Laser-Induced Fluorescence (PLIF) imaging that a collimated moderately underexpanded (e = 5.4) turbulent nitrogen jet at Mach 2.6 has a supersonic core length to a distance of 31*d*. Scroggs and Settles [1968] show with Schlieren imaging that the supersonic core length increases with jet expansion ratio and Mach number. They recorded supersonic core lengths on the order of 35*d* for e = 4 and a Mach number of 2.2.

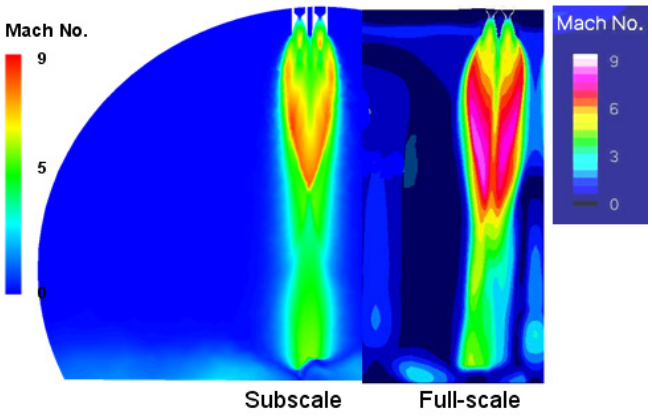

Figure A13. Subscale and full-scale numerical solutions of the Mach contours of the Phoenix REM plumes at an altitude of 25*d*. [*Gulick*, 2006]

From Figure A14, we determine the length of the shock cell, x_s, as a function of the jet expansion ratio. We see an increase in the shock cell length at higher NPR than at lower corresponding values [*Inman et al.*, 2009]. The shock cell length increases logarithmically with increasing jet expansion ratio and increases linearly with nozzle exit diameter. Shock cell length may have a weak dependence on M_e.

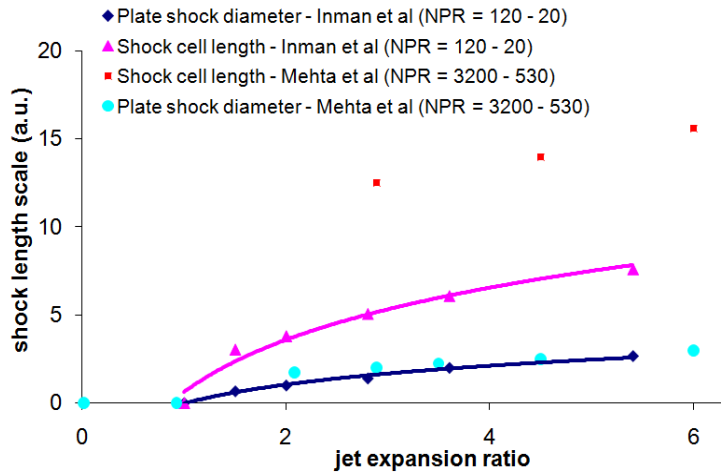

Figure A14. Normalized plate shock diameter and shock cell length as a function of the jet expansion ratio at an altitude of ~35*d*.

A.5.7 Plate shock dynamics

Plate shock dynamics lead to large ground pressure fluctuations and gradients at the surface as briefly discussed in Section 2.6.5.1. Figure A15 shows a numerical solution for the formation of a plate shock at the surface from a Mach 4.7 underexpanded jet (*e* ~4.4). Prior to initial jet impact, shock waves accelerate toward the surface which initiates coalescing of the plume density and gas compression. After jet impingement, an unstable normal shock wave, plate shock, is formed above the surface and a transient high plume density is observed below the plate shock. This concentrated and localized plume density at high velocity results in larger ground pressures relative to subsonic flow fields. Hence, the large differences in ground pressure observed with varying jet expansion ratios. Overpressure due to plate shock formation is observed for both steady (MLE) and pulsed (REM) exhaust plumes (Figs. 2.6 of Chapter 2 and A3). Overpressure occurs when the shock wave first impinges on the surface and the overpressure settles to quasi steady-state value upon stable formation of the plate shock. The non-Gaussian and high pressure gradients are characteristic of plate shock formation (Section 2.6.5) and the footprint is similar to the shock diameter.

There are some major differences in the shock dynamics between pulsed and steady (MSL) descent jets. The initial overpressure peak due to the MLE plumes are smaller than observed for the Phoenix cases and virtually absent during the engine shut-down phase and this may be due to the development of a much weaker normal shock at

the surface. This could be attributed to a larger axial distance the shockwaves need to travel and the slope of the inclined surface. This could also be attributed to slower stagnation pressure rise and fall rates. Large instabilities in the plate shock may delay the formation of a fully-developed shock. Most importantly, the characteristic ground shock frequency observed for pulsed jets was entirely absent in these steady jet cases. This is mainly the result of engine cycling. However, during plate shock formation and collapse, high instability due to axial plate shock oscillations is observed by Movie D3 (Appendix D). This instability is further supported by the highly variable settling trend for $e > 1.5$. Plate shock formation is also a function of the jet expansion ratio and altitude.

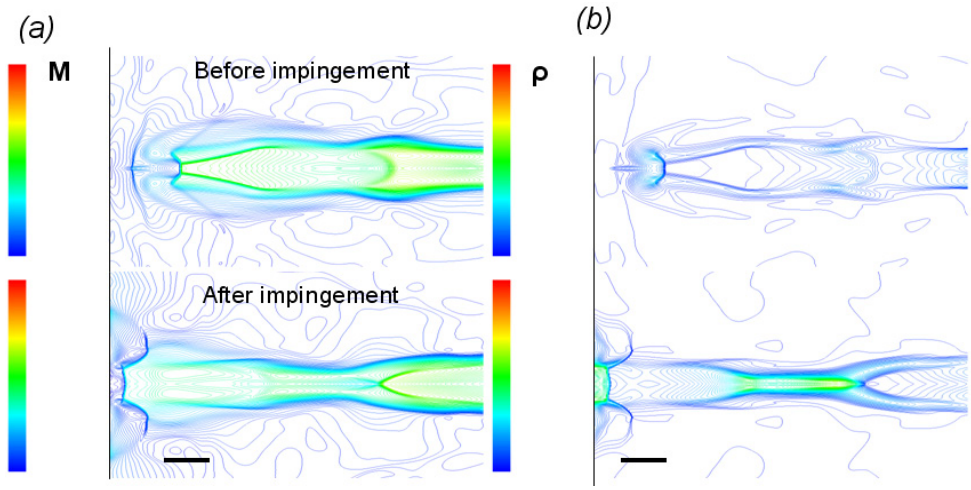

Figure A15. Numerical solutions of *(a)* Mach and *(b)* density contours of a pre and post normal shock wave interaction. Black bar depicts the length of the nozzle exit diameter.

From observations, a stable plate shock may not form for supersonic jets at e below 1.75 at altitudes of $35d$ and greater. As we approach a jet expansion ratio of one, shock cells within the plume disappear and lead to greater shock wave and static pressure attenuation at these large distances. This is also supported by Inman et al. [2009] which also shows a significant drop in the ground pressure at jet expansion ratios near and below unity.

A significant decrease in normalized ground pressure magnitude for $e < 2$ may be attributed to the plate shock within the expansion regime of the shock cell. Large pressure fluctuations occur depending on whether the plate shock is within the expansion or compression regimes of the shock cell [*Romine et al.*, 1973]. This is unlikely the result of our study due to the fact that successive points with decreasing jet expansion ratios

ranging from e = 1.90 to e = 0.30 (changing shock structure profiles) lead to relatively constant normalized ground pressure magnitudes. Hence, the significant decrease in ground pressure (Fig. A12) is mainly due to the inability for a plate shock to develop at these expansion ratios and large downstream distances.

From Figure A14, the plate shock diameter is independent of both NPR and M_e, but shows logarithmic dependence on the jet expansion ratio and linear dependence on the nozzle exit diameter. These length scales profiles were determined by both numerical and experimental observations noted in this Appendix.

A.5.8 Comparisons between subscale and full-scale tests

To ensure similar plume structure and ground pressure profiles between our subscale tests and exhaust plumes from both MSL and Phoenix rocket motors, scaling parameters derived in Section 2.6.2.2 were used. There parameters govern the flow regime, specific plume energy density, compressibility and unsteady effects and the jet expansion ratio. Our goal is to determine whether these theoretical scaling parameters accurately determine the plume flow dynamics between cold gas jets and rocket plumes. These parameters are approximately similar between subscale and full-scale cases for both test programs (Table A1): Phoenix REM and MSL MLE. Experimental measurements (Chapter 2) and numerical solutions show that the Mach number, shock structure and spatial and temporal pressure profiles are in good agreement between cold flow subscale and full-scale systems, Phoenix rocket exhaust plumes, at altitudes of 25d and 8.4d. This is observed for both single and dual thruster systems. For example, Figure A16 shows a numerical solution of a full-scale temporal and spatial ground pressure profiles for a full-scale rocket plume interaction from a single Phoenix descent engine (note the similarity in Fig. 2.9). Good agreement in ground pressure magnitude and spatial profile is observed for dual thruster systems as shown in Figures 2.10 and 2.11 for a mean altitude of ~23d. The numerical solutions of the Mach contours between the subscale and full-scale MLE plumes show relatively good agreement in both magnitude and shock structure (Fig. A7). The numerical solutions and experimental observations of the spatial ground pressure profiles between the MLE subscale and full-scale cases also

show relatively good agreement in pressure footprint area, normalized magnitude, asymmetry and pressure gradients (Fig. A8).

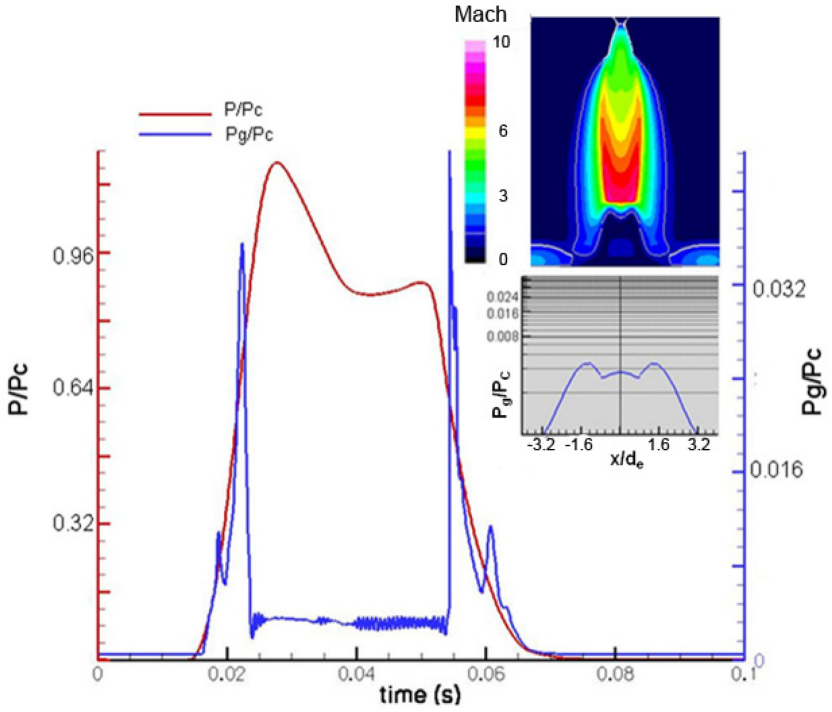

Figure A16. Full-scale (singe Phoenix REM plume interaction) numerical results of the spatial (t = 0.036 s) and temporal normalized ground pressure profiles at an altitude of 8.4d at Mars atmospheric environment. [*Gulick*, 2006]

Numerical simulations were used to characterize the effects of rocket plumes on the ground at various altitudes. There are no large discrepancies observed for the numerical solutions of the Phoenix test cases, but the MSL test cases did show some minor differences. The ground pressure magnitude for the MSL cold gas jets is greater than the rocket plumes by a factor of 0.25. The plumes at subscale conditions are more compacted and collimated than for the full-scale case. The subscale jets also exhibit more frequent and shorter shock cells within the collimated plume. This most likely is attributed to a difference in the jet expansion ratio (Table A1).

Subscale experimental spatial and temporal ground pressure measurements show relatively good agreement with the full-scale numerical solutions for rocket plume impingement. The Phoenix and MSL test cases show few discrepancies, but overall show similar pressure footprint area, normalized magnitude and pressure gradients. Due to limited pressure sensors and a decrease in resolution, we were not able to capture the asymmetry. Due to limitations in obtaining low vacuum in the chamber, we were not able

to achieve exactly the same jet expansion ratio for the MLE cases as seen for the full-scale numerical simulations (Table A1). As a result of this extensive study, these scaling parameters applied to cold gas jets are critical in properly simulating rocket plume impingement effects. Further controlled experimental studies between full-scale rocket motors and supersonic cold gas jets are needed to confirm these results

A.5.9 Erosion effects due to plume-soil interactions

Soil erosion due to jet impingement is very sensitive to ground pressure. The temporal and spatial profiles and magnitude of the ground pressure can determine which erosion processes are dominant as discussed in Chapter 3. Hence, it is important to accurately simulate both the thruster inlet stagnation pressure and the atmospheric pressure environments of planetary bodies.

A.6 Conclusions.

This research investigation was ultimately undertaken to assess landing site alteration due to rocket plume impingement during spacecraft landings. The first approach, presented here, is to provide insight into plume shock structure and dynamics and their effect on ground pressure profiles. From our extensive numerical and experimental analyses, we show that moderately underexpanded jets (e between two and five) demonstrate collimated shock structures, compact radial pressure footprints, large supersonic core lengths, plate shock dynamics and maximum pressure loads. For e less than 2 and greater than 10, we illustrate a significant decline in the ground pressure loads by a factor of four with large Gaussian pressure footprints which is mainly attributed to large changes in the plume shock structure. We show that the plate shock dynamics is responsible for the following effects at the surface: increases the pressure gradients, fluctuations and average magnitudes and develops pressure asymmetry and overpressures. Therefore there is sensitivity in both shock structure and ground pressure dynamics to both the jet expansion ratio and Strouhal number (pulsed or steady). Most importantly, the flow dynamic studies at Mars atmosphere (e ~2-5) show that rocket plumes possess large collimated shock cells greater than ~10d and generate maximum ground pressure load with respect to either lunar or terrestrial atmospheric regimes.

Hence, extensive numerical and experimental investigations of plume interactions with large variations in the scaling parameters defined in Table A1 are needed to reduce mission risk associated with landing spacecrafts on Mars.

We observe good agreement between measurements and numerical solutions for both subscale REM and MLE nozzle plumes at various altitudes. This validates the numerical solvers as well as provides insight to the flow physics occurring at the surface. We also observe relatively good agreement in shock structure and ground pressure dynamics between subscale and full-scale systems. Most importantly, these results show that the scaling laws developed can properly simulate the ground interaction physics due to rocket exhaust plumes.

The next approach is using this study to understand jet-induced erosion mechanisms due to spacecraft landings (as discussed in Section 5.6). The plate shock dynamics and plume structure directly affects the ground pressure which influences particular erosion mechanisms and cratering dynamics as discussed in detail in Appendix C.

APPENDIX B

Supplementary Information for Chapter 3

B.1 Calculations of crater dimensions and ammonia contamination at the Phoenix Landing Site using RAC images.

The radius of exposed ice under the lander was estimated by the analysis of images using the centerline -Y (eastern) footpad coordinates of the Phoenix spacecraft as a reference. These coordinates were provided in the Payload Frame (Eq. B1) which was converted to Lander Centerline Frame (Eqn. B2). By observing images of "Snow Queen" (Fig. B1) which showed the outer portion of the exposed ice, we were able to approximately assess the distance between the outer exposed ice and the –Y footpad edge. This distance scales from 1.2 to 0.9 footpad diameters ($d_{footpad}$). As a result by applying equation B4 and estimating the radius of soil deposition near the centerline of the spacecraft (r_{cl}) (Fig. 3.9), the ice exposed by the rocket plume impingement spans a length in the –Y direction, L_c, between 65 and 55 cm. Approximating that a crater with an elliptical profile was produced per every four descent thrusters (Fig. 3.9), we geometrically calculated the crater dimensions such as its perimeter (p_c), semi-major length (a_c), semi-minor length (b_c), volume (V_c) and mass of total ejecta (m_c) by applying equations B6 to B9 to known quantities such as the crater depth and angle of repose (Θ_r). Although soil depths greater than 10 cm have been recorded within Phoenix's workspace, the average depths between 5 cm and 10 cm were used in our calculations. Shadow projection on the martian surface were used to estimate the soil depth. It should be made clear that these are approximations generated from limited RAC images. No adequate digital elevation maps were created to confirm these values. By knowing the time during descent when ground effects begin until touchdown of the spacecraft, t_L, the average normalized erosion rate (Eqn. B10) estimated from the Phoenix landing site is between 35 and 100.

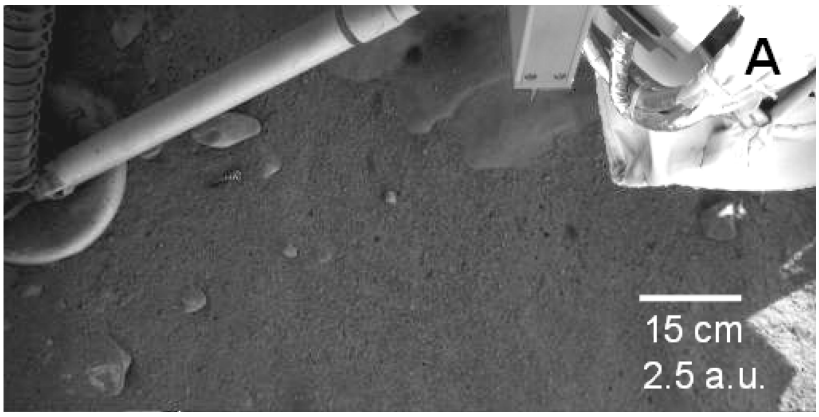

Figure B1. Subsurface ice, "Snow Queen", shown exposed below the lander near the eastern footpad (RS005EFF896662260_11736MDM1). *Courtesy of NASA/JPL-Caltech/U. of Arizona/Max Planck Inst.*

-Y footpad centerline in payload frame: $[x, y, z]_{payload}$ = [7.4, 53.6, 107.0] cm (B1)

-Y footpad centerline (FC) in lander frame: $[x, y, z]_{lander}$ = [60.8, 107.0, 123.1] cm (B2)

Lander centerline (LC) in lander frame: $[x, y, z]_{lander}$ = [0.0, 0.0, 123.1] cm (B3)

$$R = \sqrt{(x_{LC} - x_{FC})^2 + (y_{LC} - y_{FC})^2 + (z_{LC} - z_{FC})^2} + \frac{d_{footpad}}{2} \quad \text{(B4)}$$

$$L_c \sim R - 2d_{footpad} - r_{cl} \quad \text{(B5)}$$

$$p_c \sim \frac{4}{3}\pi\left(R - 2d_{footpad}\right) \quad \text{(B6)}$$

$$a_c = \frac{L_c}{2};\ b_c \sim \sqrt{\left(\frac{p_c}{\pi}\right)^2 \frac{1}{2} - a_c^{\,2}} = \frac{1}{6}\sqrt{32\left(R - 2d_{footpad}\right)^2 - 9L_c^{\,2}} \quad \text{(B7)}$$

$$V_c \sim \pi a_c b_c h + \frac{\pi h^2}{2\tan(\theta_r)}\left(\frac{h}{\tan(\theta_r)} + a_c + b_c\right) \quad \text{(B8)}$$

$$m_c \sim \rho_p n V_c \quad \text{(B9)}$$

$$\frac{\dot{m}_c}{\dot{m}} = \frac{m_c}{t_L \dot{m}} = \text{normalized erosion rate} \quad \text{(B10)}$$

The total mass of ammonia, m_{NH_3}, that may have interacted with the ice surface due the Phoenix landing propulsion system was determined based on a pair of thrusters' exhaust properties such as the mass flow rate, $\dot{m}$, and mass fractions, f (Eqn. B11). The mass fraction of ammonia of 0.49 was determined from the Phoenix hot thruster firing tests performed in a vacuum chamber at Mars atmospheric conditions (Chapter 2). The t' is the time differential between t_L and the time to expose the subsurface ice (< 1 s).

$$m_{NH_3} = 6\,\dot{m}\,f_{NH_3}\,(0.45t') \qquad \text{(B11)}$$

B.2 Jet-soil interaction dimensional analysis

Buckingham-Pi dimensional analysis theory was used to obtain dimensionless parameters given the important input conditions needed for describing jet-soil interactions. A jet with velocity, U, density, ρ_a and viscosity, μ, exhausting from a nozzle diameter, D, interacts with granular media with a particle diameter of d, density, ρ_p, porosity, n, shear strength, Y, and depth, l. The jet of mass flow rate, $\dot{m}$, interacts with the granular media for a certain time duration, t, at an altitude, h, from the surface, generates a pore pressure differential ΔP within the granular media, and leads to the formation of a crater with a volume of V_c. We are able to calculate the average erosion rate, $\dot{m}_c$ due to the various erosion processes. There are 15 dimensional parameters (n_{PI}) which satisfy three units (p_{PI}): length, time, and mass. Hence, 12 pi terms are needed to govern the physics.

According to previous literature and normalizing the particle mass transport rate equations [*Greeley and Iversen*, 1985], we believe that only a few parameters as shown in Section 3.2.1 need to be matched to produce dynamically similar flows. The bulk particle Reynolds number (Re_p) for fluid flow through a packed bed is shown in equation B18 with particle diameter, $\overline{d}$, and porosity, n is dependent on jet density, ρ_a, jet viscosity, μ and impinging jet velocity, U. The Re_p values increase by many factors during the DGEE process due to an increase in soil porosity. The Kn is dependent on the Boltzmann constant, k_B, the ambient atmospheric pressure and temperature, P_{amb} and T_{amb}, diameter of the atmospheric molecule, σ, and particle size. Based on Kn at the surface atmospheric conditions of Mars and experiment, the flow dynamics are within the continuum regime. We have tabulated other dimensionless numbers such as Kn, γ and nozzle area ratio for completeness (Table 3.3). From dimensional analysis theory, all the pi terms calculated from the experiments should be equal to the pi terms seen at full-scale to ensure complete similarity (Eqn. B29) [*Barenblatt,* 2003]. This is difficult to achieve for granular processes, but some pi terms have negligible effects on the physics being studied as discussed in Section 3.2.1.

$$V_c = f(U, D, \rho_a, g, \rho_p, \bar{d}, \mu, h, Y, n, l, t, z, c_s, \Delta P) \quad \text{(B12)}$$

$$\Delta\rho = \rho_p - \rho_a \approx \rho_p \quad \text{(B13)}$$

$$\Pi_1 = \frac{4V_c\rho_p n}{t\rho_a UD^2} = \frac{\dot{m}_c}{\dot{m}} \quad \text{(B14)}$$

$$\Pi_2 = \frac{U}{\sqrt{g\bar{d}}} = \mathrm{Fr} \quad \text{(B15)}$$

$$\Pi_3 = \frac{\rho_a}{\rho_p} \quad \text{(B16)}$$

$$\Pi_2\sqrt{\Pi_3} = \frac{U}{\sqrt{\left(\frac{\rho_p}{\rho_a}\right)g\bar{d}}} = \mathrm{Fr_d} \quad \text{(B17)}$$

$$\Pi_4 = \frac{\rho_a U\bar{d}}{\mu(1-n)} = \mathrm{Re_p} \quad \text{(B18)}$$

$$\Pi_5 = \frac{Y}{\rho_a U^2} = \frac{Y(c, \theta_i)}{\rho_a U^2} = \beta \quad \text{(B19)}$$

$$\Pi_6 = \frac{2l^2\, n\mu}{kPt} = \frac{4l^2\, n\mu}{k(n,d)\rho_a U^2 t} = \frac{\tau}{t} \quad \text{(B20)}$$

$$\Pi_7 = \frac{h}{D} \quad \text{(B21)}$$

$$\Pi_8 = \frac{l}{D} \quad \text{(B22)}$$

$$\Pi_9 = \frac{\bar{d}}{D} \quad \text{(B23)}$$

$$\Pi_{10} = \frac{f(\rho_a, \rho_p, \bar{d}, g)}{f\left(U, z, \bar{d}\right)} = \frac{u_{*t}}{u_*} \quad \text{(B24)}$$

$$\Delta P = P_p - P_{amb} \quad \text{(B25)}$$

$$\Pi_{11} = \frac{3\Delta P}{2\rho_p g\bar{d}} = \Delta P^* \quad \text{(B26)}$$

$$\Pi_{12} = \frac{U_g}{c_s} = \frac{f\left(\Delta P, \rho_p, g, \bar{d}\right)}{c_s} = \mathrm{Ma_g} \quad \text{(B27)}$$

$$\frac{\dot{m}_c}{\dot{m}} = \phi\left(\frac{u_{*t}}{u_*}, \mathrm{Fr_d}, \mathrm{Re_p}, \mathrm{Ma_g}, \frac{\tau}{t}, \beta, n, \frac{h}{D}, \frac{l}{D}, \frac{\bar{d}}{D}, \Delta P^*\right) \quad \text{(B28)}$$

$$\phi\left(\Pi_1, \Pi_2, \Pi_3 \ldots \Pi_{n_{pi}-k_{pi}}\right)_{\exp} = \phi\left(\Pi_1, \Pi_2, \Pi_3 \ldots \Pi_{n_{pi}-k_{pi}}\right)_{fs} \quad \text{(B29)}$$

$$\mathrm{Kn} = \frac{k_B T_{amb}}{\sqrt{2}\pi\sigma^2 P_{amb}\,\bar{d}} \qquad \text{(B30)}$$

B.3 Normalized crater dimensions from site-alteration experiments at NASA Ames – PAL

Test	Crater depth (a.u.)	Crater radius† (a.u.)	Exposed radius (a.u.)
1	6.4	17.6	13.6
2	1.6	19.5	13.8
3	1.6	19.8	13.7
4	7.5	28.8	10.3
5	7.4	24.6	11.4
6	7.7	24.3	10.7
7	5.1	25.9	--
8	5.9	24.3	--
9	6.0	25.6	--
10	4.8	24.3	--
11	1.6	27.3	2.6
12	2.1	4.8	--
13	0.2	4.8	--
14	2.6	4.8	--
15	1.1	6.1	--
16	2.2	3.0	--
17	1.0	7.2	--
18	1.3	8.0	--
19	2.0	8.4	--
20	2.0	8.0	--
21	1.6	35.2	20.0
22	6.4	35.8	18.1
23	1.1	4.0	--
24	1.3	3.6	--

†Crater volume calculation. Tests 1-11, 21-22: 1/6 x V_c from Equation 3.11. Tests 12-20, 23-24: 1 x V_c

Table B1. Normalized crater dimensions

B.4 Calculations of soil volume fraction from photometric analysis

According to Valverde et al. [2003], reflectance vs. soil volume fraction profile has been used to determine the soil volume fraction during the fluidized regime. Other researchers described in Chapter 3 have also used these photometric techniques to determine soil volume fraction (f_s) or soil density. The intensity of the backscatter of light (I) is recorded for various soil volume fractions as depicted in Figure B2. The more closely the particles are packed together (higher soil volume fraction), the higher the number of photons reflected [*Hapke*, 2008], causing an increase in the areal energy density of light recorded by the CMOS sensor of the camera that uses a linear gamma

function. This correlates to a higher reflectance (the ratio of reflected to incident light energy) since the incident light energy on the test section is constant during all experiments.

According to Figure B2, our experiments show a linear correlation between reflectance and soil volume fraction with a correlation coefficient of 0.98. This is in good agreement with experiments performed by Valverde et al., [2003]. We calibrated the reflectance intensity (RI) from high resolution monochromatic images at three different stages: zero soil volume fraction (58 RI = no sand grains), 1.0 soil volume fraction (256 RI = a wooden object with close to unity in porosity) and the nominal soil volume fractions (pre-jet impact) for various granular media. The high RI observed for the 1.0 soil volume fraction case may partially be attributed to specular reflectance [*Hapke*, 2008]. As a result, larger uncertainty in f_s may exist at I greater than ~200 RI. In a separate experiment with similar optical setup, we compressed the fine sand and recorded its porosity (soil volume fraction) and reflectance intensity. We did this for one case and use four data points available to determine the reflectance vs. soil volume fraction relationship (or calibration curve). All experiments were illuminated by 1500 Watts (~10^4 lux) of light (Fig. 3.4C).

More data points can be used to improve the fidelity of this calibration curve, but these results along with other published articles support a linear trend. According to Hapke [2008], this relationship is only valid for soils with an albedo smaller than ~0.9. The empirical equation (Eqn. B31) derived from this curve for crushed walnut shells sized to fine sand determines the soil volume fraction from the reflectance intensity of high speed and high resolution monochromatic images.

$$f_s = \frac{I - 65.344}{199.15} \quad \text{(B31)}$$

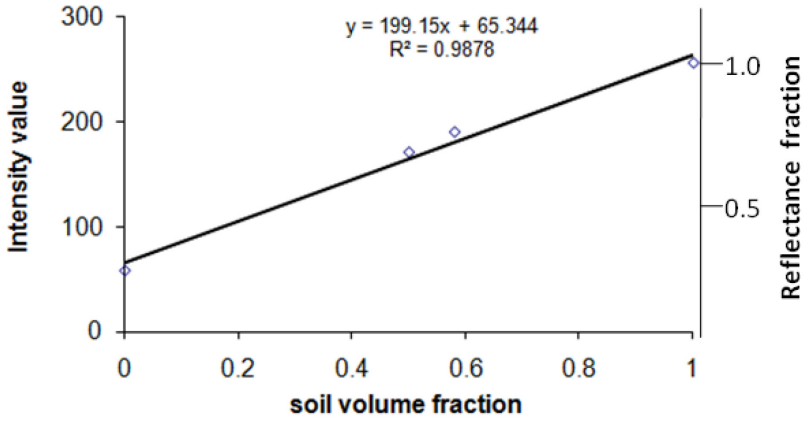

Figure B2. Reflectance vs. soil volume fraction for laboratory simulations with fine sand simulant composed of crushed walnut shells (Tests 4-20).

B.5 Calculations of radial distance of dust lifting by VSE and crater volume ratio

Conservation of mass of the rocket exhaust plume is applied in determining the radial distance at which VSE dominates (Eqns. B32 and B33). We assume that the compressibility effects of the impinging plume is negligible at large radial distances (r) from the centerline (e.g., outside the crater). Assuming steady-state, the freestream velocity (u_∞) at the centerline height (z) of the exhaust plumes (Eqns. B34 and B35) needs to be larger than the threshold freestream velocity ($U_{\infty t}$) to move sand grains [*Greeley and Iversen*, 1985]. The jet mass flow rate from all 12 nozzles, $\dot{m}$, at the impingement region were approximated from the nozzle exit conditions. The threshold freestream velocity is dependent on u_{*t} (Eqn. 3.6), the aerodynamic roughness length (z_0) and the von Karman constant (κ) and described by equation B34. The aerodynamic roughness length is the height above the surface at which the flow velocity is zero and an increase in this length scale increases the value of shear stress required to initiate grain movement. The roughness length is dependent on the sand grain size. Hence, the radial distance at which VSE lifts sand grains can be calculated from equations B32-B35.

$$\frac{\partial \rho_a}{\partial t} + \nabla \cdot (\rho_a u) = 0 \qquad \text{(B32)}$$

$$\dot{m} = \rho_a u A = \rho_a u_\infty \pi r^2 = \text{constant} \qquad \text{(B33)}$$

$$z_0 \approx \frac{2\bar{d}}{30}; U_{\infty t} = \frac{1}{\kappa} u_{*t} \ln\left(\frac{z}{z_0}\right) \qquad \text{(B34)}$$

$$u_\infty(z) > U_{\infty t} \quad \text{Lifting of sand grains} \qquad \text{(B35)}$$

We calculated the volume fraction of the landing site within the Phoenix workspace that was eroded and denoted this term as the crater volume ratio. This is the ratio of crater volume calculated from Section 3.2.2, V_c, to a reference soil volume, V_{ref} which is the amount of undisturbed regolith (prior to landing) that extends to a radius of 40D from the spacecraft centerline (Eqn. B36). This is approximately the Phoenix work space area. The total crater volume is calculated (Eqn. 3.10) from the erosion caused by a pair of Phoenix thrusters and multiplied by six to represent all the REMs as depicted in Fig. 3.3A. The average crater volume ratio is obtained from experiments with soil depths of 5 cm and 20 cm with each type of simulant at Mars atmospheric pressure (Tests 1, 2, 9, 20, 21-24). These ratios derived from the experiments are compared to the crater volume ratio calculated at the Phoenix landing site (Appendix B.1). We approximate the Phoenix landing site by a flat surface with soil of uniform depth over an impermeable layer (subsurface ice).

$$\text{Crater Volume Ratio} = \frac{V_c}{V_{ref}} = \frac{V_c}{\pi(40D)^2 l} \qquad \text{(B36)}$$

B.6 Images of rocket plume – induced cratering of landing sites from previous spaceflight missions to Mars and the Moon

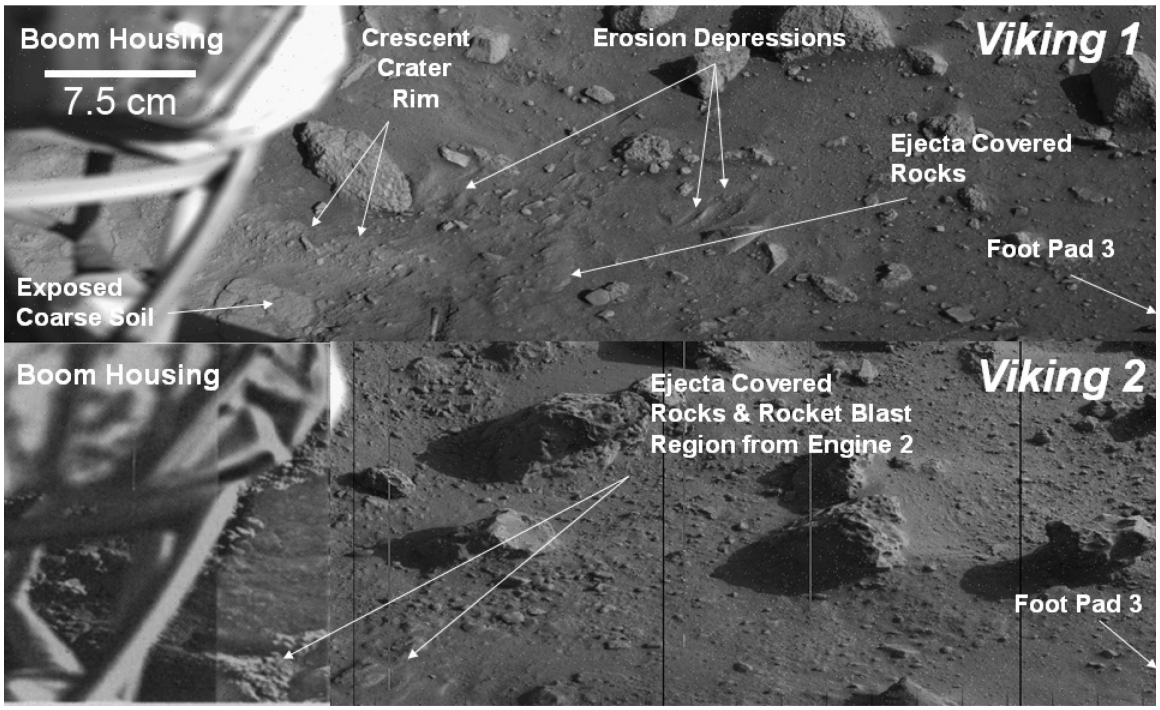

Figure B3 Rocket plume-induced erosion of the Viking 1 and 2 Landing Sites at the mid-latitude regions of Mars. Minor cratering observed 30 cm from the engine centerline (left side of image). Camera Images: 12A01-BB1 and 12A081-BB1. *Courtesy of NASA Planetary Data System*.

Figure B4. Rocket plume-induced erosion of the Apollo 12 Landing Site at the mid-latitude regions of the Moon. Lunar descent engine observed at the top of the figure [NASA AS11-40-5920] *Courtesy of NASA* . Surface scrubbing mainly observed and noted by astronauts Neil Armstrong and Buzz Aldrin [*Orloff and Harland*, 2006]

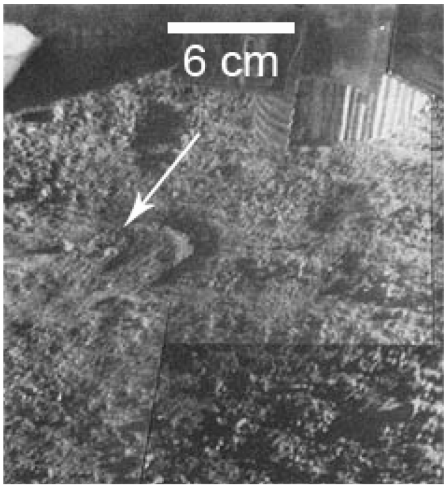

Figure B5. Rocket plume-induced erosion of the Surveyor 6 Landing Site at the mid-latitude regions of the Moon. Crater site shown by white arrow. *Courtesy of NASA.,* Crater depth was observed to be less than 1 cm. [*Mason and Nordmeyer*, 1969]

B.7 Shadowgraph and Schlieren images of shock waves in gas media

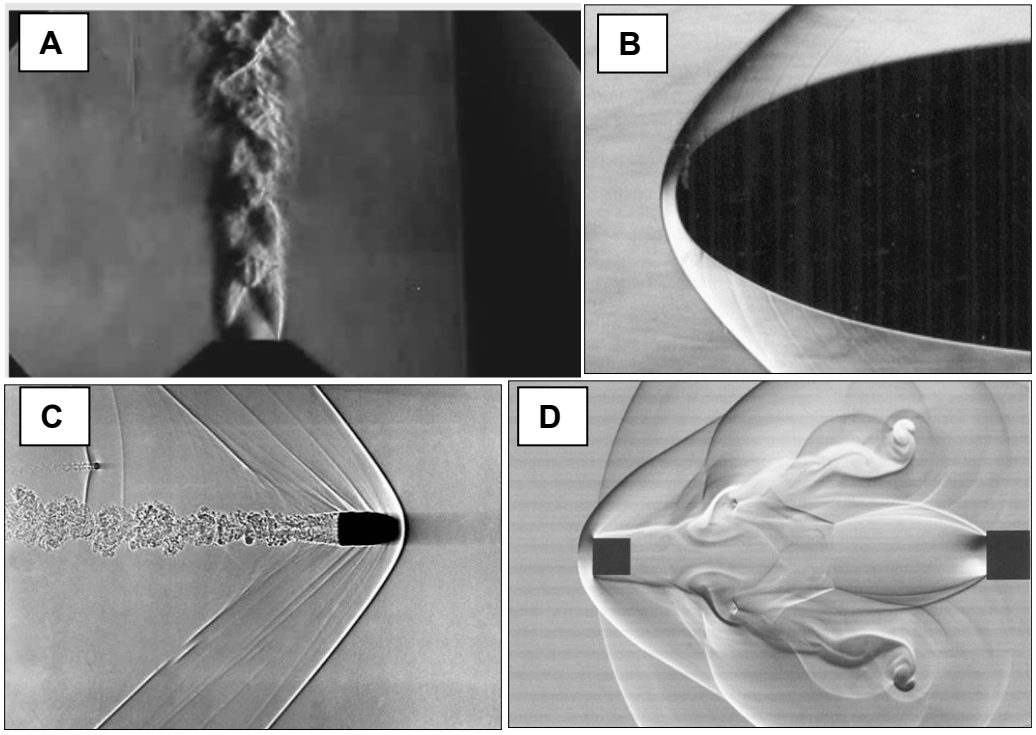

Figure B5. (A) Shadowgraph images of helical instability in an underexpanded jet with a stagnation pressure to ambient pressure ratio of 4. *Courtesy of Laboratory for Turbulence Research in Aerospace and Combustion (LTRAC) at Monash University*. (B) Schlieren image of supersonic flow over a bluff body. *Courtesy of Avco Everett Research Laboraotry, Inc*. (C) Shadowgraph of a bullet traveling at Mach 1.5. *Courtesy of Rochester Institute of Technology*. (D) Computer generated Schlieren image of emergence of supersonic bullet.

APPENDIX C

Cratering on planetary bodies due to spacecraft landings

C.1 Introduction

Due to increasing payload mass requirements and landing accuracy to improve science return, landed missions to Mars and the moon must use retro-propulsive engines to achieve their final propulsive descent to the surface. In 2012, the Mars Science Laboratory (MSL) will be the latest NASA rover to use retro-propulsive descent with the addition of a sky-crane maneuver to increase altitude above the surface at engine cut-off at ~6 m above the surface.

The quantification of surface alteration that occurs as a result exhaust plume interactions during landing is an engineering and science challenge [*Scott et al*., 2006]. The reflected plumes can entrain the eroded media resulting in a particulate-environment with the potential to damage coatings and contaminate mechanisms and instruments on the lander. The hot exhaust gases, namely ammonia (NH_3), can also present a thermal and compatibility materials issues. The dusty environment and ionized species in the plume can create radar interference [*Pollard et al*, 2007; *Ho et al*., 2007]. Lastly and most importantly, the cratering that results beneath the plume can both alter the chemical state and mechanical stability of the landing site with obvious scientific and engineering implications.

To quantify this environment a subscale test program was conducted to measure the flux of entrained particulates and resultant excavation from exhausting a standard Mars Landing Engine into representative Martian media. These results are compared to both spaceflight data and previous experimental studies conducted in support of the NASA Apollo, Surveyor, Viking and Phoenix planetary missions. Findings from this research program and their theoretical context are presented in this Appendix.

Underexpanded, supersonic exhaust plumes impinging the surface during landing create a complex environment for the lander and rover (Fig. C1). Due to the well collimated nature of these plumes at martian atmospheres (Chapter 2) in addition to

limited energy dissipation in the shock-cell structure, these plumes intersect the surface with high (>2000 Pa) surface impingement pressure resulting in various cratering processes. As observed in Section A.5.3, the MLE plumes remain collimated to distances of greater than ~35*d*.

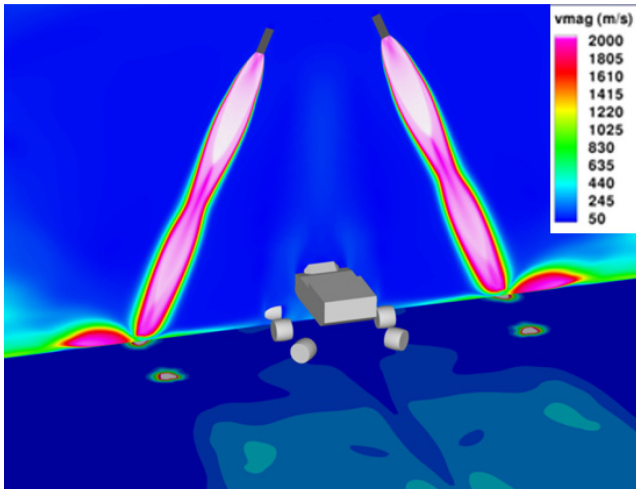

Figure C1. Numerical simulation of velocity magnitude from two engines impinging the surface for a sky-crane landing architecture. Note the location of the rover between the reflected plumes.

The plume impingement ground-interaction environment is dependent upon the thruster exit plane properties, Mars ambient environment (pressure, density), and soil properties. The soil mechanics applicable to this environment include viscous shear erosion (VSE), bearing capacity failure (BCF), diffusion-driven flow (DDF) [*Metzger et al*., 2009], diffused gas erosion [*Scott and Ko*, 1968] and explosive erosion (DGEE) (see Section 3.4).

VSE describes removal of media by surface shear forces from the impinging jet. VSE is characteristic of highly over-expanded exhaust plumes which lead to a rapid dissipation of the shock structure and modest surface pressures (see Section 3.5.1). VSE was experienced by the Apollo program where the vacuum environment of the lunar surface resulted in diffuse, un-collimated plume expansion. Due to the modified 18-nozzle Viking engines which reduced the ground pressure below the threshold value due to enhanced turbulent mixing, VSE was the dominant mechanism leading to shallow craters [*Shorthill et al*, 1976]. VSE is achieved when the shear strength (τ_s) of the soil is

exceeded by the shear stress of the impinging jet (τ_j) as shown in equation C1. This is further characterized by the threshold friction velocity by *Greeley et al*., 1988 which states that erosion rate will increase when there is larger deviation between plume and threshold friction velocities.

$$\tau_s - \tau_j < 0 \quad (C1)$$

BCF, sometime referred to as pressure cratering, occurs when the gas impingement pressure or normal stress (σ) exerted by the jet exceeds the shear strength (τ_s) of the soil (see Section 3.5), resulting in cratering of the media [*Metzger et al*., 2009]. This process usually occurs in conjunction with diffusion-driven flow.

$$\tau_s - \sigma < 0 \quad (C2)$$

As first discovered by the Viking era research, Mars landings are sensitive to this mechanism due to the development of highly collimated plumes. This mechanism would dominate over VSE for a threshold with a surface impingement pressures exceeding ~2000 Pa [*Romine et al*., 1973].

The final mechanism of interest shows that the most violent removal of regolith by jet interactions occurs by DGEE as observed during the Phoenix landing (see Section 3.4). This mechanism forced by impinging pulsed jets develops locally fluidized regions and forms cyclic granular shock waves which propagate within the soil media. This led to a large exposure of subsurface water ice (~1.6 m in diameter) under the lander. Temporal and spatial pressure gradients within the soil as described by Darcy's equation (Eqn. C3) may be used to describe this mechanism, as shown in Section 3.6, and diffusion-driven flow (*Longwell et al*., 2002; *Metzger et al*, 2009).

$$\nabla^2 p^2 = \frac{2n\mu}{k}\frac{\partial p}{\partial t} \quad (C3)$$

Where permeability (k), porosity (n), gas viscosity (μ), the soil pore pressure (p), and relevant plume properties define the physics of this type of erosion.

C.2 Methodology

A subscale cold gas thruster test was conducted with an experimental approach similar to that taken of the Phoenix studies (see Chapter 3). The test parameters are

shown in Table C1. As shown in Figure C1, a quarter-scale Viking-type Mars lander engine with a nozzle exit diameter (*d*) of 5 cm was constructed and mounted to a quarter symmetry test-bed with a 22.5 degree cant angle. Two clear baffle planes at 90º on either side of the engine were used to simulate the neighboring thruster plumes as shown in Figure A2, representing a nominal configuration of 4 engines interacting with each other as discussed in Section 2.6. The nozzle geometry and configuration were simulated to match the dimensions of the MSL descent stage spacecraft. Quarter symmetry was selected to minimize complexity and cost of multiple engine operation. It is also known that the stagnation plane interaction with neighboring jet plays a major role in the erosion process [*Romine et al*., 1973]. A high-speed video camera was positioned to capture the erosion dynamics through the baffle plane at the impingement site.

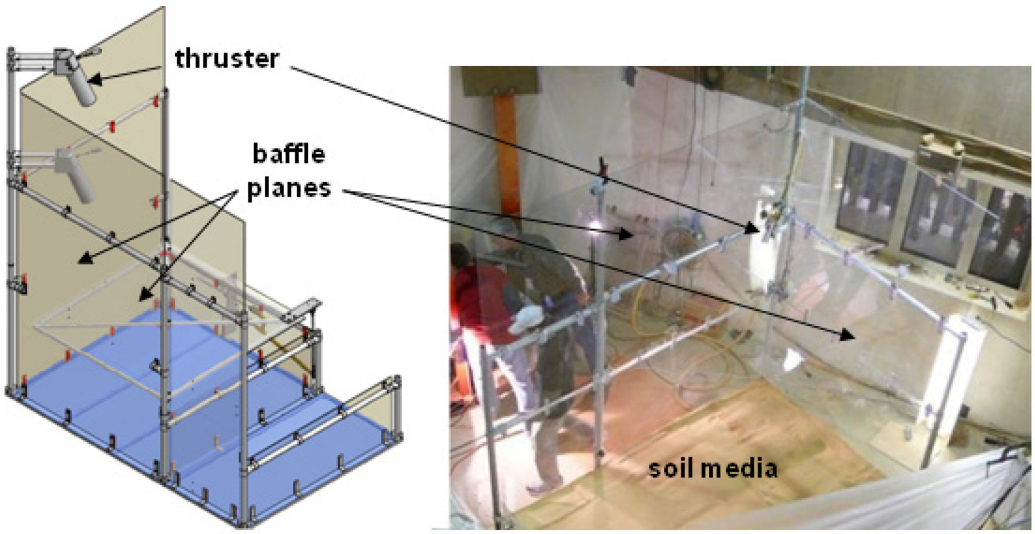

Figure C2. (Left) Schematic of test-bed indicating thruster mounting location, altitude variation, and symmetry planes which are similar to the configuration of the MSL descent stage. (Right) Photo of test-bed with soil media in place at NASA Ames Research Center.

Similarity parameters were used to scale the earth-based test to represent a Mars landing environment, i.e. the plume expansion and gravity. These parameters are tabulated in Table 3.6 and extensively described in Section 3.2.1. The soil cohesion, porosity, angle of repose, and ambient pressure conditions were similar to that experienced for a normal Mars landing. Two particle sizes were investigated, 100 and 1000 μm, intended to represent the bimodal distribution of Mars. The test soil media are ground walnut shells with 1/3 the density of pure silica (primary Mars soil constituent).

The lower density of the test-media provides Froude scaling for the earth's higher gravity relative to Mars, therefore matching the ballistic coefficient simulating lifting, entrainment, and particle trajectories expected in a 1/3 gravity environment of Mars. Also, erosion and deposition rates scale with densimetric Froude number [*Greeley et al*, 1985]. The operating gas is nitrogen yielding a ratio of specific heats similar to that of the hydrazine exhaust products (NH_3, N_2, H_2). Two ground slopes were investigated; 0 and 22.5 degrees. As the engine was mounted at 22.5º, a normal impingement angle was achieved by raking the soil media to achieve a 22.5º ground slope.

The test was conducted in a large vacuum chamber at NASA Ames Research Center Planetary Aeolian Laboratory (PAL). As mentioned previously, matching Mars ambient surface pressure is required to simulate the supersonic plume expansion and gas diffusion into the soil bed.

Parameter	**Value**
Nozzle Diameter (cm)	5
Jet Expansion Ratio	4.3-0.0
Mach Similarity Parameter	15
Mach Number	5.1
Froude Number	300 - 50
Reynolds Number	25-15 x 105
Shear strength parameter	~0.6
Normalized threshold friction velocity	0.04 - 0.01
Ambient Pressure (Pa)	950-650
Plume Gas	N_2
Ratio of Specific Heats	1.4
Media Particle size (μm)	100,1000
Exit Pressure (Throttle level) (Pa)	2800 – 850

Table C1. Test parameters

The test matrix explored soil erosion as a function of engine throttle level, altitude above the surface, ground slope, and media size (Table C2). Run durations were for 1 s each. High-speed video (500 frames per second) of the approximate axisymmetric crater formation and post-test measurement of eroded depth and diameter were used to obtain erosion rate (instantaneous and average). The quarter-space technique was used to adequately visualize the crater growth process. Throttle conditions were determined and controlled from a pressure transducer in the engine chamber and pressure regulator and valve in the feed system. Particle tracking of the video data was also performed to determine that particle entrainment velocities. Most importantly, these tests were all done

at steady jet conditions (not pulsed) to similar throttle conditions expected during the MSL sky-crane maneuver.

Test	Duration (s)	Media (μm)	Ground Slope (deg)	Non Dimensional Altitude	Throttle (%)
2	1	100	0	35	60
4	1	100	22.5	35	60
5-8	4	100	0	35	100,60,30,60
12-13	2	100	22.5	50	100,60
14-16	3	1000	22.5	35	100,60,30
17-18	2	1000	22.5	50	100,60
19-21	3	1000	0	35	100,60,30
22-23	3	1000	0	50	100,60,60

Table C2. Test matrix.

In order to provide a consummate comparison wherever feasible of cratering due to spacecraft landings from both spaceflight data and experiments, we calculated the erosion rates, densimetric Froude number, threshold friction velocity and jet expansion ratio for all cases in terrestrial, lunar and martian environments. All erosion rates recorded are calculated from the final crater profiles. We use a paraboloid equation (Eqn. 3.10) to calculate the final crater volume. The mass flow rate, thrust and nozzle exit conditions are calculated from isentropic relations and measured stagnation chamber pressures. The densimetric Froude number is obtained from particle properties and nozzle exit conditions. The erosion rate is normalized by the exhaust mass flow rate. The values for controlled tests and spaceflight data are indicated by open and closed symbols, respectively. The square, circle and triangle symbols indicate VSE, BCF/DDF and DGEE dominant processes, respectively. These erosion processes are ascertained from high-speed visual imaging, ground pressure profiles and final crater morphologies characterized in Chapter 3. The spaceflight derived data indicated as solid symbols are more approximate due to limited visual observations of the altered landing site and high variability in the regolith's particle sizes.

C.3 Results

High speed video data was collected for all 23 runs listed in Table C2. High speed imaging revealed that bearing capacity failure and diffusion-driven flow of the soil was the primary erosion mechanism as observed in Section 3.5.2. This process is shown for

the 100 (Fig. C3B) and 1000 μm media (Fig. C3A) respectively. After steady supersonic jet impingement with the surface, the soil was excavated into a cylindrical crater with an average diameter of ~6 cm within 0.8 s for both soil media. The granular flow was significantly more turbulent and the profile was more parabolic for the larger media. Particle tracking of the video data yielded initial entrainment velocities on the order of 0.1 to 2 m/s, depending on the condition and time in the excavation process. Rapid collapse and filling of the transient crater after engine shut-down leads to the post-test crater image shown in Figure C4B. Figure C4A shows the differences in soil depth prior to plume impingement, during maximum cratering, and after the re-deposition of the soil particles. As a result, the average erosion rates for these processes are much smaller than those observed from transient erosion rates. For experimental tests done at earth atmospheric pressure resulting in a highly over-expanded exhaust plume, we observe minimal to no cratering at altitudes of 35*d*.

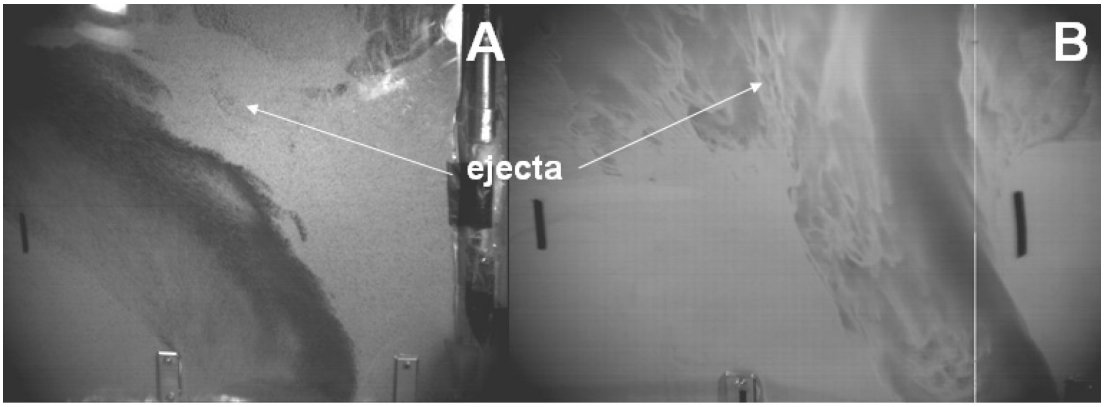

Figure C3. High-speed image at maximum crater growth for Test 19 (A) and Test 5 (B). See Movie D9 and D10.

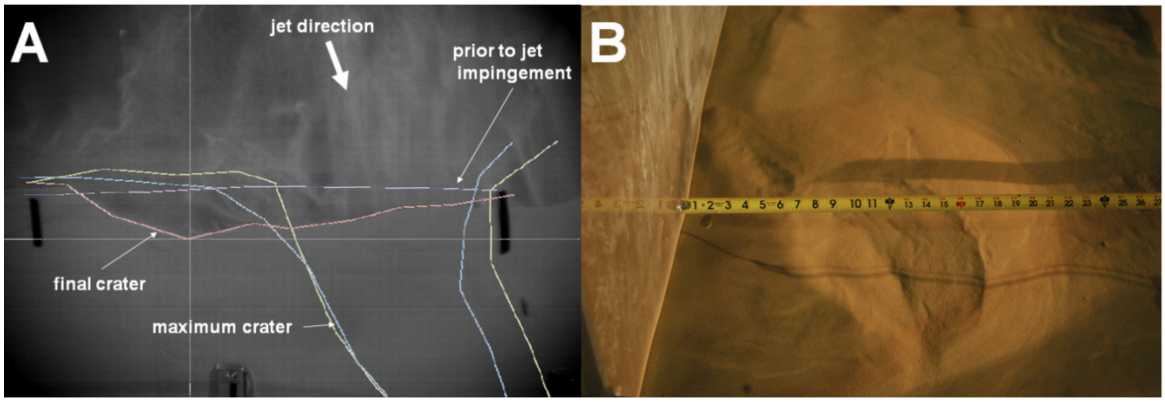

Figure C4. (A) Image has an overlay that shows the image post processing analysis that captured the crater evolution of Test 2, allowing measurement of the instantaneous and average erosion rate. (B) Image of a post-test crater of Test 2.

Figure C5 is a plot of the measured erosion rate of tests conducted at an altitude of 35*d*. The overall finding is that the erosion rate was highly dependent on particle size, throttle level, and ground slope. There was a non-linear, direct dependence with throttle level, related to the nonlinear increase in surface impingement pressure from the jet with the soil. The normal impingement angle significantly increased erosion, relative to the cases where the jet was at a 22.5 degree angle relative to the ground. The 1000 micron media also experienced a higher erosion rate for the same altitude and throttle level, likely related to the increased porosity and enhanced jet penetration which may have resulted in a larger contribution to diffusion-driven flow. The altitude dependence was not clear. The finding here is that ground erosion is most sensitive to throttle level and ground slope and to a lesser degree altitude.

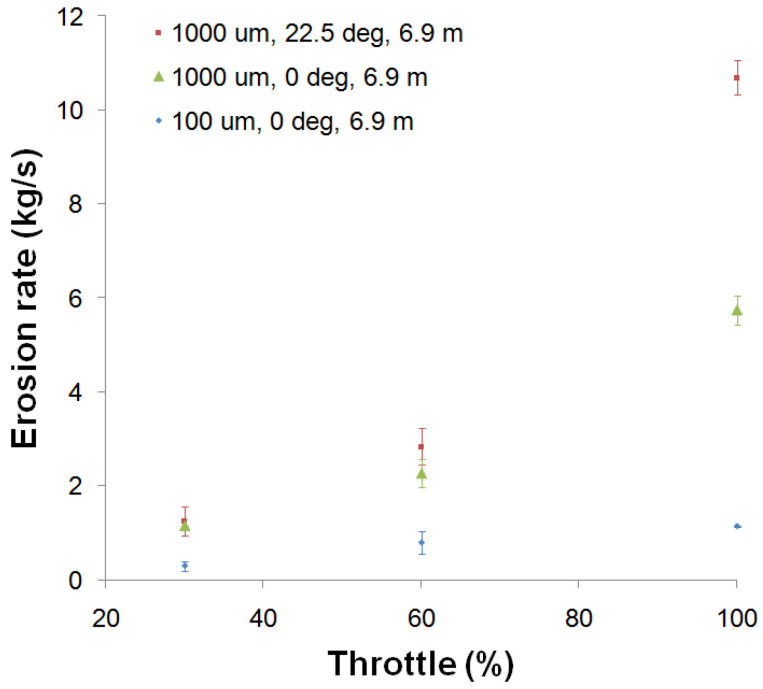

Figure C5. Erosion rate as a function of throttle level, particle size, and ground slope, for a non-dimensional altitude of 35*d*.

To elucidate the differences between the various erosion processes due to planetary landings (e.g. VSE, BCF/DDF, DGEE and DGE), we have tabulated in Table

C3 the crater profiles (depth and size) from spaceflight missions and experimental tests in support of these missions. Since there is usually more than one rocket nozzle used during landing, we normalize the crater dimensions with respect to the equivalent nozzle diameter (d_{eq}) (Eqn. C4) where b is the number of nozzles and A_e is the nozzle exit area.

$$d_{eq} = \sqrt{\frac{4bA_e}{\pi}} \qquad \text{(C4)}$$

Studies	Erosion depth (y/d_{eq})	Erosion size (x/d_{eq})	Comments
APOLLO 11	~0.0	~1.2 (erosion)	Surface scrubbing
SURVEYOR 5 & 7	<0.1	~9.3 – 3.1 (erosion)	Surface scrubbing
VIKING 1	~0.2 – 0.1	~5.0 – 3.8 (crater)	10 cm x 20 cm crater
VIKING 2	~0.3 – 0.2	~8.8 – 6.3 (crater)	3 6-cm diameter craters
PHOENIX	~0.8 – 0.5	~47.2 (erosion) ~14.5 (crater)	Exposed ice (~12.9) 3 ~85-cm diameter craters
Viking WSTF Test 1 Lunar Nominal	<0.1	~0.0	No craters
Viking WSTF Test 2 Sand dune	~0.2	~7.6 (crater)	18 5-cm diameter craters
Phoenix ARC Test 1 S-type walnut shells	3.0 – 0.8	~23.2 – 21.8 (crater)	Extensive cratering
Phoenix ARC Test 2 B-type walnut shells	3.1 – 0.8	~15.8 (crater)	Exposed surface (~12.9) Extensive cratering
Phoenix ARC Test 3 F-type walnut shells	3.1 – 0.8	>31.7 (crater)	Exposed surface (~11.6) Extensive cratering
Phoenix ARC Test 4 C-type walnut shells	0.6	3.5 (crater)	Minor erosion
MSL ARC Test 1 S-type walnut shells	~0.7	~6.2 (crater)	Transient steep crater
MSL ARC Test 2 C-type walnut shells	~0.7	~8.0 (crater)	Transient steep crater
Phoenix ARC Earth Test 1 S-type walnut shells (pulsed)	0.5	4.9 (crater)	Parabolic crater
Phoenix ARC Earth Test 2 S-type walnut shells (steady)	1.0	2.9 (crater)	Parabolic crater

Table C3. Normalized mean erosion depth and size for various planetary surface missions and vacuum chamber experimental tests.. Measurements are made per descent engine cluster.

C.4 Discussion

Particulate ejecta and their subsequent entrainment in the reflected plume resulted. The collimated nature of the plume and its effect on soil erosion can be seen in Figure C3. The steep cylindrical crater is also formed as influenced by the shock structure which demonstrates large pressure gradient loads. At altitudes below 50d, the ground

pressure with respect to changing altitude is non-linear due to whether the shock cell near the surface is within the expansion or recompression regime. This leads to the smaller dependence of altitude on erosion rates.

Although there is significant scatter in the data due to various initial conditions of each study, it can be seen from the jet expansion ratio vs. erosion rate profiles, in Figure C6 that the most erosion takes place within the Mars atmospheric regime. The jet expansion ratio between 2 and 5 leads to a well-collimated shock structure which leads to large ground pressure values as observed in Chapter 2. Hence, the atmospheric environment, ground pressure footprint and profile are important to accurately simulate the erosion processes. A decrease in erosion rates is observed for the lunar (e >100) and terrestrial (e <1) atmospheric regimes. This shows similar correlation to normalized ground pressure-expansion ratio profiles shown in Figure A12.

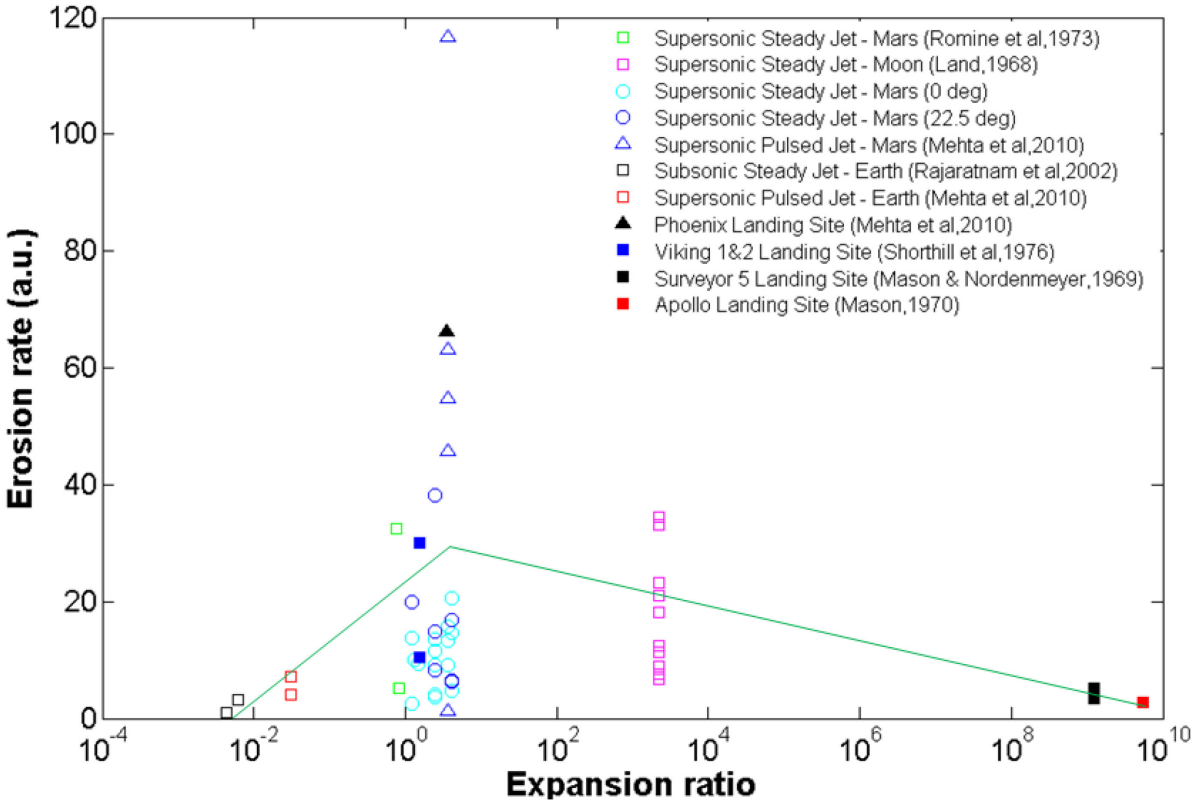

Figure C6. Normalized erosion rate vs. jet expansion ratio for both controlled experimental studies and spaceflight missions. [*Romine et al*., 1973; *Land and Scholl*, 1969; *Rajaratnam et al*, 2002; *Shorthill et al*, 1976; *Mason and Nordmeyer*, 1969*; Mason*, 1970]

The most prevalent cratering mechanism during spacecraft landings to date is VSE as observed for the NASA Apollo, Surveyor and Viking missions. This occurs for relatively low ground pressure values when the shear stress forces of the jet exceed the cohesive and friction forces of the granular medium. Figure C7 shows the characteristic erosion rate profile, normalized erosion rate vs. densimetric Froude number (*Fr*), of all jet-induced erosion processes on planetary bodies due to spacecraft landings. Relative to the large variations of particle diameter (ranging from 1 μm to greater than 1500 μm), the ratio of dynamic pressure of the exhaust plumes to specific weight of granular media for each study are similar for each erosion process. For VSE dominant process (shown as a green curve in Fig. C7), there is a semi-log linear rise in erosion rate (gravitational regime) to a maximum at *Fr* ~50 and then a decline (shear strength regime) to *Fr* ~1000. Since the dynamic pressure to specific weight is relatively constant for all tests within each erosion mechanism, with decreasing *Fr*, the granular particle sizes increase which inhibits its' movement due to increase in particle weight and this is known as the gravitational regime. With increasing *Fr*, the particle sizes decreases which results in an asymptotic decrease in erosion rates due to the increase in the interparticle cohesive forces (Fig. C7) and accounts for the shear strength regime. These curves were developed from landing site and experimental data. Scattering of the data is primarily due to variations in specific weight and dynamic pressure. This is further supported by green curve in Figure C8, normalized erosion rate- normalized threshold friction velocity profiles for VSE. It can be seen that as the threshold friction velocity increases, the erosion rate asymptotically decreases for this cratering mechanism due to increases in the interparticle forces. This is also observed by the derivation of the particle mass transport rate equation by Greeley et al. [1988].

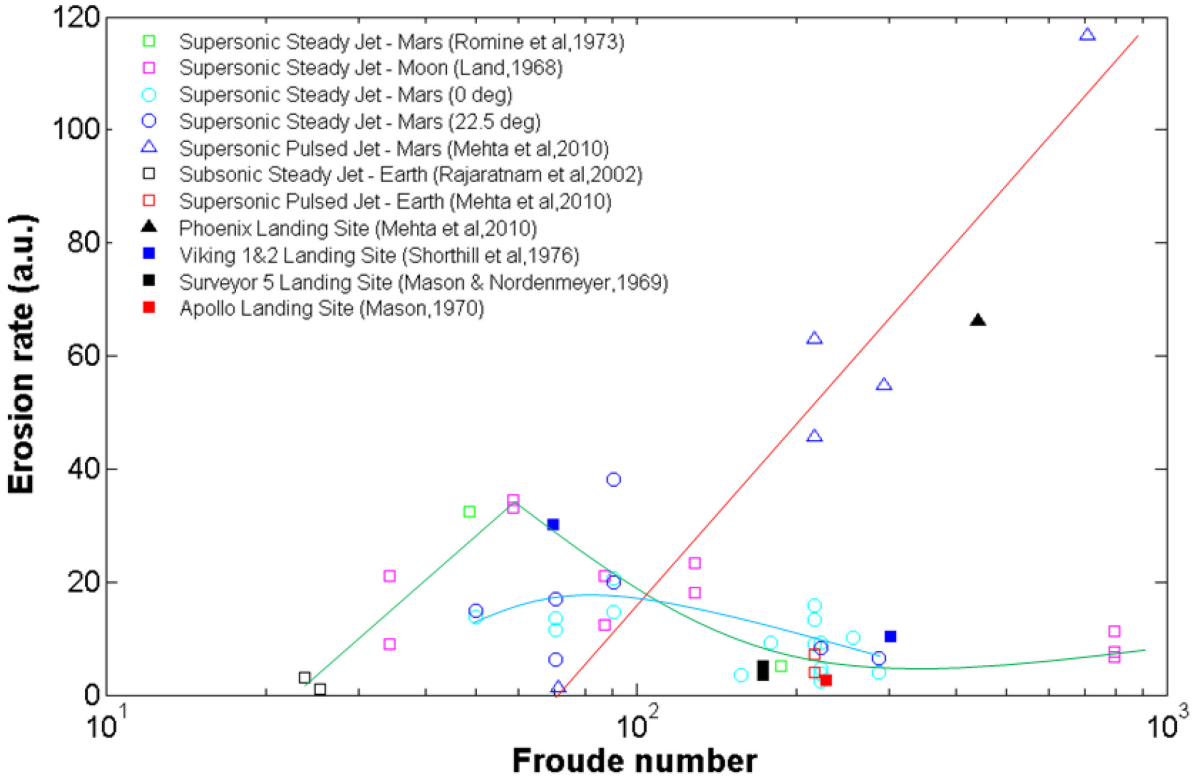

Figure C7 . Normalized erosion rate vs.densimetric Froude number for both controlled experimental studies and spaceflight missions.[*Romine et al*., 1973; *Land and Scholl*, 1969; *Rajaratnam et al*, 2002; *Shorthill et al*, 1976; *Mason and Nordmeyer*, 1969*; Mason*, 1970]

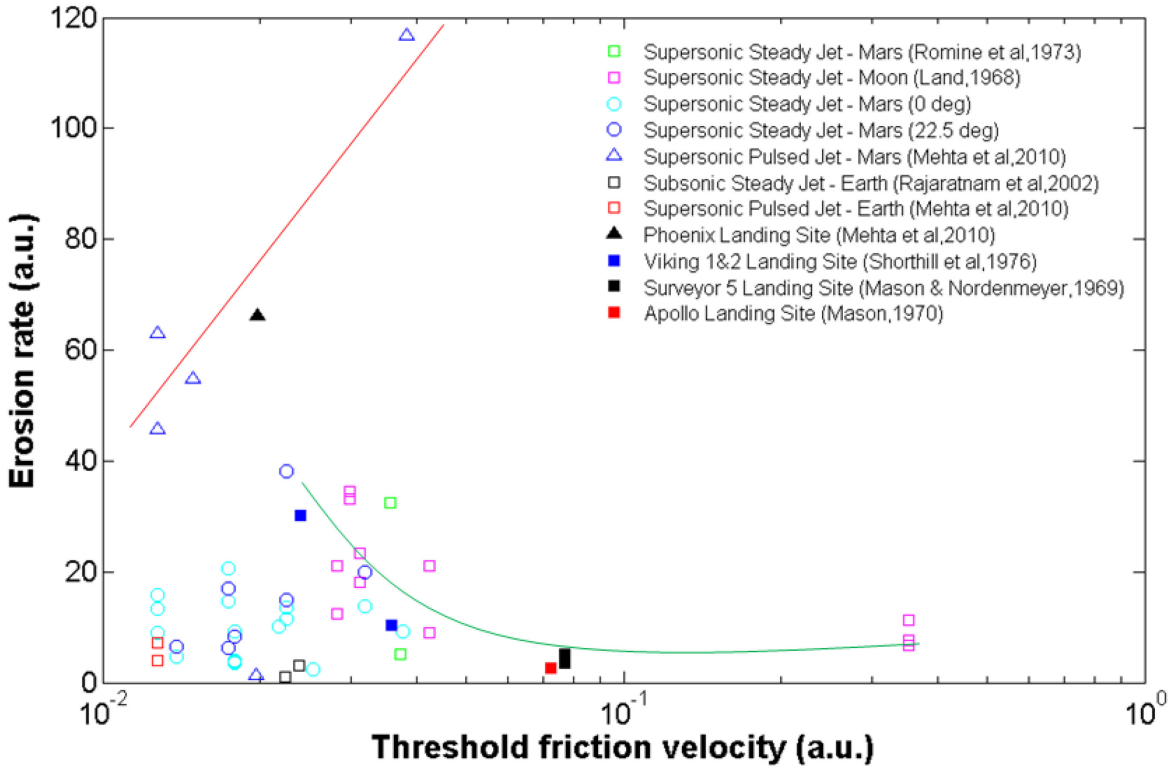

Figure C8. Normalized erosion rate vs. normalized threshold friction velocity for both controlled experimental studies and spaceflight missions. [*Romine et al*., 1973; *Land and Scholl*, 1969; *Rajaratnam et al*, 2002; *Shorthill et al*, 1976; *Mason and Nordmeyer*, 1969*; Mason*, 1970]

The second erosion process which may dominate is the combination of bearing capacity failure (BCF) and diffusion-driven flow (DDF) which was observed from recent experiments performed in this study. This occurs when the pressure loads of the jets exceeds soil shear strength and forms steep parabolic/cylindrical craters that are partially redeposited immediately after jet termination. The erosion rate and final crater size are on the average larger than those observed for VSE as shown in the blue curve in Figure C7. Similar characteristic Froude-erosion rate curves as observed in VSE are seen where an asymptotic decrease in erosion rate is observed due to the shear strength regime. No characteristic trend of the erosion rate as function of the threshold friction velocity is observed for the BCF/DDF process.

The new erosion process named diffusive gas explosive erosion (DGEE) due to pulsed underexpanded impinging jets in tenuous atmospheres does not obey this characteristic erosion rate curve for the range of *Fr* studied. We observe a semi-log linear increase in erosion rate with *Fr* (red curve in Fig. C7) and the decreasing trend are not observed. This is mainly due to the local fluidization and granular shock wave formation and propagation associated with this erosion mechanism. The fluidization breaks interparticle forces, separating the particles from one another, and as a result, the erosion rate is mainly dependent on the pressure gradient, shock strength and particle weight. Hence, craters in fine simulant are the largest as indicated in Figure C7. Soil permeability and atmospheric pressure both affect the developing pressure gradient. The shear strength regime is absent for the DGEE process or it may be observed at much higher *Fr* numbers. This is also supported by erosion rate-threshold friction velocity profiles shown by the red curve in Figure C8 where we observe a similar linear increase due to a stronger correlation to particle weight (size). DGEE produces erosion rates many orders of magnitude larger than other jet-induced cratering mechanisms. To provide a qualitative assessment, the erosion effects at the Phoenix landing site are compared to previous planetary missions (Table C3).

Erosion rate characteristic curves most particularly can provide information on the amount of external cohesion present. The erosion rates are averaged values from tests

performed with dry martian simulant at depths between 5 cm and 20 cm, the range recorded at the landing site [*Smith et al*, 2009]. From the red curve in Fig C7 and particle size distribution determined by the Optical Microscope [*Goetz et al.,* 2010], we show that external cohesion is present at the Phoenix landing site due to a deviation from the DGEE characteristic curve. External cohesive agents would show a decrease in normalized erosion rates for similar *Fr*. The external cohesion may be attributed to salts and pockets of brines within the regolith as observed by Renno et al. [2009]. If we can quantify the cohesion present, these curves can more accurately determine soil properties at various landing sites. More importantly, we may be able to assess the effect of brines on soil cohesion.

It should be noted that these trends are mainly to provide qualitative insight into the cratering physics associated with jet interactions. More in-depth analyses for all erosion processes need to be investigated and correlated to this study.

C.5 Conclusions

Rocket engine plumes interacting with the ground on Mars result in a particulate erosion and contamination environment. Experimental results obtained from this study indicate that the erosion caused by steady supersonic jets at an altitude of ~35*d* is dominated by BCF/DDF. The resultant erosion rate was found to be highly dependent on particle size, throttle level and ground slope. A smaller correlation was seen with altitude due to under-expanded shock-cell structure. More importantly, erosion rates are directly dependent on ground pressure which is a function of the jet expansion ratio. To properly simulate the erosion dynamics due to impinging rocket plumes, this study shows that the jet expansion ratios between full-scale and subscale tests should be satisfied. Densimetric Froude number and threshold friction velocity parameters show a characteristic curve for both the VSE and to a lesser degree BCF/DDF processes. However, DGEE does not obey these characteristic curves due to significantly different cratering physics explored in Chapter 3.

APPENDIX D

Supplementary Movies

All supplementary movies can be found at http://deepblue.lib.umich.edu.

Movie D1: Animation of the Entry, Descent and Landing (EDL) sequence of the NASA Phoenix Mars spacecraft. Courtesy of NASA/JPL-Caltech/U. of Arizona. http://phoenix.lpl.arizona.edu/videos_pr.php

Movie D2: Transient axisymmetric numerical simulation of the Mach contours for a pulsed supersonic jet interacting with a flat surface at a nozzle-surface distance of 25*d*.

Movie D3: Transient axisymmetric numerical simulation of the Mach contour and spatial ground pressure profiles for a pulsed Phoenix REM plume interacting with a flat surface at a nozzle-surface distance of 8.4*d* (Phoenix touchdown altitude). Courtesy of Lockheed Martin Space Systems.

Movie D4: High speed video of the 'explosive erosion" dynamics observed in Test 9 (Table 3.4) at 500 frames per second with a resolution of 1280 by 1024 pixels. The camera was placed approximately normal to the baffle plane, imaging approximately a 2-D axisymmetric section of the crater growth process. The time duration of the video is ~1.2 s. Granular shock waves, soil fluidization regions and ejecta particle velocities were tracked. Similar dynamics were observed for the silt and silt/fine sand simulants.

Movie D5: High speed video of the viscous shear erosion dynamics observed in Test 17 (Table 3.4). The erosion dynamics due to the viscous shear erosion process is studied using similar camera settings as Movie D4. The time duration of the video is ~1.7 s. Similar dynamics are also observed at lower impingement pressures on Mars, indicating VSE at Mars atmosphere.

Movie D6: High speed video of bearing capacity failure/diffusion-driven flow dynamics in Test 18 (Table 3.4). The erosion dynamics due to the bulk shear failure process is studied using similar camera settings as Movie D4. The time duration of video is ~1.6 s.

Movie D7: Transient simulation of ground pressure spatial profiles for Test 2 (Table A3).

Movie D8: Transient simulation of ground pressure spatial profiles for Test 22 (Table A3).

Movie D9: High speed video of bearing capacity failure/diffusion-driven flow dynamics in Test 19 (Table C2). This is for a 22.5 degree canted subscale nozzle. The erosion dynamics is studied using similar camera settings as Movie D4. The time duration of video is ~2 s.

Movie D10: High speed video of bearing capacity failure/diffusion-driven flow dynamics in Test 5 (Table C2). This is for a 22.5 degree canted subscale nozzle. The erosion dynamics is studied using similar camera settings as Movie D4. The time duration of video is ~2 s.

APPENDIX E

List of publications derived from this thesis

Peer-Reviewed

1. Renno, N.O. and M. Mehta (2010) Deliquescence, liquid water, and the search for sources and sinks of methane on Mars, *Proc. SPIE,* 7819-13.

2. Mehta, M. and N.O. Renno, (2010) Photometric and broadband spectral evidence for deliquescence and liquid saline water on Mars, *Nature*, in rev.

3. Sengupta, A., J.G. Kulleck, J.W. Van Norman and M. Mehta (2010) Thermal Coating Erosion in Simulated Martian Landing Environment, *Wear*, in rev.

4. Mehta, M, N.O. Renno, M.R. Grover, A. Sengupta, N. Rusche, R.E. Arvidson, W. Markiewicz, M.T. Lemmon and P.H. Smith (2010) Explosive erosion during the Phoenix landing exposes subsurface water on Mars. *Icarus,* in rev.

5. Zent, A. P, M.H. Hecht, D.R. Cobos, G.S. Campbell, C.S. Campbell, G. Cardell, M.C. Foote, S.E. Wood and M. Mehta (2009) Thermal and Electrical Conductivity Probe (TECP) for Phoenix, *J. Geophys. Res.*, 114, E00A27.

6. Arvidson, R.E…M. Mehta et al (2009) Results from the Mars Phoenix Lander Robotic Arm experiment**,** *J. of Geophys. Res*., 114, E00E02.

7. Renno, N.O...M. Mehta et al (2009) Possible Physical and Thermodynamical Evidence for Liquid Water on Mars. *J. of Geophys. Res.*,114, E00E03.

8. Renno, N.O., M. Mehta, B. Block and S. Braswell (2009) The discovery of liquid water on Mars and its implications for astrobiology, *Proc. SPIE*, 7441, 74410C.

9. Plemmons, D. H., M. Mehta, B.C. Clark, S. P. Kounaves, L.L. Peach, N.O. Renno, L. Tamparri and S.M.M. Young (2008) Effects of the Phoenix Lander descent thruster plume on the Martian surface, *J. Geophys. Res.*,113, E00A11.

Conference

10. Renno, N.O. and M. Mehta (2010) The discovery of liquid water on Mars and its implications. 61st International Astronautical Congress, 7553, Prague, Czechoslovakia .

11. Mehta, M. et al (2010) Mars landing engine plume impingement ground interactions, ASCE Conf. Proc., 4th NASA/ARO/ASCE Workshop on Granular Materials in Lunar and Martian Exploration, 366, 17, Honolulu, HI.

12. Mehta, M. et al (2010) Cratering on Planetary Bodies due to Spacecraft Landings, 41st LPSC, Lunar & Planetary Inst., Houston, TX, abst 2350

13. Sengupta, A...Mehta, M. et al (2009) Main Landing Engine Plume Impingement Environment of the Mars Science Laboratory, IEEE Aerospace Conf., paper no.1349.

14. Mehta, M. et al (2008) Erosion Dynamics during Phoenix Landing on Mars, *Eos AGU Trans. Fall Meeting Suppl.*, abst U11B-0028

15. Mehta, M. et al (2007) Characterization of the Impingement Dynamics of Pulsed Rocket Plumes with the Ground at Low Ambient Pressure, AIAA 2007-5707 43rd AIAA/ASME/SAE/ASEE Joint Propulsion Conference & Exhibit, Cincinnati, OH

16. Mehta, M. et al (2006) The interaction dynamics of pulsed retro-rocket plumes with the ground during spacecraft descent on Mars, 4th International Planetary Probe Workshop (IPPW) Proc., NASA JPL, Pasadena.

Peer-review articles in preparation

17. Mehta, M., A. Sengupta, M. Pokora, J.W. Van Norman, N.O. Renno, D.S. Gulick and P.G. Huseman (2010) Underexpanded supersonic plume surface interactions: applications for planetary landings, in prep.

18. Mehta, M., A. Sengupta, N.O. Renno, M. Pokora and L. Hall (2010) Cratering on planetary bodies due to spacecraft landings, in prep.

APPENDIX F

Aerial view of the Phoenix Landing Site on Mars

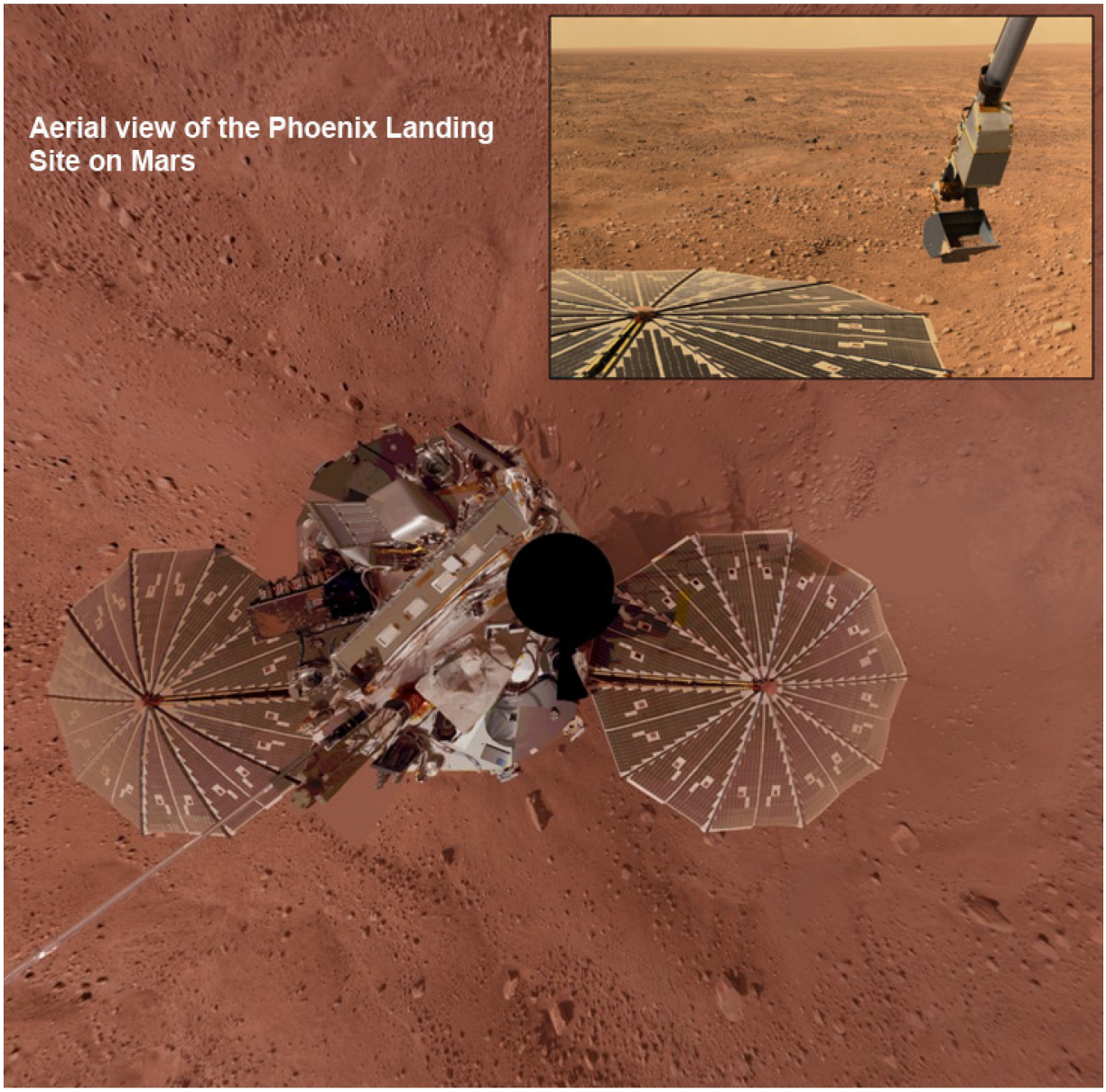

Vertical projection of more than 500 images taken from the Surface Stereo Imager camera showing the NASA Phoenix Lander at the landing site. Courtesy of NASA/JPL-Caltech/U. of Arizona/Texas A&M

BIBLIOGRAPHY

Alexander, J.D., W.M. Roberts and R.F. Scott (1966), Soil erosion by landing rockets, Hayes Int. Corp, Brimingham, AL.

Amarouchene, Y., et al. (2001), Dynamic Sand Dunes, *Phys. Rev. Lett.*, 86, 4286-4289.

Amarouchene, Y., and H. Kellay (2006), Speed of sound from shock fronts in granular flows, *Phys. of Fluids* 18, 3, 031707-1—031707-4.

Anderson, J. D. (2004), *Modern Compressible Flow*, McGraw-Hill, New York.

Arvidson, R. E., et al. (2009), Results from the Mars Phoenix Lander Robotic Arm Experiment. *J. Geophys. Res.*, 114, E00E02.

Atreya, S.K., P.R. Mahaffy and AS. Wong (2007), Methane and related trace species on Mars: Origin, loss, implications for life and habitability, *Planet & Space Science*, 55.

Bailey, E., P. Desai, R. Kornfeld, S. Shaffer, M. Schoenenberger, D. Skulsky (2008), Phoenix EDL Reconstruction, NASA Headquarters Meeting, Washington, D.C.

Balme, M. and A. Hagermann (2006), Particle lifting at the soil-air interface by atmospheric pressure excursions in dust devils, *Geophys. Res. Lett*., 33, L19S01.

Bandfield, J. L. (2007), High-resolution subsurface water-ice distributions on Mars, *Nature*, 447, 64-65.

Bandfield, J.L, T.D. Glotch and P.R. Christensen (2003), Spectroscopic identification of carbonate minerals in the martian dust, *Science*, 301, 5636.

Barenblatt, G. I. (2003), *Scaling*, Cambridge University Press, Cambridge, England.

Bart, G.D. (2007), Comparison of small lunar landslides and martian gullies, *Icarus*, 187, 2.

Bird, R. B. (1996), *Transport Phenomena*, John Wiley & Sons, Madison, Wisconsin.

Boetius, A. and S. Joye (2009), Thriving in salt, *Science*, 324, 1523-25.

Bougie, J., et al. (2002), Shocks in vertically oscillated granular layers, *Phys. Rev. E*, 66, 051301.

Boynton, W. V. et al. (2001), Thermal and Evolved-Gas Analyzer: Part of the Mars Volatile and Climate Surveyor integrated payload, *J. Geophys. Res*., 106, E8.

Boynton, W.V. et al. (2002), Distribution of hydrogen in the near surface of Mars: Evidence for subsurface ice deposits, *Science*, 297, 81.

Braun, R.D. and R.M. Manning (2006), Challenges of Mars Entry, Descent and Landing, IEEE Aerospace Conf., Paper No. 0076, Big Sky, MT.

Buning, P.G., W.M. Chan, K.Z. Renze, D.L. Sondak, I.-T. Chiu, J.P. Slotnick (1993) *OVERFLOW User's Manual, Version 1.6ab,* NASA Ames Research Center, Moffett Field, CA, Jan.

Caesar - Ton That, T. C., et al. (2008) Effects of polyacramide and organic matter on microbes associated to soil aggregation of Norfolk loamy sand, *Appl. Soil Ecology*, 40.

Carling, J. C., and B. L. Hunt (1974), The near wall jet of a normally impinging, uniform axisymmetric, supersonic jet, *J. Fluid Mechanics,* 66, 11-19.

Carter, J. F. Poulet, J.-P. Bibring and S. Murchie (2010), Detection of hydrated silicates in crustal outcrops in the northern plains of Mars, *Science*, 328, 5986.

Chevrier V. F. *et al.* (2009), Stability of perchlorate hydrates and their liquid solutions at the Phoenix landing site, *Geophys. Res. Lett.,* 36**,** L10202.

Choutapalli, I., A. Krothapalli and J.H. Arakeri (2009) An experimental study of an axisymmetric turbulent pulsed air jet, *J. of Fluid Mech.* 631, 23-63

Christensen, E. M., et al. (1967), Surveyor V: Lunar Surface Mechanical Properties, *Science* 158, 6301.

Christensen, P.R. (2003), Formation of recent martian gullies through melting of extensive water-rich snow deposits, *Nature*, 422, 45-48.

Clark, L., and W. Conner (1969a), Exploratory study of scaled experiments to investigate site alteration problems for Martian soft-lander spacecraft, NASA LWP-765, NASA Langley Research Center, Hampton, VA.

Clark, L.V. (1969b). Bi-propellant and monopropellant rocket exhaust impingement effects on a flat plate at simulated Martian pressures. NASA Langley Research Center Working Paper, NASA LaRC WP-720, NASA Langley Research Center.

Clark, L. V. (1970), Effect of retrorocket cant angle on ground erosion – a scaled Viking study, NASA Technical Memorandum. NASA TM X-2075, NASA

Langley Research Center.

Clark, R. N. (1981), Water frost and ice: The near-infrared spectral reflectance 0.65 - 2.5 μm, *J. Geophys. Res.,* 86*,* B4.

Costa, A. (2006), Permeability-porosity relationship: A reexamination of the Kozeny-Carman equation based on a fractal pore-space geometry assumption, *Geophys. Res. Lett.* 33, L02318.

Courant, R., and K. O. Feidrich (1999), *Supersonic Flow and Shock Waves,* Applied Mathematical Science Series, *v21*, Springer Publishing, New York.

Davila, A.F. et al (2010), Hygroscopic salts and the potential for life on Mars, *Astrobiology*, 10, 6.

Dawson, M., G. Brewster, C. Conrad, M. Kilwine, B. Chenevert and O. Morgan (2007), 700 lbf throttling terminal descent engine for Mars Science Laboratory, 40th AIAA/ASME/SAE/ASEE Joint Propulsion Conference, AIAA 2007-5481, Cincinnati, OH.

Delamere, W. A. (2010), Color imaging of Mars by the High Resolution Imaging Science Experiment (HiRISE), *Icarus*, *205,* 38-52.

Desai, P. N. J.L. Prince, E.M. Queen, J.R. Cruz and M.R. Grover (2008), Entry, Descent and Landing Performance of the Mars Phoenix Lander, AIAA/AAS Astrodyn.Conf,7346.

Di Lorenzo, M. and K. Kremer (2008) Phoenix and the Holy Cow, NASA Astronomy Picture of the Day. NASA. http://apod.nasa.gov/apod/ap081112.html

Donaldson, C. D., et al. (1971), A study of free jet impingement part 2: free jet turbulent structure and impingement heat transfer, *J. Fluid Mechanic*s*,* 45*,* 477-512.

Forterre, Y. and O. Pouliquen (2001), Longitudinal vortices in granular flow, *Phys. Rev. Lett.*, 86, 5886-5889.

Frei, T.E., T.L. Fischer and J.M. Weiss (2001), Mars Polar Lander thruster cold start validation testing, 37th AIAA/ASME/SAE/ASEE Joint Propulsion Conf. AIAA 2001-3261, Salt Lake City, UT.

Goetz, W., et al. (2009), Microscopy analysis of soils at the Phoenix Landing Site, Mars: Classification of soil particles and description of their optical and magnetic properties, *J. Geophys. Res.*, 115, E00E22.

Gray, J.M.N.T., Y.-C. Tai and S. Noelle (2003), Shock waves, dead zones and particle-free regions in rapid granular free-surface flows, *J.Fluid Mech*., 491, 161-181.

Greeley, R. and J. D. Iversen (1985), *Wind as a geological process on Earth, Mars, Venus and Titan*, Cambridge University Press, Cambridge, England.

Greeley, R., et al. (1980), Threshold Windspeeds for Sand on Mars: Wind Tunnel Simulations, *Geophys. Res. Lett.*, 7, 2, 121-124.

Greeley, R., et al. (2000), Windblown dust on Mars: laboratory simulations of flux as a function of surface roughness, *Planet. Space Science*, 48, 1349-1355.

Greeley, R. (2002), Saltation impact as a means for raising dust on Mars, *Planet. Space Science*. 50, 151-155.

Greeley, R., et al. (1974), Wind tunnel simulations of light and dark streaks on Mars, *Science*, 183, 4127, 847-849.

Greeley, R., et al. (1982), Rate of Wind Abrasion on Mars, *J. Geophys. Res*., 87, B12, 10009-10024.

Grover, M. R., et al. (2005), Phoenix EDL critical design review report, NASA Phoenix CDR Meeting, NASA JPL.

Gulick, D.S. (2006), Phoenix Mars Lander Descent Thruster Plume/Ground Interaction Assessment, WS-06-002 Lockheed Martin Interoffice Memo, Lockheed Martin Space Systems, Denver.

Haberle, R. M, *et al.* (2001), On the possibility of liquid water on present-day Mars, *J. Geophys. Res.*, *106,* 23317-26.

Hapke, B. (2008), Bidirectional reflectance spectroscopy 6. Effects of porosity, *Icarus*, 195, 918-926.

Hanna, J. C. and R. J. Phillips (2005), Hydrological modeling of the Martian crust with applications to the pressurization of aquifers, *J. Geophys. Res*, 100, 12E01004.

Hecht, *et al.* (2009)*,* Detection of perchlorate and the soluble chemistry of Martian soil at the Phoenix Lander site, *Science,* 325*,* 64-67.

Henderson, B., et al. (2005), An experimental study of the oscillatory flow structure of tone-producing supersonic impinging jets, *J.Fluid Mechanics,* 542*,* 115-137.

Hoefen, T.M., R.N. Clark, J.L. Bandfield, M.D. Smith, J.C. Pearl and P.R. Christensen (2003), Discovery of olivine in the Nili Fossae Region of Mars, *Science*, 302, 5645.

Holsapple, K. A. (1993), The scaling of impact processes in planetary sciences, *Ann. Rev. Earth Planet. Sci.,* 21, 333-373.

Huang, K. (2006), Shock wave propagation in vibrofluidized granular materials, *Phys. Rev*., 73, 041302-1—041302-5.

Huseman, P. G. and J. Bomba (2000), CFD Analysis of Terminal Descent Plume Impingement for Mars Landers, AIAA Thermophysics Conf., 2000-2501.

Hutton, R. E., et al. (1980), Surface erosion caused on Mars from Viking descent engine plume, *Earth, Moon & Planets*, 23, 3, 293-305.

Inman, J.A., P.M. Danehy, R.J. Nowak and D.W. Alderfer (2008) Fluorescence imaging study of impinging underexpanded jets, 46th AIAA Aerospace Sciences Meet., AIAA 2008-619.

Jaeger, H.M., S.R. Nagel and R.P. Behringer (1996) Granular solids, liquids and gases, *Rev. Mod. Phys.,* 68, 1259-1278.

Janos, J. J., and S. Hoffman (1968), Forces and moments produced by air and helium jets exhausting parallel to a flat plate in a near vacuum, NASA Tech. Memo. NASA TN D-4408, NASA Langley Research Center.

Jezek, K. C., and G. Koh (1987) Effects of water and ice layers on the scattering properties of diffuse reflectors, *Appl. Opt.*, *26,* 5143-47.

Junge, K., et al. (2001), *In Selected Papers of the International Symposium on Sea ice and Its Interactions with Ocean, Atmosphere, and Biosphere*, Fairbanks, Alaska, 18-23 June 2000, M.D. Jeffreies and H. Eicken (eds.), *Annals of Glaciology*, 33, 304-310.

Kereszturi, A., et al. (2009), Recent rheologic processes on dark polar dunes on Mars: Driven by interfacial water? *Icarus,* 618.

Knight, J.B., E.E. Ehrichs, V. Kuperman, J.K. Flint, H.M. Jaeger and S.R. Nagel (1996) Experimental study of granular convection, *Phys. Rev. E*, 54, 5726-5738.

Kok, J. F. and N. O. Renno (2010), A comprehensive numerical model of steady state saltation (COMSALT), *J. Geophys. Res*., 114, D17204.

Kolle, J. J. (1994), Developing a hydraulic pulse generator, *Mechanical Engineering – CIME,* 1-7.

Kounaves, S. P., et al. (2007), The MECA Wet Chemistry Laboratory on the 2007 Phoenix Mars Scout Lander, *J. Geophys. Res.,* 114, E00A19.

Krothopalli. A., E. Rajkuperan, R. Alvi, and L. Lourenco (1999), Flow field and noise characteristics of a supersonic impinging jet, *J. Fluid Mechanics,* 392*,* 174-188.

Lamont, P. J., and B. L. Hunt (1980), The impingement of underexpanded axisymetrical jets on perpendicular and inclined flat plates, *J. Fluid Mechanics*, 100, 471-475.

Land, N., and H. Scholl (1966), Scaled LEM jet erosion tests, NASA Langley Working Papers, LWP–252, NASA Langley Research Center.

Land, N.S. and H.F. Scholl (1969), Scaled lunar module jet erosion experiments, NASA Technical Note, NASA TN-D-5051, NASA Langley Research Center.

Lee, C. (2007), Numerical modeling of mixed sediment resuspension, transport, and deposition during March 1998 episodic events in southern Lake Michigan, *J. Geophys. Res.*, 112.

Lekner, J. and M.C. Dorf (1988), Why some things are darker when wet, *Applied Optics*, 27, 1278-1280.

Longwell, P.A., (2002). *Mechanics of Fluid Flow*, Mc-Graw-Hill, New York, 1966.

Liu C. and S. R. Nagel (1992), Sound in Sand, *Phys Rev. Lett*., 68, 15.

Lyon, W. C., (1971), Monopropellant thruster exhaust effects on spacecraft, *J. Spacecraft and Rockets,* 8*,* 689–701.

Markham, J. R., et al. (2004), Integrated gas analyzer for complete monitoring of turbine engine test cells, *Applied Spectroscopy, 58*, 130–136.

Markiewicz, W. J., et al. (2009), Sublimation of exposed Snow Queen surface water ice as observed by the Phoenix Mars Lander, Lunar and Planet. Sci. Conf., 1667.

Marshall, J., et al. (2007), Phoenix touchdown tests, NASA Phoenix Project Internal Report, NASA JPL.

Martin, T.A. and L.E. Rockwell (1998) Test and modeling of the Mars ’98 Lander descent propulsion system waterhammer, 34th AIAA/ASME/SAE/ASEE Joint Propulsion Conf., AIAA 1998-3665, Cleveland, OH.

Mason, C. C. (1970), Comparison of actual vs. predicted lunar surface erosion caused by Apollo 11 descent engine, *Geol. Soc. Amer. Bull*., 81,6, 1807-1812.

Mason, C.C. and E.F. Nordmeyer (1969), An empirically derived erosion law and its application to lunar module landing, *Geo.Soc.Amer.Bull*, 80, 9, 1783-1788.

Mate, B., I. A. Graur, T. Elizarova, I. Chirokov, G. Tejeda, J. M. Fernandez and S. Montero (2001), Experimental and numerical investigation of an axisymmetric supersonic jet, *J. of Fluid Mech.*, 426, 177-197

Mazurek, K. A. and N. Rajaratnam (2005), Erosion of sand beds by obliquely impinging plane turbulent air jets, *J. Hyd. Res*., *43*, 5.

McBride, B. S., and S. Gordon (1996), Computer program for calculation of complex chemical equilibrium compositions and applications II, users manual and program description," NASA Reference Publication 1311, Lewis Research Center.

McCord, T.B. and J.H. Elias (1971), Mars: The spectral albedo (0.3 – 2.5μ) of small bright and dark regions, *Icarus*, *14,* 245-251.

McEwen, A.S. et al. (2009), The High Resolution Imaging Science Experiment (HiRISE) during MRO's Primary Science Phase (PSP), *Icarus*, 205, 1.

Mehta, M., et al. (2007), Characterization of the Impingement Dynamics of Pulsed Rocket Plumes with the Ground at Low Ambient Pressure, AIAA/ASME/ASEE/ SAE Joint Prop. Conf., 5707.

Mehta, M., et al. (2008), Site alteration and dust lifting during simulated Phoenix Mars landing, NASA JPL Internal Memorandum.

Mehta, R.C. (2008), Computations of flow field over Apollo and OPEX reentry modules at high speed, *Indian J. of Eng. & Materials*, 15, 30-40.

Mellon, M.T., et al. (2009) Ground ice at the Phoenix Landing Site: Stability state and origin, *J. Geophys. Res*., 114, E00E07

Menikoff, R. and B.J. Plohr (1989) The Riemann problem for real materials, *Rev.Mod. Physics*, 61, 75-130.

Metzger, P. T., et al. (2009), Jet-induced cratering of a granular surface with applications to lunar spaceports, *J. Aero. Engin*., 22, 1.

Metzger, P. T., et al. (2009), *Cratering and blowing soil by rocket engines during lunar landings*. Ed. H. Beneraoya, Lunar Settlements, CRC Press.

Mikucki, J. A., *et al.* (2009), A contemporary microbially maintained subglacial ferrous "ocean," *Science, 324,* 397-400.

Mohlmann D., A. Kereszturi (2010a), Viscous liquid film flow on dune slops of Mars, *Icarus*, 207, 654-658.

Mohlmann D. (2010b), The three types of liquid water on the surface of present Mars, *Int. J.*

of Astrobiology, 9, 1.

Moran, M., et al. (2005), Desert methane: Implications for life detection on Mars, *Icarus*, *178,* 277-280.

Mumma, M., *et al.* (2003), Strong release of methane on Mars in northern summer, *Science*, *323*, 1041-45.

Neakrase, L. D. V. and R. Greeley (2009), Dust devil sediment flux on Earth and Mars: Laboratory simulations, *Icarus, 206*, 1, 306-318.

Nichols, R.H. (2000), Turbulence Models and Their Application to Complex Flows, University of Alabama at Birmingham, Rev. 3.0.

Orloff, R.W. and D.M. Harland (2006) *Apollo: The Definitive Sourcebook*, Springer-Praxis Publishing, Chichester, UK.

Osterloo, M.M. et al. (2008), Chloride-bearing materials in the southern highlands of Mars, *Science*, 319, 5870.

Papp, J.L. and K.N. Ghia (1998). Study of turbulent compressible mixing layers using two-models including RNG k-ε model. AIAA paper 98-0320.

Pattison, C. S., et al. (2007), Cold gas dynamic manufacturing: a non-thermal approach to freeform fabrication, *Internat. J. of Machine Tools & Manufacture, 47;* 627-634.

Perovich, D.K. (1996), *The optical properties of sea ice*, US Army Corps of Engineers, Cold Regions Research & Engineering Laboratory Monograph 96-1.

Pestova, O. N. (2005), Polythermal study of the systems M(ClO4)2-H2O (M2+ = Mg2+, Ca2+, Sr2+, Ba2+), *Russ. J. Appl. Chem.,* Engl. Transl., *78,* 409-13.

Plemmons, D. H. (2008), Effects of the Phoenix Lander descent thruster plume on the Martian surface, *J. Geophys. Res*., 113, E00A11.

Plemmons, D., et al. (2007), Spectroscopic plume analysis of the Phoenix Mars Lander hydrazine monopropellant thrusters, AIAA/ASME/SAE/ASEE Joint Propulsion Conf. & Exhibit.

Pollard, B., Berkun, A., Tope, M., Andricos, C., Okonek, J., and Lou, Y., (2007).“Ka-Band Radar Terminal Descent Sensor,” NASA Tech Brief, NPO-44462, Sept.

Pudasaini, S. P. and C. Kroner (2008), Shock waves in rapid flows of dense granular materials: Theoretical predictions and experimental results, *Phys. Rev. E*, 041308.

Queen, E., Prince, J., and Desai, P., (2008). “Multi-Body Modeling and Simulation for the Mars Phoenix Lander Entry, Descent and Landing” AIAA-2008-7347.

Rajaratnam, N. et al., (2002). "Erosion of a polystyrene bed by obliquely impinging circular turbulent air jets" *J. Hydr. Eng.*, Vol. 40, No. 6.

Renno, N. O., et al. (2009), Possible Physical and Thermodynamical Evidence of Liquid Water at the Phoenix Landing Site, *J. Geophys. Res*., *114,* E00E03.

Roberts, B., et al. (1982), Plume base flow simulation technology, NASA TR – 19820023542, NASA Johnson Space and Marshall Space Flight Centers.

Romine, G. L., et al. (1973), Site alteration effects from thruster exhaust impingement during a simulated Viking Mars landing: nozzle development and physical site alteration, NASA Langley Contractor Report, CR-2252, Martin Marrieta Co.

Sayer, C. F. (1970), The decomposition of hydrazine on the Shell 405 catalyst, AIAA Propulsion Joint Specialist Conf.

Schultz, P. H., et al. (2007), The Deep Impact oblique impact cratering experiment. *Icarus, 190*, 2, 295-333.

Scroggs, S.D and G.S. Settles (1996), An experimental study of supersonic microjets, *Experiments in Fluids*, 21, 401- 409.

Scott, R. F. and H-Y. Ko (1968), Transient Rocket-Engine Gas Flow in Soil, *AIAA J.*, 6.2, 258-26.

Seinfeld, J. H., and S. N. Pandis (2006), *Atmospheric Chemistry and Physics: From Air Pollution to Climate Change*, 2nd ed., 1203pp,Wiley, New York.

Sengupta, A., et al. (2009), Mars Landing Engine Plume Impingement Environment of the Mars Science Laboratory, IEEE/AIAA Aerospace Conf., 1349.

Shao, Y. and H. Lu (2000), A simple expression for wind erosion threshold friction velocity, *J. Geophys. Res*., *105*, D17, 22437-22444.

Shaw, A., et al. (2009), Phoenix soil physical properties investigation, *J. Geophys. Res*., 114, E00E05.

E. Shimshi, G. Ben-dor, and A. Levy (2009), A. Viscous simulation of shock-reflection hysteresis in over-expanded planar nozzles. *J. of Fluid Mech.*, 635, 189-206.

Shorthill, R. W. (1976a), Physical properties of the Martian Soil Surface from Viking 1 Lander: Preliminary Results, *Science*, 193, 805 – 809.

Shorthill, R. W., et al. (1976b), The Environ of Viking 2 Lander, *Science*, 194, 1309-1318.

Sizemore, H. G., et al. (2009), In Situ Analysis of Ice Table Depth Variations in the Vicinity of Small Rocks at the Phoenix Landing Site, *J. Geophys. Res*, 115, E00E09.

Sizemore H. G. and M. Mellon (2008), Laboratory characterization of the structural properties controlling dynamical gas transport in Mars-analog soils, *Icarus*, 197, 2.

Smith, P. H., et al. (2009), H_2O at the Phoenix Landing Site, *Science*, *325*, 5936, 58-61.

Smith, R. B. (2005), *Computing radiances, reflectance and albedo from DN's*, Yale University Press.

Space Studies Board, National Research Council (2002), *Signs of life: A report based on the April 2000 Workshop on Life Detection Techniques*, National Academy Press, Washington, D.C.

Steltzner, A. et al., (2006). "Mars Science Laboratory Entry, Descent, and Landing System," Proc IEEE Aerospace Conference, Big Sky, MT.

Stitt, L.E. (1963), Interaction of highly underexpanded jets with simulated lunar surfaces, NASA-TN-D-1095, NASA Glenn Research Center, Cleveland, OH.

Sutton, G.P. and O. Biblarz (2001), *Rocket Propulsion Elements*, 7th edition , John Wiley & Sons Pub., New York.

Squyres, S. W., et al. (2004), In situ evidence for an ancient aqueous environment on Mars, *Science*, *306,* 1709-1714.

Taylor, P. et al. (2010), On pressure measurement and seasonal pressure variations during the Phoenix Mission. *J. Geophys. Res.*, 115, E00E15.

Teruel, F. E. and Rizwaan-uddin (2009), A new turbulence model for porous media flows. Part II: Analysis and validation using microscopic simulations, *Int. J. Heat & Mass Transf.*, 52, 5193-5203.

Terzaghi, K., *The Structure of Turbulent Shear Flow,* Theoretical Soil Mechanics, John Wiley and Sons, New York, 1943.

Twomey, S. A., et al. (1986), Reflectance and albedo differences between wet and dry surfaces, *Applied Optics*, *25,* 431-37.

Umbanhowar, P.B., F. Melo and H.L. Swinney (1996) Localized Excitations in a Vertically Vibrated Granular Layer. *Nature* 382: 793-796.

Valverde, J. M., et al. (2003), Experimental study on the dynamics of gas-fluidized beds. *Phys. Rev. E.*, 67, 016303.

Van Leer, B. (1982). Flux-vector splitting for the Euler equations, in *Lecture Notes in Physics*. 170. Springer, Berlin. pp. 507-512.

Van Norman, J. W. and L. Novak (2009), CFD support of MSL MLE plume simulations. NASA Contractor Report, No. NNL04AA03Z.

Vergin, M.I. et al. (2008), Analysis of the 3-D shape of the terrestrial bow shock by interball/magion 4 observations, *Advances in Space Research*, 28, 45-55.

Vick, A.R. and E.H. Andrews Jr. (1964), An experimental investigation of highly underexpanded free jets impinging upon a parallel flat surface, NASA Technical Note, NASA TN-D-2326, NASA Langley Research Center, Washington, D.C.

Vitton, S., et al. (1990), Liquefaction and flow failure during seismic exploration, *J. Geotech. Engin., 116,* 1881-1899.

Walters, R. W., P. Cinnella, and D.C. Slack (1993), Characteristic-Based Algorithms for Flows in Thermo-Chemical Non-Equilibrium, *AIAA J.* **30**, 1304-1313

Way, D., Powell, R., Chen, A., and Steltzner, A. (2006). "Asymptotic Parachute Performance Sensitivity" IEEE Aerospace Conference, Big Sky, MT, March.

Whetsel, C., et al. (2000), Jet Propulsion Laboratory MPL Investigation Board, Report on the Loss of the Mars Polar Lander and Deep Space 2 Missions, JPL D-18709.

Whiteway, J. A., et al. (2009), Mars water ice clouds and precipitation, *Science, 325,* 68-70.

Wong, E., and J. P. Masciarelli (2002), Autonomous guidance and control design for hazard avoidance and safe landing on Mars, AIAA Atmospheric Flight Mechanics Conf.

Youd, T. L. and I. M. Idriss (2001), Liquefaction resistance of soils: Summary report from the 1996 NCEER and 1998 NCEER/NSF workshops on evaluation of liquefaction resistance of soils, *J.Geotech. and Geoenviron. Engin., 127,* 297-313.

Zorzano, M.-P, (2009), The stability of liquid saline water on Mars. *Geophys. Res. Lett., 36,* L20201.